

Durham E-Theses

Luminescent Transition Metal Complexes of Terdentate Quinoline-Based Ligands for Light-Emitting Devices

PARKES, LOUISE,FRANCESCA

How to cite:

PARKES, LOUISE,FRANCESCA (2012) *Luminescent Transition Metal Complexes of Terdentate Quinoline-Based Ligands for Light-Emitting Devices*, Durham theses, Durham University. Available at Durham E-Theses Online: <http://etheses.dur.ac.uk/3461/>

Use policy

The full-text may be used and/or reproduced, and given to third parties in any format or medium, without prior permission or charge, for personal research or study, educational, or not-for-profit purposes provided that:

- a full bibliographic reference is made to the original source
- a [link](#) is made to the metadata record in Durham E-Theses
- the full-text is not changed in any way

The full-text must not be sold in any format or medium without the formal permission of the copyright holders.

Please consult the [full Durham E-Theses policy](#) for further details.

Luminescent Transition Metal Complexes
of
Terdentate Quinoline-Based Ligands
for
Light-Emitting Devices

LOUISE FRANCESCA PARKES

2012



SUBMITTED IN CONFORMITY WITH THE REQUIREMENTS FOR
THE DEGREE OF DOCTOR OF PHILOSOPHY

Acknowledgements

I would like to express my sincere thanks to Dr. J. A. Gareth Williams for his support and advice throughout my PhD. Acknowledgement goes to Durham University and the EPSRC for funding to carry out this research. I am also grateful to Dr. Phil Dyer and Dr. Chris Greenwell for the support and understanding shown during my thesis-writing.

Thanks to all the members of the Williams group for their help, advice and friendship: Victoria, Will, Lisa, Pierpaolo, Gemma, Stéphanie, Jonathan and Fabian, and the fourth year and summer students. Thanks also to all in lab. 101 who have put up with me whilst writing up!

I am indebted to the chemistry services at Durham and my gratitude goes to: Dr. Alan Kenwright, Catherine Heffernan, Ian McKeag, Dr. David Apperley and Fraser Markwell for NMR spectroscopy, particularly Alan and David for assistance with my thesis; Dr. Mike Jones, Lara Turner, Dr. Jackie Mosely, Dr. Dave Parker and Peter Stokes for mass spectrometry; Dr. Andrei Batsanov and Dr. Hazel Sparkes for crystallography; Judith Magee for elemental analysis and Dr. Aileen Congreve for LCMS and tea-break chats! Thanks to everyone who made the department a great place to work: the tea ladies, glassblowers and everyone in stores and the workshops.

I am grateful to Brad for temporary use of his fumehood, Michael for help with DFT, Latex and printing, and Emma and Sarah for support through the final stages. Thanks to Dr. Chris Pearson, Prof. Mike Petty, Dr. Massimo Cocchi and Dr. Valeria Fattori for OLED fabrication, and to Prof. Hartmut Yersin and Dr. Andreas Rausch for cryogenic spectroscopy and their kindness in hosting me in Regensburg.

My thanks go to my friends in Durham who made my time here so enjoyable; amongst many others, thanks to: Aruna, Laura, Rachael, Marie-Hélène, Pippa, Andy I., Maykel, Andy G., Adam, Dan, Geri, Lucas, Ben and Sam. Finally, thank you to Richard for support and help with so many things (and tea!), and to my family for all their love, support and encouragement over the years. Thank you very much!

Abstract

Luminescent transition metal complexes are of interest due to their applications in areas such as organic light-emitting devices (OLEDs), solar cells and biological probes and sensors. The use of heavy transition metals promotes phosphorescent emission from the triplet state. In OLEDs, this enables the quantum efficiency of devices to reach a theoretical maximum of 100 % through harvesting photons from both singlet and triplet excited states.

The synthesis of cyclometallated N[^]C[^]N-coordinated iridium(III) complexes and two representative rhodium(III) analogues, based upon a series of isomeric 1,3-(diquinolyl)benzene ligands, is presented. The d⁶ complexes take the form M(N[^]C[^]N)(X[^]Y)Z, where X[^]Y denotes a bidentate ligand binding through N[^]C⁻ or N[^]N-coordination, and Z denotes a monodentate ligand, such as chloride. Platinum(II) complexes containing terdentate ligands, of the form Pt(N[^]C[^]N)Cl, have also been investigated. All complexes are luminescent at room temperature and at 77 K, emitting in the red-to-yellow region of the visible spectrum. The photophysical properties are interpreted with the aid of electrochemical and computational analyses. Preliminary results from incorporation of three of the complexes into OLEDs are described. In addition, an iridium phosphor used in conjunction with a blue emitter produces a white device which displays excellent white light characteristics.

The platinum(II) complex of 1,3-di(8-quinolyl)benzene features six-membered chelate rings, a rarer feature than the usual five-membered chelate rings common to the majority of metal complexes studied to date. The related N[^]N[^]N-coordinating ligand, 2,6-di(8-quinolyl)pyridine, has also been used to prepare a complex of the form [Pt(N[^]N[^]N)Cl]⁺, which, unlike [Pt(tpy)Cl]⁺, displays moderately intense luminescence in solution, attributed to a more favourable bite angle. The corresponding [Ir(N[^]N[^]N)₂]³⁺ complex is also reported.

Declaration

The work described herein was carried out at Durham University between October 2007 and March 2011 under the supervision of Dr J. A. Gareth Williams. Unless otherwise stated all the work is my own and has not been submitted previously for a degree at this or any other university.

Louise F. Parkes

Statement of Copyright

The copyright of this thesis rests with the author. No quotation from it should be published without the prior written consent and information derived from it should be acknowledged.

Contents

Contents	iv
Abbreviations	vii
1 Introduction	1
1.1 Introduction	1
1.1.1 Origins of luminescence	1
1.2 Octahedral d ⁶ complexes	4
1.2.1 Ruthenium(II) polypyridyl complexes	4
1.2.2 Iridium(III) polypyridyl complexes	7
1.2.3 Cyclometallated iridium(III) complexes	9
1.2.4 Iridium(III) complexes containing terdentate ligands	10
1.2.4.1 [IrN ₅ X] ²⁺ -Coordination	11
1.2.4.2 [IrN ₄ X ₂] ⁺ -Coordination	12
1.2.4.3 [IrN ₃ X ₃]-Coordination	14
1.2.5 Rhodium(III) polypyridyl complexes	15
1.2.5.1 Cyclometallated rhodium(III) complexes	16
1.3 Square planar d ⁸ polypyridyl complexes	18
1.3.1 Platinum(II) polypyridyl complexes	18
1.3.1.1 Platinum(II) complexes containing neutral terden- tate ligands	20
1.3.1.2 Cyclometallated platinum(II) complexes	22
1.3.1.3 Pt(N [^] N [^] C)Z	22
1.3.1.4 Pt(N [^] C [^] N)Z	24
1.3.1.5 [Pt(C [^] N [^] C)Z] ⁻	27
1.3.2 Theoretical study of cyclometallated platinum(II) complexes .	28
1.3.3 Platinum(II) complexes containing six-membered chelate rings	30
1.4 Organic light-emitting devices (OLEDs)	33
1.4.1 Transition metal complexes in OLEDs	37

1.4.2	White organic light-emitting devices (WOLEDs)	40
2	Synthesis of iridium, rhodium and platinum complexes	43
2.1	Synthesis of ligands and precursors	43
2.1.1	Cyclometallating terdentate N [^] C [^] N ligands	45
2.1.1.1	Synthesis of parent cyclometallating ligands	45
2.1.1.2	Substituted N [^] C [^] N ligands	49
2.1.1.3	Synthesis of an asymmetric ligand	51
2.1.2	Terdentate N [^] N [^] N ligands	52
2.1.3	Tetradentate ligands	53
2.2	Synthesis of d ⁶ iridium(III) and rhodium(III) complexes	54
2.2.1	Cyclometallated N [^] C [^] N iridium(III) complexes	55
2.2.2	Cyclometallated N [^] C [^] N rhodium(III) complexes	61
2.2.3	Synthesis of an N [^] N [^] N iridium(III) complex	62
2.3	Synthesis of d ⁸ platinum(II) complexes	63
2.3.1	Terdentate cyclometallated platinum(II) N [^] C [^] N complexes	63
2.3.2	Terdentate platinum(II) N [^] N [^] N-coordinated complexes	66
2.3.3	Tetradentate-coordinated platinum(II) complexes	67
2.4	Metathesis reactions with alkynes	68
2.5	Crystal structure elucidation by X-ray diffraction	70
2.5.1	Organic precursors and ligands	70
2.5.2	Complexes	75
2.6	NMR studies of [Pt(dqp)Cl]PF ₆	80
2.6.1	Chemical shift anisotropy-induced relaxation	81
2.6.2	Solid state NMR spectroscopy	85
2.7	Concluding remarks	87
3	Photophysical, electrochemical and computational studies of d⁶ complexes	91
3.1	Complexes based upon 1,3-di(1-isoquinolyl)benzene, 1-diqb, 1	91
3.1.1	Computational studies	92
3.1.2	Electrochemistry	95
3.1.3	Absorption spectroscopy	99
3.1.4	Emission spectroscopy	102
3.2	Iridium(III) complexes based upon further isomers of terdentate quinolyl ligands	105
3.2.1	Computational studies	106
3.2.2	Electrochemistry	109

3.2.3	Absorption spectroscopy	110
3.2.4	Emission spectroscopy	112
3.2.5	Concluding remarks	114
4	Photophysical, electrochemical and computational studies of d⁸ complexes	118
4.1	Platinum complexes containing five-membered chelate rings	118
4.1.1	Computational studies	119
4.1.2	Electrochemistry	121
4.1.3	Absorption spectroscopy	123
4.1.4	Emission spectroscopy	125
4.2	Platinum complexes containing six-membered chelate rings	128
4.2.1	Computational studies	129
4.2.2	Electrochemistry	136
4.2.3	Absorption spectroscopy	138
4.2.3.1	N [^] C [^] N-coordination	138
4.2.3.2	N [^] N [^] N-coordination	140
4.2.4	Emission spectroscopy	141
4.2.4.1	N [^] C [^] N-coordination	141
4.2.4.2	N [^] C [^] N-coordination	144
4.2.5	Concluding remarks	150
5	Iridium versus platinum: cryogenic studies and OLED fabrication	151
5.1	Cryogenic spectroscopy	151
5.1.1	Cryogenic studies of Ir(1-diqb)(ppy)Cl	153
5.1.2	Cryogenic studies of Pt(1-diqb)Cl	154
5.2	Organic light-emitting device (OLED) fabrication	157
5.2.1	OLEDs fabricated by thermal evaporation under vacuum	158
5.2.2	OLEDs fabricated by spin-coating	160
5.2.3	Fabrication of dual phosphor white OLEDs (WOLEDs)	165
5.3	Concluding remarks	169
5.4	Research Conclusion	171
6	Experimental	172
6.1	Synthetic reagent specifications and characterisation equipment	172
6.2	Photophysical measurements	173
6.3	Electrochemical measurements	175
6.4	Density functional theory (DFT) calculations	176
6.5	Synthesis	176

CONTENTS

6.5.1	General synthetic procedures	176
6.5.2	Catalysts and precursors	177
6.5.3	Ligands	184
6.5.4	Chloro-bridged metal dimers	195
6.5.5	Iridium complexes	197
6.5.6	Rhodium complexes	205
6.5.7	Platinum complexes	207
References		214
Appendix A		232
Appendix B		247
Appendix C		254

Abbreviations

Acronyms

$\Delta d d_{occ}$	Splitting Between Highest Occupied d-orbitals
$\Delta d d^*$	Splitting Between Highest Occupied and Lowest Unoccupied d-orbitals
η_{ext}	External Quantum Efficiency
η_{int}	Internal Quantum Efficiency
Φ_{lum}	Photoluminescent Quantum Yield
τ	Emission Decay Lifetime
k_r	Rate Constant of Radiative Decay
ASAP	Atmospheric Solids Analysis Probe
COSY	Correlation Spectroscopy
CRT	Cathode Ray Tube
CSA	Chemical Shift Anisotropy
DFT	Density Functional Theory
DMSO	Dimethylsulfoxide
EBL	Electron Blocking Layer
EIL	Electron-Injection Layer
EL	Electroluminescence
EML	Emissive Layer
EQE	External Quantum Efficiency

ES	Electrospray
ETL	Electron Transport Layer
HBL	Hole Blocking Layer
HF	Hartree–Fock
HIL	Hole-Injection Layer
HMBC	Heteronuclear Multiple Bond Correlation Spectroscopy
HOMO	Highest Occupied Molecular Orbital
HSQC	Heteronuclear Single Quantum Correlation/Coherence Spectroscopy
HTL	Hole Transport Layer
IC	Internal Conversion
IL	Intraligand
ISC	Intersystem Crossing
ISC'	Back Intersystem Crossing
ITO	Indium Tin Oxide
LC	Ligand Centred
LCD	Liquid Crystal Display
LED	Light-Emitting Diode
LLCT	Ligand-to-Ligand Charge Transfer
LMCT	Ligand-to-Metal Charge Transfer
LUMO	Lowest Unoccupied Molecular Orbital
MC	Metal Centred
MLCT	Metal-to-Ligand Charge Transfer
MS	Mass Spectrometry
MTL	Mixed Transition Layer
N-het	Monodentate N-heterocyclic Ligand

NMR	Nuclear Magnetic Resonance
NOESY	Nuclear Overhauser Effect Spectroscopy
OLED	Organic Light Emitting Device
OPVD	Organic Vapour Phase Deposition
PDP	Plasma Display Panel
PL	Photoluminescence
PLED	Polymer Light Emitting Device
QToF	Quadrupole Time-of-Flight
SBLCT	σ -Bond-To-Ligand Charge Transfer
SCE	Saturated Calomel Electrode
SOC	Spin Orbit Coupling
ssNMR	Solid-State Nuclear Magnetic Resonance
TD-DFT	Time-Dependent Density Functional Theory
THF	Tetrahydrofuran
VR	Vibrational Relaxation

Compounds

Alq ₃	tris(8-hydroxyquinolato)aluminium
bmpqp	2,6-bis(7'-methyl-4'-phenyl-2'-quinoly)pyridine
BPhen	4,7-diphenyl-1,10-phenanthroline
BPI	bis(2-pyridylimino)isoindoline
bpy	2,2'-bipyridine
dppy	2,6-diphenylpyridine
dpyb	1,3-di(2-pyridyl)benzene
dpyx	1,3-di(2-pyridyl)-4,6-dimethylbenzene
dqp	1,3-di(quinoly)pyridine

FIrpic	bis[(4,6-difluorophenyl)-pyridinato- <i>N, C</i> ^{2'}]picolinatoiridium
hat	1,4,5,8-tetraazaphenanthrene
Mebib	bis(<i>N</i> -methylbenzimidazolyl)benzene
Mebip	bis(<i>N</i> -methylbenzimidazolyl)pyridine
N-BDAVBi	<i>N</i> -(4-((<i>E</i>)-2-(6-((<i>E</i>)-4-(diphenylamino)styryl)naphthalen-2-yl)vinyl)phenyl)- <i>N</i> -phenylbenzenamine
NBP	<i>N, N'</i> -bis(1-naphthyl)- <i>N, N'</i> -diphenyl-1,1'-biphenyl-4,4'-diamine
NPD	4,4'-[bis(1-naphthyl)(phenyl)amino]-1,1'-biphenyl
Np	naphthalene
Phbpy	6-Phenyl-2,2'-bipyridine
PPV	poly(<i>p</i> -phenylenevinylene)
ppy	2-phenylpyridine
PtOEP	2,3,7,8,12,13,17,18-octaethyl-21H,23H-porphine platinum(II)
tap	1,4,5,8,9,12-hexaazatriphenylene
TAZ	3-phenyl-4-(1'-naphthyl)-5-phenyl-1,2,4-triazole
TEMPO	2,2',6,6'-tetramethylpiperidin-1-yloxy
tphbpy	4'-tolyl-6'-phenyl-2,2'-bipyridine
TPD	<i>N, N'</i> -diphenyl- <i>N, N'</i> -bis(3-methyl)-1,1'-biphenyl-4,4'-diamine
tpy	2,2':6',2''-terpyridine
ttpy	4'-tolylterpyridine

Chapter 1

Introduction

1.1 Introduction

Luminescent heavy metal complexes have been studied for over fifty years for their photophysical properties, which allow them to be used in applications requiring light emission upon application of a stimulus. Research has been driven by the numerous uses for these phosphors such as in organic light emitting devices or diodes (OLEDs),^{1,2,3,4} chemosensing,^{5,6} non-linear optics,^{7,8} bioimaging agents^{9,10} and biological probes.^{11,12}

1.1.1 Origins of luminescence

Luminescence is the emission of light due to relaxation of a molecule in the excited state after an excitation process has taken place. Electroluminescence (EL), as employed in OLED technology, is induced by an applied current/voltage whereas photoluminescence (PL) is stimulated by light. In photoluminescence, absorption of energy in the form of light radiation that corresponds to a specific electronic transition energy, excites a molecule from the ground state to a higher energy manifold, termed an excited state. Classically, the Franck–Condon principle states that electronic transitions are more likely to occur without changes in the position of the nuclei in the molecular entity and its environment, thus the resulting transition is termed a vertical transition (Fig. 1.1).¹³ In quantum terms, this requires a similar nuclear configuration and positive overlap of the wavefunctions in the initial and final states for the transition to occur, whereby the intensity of a transition is proportional to the square of the overlap integral between the vibrational wavefunctions of the states involved in the transition.¹⁴ Typically, the molecule is excited from the ground state into the lowest excited state, upon which, it relaxes back to the ground

state *via* either radiative or non-radiative decay. The vast majority of ground state molecules exist as singlet states, where the overall spin, S , is equal to 0, due to all the electrons being paired electrons, whereas after excitation the total spin can either be 0 (spins anti-parallel) or 1 (spins parallel). This gives rise to singlet (S) and triplet (T) states, respectively, with the ground state denoted as S_0 and higher vibrational states termed S_1, S_2, \dots, S_n and T_1, T_2, \dots, T_n .

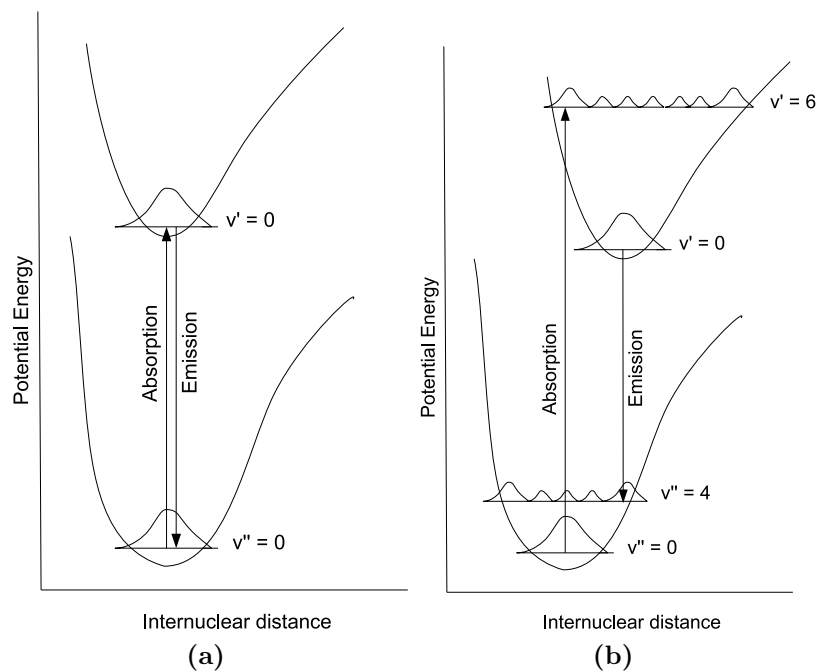


Fig. 1.1 Schematic representation of high probability electron transitions from the lowest vibrational state for: (a) a small geometric change between ground and excited states, and (b) a large geometric change between ground and excited states.

The transitions that occur upon excitation are best visualised using a Jablonski diagram (Fig. 1.2). After excitation, the emissive states decay either *via* non-radiative pathways due to vibrational relaxation, or *via* emission of light in the form of either fluorescence or phosphorescence. Fluorescence is a quantum mechanically spin-allowed process between states of the same multiplicity (*i.e.* $\Delta S = 0$, therefore $S \leftarrow S$ or $T \leftarrow T$), whilst phosphorescence is a formally spin-forbidden process involving a transition between states of differing multiplicities (*i.e.* $S \leftarrow T$). Accordingly, fluorescence occurs on a much faster timescale and has a shorter lifetime (of the order of 10^{-9} – 10^{-7} s compared to 10^{-3} – 10^2 s for phosphorescence). Due to energy loss by simultaneous non-radiative decay processes, the energy of the emitted photon is lower than the absorption energy, which is observed as a red-shift, known as a Stokes' shift.¹⁵ The magnitude of this shift is dependent on the degree of geometric reorganisation occurring for transitions between the ground and excited states.

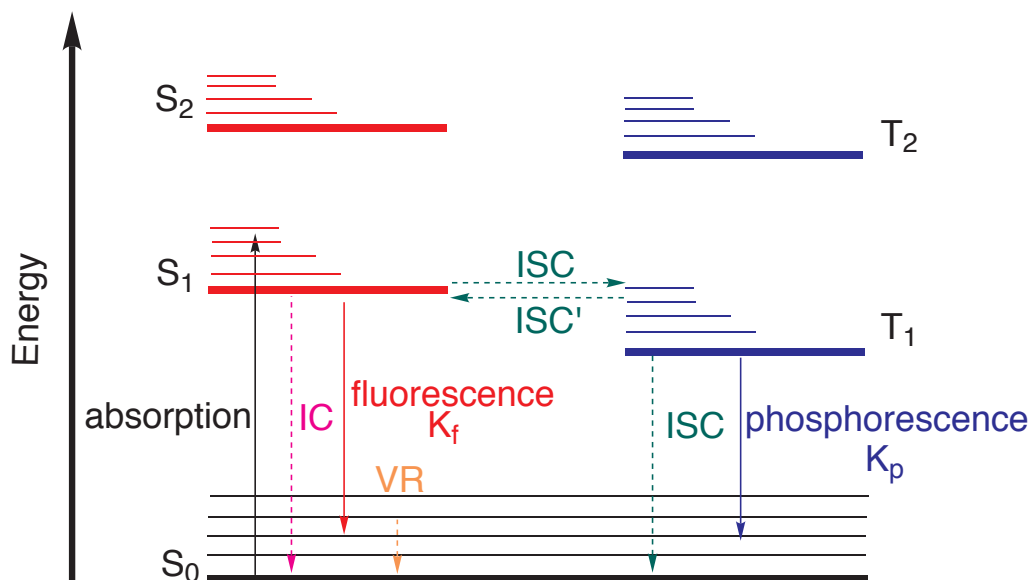


Fig. 1.2 Jablonski Diagram; solid lines and dotted lines represent radiative transitions and non-radiative transitions, respectively.

The triplet states in a molecule are lower in energy than the equivalent singlet states because of the quantum mechanical property of spin correlation, with the result that phosphorescent emission is lower in energy than the corresponding singlet emission. Fluorescence almost always originates from the lowest vibrational levels of the first excited state, S₁, an observation known as Kasha's rule, owing to the competing non-radiative pathways from higher vibrational excited states occurring much more readily than radiative decay.¹⁶ These radiationless pathways consist of internal conversion (IC), intersystem crossing (ISC), reverse- or back-intersystem crossing (ISC') and vibrational relaxation (VR). Excitation causes population of higher vibrational levels of S_n, where rapid IC, an allowed transition between states of the same multiplicity and the non-radiative analogue of fluorescence, occurs to lower singlet states. In turn, energy is lost by fast VR processes (10⁻¹⁴–10⁻¹¹ s) from higher vibrational levels of the singlet states to lower vibrational levels.

In order to observe phosphorescence, IC to S₀^v (where *v* indicates a vibrationally excited state) must be inefficient relative to ISC. Fluorescence is commonly seen in organic fluorophores where the rate of ISC is slow, so population of the triplet state does not occur readily. In organometallic compounds, however, even if a transition is formally spin-forbidden based upon symmetry, there are several cases in which phosphorescence is observable; vibronic coupling may permit vibronic transitions and the incidence of spin-orbit coupling (SOC), magnified by the use of heavy transition metal atoms, promotes phosphorescent emission. The so called 'heavy-atom' effect increases spin-orbit coupling due to the larger nuclear charge present (the

magnitude of the coupling is approximately dependent on Z^4 , where Z = nuclear charge).¹⁷ As a consequence of the rise in interactions between the spin angular momentum and orbit angular momentum, S is no longer a strictly valid quantum number and so the $\Delta S = 0$ selection rule based upon it is inappropriate.¹⁸ The outcome of this is that any process involving a change in multiplicity becomes more favourable because the rate coefficients for all transitions involving both the singlet and triplet states are increased, thereby promoting phosphorescence.

Optimising metal complexes to favour triplet emission is highly desirable for the production of OLEDs, using a technique called triplet harvesting. Nevertheless, this process is not straightforward due to the variety of excited states and transitions possible in a many-electron set-up. Excited states are generated when electromagnetic radiation exactly corresponds to the energy difference between two orbitals; the origin of which determines the nature of emission. The excited states and transitions can be classified as follows:

- *Ligand-centred (LC)/ Intraligand (IL) π - π^* or n- π^** : Transfer of an electron from a ligand-based π - or non-bonding orbital to a π^* anti-bonding orbital.
- *Metal-centred (MC) d-d*: Transfer of an electron between non-degenerate d-orbitals, which arise from the splitting of the d-orbitals upon ligand coordination.
- *Metal-to-ligand charge transfer (MCLT) d- π^** : Transfer of an electron from a metal-centred d-orbital to a ligand-centred π^* -antibonding orbital.
- *Ligand-to-metal charge transfer (LMCT) π -d*: Transfer of an electron from a ligand-centred π -orbital to a vacant metal-centred d-orbital.
- *Ligand-to-ligand charge transfer (LLCT) π - π^** : Transfer of an electron from a ligand-centred π -orbital to a ligand-centred π^* -antibonding orbital on a different ligand.

1.2 Octahedral d^6 complexes

1.2.1 Ruthenium(II) polypyridyl complexes

Since the initial studies of luminescent heavy metal complexes in the 1950s, research into polypyridyl complexes of the platinum group metals has flourished. In 1959 Paris and Brandt reported (incorrectly) the now ubiquitous compound $[\text{Ru}(\text{bpy})_3]^{2+}$, containing the N^N-coordinating ligand 2,2'-bipyridine (bpy), (Fig. 1.3a) as being

a fluorescent molecule¹⁹ and from that time onwards, interest in its attractive properties steadily increased.^{20,21,22} From the 1970s, when it was first proposed as a potential energy transfer agent,²³ $[\text{Ru}(\text{bpy})_3]^{2+}$ has become the most widely studied luminescent compound due to its unequivocal ³MLCT excited state character and long lifetime. Accordingly, related polypyridyl ligands have been thoroughly investigated for ruthenium(II) and osmium(II) systems.²⁴

Complexes containing terdentate ligands have received less attention than those including bidentate ligands, despite having several advantages over tris(bidentate) species. Firstly, a more extended coordination framework is associated with terpyridyl-type ligands, which presents an increased π -conjugated network, and so the possibility of increased charge-transfer exists. Furthermore, terdentate species are typically more rigid than bidentate systems, thus are less susceptible to distortions on creation of an excited state. This is preferable in comparison with molecules that undergo large geometry changes on excitation as this can cause quenching. A significant advantage of bis(terdentate) species when regarding more elaborate chemistry lies in the fact that they are achiral, whereas tris(bidentate) compounds are intrinsically chiral with D_{2d} symmetry or lower (D_3 and C_2 are common point groups for tris(bidentate) complexes). This axial symmetry allows molecules to be connected linearly in dyads or triads, without formation of diastereomers.^{25,26}

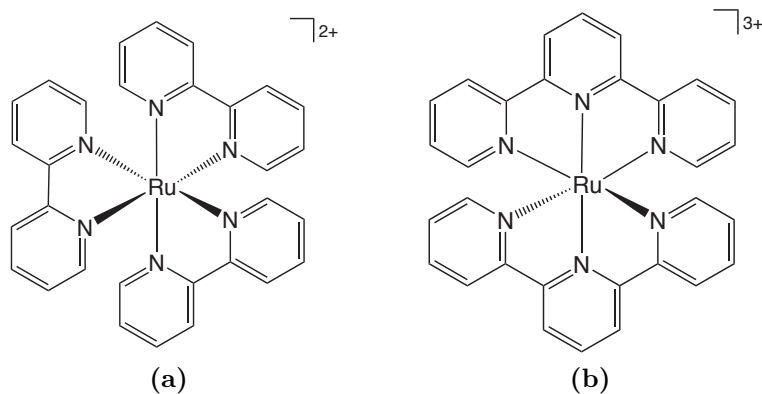


Fig. 1.3 Structure of (a) $[\text{Ru}(\text{bpy})_3]^{2+}$ and (b) $[\text{Ru}(\text{tpy})_2]^{3+}$.

As a terdentate analogue of $[\text{Ru}(\text{bpy})_3]^{2+}$, the 2,2':6',2''-terpyridine (tpy) compound $[\text{Ru}(\text{tpy})_2]^{3+}$, (Fig. 1.3b) was first prepared in 1934,²⁷ and displays intense luminescence from a ³MLCT state at 77 K, yet at room temperature it is practically non-emissive with a lifetime of 250 ps.²⁸ Interpretation of this result led to the theory of close-lying d-d MC states that lead to deactivation of the MLCT state *via* non-radiative decay pathways.²⁹ It was later suggested by Meyer *et al.* that the quenching effect arises from the unfavourable bite angle of the tpy ligand resulting

in weak ligand field splitting, causing a lowering of the d-d states.³⁰

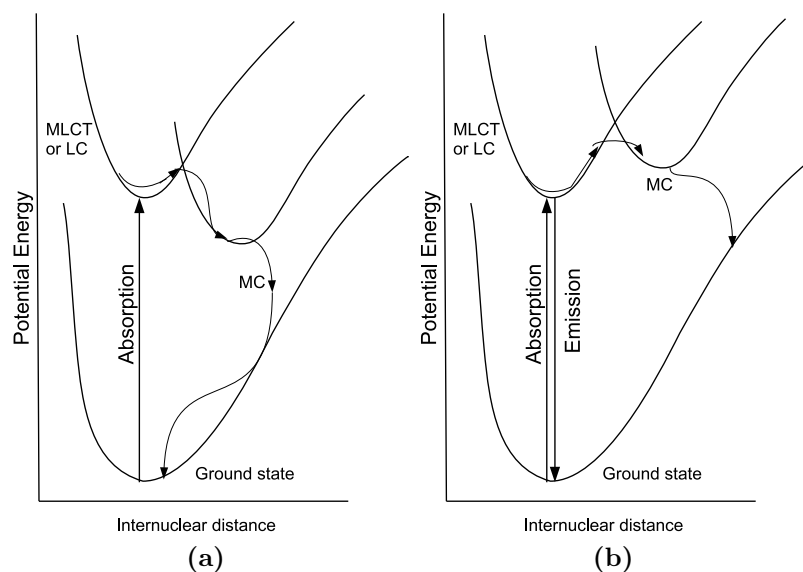


Fig. 1.4 Potential energy surfaces for: (a) a deactivating MC d-d state lower in energy than the emissive states, thus causing non-radiative decay, and (b) a higher energy d-d state allowing luminescent decay from a CT or LC state.

The unfavourable bite angle of the tpy ligand causes its complexes to be sterically strained, which has led to investigation into alternative terdentate ligands with increased ligand field strength. Various adaptations of the tpy framework have been adopted to form complexes exhibiting the unusual chelating effect of encasing the metal centre in six-membered rings, rather than the five-membered rings seen in the majority of heavy metal complexes. This has the effect of generating a more favourable bite angle, so that the N–Ru–N bond angle is approaching 180°. The groups of Ruben³¹ and Heinze³² have each synthesised ruthenium(II) complexes containing carbon- or nitrogen-based bridging groups between the pyridyl rings of tpy, such that some or all of the chelates formed are six-membered rings (Fig. 1.5). The bond angles found in the crystal structure of the complex with carbonyl bridges (Fig. 1.5a) are almost linear at ca. 178°, allowing a more favourable octahedral geometry than seen for $[\text{Ru}(\text{tpy})_2]^{2+}$, which has N–Ru–N angles of 158.4°. ³³ This should generate a stronger ligand field and ideally lower the population of the deactivating MC states whilst raising the energy of the d-d states. An increase in quantum yield and decay lifetime was seen in each case for these expanded ring systems, in comparison with the scarcely emissive $[\text{Ru}(\text{tpy})_2]^{2+}$. Heinze *et al.* reported quantum yields of the order 10^{-3} with a slight increase in lifetime on the nanosecond timescale,³² whilst the carbonyl-bridged compound has a far superior quantum yield of 0.3 in degassed MeCN with a lifetime of 3.3 μs .³¹

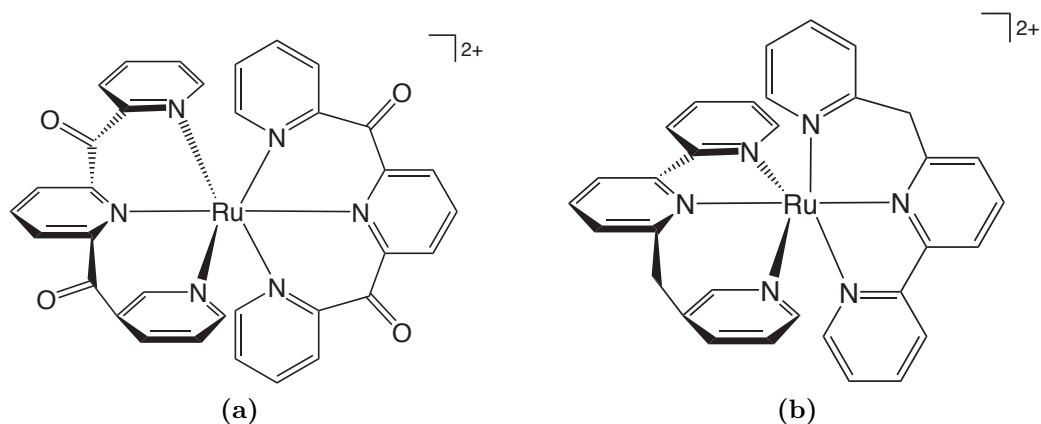


Fig. 1.5 Structures of Ru(II) complexes containing six-membered chelates: (a) Ketonic compound published by Ruben *et al.*,³¹ and (b) Example of a bridged complex published by Heinze *et al.*³²

Hammarström *et al.* carried out further elaboration of the ruthenium(II) N[^]N[^]N[^]-coordinated systems by incorporating quinolyl groups into the ligands in place of pyridyl groups,³⁴ as a continuation of a series of all-nitrogen donor ligands,^{35,36} prepared to increase the bite angle at the metal centre. The ligand, 2,6-di(quinolyl)pyridine, dqp, binds with a bite angle of 179.6°, resulting in room temperature emission from [Ru(dqp)₂]²⁺ (Fig. 1.6) with $\Phi_{\text{lum}} = 0.02$ and a lifetime of 3 μs .

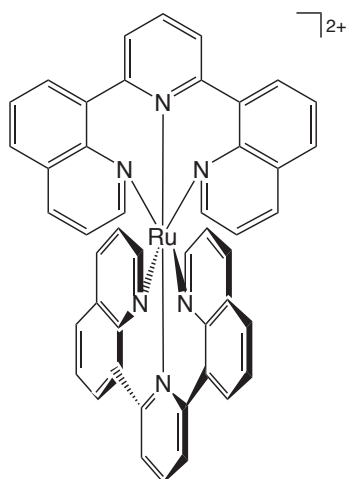


Fig. 1.6 Structure of [Ru(dqp)₂]²⁺.³⁴

1.2.2 Iridium(III) polypyridyl complexes

Polypyridyl chemistry of iridium has come to the fore only in more recent years, progress being hampered by the kinetic inertness of the Ir(III) coordination sphere, the harsh reaction conditions required for synthesis of complexes from iridium chlo-

ride salts and laborious purifications necessary to isolate the products, in addition to the higher cost of iridium salts compared to ruthenium salts. Initial attempts to synthesise $[\text{Ir}(\text{bpy})_3]^{3+}$ (Fig. 1.7a)³⁷ resulted in the dichloro bis(bpy) species instead³⁸ and it was almost twenty years later in 1975 that the desired compound was prepared. A mixture of $\text{K}_3\text{IrCl}_6 \cdot 3\text{H}_2\text{O}$, $\text{K}_2\text{S}_2\text{O}_8$ and KHSO_4 was boiled in water to evaporation before fusion in air and treatment with an aqueous solution of bpy under a CO_2 atmosphere. An arduous work-up and purification led to the isolation of the desired product as the NO_3^- salt, which was converted to the perchlorate salt.³⁹

The photophysical properties of $[\text{Ir}(\text{bpy})_3]^{3+}$, like the majority of Ir(III) complexes, are less clear-cut than those of the ruthenium analogue, with a higher degree of mixing of excited states. In general, emission from triplet MLCT states tends to be broad and structureless, whereas iridium species containing excited states composed of singlet and triplet CT and LC states possess more structured emission. They also more commonly display rigidochromism (the difference in emission maxima at room temperature and low temperature), which advocates transitions involving charge transfer character or orbital mixing. At 77 K $[\text{Ir}(\text{bpy})_3]^{3+}$ shows highly structured emission and a lifetime of ca. 80 μs , which was assigned as LC $\pi\text{-}\pi^*$ phosphorescence.³⁹ Complexes containing exclusively neutral donors tend to exhibit luminescence from LC states rather than CT states as there is insufficient donation of electron density to the metal ion to favour CT transitions.

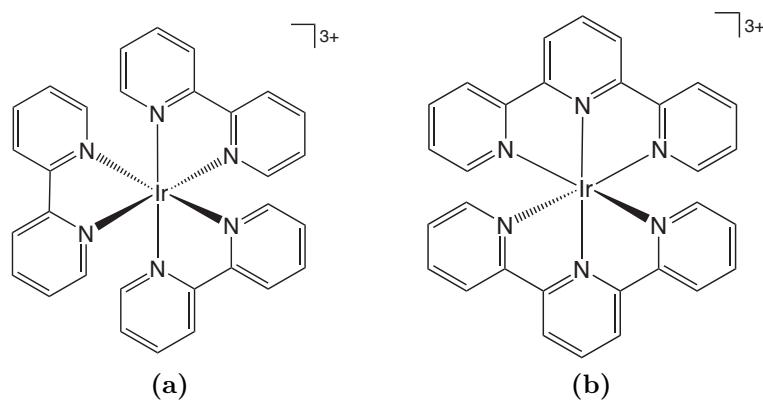


Fig. 1.7 (a) $[\text{Ir}(\text{bpy})_3]^{3+}$ and (b) $[\text{Ir}(\text{tpy})_2]^{3+}$.

The synthesis of iridium(III) bis(terpyridine), $[\text{Ir}(\text{tpy})_2]^{3+}$ (Fig. 1.7b) was first reported by Demas *et al.*⁴⁰ employing the same method as used to prepare $[\text{Ir}(\text{bpy})_3]^{3+}$. Following an arduous purification, the NO_3^- and perchlorate salts were prepared, which were discovered to emit highly structured blue-green luminescence with vibrational spacing that suggests a primarily LC $\pi\text{-}\pi^*$ excited state and little metal involvement.^{40,41} This contrasts with the MLCT emission observed for $[\text{Ru}(\text{tpy})_2]^{2+}$,

and stems from the difference in oxidation states between the two metals: oxidation of the formal Ru(II) state to Ru(III) is relatively facile, whilst the Ir(III)/Ir(IV) potential is much higher and pushes the energies of the MLCT states above that of the ligand-centred states.⁴² The harsh reaction conditions necessary to effect the complexation led Collin *et al.*⁴¹ to investigate a milder stepwise route *via* an Ir(tpy)Cl₃ intermediate, by heating IrCl₃ and tpy in ethylene glycol. The second step is addition of a second tpy ligand to the Ir(III) centre, therefore this method can also be utilised to form heteroleptic complexes by the addition of an alternative terdentate ligand at the second stage. By careful control of reaction times to prevent ligand scrambling, a series of Ir(III) complexes incorporating 4'-substituted tpy ligands have been prepared using this method,^{26,41,43,44,45} where the effect of the pendent group on the excited state is largely dependent on the extent of the increased conjugation. Although π - π^* character is still dominant in the excited state, there is a systematic red-shift and broadening of the emission spectra as the amount of conjugation present increases.

1.2.3 Cyclometallated iridium(III) complexes

The desire to create more emissive compounds has led to the development of several techniques for improving the PL quantum yield of polypyridyl systems. Whilst the method of using substituted terpyridyl ligands has proved successful in increasing luminescent quantum yields of platinum(II) compounds⁴⁶ (*vide infra*), the same improvement is not seen for the iridium species. A common method of introducing a higher degree of metal contribution and charge transfer character to the emitting state is the use of cyclometallating ligands, which, in addition to nitrogen donors, bind through one or more formally anionic carbon donors. Complexes formed by cyclometallation are favourable for the production of highly emissive compounds owing to their σ -donor and π -acceptor properties that give rise to low-lying MLCT states. Furthermore, the strong ligand field of the carbon donor and the possibility of π -back-donation into the chelate ring raises the energy of the deactivating MC d-d states, thus diminishing their deactivating effects.

By far the most well-established cyclometallating ligand is the bidentate donor 2-phenylpyridine, 2-ppyH, which has been used in many studies of the most famous of iridium phosphors, *fac*-Ir(ppy)₃ (Fig. 1.8a), the benchmark by which luminescent Ir(III) species are typically evaluated. First reported in 1985 in pioneering work by Watts *et al.*,⁴⁷ following on from the confirmation of cyclometallated binding in bpy complexes of iridium,^{48,49,50} the complex was obtained as a side-product in the preparation of the dimer [Ir(ppy)₂Cl]₂. The facial isomer is formed preferentially as

the thermodynamic product, owing to the strong *trans*-directing effect of the cyclometallating carbon donor, which directs the nitrogen on an adjacent ligand into a *trans*-disposition. The meridional isomer *mer*-Ir(ppy)₃ (Fig. 1.8b) was first isolated in 2003 by Thompson *et al.*, by heating [Ir(ppy)₂Cl]₂ with 2-ppyH at lower temperatures to enable formation of the kinetic product.⁵¹ Where Ir(ppy)₃ is discussed henceforth, the most commonly encountered facial isomer is the implied geometry.

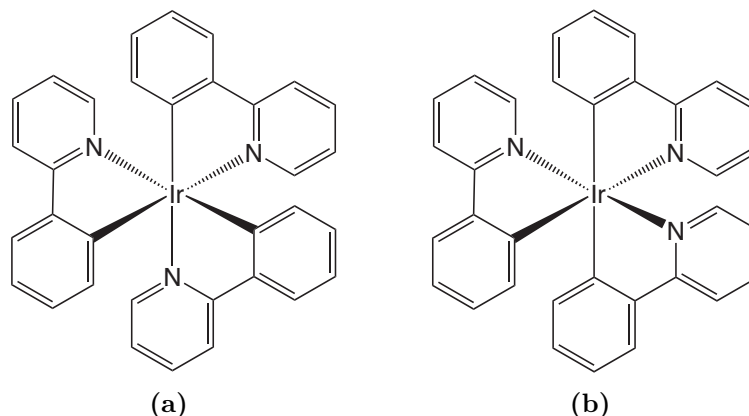


Fig. 1.8 Structure of (a) *fac*-Ir(ppy)₃ and (b) *mer*-Ir(ppy)₃.

Both isomers of Ir(ppy)₃ are green MLCT emitters, although emission for the facial isomer is an order of magnitude above that of the meridional isomer (0.4 compared to 0.036) and emission is red-shifted and broadened for *mer*-Ir(ppy)₃.⁵¹ The decay lifetimes for the two compounds are 1.9 μ s and 0.15 μ s, respectively and the radiative rate constants are comparable, therefore non-radiative decay pathways are thought to be the cause of the different emissive properties of the two isomers. The Thompson group performed extensive research into iridium compounds containing bidentate cyclometallating ligands (denoted C^N) and prepared a wide range of complexes,^{51,52} the majority of which exhibit phosphorescence, with quantum yields in the range 0.1–0.6 and lifetimes in the microsecond regime up to 14 μ s (Fig. 1.9).

1.2.4 Iridium(III) complexes containing terdentate ligands

Combining two of the favourable features for luminescence – the rigidity of terdentate ligands and the strong σ -donor effect of cyclometallation – should have a positive impact on luminescent quantum yields, yet this field of research has only been explored in any detail in the last decade. Various adaptations of the [Ir(tpy)₂]³⁺ motif have been synthesised to produce complexes of the forms [IrN₅X]²⁺, [IrN₄X₂]⁺ and [IrN₃X₃], where X represents a cyclometallating carbon atom or a monoanionic donor ligand, such as chloride.

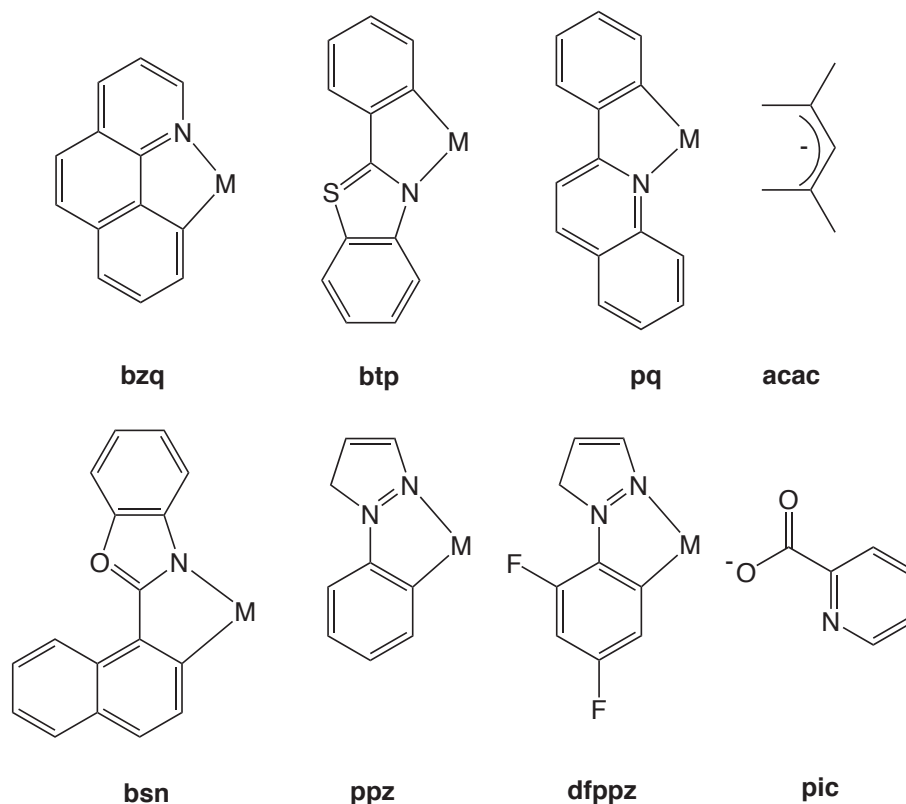


Fig. 1.9 Examples of bidentate polypyridine ligands and β -diketonato ligands employed by Thompson *et al.*^{51,52}

1.2.4.1 $[\text{IrN}_5\text{X}]^{2+}$ -Coordination

Introduction of an anionic chloride into a terdentate iridium system, $[\text{IrN}_5\text{Cl}]^{2+}$, has been reported to increase the MLCT character of the excited state in comparison with $[\text{IrN}_6]^{3+}$ complexes due to an increased metal participation and higher energy HOMO (highest occupied molecular orbital). Haga *et al.* synthesised such systems utilising tolylterpyridine (ttpy) and benzimidazole ligands Mebip and Mebib (Fig. 1.10) in conjunction with bpy.⁵³ It was found that when chloride occupied the sixth coordination site, emission was shifted to the red with a higher radiative constant for $[\text{Ir}(\text{ttpy})(\text{bpy})\text{Cl}]^{2+}$ compared to $[\text{Ir}(\text{ttpy})_2]^{3+}$, a trend repeated for the Mebib-containing complexes, where the bis(terdentate) complex $[\text{Ir}(\text{N}^{\wedge}\text{N}^{\wedge}\text{N})\text{-Mebip}(\text{N}^{\wedge}\text{C}^{\wedge}\text{N})\text{-Mebib}]^{2+}$ has a lower quantum yield (0.10) than the corresponding bpy complex $[\text{Ir}(\text{N}^{\wedge}\text{N}^{\wedge}\text{N})\text{-Mebip}(\text{bpy})\text{Cl}]^{2+}$ (0.19).⁵³

Results from our own group pertaining to $\text{N}^{\wedge}\text{C}^{\wedge}\text{N}$ -coordinating ligands on an iridium centre indicate that the inclusion of a single cyclometallating carbon atom does not always enhance emission quantum yields significantly. $[\text{Ir}(\text{dpyx})(\text{tpy})]^{2+}$ and $[\text{Ir}(\text{dpyx})(\text{ttpy})]^{2+}$ (Fig. 1.11), where dpyx represents the 4,6-dimethylsubstituted analogue of 1,3-di(2-pyridyl)benzene (dpyb), were prepared after the failure of the

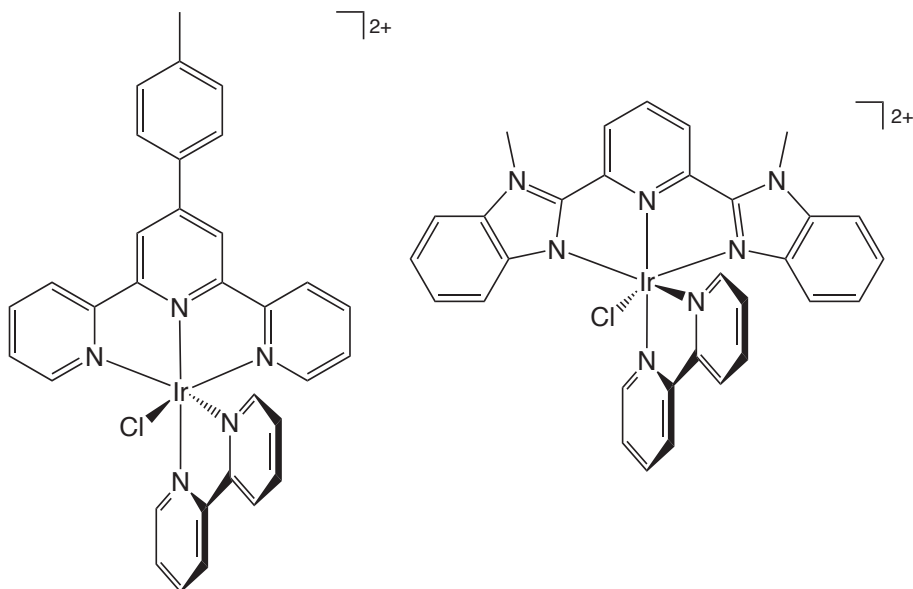


Fig. 1.10 Structures of bpy-containing complexes $[\text{Ir}(\text{ttpy})(\text{bpy})\text{Cl}]^{2+}$ and $[\text{Ir}(\text{Mebip})(\text{bpy})\text{Cl}]^{2+}$ published by Haga *et al.*⁵³

unsubstituted ligand to bind successfully due to competitive binding in the alternative bidentate binding mode (binding mode II in Fig. 1.12).⁵⁴ These compounds display only weak luminescence due to a predominantly LLCT excited state, as determined by density functional theory (DFT) calculations. Mamo, Campagna *et al.* had discovered similar weak emission in their own investigations into complexes containing the ligand 2,6-bis(7'-methyl-4'-phenyl-2'-quinolyl)pyridine (bmqpp)⁵⁵ where binding occurs as either a neutral ($\text{N}^{\wedge}\text{N}^{\wedge}\text{N}$, Fig. 1.13a) or anionic ($\text{N}^{\wedge}\text{N}^{\wedge}\text{C}$, Fig. 1.13b) ligand. The heteroleptic $[\text{Ir}(\text{N}^{\wedge}\text{N}^{\wedge}\text{N})(\text{N}^{\wedge}\text{N}^{\wedge}\text{C})]^{2+}$ species, where both binding modes are present, has a quantum yield of 0.005, compared to the homoleptic $[\text{Ir}(\text{N}^{\wedge}\text{N}^{\wedge}\text{C})_2]^+$ species, an $[\text{IrN}_4\text{X}_2]^+$ system, which emits with $\Phi_{\text{lum}} = 0.066$.

1.2.4.2 $[\text{IrN}_4\text{X}_2]^+$ -Coordination

The latter complex discussed above, $[\text{Ir}(\text{N}^{\wedge}\text{N}^{\wedge}\text{C}-\text{bmqpp})_2]^+$, is an example of the trend in $[\text{IrN}_4\text{X}_2]^+$ systems displaying more promising results with regard to phosphorescent emission. The photophysics of $[\text{IrN}_4\text{X}_2]^+$ complexes does, however, depend strongly on the relative geometry of the carbon and nitrogen donor atoms. When the cyclometallating carbon atoms are in different ligands, as in ppy-containing complexes with $[\text{Ir}(\text{C}^{\wedge}\text{N}^{\wedge}\text{N})(\text{C}^{\wedge}\text{N})\text{X}]$ or $[\text{Ir}(\text{N}^{\wedge}\text{C}^{\wedge}\text{N})(\text{C}^{\wedge}\text{N})\text{X}]$ structures, quantum yields are typically higher than compounds containing carbon donors in the same ligand i.e. $\text{C}^{\wedge}\text{N}^{\wedge}\text{C}$ -coordination. An $[\text{Ir}(\text{C}^{\wedge}\text{N}^{\wedge}\text{C})(\text{tpy})]^+$ complex prepared in 2004 by Scandola *et al.*⁵⁶ (Fig. 1.14) was the first example of an Ir(III) bis-cyclometallate

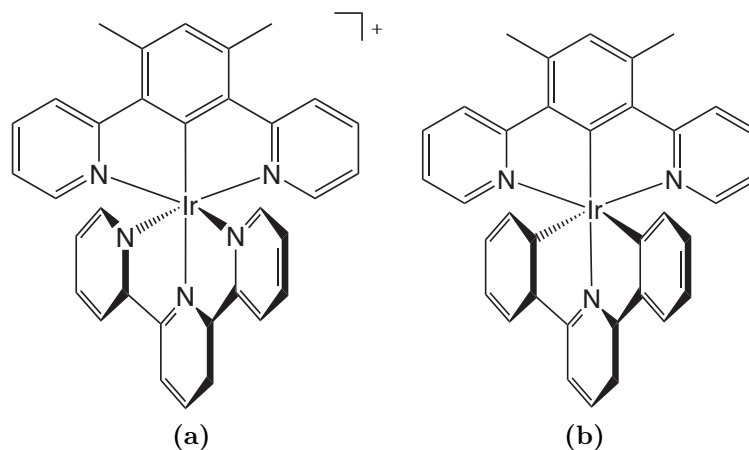


Fig. 1.11 Structure of dpyx-containing complexes (a) $[\text{Ir}(\text{dpyx})(\text{tpy})]^{2+}$ ⁵⁴ and (b) $\text{Ir}(\text{dpyx})(\text{dppy})$ ⁵⁴ (see Section 1.2.4.3)

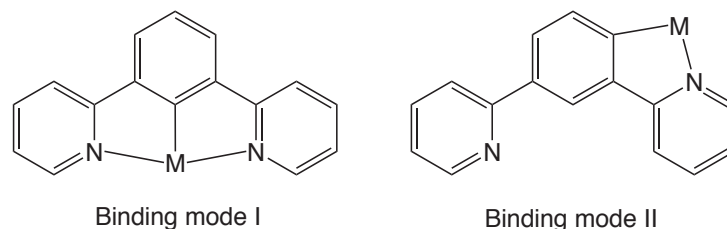


Fig. 1.12 Competitive binding modes of dpybH

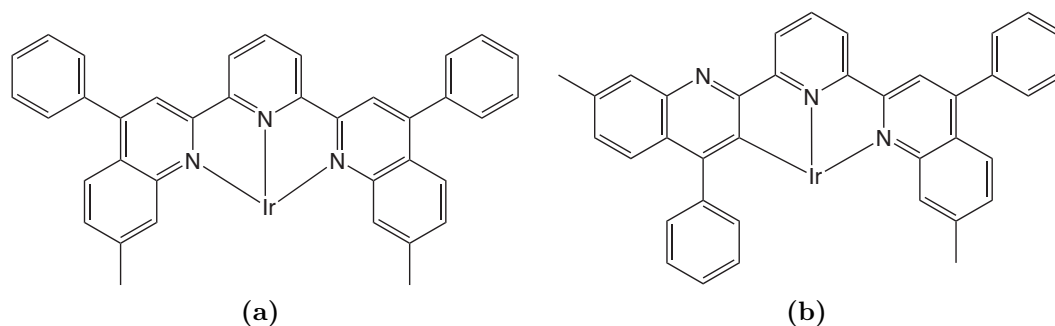


Fig. 1.13 (a) $\text{N}^{\wedge}\text{N}^{\wedge}\text{N}^-$ versus (b) $\text{N}^{\wedge}\text{N}^{\wedge}\text{C}$ -coordination of bmpqq to $\text{Ir}(\text{III})$.⁵⁵

with terdentate ligands, and its charge transfer-based luminescence was suggested to be due to the asymmetric nature about the iridium centre. Low-energy red emission with a quantum yield of 0.032 and a lifetime of 1.7 μs implies a low radiative rate constant, which was explained by DFT calculations that predict a HOMO based predominantly on the $\text{C}^{\wedge}\text{N}^{\wedge}\text{C}$ ligand and a tpy-based lowest unoccupied molecular orbital (LUMO).⁵⁷ This is indicative of a significant amount of LLCT character and low metal participation in the excited state.

$\text{Ir}(\text{III})$ complexes which contain a cyclometallated carbon and anionic ancillary such as chloride typically display higher quantum yields than the bis(terdentate)

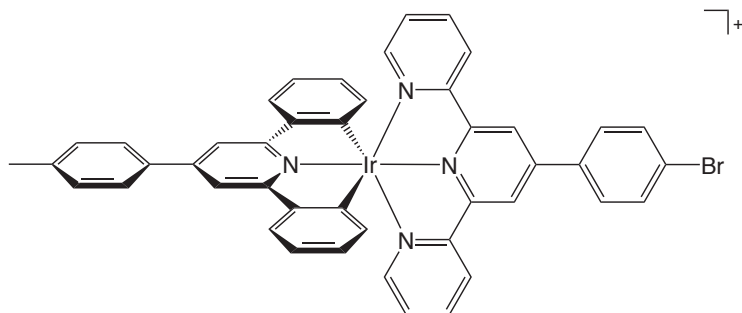


Fig. 1.14 Structure of the first Ir(III) bis(cyclometallate).⁵⁶

species, analogous to the improvement seen for tpy species containing a bpy and chloride ($[\text{Ir}(\text{N}^{\wedge}\text{C}^{\wedge}\text{N})(\text{N}^{\wedge}\text{N})\text{Cl}]$) as opposed to solely bis(terdentate) neutral ligands as in Section 1.2.4.1). A quantum yield of 0.16 has been reported for both $[\text{Ir}(\text{N}^{\wedge}\text{N}^{\wedge}\text{N})\text{-Mebip}(\text{ppy})\text{Cl}]^{+58}$ (Fig. 1.15a), and $[\text{Ir}(\text{tpy})(\text{N}^{\wedge}\text{C}^3\text{-tphbpy})\text{Cl}]^{+59}$ (Fig. 1.15b).

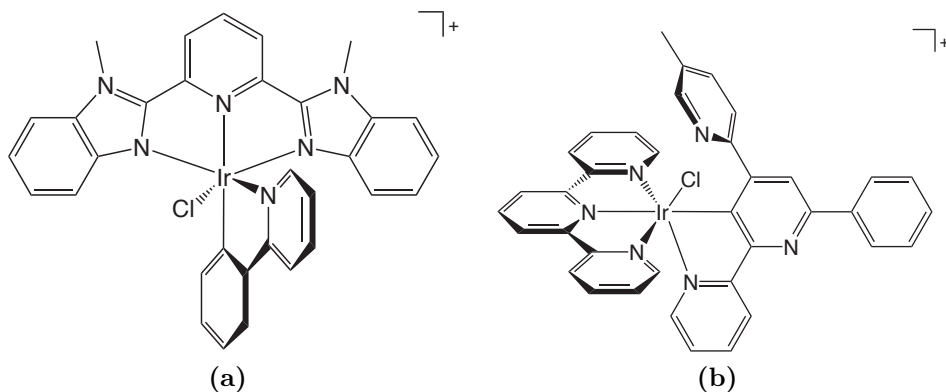


Fig. 1.15 (a) $[\text{Ir}(\text{Mebip})(\text{ppy})\text{Cl}]^{+58}$ and $[\text{Ir}(\text{tpy})(\text{N}^{\wedge}\text{C}^3\text{-tphbpy})\text{Cl}]^{+59}$.

1.2.4.3 $[\text{IrN}_3\text{X}_3]$ -Coordination

Introduction of a third anionic donor typically causes an improvement in emission from the resulting neutral compounds, which are favourable for use in OLEDs due to the ion migration associated with charged complexes. $\text{Ir}(\text{N}^{\wedge}\text{C}^{\wedge}\text{N-dpyx})(\text{C}^{\wedge}\text{N}^{\wedge}\text{C-dppy})$ (1.11b) is essentially the bis(terdentate) analogue of the ubiquitous Ir(III) complex $\text{Ir}(\text{ppy})_3$, with two methyl groups to prevent competitive binding. The broadband emission profile originates from mixed LC/CT character, due to a widely dispersed HOMO and a LUMO residing upon the terdentate ligand.⁵⁴ The bis(terdentate) complex has a quantum yield of 0.21 and is red-shifted in comparison to $\text{Ir}(\text{ppy})_3$ due to the more delocalised electronic nature of the $\text{N}^{\wedge}\text{C}^{\wedge}\text{N}$ ligand compared to the $\text{N}^{\wedge}\text{C}$ ligand, which leads to a lower energy LUMO.

The use of ppy in conjunction with a cyclometallating terdentate ligand and a chloride ancillary has proved in many cases to be the most effective method of

improving the luminescence properties of d^6 octahedral compounds. $\text{Ir}(\text{N}^{\wedge}\text{C}^{\wedge}\text{N-dpyx})(\text{ppy})\text{Cl}$ shows a significant augmentation of quantum yield over the bis(terdentate) species (0.76 and 0.21, respectively)⁶⁰ whilst Haga *et al.* continued the aforementioned research into benzimidazole ligands through use of the cyclometalating $\text{N}^{\wedge}\text{C}^{\wedge}\text{N}$ -donor Mebib. The series of ppy-containing complexes resulted in extremely luminescent complexes exhibiting excellent quantum yields of up to 0.95, amongst the highest quantum yields yet reported.⁵⁸ The parent complex $[\text{Ir}(\text{N}^{\wedge}\text{C}^{\wedge}\text{N-Mebib})(\text{ppy})\text{Cl}]$ emits with $\Phi_{\text{lum}} = 0.78$, with the highest quantum yield of 0.95 corresponding to the analagous complex containing Phbib instead of Mebib.

Table 1.1 Photophysical data for key examples of octahedral complexes containing terdentate ligands.

Complex ^a	λ_{abs} /nm	λ_{max} /nm	Φ_{lum} $\times 10^2$	τ / μs
$[\text{Ir}(\text{tpy})_2][\text{PF}_6]_3$ ^b	210, 221, 251, 277, 313	458	2.5	1.0
$\text{Ir}(\text{tpy})(\text{N}^{\wedge}\text{C}^{\wedge}\text{tphbpy})$ ^c	237, 271, 328, 376, 463, 494	541	16	3.2
$[\text{Ir}(\text{dpyx})(\text{ppy})\text{Cl}]$ ^d	239, 258, 285, 353, 369, 399, 417	508	0.76	1.6
$[\text{Ir}(\text{dpyx})(\text{dppy})]$ ^e	240, 265, 294sh, 367, 411, 479	632	2.3	0.12
$\text{Ir}(\text{Brp-tpy})(\text{dppy})$ ^f	284, 320, 484sh, 520	690	0.032	1.8
$[\text{Ir}(\text{N}^{\wedge}\text{N}^{\wedge}\text{N})(\text{N}^{\wedge}\text{N}^{\wedge}\text{C})]^{2+\text{g}}$	262, 305, 390	620	0.005	0.33
$[\text{Ir}(\text{N}^{\wedge}\text{N}^{\wedge}\text{C})_2]^{+\text{g}}$	238, 313, 357, 418sh	630	0.066	2.3
$\text{Ir}(\text{Mebib})(\text{ppy})\text{Cl}^{\text{h}}$	244, 299, 360, 404, 425, 472, 523	555	0.78	1780
$[\text{Rh}(\text{tpy})_2][\text{PF}_6]_3$ ⁱ	244, 268, 324, 338, 355	–	(0.09) ^j	(8.0) ^j

^a In degassed MeCN at 298 K, except where stated otherwise.

^b Data from ref⁵⁹. ^c Data from ref⁴¹. ^d Data from ref⁶⁰.

^e Data from ref⁶¹. ^f Data from ref⁵⁶. ^g Data from ref⁵⁵.

^h Data from ref⁵⁸; in CHCl_2 . ⁱ Data from ref⁶²; as the ClO_4^- salt in 10^{-3} M HClO_4 (aq.). ^j Non-emissive at room temperature, data given for complex in an ethanol/methanol glass at 77 K.

1.2.5 Rhodium(III) polypyridyl complexes

Rhodium compounds tend to exhibit measurable emission only at low temperatures, owing to their lower nuclear charge as a second row transition metal. Phosphorescent emission is limited by the lower spin-orbit coupling constant of Rh(III), which, in turn, leads to reduced mixing of singlet and triplet states, and the same kinetic inertness as seen for the Ir(III) ion dissuades extensive research into these relatively non-emissive compounds.

The archetypal rhodium polypyridyl complex $[\text{Rh}(\text{bpy})_3]^{3+}$ (Fig. 1.16a) was isolated by Martin and Waide in 1958.³⁷ Displaying much less intense luminescence

than $[\text{Ir}(\text{bpy})_3]^{3+}$, the excited state typifies this class of Rh(III) complexes in being composed of LC π - π^* character with a structured emission profile and very short decay lifetime at room temperature (<15 ns), and much longer-lived luminescence of 2.2 ms at 77 K.³⁹ Mixed species containing bpy and phenanthroline (phen) show similar photophysical properties and also emit from a π - π^* state.^{23,63} The terdentate species $[\text{Rh}(\text{tpy})_2]^{3+}$ (Fig. 1.16b) was reported in 1963⁶⁴ *via* a fusion reaction in ethanol with addition of charcoal; subsequent PL studies found that emission was not observed at room temperature.⁶² At 77 K a broad luminescence band and a lifetime of 8.0 μs were detected, which were assigned to an MC state.⁶² The lack of room temperature emission was postulated to originate from the small bite angle of the tpy ligand, which is considerably less than 180° and causes the lateral Rh–N bond distances to be significantly longer than the central Rh–N bond, resulting in a large splitting of the d-d states and a weak ligand field.

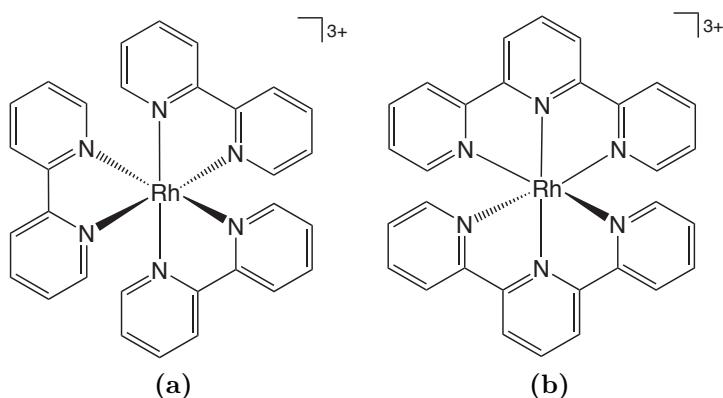


Fig. 1.16 (a) $[\text{Rh}(\text{bpy})_3]^{3+}$ (b) $[\text{Rh}(\text{tpy})_2]^{3+}$.

There are few examples in the literature of monometallic emitters containing rhodium that emit at ambient temperature, and frequently the metal is employed in conjunction with a second metal, such as ruthenium(II) in photoinduced electron transfer agents, whereby electron transfer occurs from the Ru(II) to the Rh(III) component in a dyad.^{65,66,67,68} In addition to their usage as electron transfer agents, homodinuclear Rh(III) systems (which are non-luminescent in solution) and Rh(III)-Ru(II) dyads act as DNA intercalators⁶⁹ and can also be used to produce dihydrogen.⁷⁰

1.2.5.1 Cyclometallated rhodium(III) complexes

Tris(cyclometallated) compounds of rhodium have been less extensively studied than those of Ir(III) and bis(cyclometallates) of Rh(III) are more common than tris(cyclometallates). The tris species *fac*-Rh(ppy)₃ was not synthesised success-

fully until 1994 when Güdel *et al.*⁷¹ mixed the dimer $[\text{Rh}(\text{ppy})_2\text{Cl}_2]$ with 2-ppyH and silver trifluoromethanesulfonate (silver triflate) to act as a chloride scavenger then heated the mixture at 110 °C for 24 h. The resulting product showed structured emission at ambient temperature and at 77 K, assigned as originating from a $^3\pi\text{-}\pi^*$ state on the basis of the band shape and energy, alongside the observation of line-narrowing in the low temperature spectra.⁷¹ The altered intensity distribution of peaks in the room temperature emission spectrum indicates that there may be a weak $^3\text{MLCT}$ contribution. The substantially shorter emission lifetime of 45 μs at 77 K in comparison with the heteroleptic complex $[\text{Rh}(\text{ppy})_2(\text{bpy})]^+$, which has a lifetime of 170 μs ,⁷² provides evidence of mixing between the LC and MLCT states, suggesting that the effect of cyclometallation is to lower the energy of the MLCT states.

In contrast to the majority of Rh(III) complexes studied, significant mixing of states is observed in the bidentate species based on polypyridines (Fig. 1.17a and Fig. 1.17b) reported by Kirsch-De Mesmaeker *et al.*, which exhibit intense broad luminescence bands and a hypsochromic shift at 77 K, originating from a distorted CT state.⁷³ Electrochemical and absorption data reinforce the assignment of a mixed MLCT-SBLCT (σ -Bond-to-Ligand Charge Transfer) state, with unstructured low temperature emission spectra suggestive of a high degree of reorganisation in the excited state, consistent with SBLCT character. Lifetimes for the compounds at 77 K are significantly shorter than Rh(III)polypyridyl systems with $\tau = 10.5 \mu\text{s}$ and 7.4 μs for $[\text{Rh}(\text{ppy})_2(\text{tap})]^+$ (Fig. 1.17a) and $[\text{Rh}(\text{ppy})_2(\text{hat})]^+$ (Fig. 1.17b), respectively. Subsequent experimental and theoretical studies by the same group into related optically active complexes⁷⁴ led to the conclusion that LLCT character was an appropriate description of the pinene-containing derivatives owing to the largely ligand-based frontier orbitals. Bidentate complexes synthesised by Lo *et al.* also emit from a mixed state, assigned as $^3\text{IL-}^3\text{MLCT}$ with quantum yields ranging from 0.015–0.032 (Fig. 1.17c).⁷⁵

Rhodium(III) complexes incorporating cyclometallating terdentate ligands are rare in the literature and photophysical studies of rhodium complexes are based exclusively on those comprising bidentate ligands. The $\text{N}^{\wedge}\text{N}^{\wedge}\text{C}$ -coordinating ligand Phbpy was complexed to a range of metals, including rhodium, by Constable *et al.*⁷⁶ Rhodium dimers containing tetradentate N_2O_2 -coordinating ligands were synthesised by Chan⁷⁷ through reaction of metal hydrides with 2,2',6,6'-tetramethylpiperidin-1-yloxy (TEMPO) to produce an $\text{O}^{\wedge}\text{N}^{\wedge}\text{N}^{\wedge}\text{O}$ -coordinating ligand that was complexed to rhodium in benzonitrile.

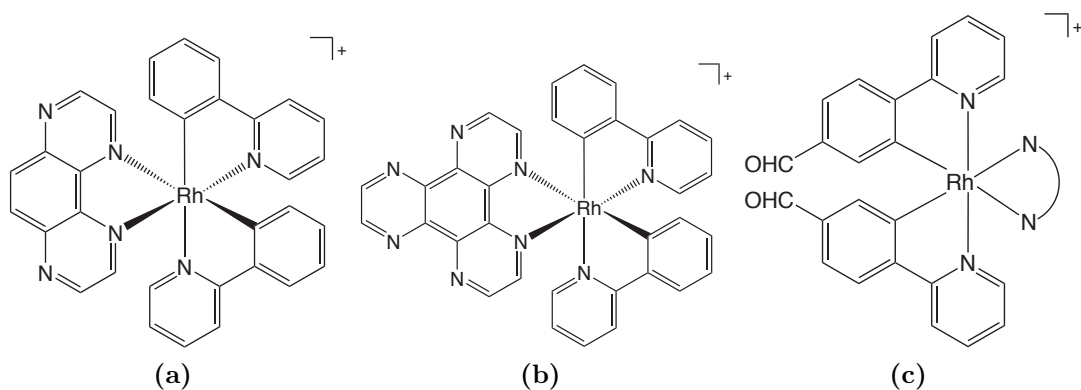


Fig. 1.17 Examples of cyclometallated Rh(III) complexes; (a) $[\text{Rh}(\text{ppy})_2(\text{tap})]^+$ ⁷³ (b) $[\text{Rh}(\text{ppy})_2(\text{hat})]^+$ ⁷³ (c) 2-ppy derivatives where $\text{N}^{\wedge}\text{N}$ = substituted bpy or substituted phen.⁷⁵

1.3 Square planar d^8 polypyridyl complexes

1.3.1 Platinum(II) polypyridyl complexes

Research into platinum(II) polypyridyl complexes has been ongoing for over 50 years, yet it is only in recent decades that luminescent studies have begun to rival those of octahedral compounds. The discovery of improved systems, based upon cyclometallated ligands and more rigid ligand frameworks, offers scope for highly emissive compounds compared to traditional platinum(II) species containing simple nitrogen-donor ligands, which are scarcely emissive at room temperature. For these latter compounds, the lack of emission is due to the proximity of deactivating d-d states to the emitting states, which provides an alternative non-radiative pathway for decay (Fig. 1.4a). The planar structure of d^8 complexes enables the formation of aggregates and exciplexes, which can alter the photophysical properties so that emission is concentration-dependent. This introduces the concept of colour tuning in OLEDs when using one complex only, a strategy that is particularly useful in white organic light-emitting devices (WOLEDs).^{4,78} Aggregates and exciplexes result from molecular interactions that often give rise to different photophysical behaviour from the monomeric species. When two molecules are involved in an absorption process the species is termed an “absorption complex”, and when two molecules act cooperatively to emit light, this is termed an “exciplex”.¹⁴ If the two components of the exciplex are of the same type, then this is known as an “excimer” (contraction of excited dimer). These phenomena are excited state effects: a molecule in the excited state combines with a molecule in the ground state and the resulting excimer decays either *via* radiative or non-radiative pathways. The equivalent ground state phe-

nomenon is called aggregation, when intermolecular interactions cause aggregates that can display different spectroscopic behaviour from the monomer.

Numerous diimine complexes comprising bidentate and monodentate ligands on a Pt(II) centre have been published; the homoleptic dicationic species $[\text{Pt}(\text{bpy})_2]^{2+}$ was first reported by von Zelewsky *et al.* in 1988.⁷⁹ This was purported to emit from an LC state at 77 K, owing to its long lifetime (24 μs), small red-shift in relation to the free ligand and high degree of vibrational structure.⁷⁹ Homoleptic cyclometallated complexes, in which the two bidentate ligands are identical, are more difficult to synthesise due to the standard route requiring lithiated precursors. Thus, there are more examples of heteroleptic compounds in the literature, which can be formed from K_2PtCl_4 *via* a dimer intermediate that can be cleaved using a bidentate or monodentate ligand.

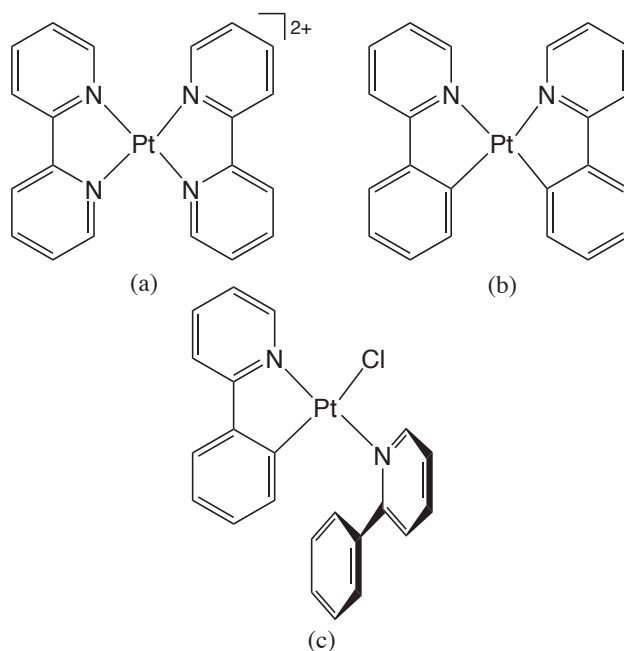


Fig. 1.18 Structure of Pt(II) complexes containing bidentate ligands.^{79,80,81,82}

The homoleptic bis(cyclometallate) $\text{Pt}(\text{ppy})_2$ was synthesised in 1984 by the von Zelewsky group⁸⁰ *via* reaction of *trans*- $\text{PtCl}_2(\text{SEt}_2)_2$ with (2-phenylpyridine)lithium in diethyl ether and tetrahydrofuran (THF). The groups of Watts and Ford independently discovered a tendency towards monodentate binding of ppy through the nitrogen only, in addition to the desired bidentate mode (Fig. 1.18).^{81,82} The resulting complex, $\text{Pt}(\text{ppy})(\text{ppyH})\text{Cl}$, showed room temperature emission in solution, assigned as originating from an $^3\text{MLCT}$ state⁸², compared with the non-emissive bidentate-bound species $\text{Pt}(\text{ppy})_2$. The decay lifetime varied widely in different solvents, from 641 ns in ethanol to 5.9 μs in CH_2Cl_2 .⁸¹ An array of literature exists on the topic of cyclometallated bidentate Pt(II) compounds, including in-depth low

temperature studies using a polycrystalline Shpol'skii matrix, to probe the excited state character of this class of compounds, which indicate that the initial assessment of a simple charge transfer of $^3\text{MLCT}$ character is an incomplete picture.^{83,84} Thompson *et al.*, for example, prepared a series of $\text{Pt}(\text{N}^{\wedge}\text{C})(\text{O}^{\wedge}\text{O})$, where $\text{O}^{\wedge}\text{O}$ represents a β -diketonato ligand (see Fig. 1.9 for examples of ligands used), that emit from a mixed $^1\text{MLCT}$ - $^3\text{MLCT}$ - ^3LC state, which gives rise to high quantum yields (0.02–0.25) and lifetimes of the order of microseconds.⁸⁵

1.3.1.1 Platinum(II) complexes containing neutral terdentate ligands

$[\text{Pt}(\text{tpy})\text{Cl}]\text{Cl} \cdot 3\text{H}_2\text{O}$ (Fig. 1.19) was first isolated as a minor product from reaction of K_2PtCl_4 and terpyridine²⁷ but not until over four decades later was the dehydrated product obtained after much longer reaction times (20–100 h) and recrystallisation.⁸⁶ Although this simple terdentate-bound system has various counterion-dependent coloured forms in the solid-state and exhibits solid-state luminescence, it is virtually non-emissive in solution at room temperature. Emission from a 77 K frozen glass has been assigned to a π - π^* excited state⁸⁷ and so several strategies have been employed in attempts to improve the solution emission properties of tpy-based Pt(II) compounds, including the use of alternative $\text{N}^{\wedge}\text{N}^{\wedge}\text{N}$ -coordinating ligands such as pyrazoles, imidazoles and benzimidazoles.

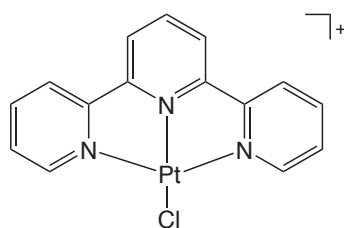


Fig. 1.19 Structure of $[\text{Pt}(\text{tpy})\text{Cl}]^+$.

Addition of substituents to the tpy ligand,^{46,88} has resulted in room temperature luminescence by altering the HOMO-LUMO energy gap such that the MLCT states play a more important role in radiative decay. The group of McMillin has been instrumental in employing this tactic, by synthesising a range of 4'-substituted emissive compounds,⁸⁹ of which many show solution-state emission at ambient temperature, with decay lifetimes from 85 ns to 1.9 μs and measurable quantum yields (approaching 0.1). Electron-withdrawing groups, such as the cyano substituent lower the energy of the MLCT state more than the deactivating d-d states, such that the MC states are less accessible to thermal population.⁴⁶ Delocalisation of the π^* orbital onto a substituent in the 4'-position of the central pyridine ring generally lowers the energy of the LUMO, which stabilises the triplet MLCT and LC states.⁹⁰ Electron-

donating groups have the greatest impact in enhancing quantum yields through the promotion of mixing of states and a switch to ILCT-³LC character.⁹¹

A second method of improving emission characteristics is metathesis of the ancillary ligand with one that offers a stronger ligand field than that of the standard chloride resulting from the K₂PtCl₄ start material. A strong σ -donor such as a cyanide or an acetylide increases the ligand field strength around the metal centre, thereby driving the MC d-d states up in energy. The CT states can also be raised, however, so that the effect on emission is largely dependent on the terdentate ligand. McMillin *et al.* carried out chloride substitution in platinum complexes by heating with silver cyanide at 60 °C in MeCN.⁹² The resulting platinum(II) cyano-derivatives (Fig. 1.20) are only weakly emissive in the case of [Pt(tpy)CN]⁺ and [Pt(4'-CN-tpy)CN]⁺ yet when the cyanide co-ligand is in conjunction with a strongly electron-rich dimethylamino substituted tpy, 4'-NMe₂-tpy, a dramatic increase in quantum yield to 0.26 and a lifetime of 22 μ s is observed.⁹² This effect is attributed to a greater mixing of the MLCT and ILCT states.

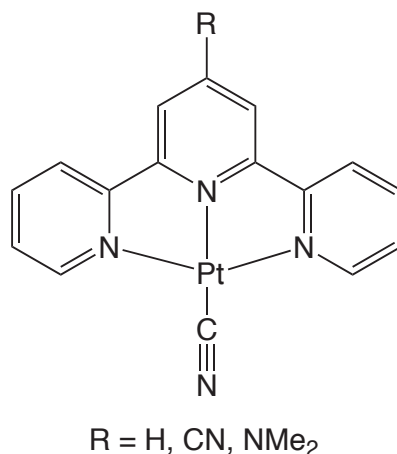


Fig. 1.20 Example structure of cyano derivatives of Pt(II) tpy complexes, [Pt(4'-R-tpy)CN]⁺, published by McMillin *et al.*⁹²

Several groups have carried out research into [Pt(tpy)Z]⁺ systems, where Z is an acetylide, leading to observation of room temperature luminescence. Yam *et al.* reported a series of Pt(II) tpy compounds containing an acetylide ligand in the fourth coordination site (Fig. 1.21a), the majority of which display red-orange luminescence with low quantum yields of less than 0.02.⁹³ Electron-rich substituents on the ethynyl group shift emission to the red, which is consistent with a ³MLCT assignment. Ziessel, Castellano *et al.* combined acetylide ancillaries on square planar Pt(II) with tpy ligands trisubstituted by *tert*-butyl groups to achieve tuneable phosphorescence with quantum yields in the range 0.035–0.17 (Fig. 1.21b).⁹⁴ DFT analysis revealed an interplay between the MLCT states, $d\pi(\text{Pt}) \rightarrow \pi^*(\text{tpy})$, and

LLCT states, $\pi(\text{C}\equiv\text{CR})\rightarrow\pi^*(\text{tpy})$, which enables the CT energies to be altered by varying the substituent on the acetylide ligand. The same group studied this system incorporating a tpy unit on the ethynyl group for complexation to a second metal (R = tpy in Fig. 1.21b) and the resulting diplatinum species showed the highest quantum yield of the series (0.2).

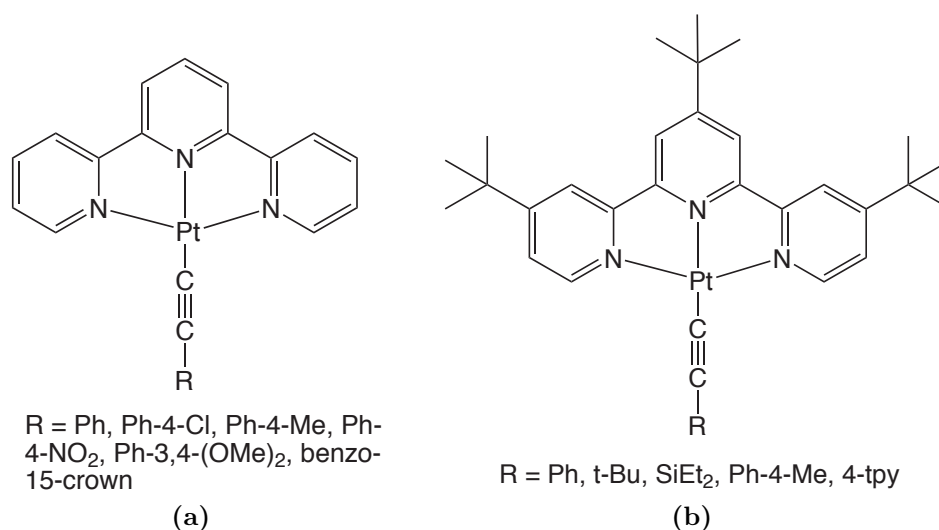


Fig. 1.21 Structure of $[\text{Pt}(\text{tpy})\text{Z}]^+$ complexes published by (a) Yam *et al.*⁹³ and (b) Castellano *et al.*^{94,95}

1.3.1.2 Cyclometallated platinum(II) complexes

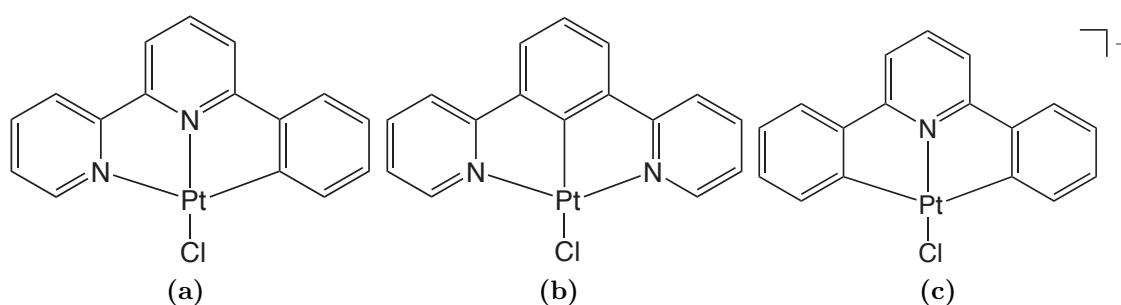


Fig. 1.22 Structures of the parent Pt(II) complexes containing terdentate cyclometallating ligands: (a) $\text{Pt}(\text{N}^{\wedge}\text{N}^{\wedge}\text{C})\text{Cl}$ (b) $\text{Pt}(\text{N}^{\wedge}\text{C}^{\wedge}\text{N})\text{Cl}$ (c) $\text{Pt}(\text{C}^{\wedge}\text{N}^{\wedge}\text{C})\text{Cl}^-$.

1.3.1.3 $\text{Pt}(\text{N}^{\wedge}\text{N}^{\wedge}\text{C})\text{Z}$

The parent $\text{Pt}(\text{N}^{\wedge}\text{N}^{\wedge}\text{C})\text{Cl}$ compound containing Phbpy (Fig. 1.22a) was first synthesised by Constable *et al.* in 1990 from either reaction of K_2PtCl_4 and PhbpyH

in water/MeCN or *via* the mercury intermediate, Hg(Phbpy)Cl, demonstrating that terdentate cyclometallated binding was feasible in a square planar system.^{96,97} Development of the Pt(N[^]N[^]C)Z system was undertaken by Che *et al.* who have been prolific in synthesising Pt(II) complexes based upon this motif.^{98,99,100,101} Pt(Phbpy)Cl displays room temperature luminescence with λ_{max} of 565 nm, a quantum yield of 0.025 and a decay lifetime of 0.51 μs , which was assigned as emanating from a ³MLCT excited state.⁹⁸ A switch to more conjugated systems incorporating a naphthalene (Np) and an isoquinoline unit with bulky substituents in the 4-position (Fig. 1.23) resulted in a strong luminescent enhancement.¹⁰¹ A variety of Pt(II) complexes were prepared and quantum yields in the range $0.01 \leq \Phi_{\text{lum}} \leq 0.68$ were reported, with the highest figure for the monometallic species containing 3,5-*t*-Bu₂Ph in the 4-position.

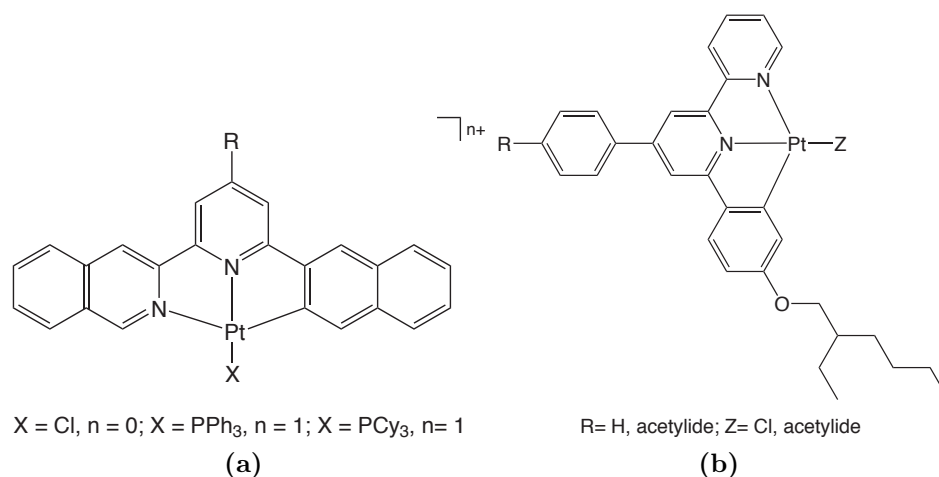


Fig. 1.23 Example structures of (a) monometallic species synthesised by Che *et al.*^{100,101} and (b) acetylide complexes synthesised by Sun *et al.*¹⁰¹

Alkyl and alkoxy substituents also provide a route to more soluble complexes, as terdentate platinum(II) compounds are frequently sparingly soluble in common organic solvents. Sun *et al.* added alkyl and alkoxy substituents to the Pt(N[^]N[^]C)Z ligand backbone and ancillary ligand (Fig. 1.23b)¹⁰² and, with a few exceptions, the compounds emit with quantum yields of the order 0.05–0.12, much higher than the unsubstituted complex.⁹⁷ The degree of mixing between states is thought to vary widely among the series, owing to differing lifetimes and solvatochromic effects, although emission likely emanates from a triplet CT state in each case. A degree of ligand-based character in the form of LLCT, ILCT or LC transitions involving the terdentate ligand is probable for both classes of compound, due to the variation between photophysical properties that is not purely dependent on the nature of the ancillary ligand.

The Che group also investigated linking two such complexes together *via* a phosphine bridge to attain lower energy absorption and emission bands than the $[\text{Ru}(\text{diimine})]^{2+}$ systems, traditionally used in photocatalysts.¹⁰⁰ This strategy led to emission of over a broad energy range and conferred an improvement in quantum yield in most cases in comparison with the parent monometallic compounds. The parent structure and its related complexes (Fig. 1.23a) were shown to undergo self-quenching and weakly excimeric behaviour at high concentrations but no excimer emission was observed for the latter complexes containing the bridged systems (Fig. Fig. 1.24) due to disruption of intermolecular π - π^* stacking.

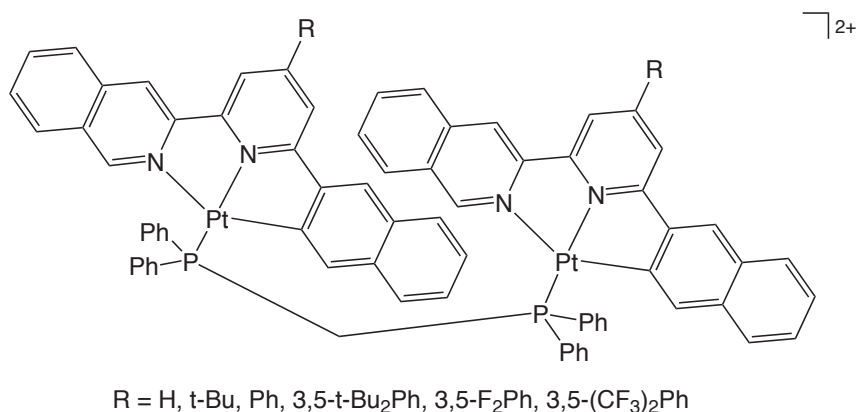


Fig. 1.24 Structures of bimetallic species synthesised by Che *et al.*¹⁰¹

Acetylides have been used as ancillaries alongside $\text{N}^{\wedge}\text{N}^{\wedge}\text{C}$ -cyclometallating ligands on platinum compounds to further increase the ligand field strength and Che *et al.* (Fig. 1.23)¹⁰³ found quantum yields in the range 0.05–0.1. The emission wavelength was tuneable in the region of 550–650 nm by varying the acetylide and the substituent on the terdentate ligand. Eisenberg *et al.* reported maxima at approximately 600 nm for their acetylide derivatives based on the same $\text{Pt}(\text{N}^{\wedge}\text{N}^{\wedge}\text{C})\text{Z}$ motif as Che (Fig. 1.23a), with a noticeable red-shift for complexes containing electron-withdrawing ester groups, consistent with a lower energy LUMO based upon the $\text{N}^{\wedge}\text{N}^{\wedge}\text{C}$ -coordinating ligand.¹⁰⁴ Quantum yields in the region of 0.05–0.07 and lifetimes of approximately 500–600 ns were reported, attributed to ³MLCT emission.

1.3.1.4 $\text{Pt}(\text{N}^{\wedge}\text{C}^{\wedge}\text{N})\text{Z}$

Research into this class of compounds has proved highly fruitful in producing intensely luminescent emitters, which typically show the best emission properties of the three types of cyclometallated compounds containing terdentate ligands discussed herein. Extensive work, originating from our own group, has been performed using the $\text{N}^{\wedge}\text{C}^{\wedge}\text{N}$ -coordinating dpyb ligand backbone. The parent unsubstituted

complex was first prepared by Cárdenas and Echavarren¹⁰⁵ in 1999 and subsequently its photophysics studied by Williams *et al.*¹⁰⁶ The most striking feature of Pt(dpyb)Cl is its extremely high quantum yield in comparison to the N[^]N[^]C-coordinated system, which is over an order of magnitude higher with values of 0.60 and 0.025, respectively.⁹⁷ An initial assessment concluded that phosphorescence originated from a state of predominantly LC $^3\pi - \pi^*$ character, owing to the very small Stokes shift, relatively long lifetime and the lack of solvatochromism. However, more recent work applying computational calculations to this and related complexes has put forth the notion of an LC-MLCT admixture.^{107,108} Data from time-dependent DFT calculations (TD-DFT) indicate a moderate amount (25 %) of $d \rightarrow \pi^*$ MLCT character, which goes some way to explaining the intense luminescence observed, since metal participation promotes mixing of the excited states due to SOC. The Pt–C bond is also much shorter than in the N[^]N[^]C-coordinated parent compound, causing the energy of the deactivating d-d states to be raised, thus limiting non-radiative decay pathways. Pt(pyqb)Cl also shows efficient formation of an excimeric emission band at higher concentrations.¹⁰⁶ Appearing at approximately 690–700 nm, the excimeric emission decays with monoexponential kinetics, as seen for the monomeric luminescence.

The Pt(dpyb)Cl system was modified by systematic substitution at the 4'-position of the central phenyl ring to produce a series of highly emissive compounds using both a standard reflux procedure¹⁰⁹ and a microwave-accelerated method.¹¹⁰ The resulting compounds displayed quantum yields ranging from 0.30 (4'-MeO-substituted) to 0.68 (4'-Me-substituted) and decay lifetimes in the region of 3.0–13.0 μ s, with the exception of the 4'-thienyl derivative, for which $\tau = 20.4 \mu$ s. Lifetime increases with decreasing energy of emission maxima, which is red-shifted as the electron density present on the 4'-substituent increases: mesityl <2-pyridyl <4-tolyl <4-biphenyl <2-thienyl. The more electron-rich thienyl and biphenyl groups have the largest red-shifts due to a higher energy HOMO that is based more upon the pendant group, according to DFT optimisation.¹⁰⁹ There is a progressive trend in Stokes shift between the 3 LC absorption band and the λ_{max} emission band in the same order, which is suggested to be a geometric effect. Torsional rearrangement must occur after absorption to align the rings in the most conjugated, approximately co-planar conformation in the excited state, whereas in the ground state dihedral angles are larger.¹⁰⁹ Photoluminescence from the 4'-dimethylamino-substituted compound differs significantly in origin from the rest of the series; its broad red-shifted unstructured emission and lack of self-quenching, but increased sensitivity to oxygen quenching and strong solvatochromism, indicates a switch from a 3 LC lowest

excited state (as seen in the remainder of this series) to one of predominantly ILCT character.

The Williams group has performed further functionalisation on the Pt(dpyb)Cl system by addition of larger pendant groups at the central 4'-position, such as crown ethers.¹⁰⁸ This series of compounds possessed high quantum yields (0.28–0.46), although none surpassed that of the parent complex ($\Phi_{\text{lum}} = 0.60$). Moreover, to shift emission to the blue, 3,5-disubstitution of the central phenyl ring with fluorine or methyl substituents, in conjunction with methoxy groups on the pyridyl side groups (Fig. 1.25) led to a distinct improvement in quantum yields, producing values amongst the highest yet reported.¹¹¹ Quantum yields were excellent for the vast majority of complexes, with a peak value of 0.87 for the complex containing 1,3-di((4-methyl)-2-pyridyl)-3,5-difluorobenzene, and further values of Φ_{lum} above 0.80 for 1,3-di(2-pyridyl)-3,5-difluorobenzene (0.85) and 1,3-di(2-pyridyl)-3,5-dimethylbenzene (0.81).

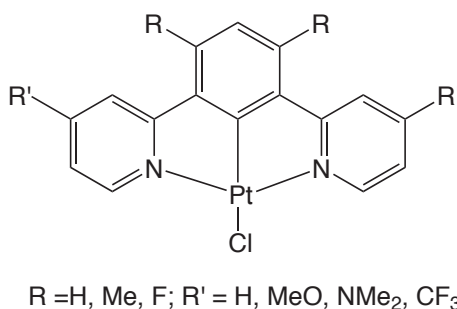


Fig. 1.25 Highly emissive substituted N[^]C[^]N-coordinated complexes.¹¹¹

The bluest phosphor in the series was 1,3-di((4-dimethylamino)2-pyridyl)-4,6-difluorobenzene (Fig. 1.25 where R = F and R' = NMe₂) which has a λ_{max} value of 455 nm. This results from the strongly electron-donating nature of the NMe₂ groups, which raise the energy of the LUMO, whilst the fluorine substituents on the central ring lower the HOMO, such that the energy gap is increased and higher energy (blue) emission is observed. Further adaptation of the N[^]C[^]N ligand framework by replacing the pyridyl rings with pyrazoles resulted in lower quantum yields than the pyridyl systems but emission was shifted further to the blue. Φ_{lum} for the unsubstituted dipyrazolyl complex (Fig. 1.26a) was 0.02 with $\lambda_{\text{max}} = 453$ nm, and emission intensity improved on addition of larger electron-rich pendant groups, or when a pyrazolyl unit was used alongside a 2-pyridyl group in an asymmetric complex (1-(1-pyrazolyl)-3-(2-pyridyl)benzene.¹¹² This combination conferred a significant improvement in luminescence over the symmetric species with a quantum yield of 0.64, which is higher than that of Pt(dpyb)Cl,¹⁰⁶ though emission is hypsochromically shifted to the green (487 nm) by the destabilisation of the LUMO due

to the electron-rich nature of the pyrazole.

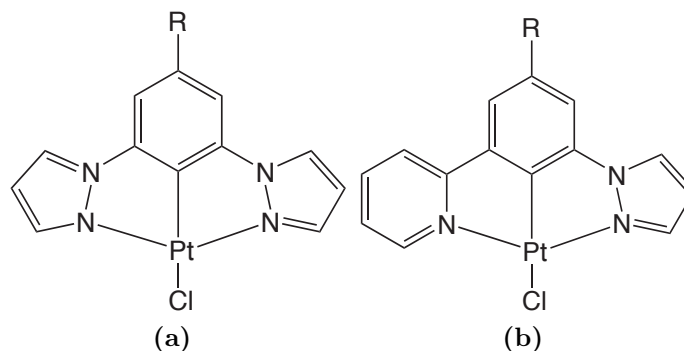


Fig. 1.26 (a) Symmetric and (b) asymmetric pyrazole-containing complexes; R = CH₃, OCH₃Ph or CH₃Ph.¹¹²

1.3.1.5 [Pt(C[^]N[^]C)Z]⁻

Ligands containing two cyclometallating carbon atoms are more difficult to bind successfully to a platinum centre, and once bound, tend to be more labile than the preceding cyclometallated terdentate-bound complexes. For this reason there are relatively few examples of Pt(C[^]N[^]C)Z in comparison with the previous complexes discussed in this section. The initial preparation of the parent compound [Pt(dppy)Cl]⁻, was carried out in 1988 by Von Zelewsky *et al.* in very low yield (Fig. 1.22c).¹¹³ The procedure consisted of a double lithiation of diphenylpyridine followed by reaction with PtCl₂(SEt₂)₂ to give the desired complex in 1.4 % yield. Subsequently, Rourke *et al.* performed the synthesis starting from K₂PtCl₄ but instead isolated a compound initially postulated to be a singly chloro-bridged species and later confirmed as chloro-bridged diplatinum compound like those seen for octahedral species (Fig. 1.27).^{114,115} This could be cleaved by dimethylsulfoxide (DMSO), and a crystal structure provided verification of C[^]N[^]C-binding.

The monomeric species Pt(C[^]N[^]C)py is non-emissive at room temperature and shows emission at 482 nm with a decay lifetime of 20 μs at 77 K.¹¹⁶ Substitution of the ancillary ligand with pyrazole or SEt₂ led to identical emission spectra, therefore metal-based and terdentate-based frontier orbitals are probable, with little input from the ancillary ligand. This leads to an assignment of MLCT character combined with LC; a relatively small red-shift of the emission energy with respect to the free protonated ligand and long lifetimes of ca. 20 μs are suggestive of a significant degree of LC character, whilst irreversible metal-based electrochemical results predict a moderate contribution from the metal centre. Further substitutions of the ancillary ligand by a strongly donating acetylide were also performed by Lalinde *et al.*, who,

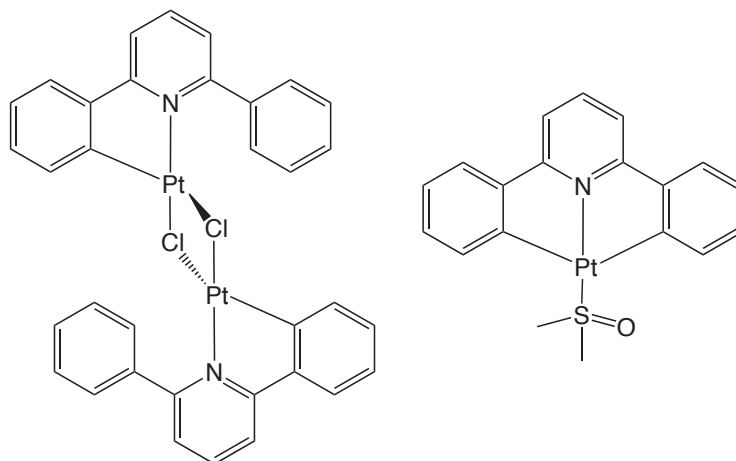


Fig. 1.27 C[^]N[^]C-coordinated dimer and cleavage with coordination of DMSO.¹¹⁵

again, found that room temperature phosphorescence was not observed, thought to be due to low-lying d-d states.¹¹⁷ Intense luminescence at 77 K was presumed to originate from a $^3\pi - \pi^*$ state, and both excimeric and aggregation effects were noted for several compounds. Complexes incorporating a bulky R group on the acetylide (t-Bu or Ph) display two bands attributed to the existence of an excimeric species and the formation of aggregates at high concentrations.¹¹⁷

1.3.2 Theoretical study of cyclometallated platinum(II) complexes

In summary, Pt(N[^]N[^]C)Z complexes combine the π -acceptor properties of bpy with a strong field donor effect of the cyclometallating carbon, such that the resulting emission occurs primarily from a $^3\text{MLCT}$ state. Compounds of the form Pt(N[^]C[^]N)Z show a wide range of phosphorescent efficiencies extending up to very high quantum yields and tend to emit from a predominantly LC $^3\pi - \pi^*$ state, with MLCT perturbations. The radiative and non-radiative rate constants are dependent on the degree of mixing of the excited states. Pt(C[^]N[^]C)Z compound characteristics resemble those of the N[^]C[^]N-coordinated complexes, consisting of a metal-perturbed LC $^3\pi - \pi^*$ emitting state, but are typically emissive only at low temperatures.

A detailed computational study by Che¹¹⁸ investigated the possible reasons for the diversity in efficiencies seen for the three classes of cyclometallated complex discussed above. Five representative complexes were examined, which were based upon the following motifs: Pt(N[^]C[^]N)Cl, Pt(N[^]N[^]C)Cl and Pt(C[^]N[^]C)C \equiv NR, with 2-pyridyl or 3-isoquinolyl groups (Fig. 1.28). The room temperature luminescence of the five compounds shown demonstrates the range of efficiencies for outwardly

similar systems: (a) Pt(dpyb)Cl and (d) Pt(Npqpy)Cl are strongly emissive,^{101,109} (b) Pt(Phbpy)Cl⁹⁸ and (e) Pt(dNppy)CN-Ph¹¹⁸ are weakly emissive (compound (e) has a quantum yield of 0.0023 in room temperature CH₂Cl₂, reported in the study by Che), whilst (c) Pt(dPhpy)CN-Ph is non-emissive;¹¹⁹ A combination of effects must be taken into account when formulating an explanation for the luminescent differences; considering any of the influential factors alone, such as d-d splitting or SOC, to predict efficiencies, cannot fully account for the experimental observations.

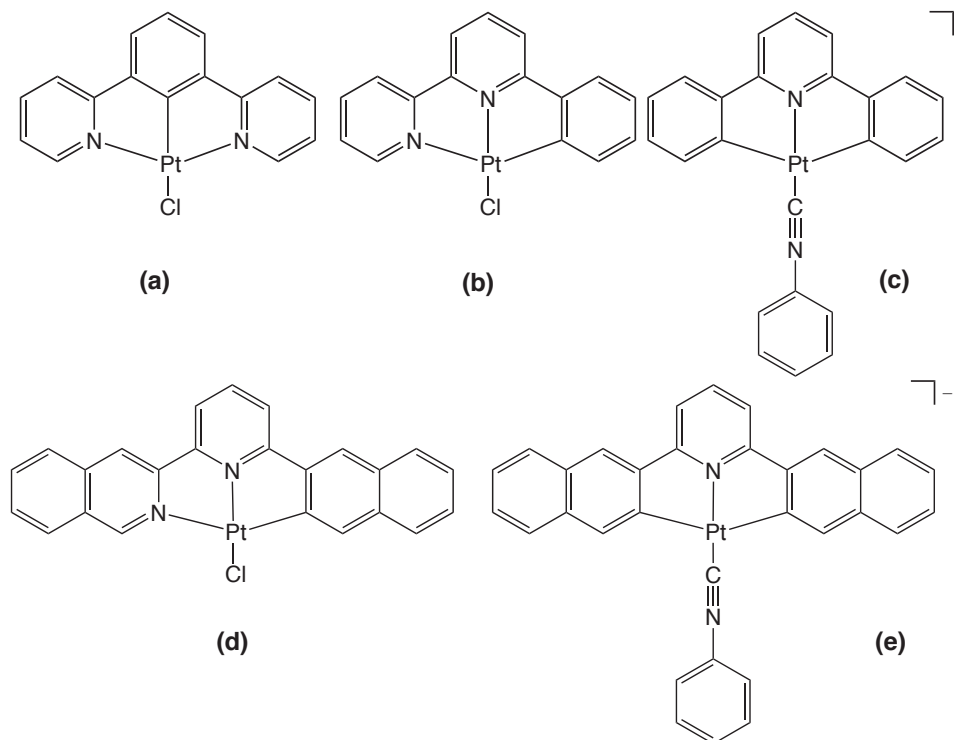


Fig. 1.28 Cyclometallated complexes investigated in a theoretical study by Che and Tong.¹¹⁸

The energy difference between the two highest-lying occupied d orbitals, $\Delta d d_{occ}$, at the S_0 and T_1 geometries has been reasoned to play a key role in emission efficiency, with a smaller $\Delta d d_{occ}$ resulting in a faster rate of radiative decay, k_r .^{1,120} The splitting between the highest occupied and lowest unoccupied d-orbitals, $\Delta d d^*$, also has an effect on the radiative rate constant, k_r : compounds with large $\Delta d d^*$ splitting tend to exhibit higher radiative rate constants. A compromise is required for this parameter, as it is preferable to push the deactivating MC states to higher thermally inaccessible energies with a large $\Delta d d^*$ splitting, but for strong spin-orbit coupling to occur between states, the states need to be close in energy. Complexes (b) and (c) have the largest $\Delta d d_{occ}$ and the smallest $\Delta d d^*$, consistent with the lack of intense emission observed. However, (e) is an anomaly since its $\Delta d d^*$ value is larger than that of (a) and (d), indicating that other factors are also important. The

degree of SOC between the T_1 triplet state and low-lying singlet states is higher for (a) and (d), whereas in (b), (c) and (e), coupling of T_1 can only occur with higher energy singlet states, leading to a smaller SOC coefficient and less efficient phosphorescent emission.¹¹⁸ A greater structural distortion occurs on moving from the ground state to the excited state in the $C^{\wedge}N^{\wedge}C$ -coordinated complex, (c), than that of the $N^{\wedge}N^{\wedge}C$ - and $N^{\wedge}C^{\wedge}N$ -coordinated complexes, causing a reduction in $\Delta d-d^*$ character, which leads to an increase in non-radiative decay.

1.3.3 Platinum(II) complexes containing six-membered chelate rings

A further method of improving the photophysical properties of transition metal complexes by increasing ligand field strength, is the use of ligands that provide a more optimal geometry at the metal centre than that seen for tpy and its related ligands, for which the angle subtended by the outer donor atoms is approximately 160° for pseudo square planar platinum complexes.^{87,121} As discussed in Section 1.2.1, polypyridyl ligands have been investigated that bind to a metal centre with the formation of six-membered chelate rings, rather than the more traditional five-membered chelates seen for the majority of platinum group metal complexes. This results in relief of ring strain, offering better orbital overlap and less interaction between the emissive MLCT states and non-emissive MC states. McMillin and Thummel demonstrated that 2-(8-quinolyl)-1,10-phenanthroline binds to a Pt(II) centre with the creation of one five-membered and one six-membered chelate ring (Fig. 1.29a).¹²² The geometry about the metal is significantly different from that of $[Pt(tpy)Cl]ClO_4$; the N–Pt–N angles for the phenanthroline-based complex is 174.8° ¹²² compared to 163.5° ⁸⁷ for the tpy-based complex, and accordingly the phenanthroline derivative shows emission in solution at room temperature ($\Phi_{lum} = 0.002$, $\tau = 310$ ns in CH_2Cl_2).

Continuing research into geometry optimisation for the relief of ring strain, a series of fused five-six-membered metallocycles were prepared by Huo *et al.*,¹²³ based upon an $N^{\wedge}N^{\wedge}C$ -coordinating ligand (Fig. 1.29b). The acetylide derivatives show a vast improvement in room temperature emission properties compared to the five-five-membered $N^{\wedge}N^{\wedge}C$ -based complexes discussed previously (see Section 1.3.1.3), although the parent chloride complexes are practically non-emissive in solution at room temperature. For example, a comparison of the $N^{\wedge}N^{\wedge}C$ -coordinated five-membered-chelate complex $Pt(Phbpy)(C\equiv CPh)^{103}$ and five-six-membered-chelate complex (Fig. 1.30) can be made. Quantum yields for the two compounds are 0.04 and 0.56, respectively, with an increase in lifetime from 0.04 to $9.2 \mu s$. Since

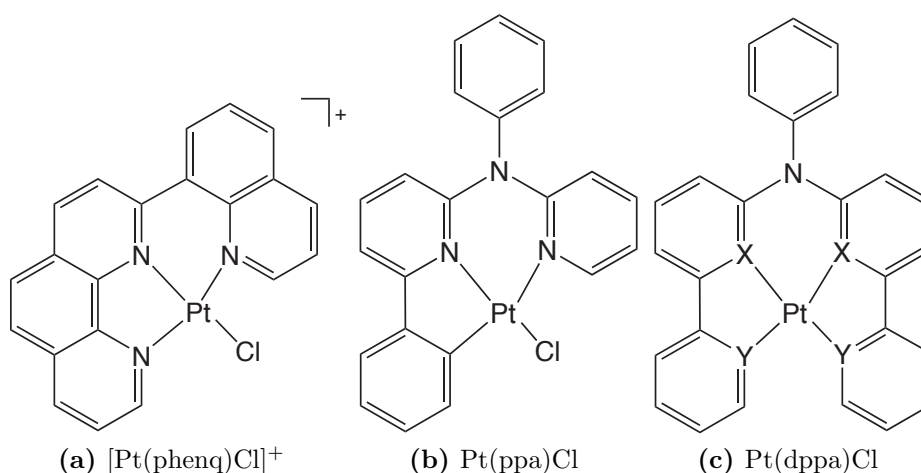


Fig. 1.29 Six-membered chelates: (a) Quinoline-based structure published by McMillin *et al.*¹²² (b) Terdentate-coordinated complexes reported by Huo *et al.*¹²³ and (c) Tetradentate-coordinated complexes reported by Huo *et al.*, where X and Y = C and N, or N and C¹²⁴

the rigidity of the two systems is not significantly different, it was suggested that the favourable bite angle for square planar geometry (ca. 174°) was the reason behind the increase in luminescence, which was attributed to LC emission with MLCT admixture.¹²³ The same group also investigated a variety of tetradentate ligands on platinum, which produce a five-six-five-chelated structure (Fig. 1.29c). N[^]C[^]C[^]N-coordinated and C[^]N[^]N[^]C-coordinated complexes displayed excellent quantum yields (0.14–0.75) attributed to a mixed excited state containing LC character with MLCT and LLCT admixture due to the cyclometallating effect of two carbon donors.¹²⁴

Chen *et al.* adopted this strategy for the synthesis of a series of platinum compounds based upon bis(2-pyridylimino)isoindoline (BPI) derivatives, which acts as an anionic N[^]N[^]N-coordinating donor through deprotonation of the central indole.¹²⁵ The complexes contain two six-membered chelate rings (Fig. 1.31), resulting in proximate square planar geometries with N–Pt–N bite angles of 172–176°. Ten of the eleven compounds prepared showed room temperature emission in solution, with quantum yields in the range 0.0003 to 0.038 and decay lifetimes from <0.01 to 4.31 μs. This was interpreted as triplet emission originating primarily from a ³π – π* state mixed with MLCT transitions, as determined from DFT calculations. Where complexes were metathesised with a monodentate N-heterocyclic ligand (denoted N-het), such as pyridine in place of chloride, an LLCT component from π(N-het) → π*(BPI) was introduced and emission was shifted according to the electronic nature of the acetylide. Electron-withdrawing substituents induced a

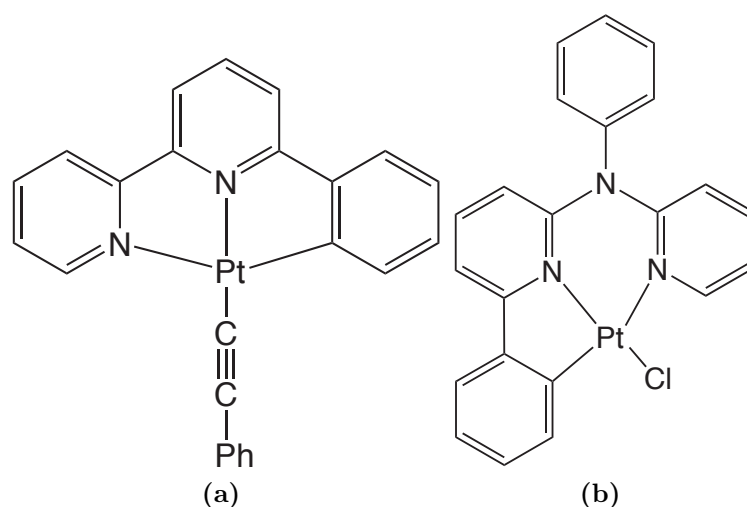


Fig. 1.30 Comparison of chelate sizes in N^2N^1C -coordinated Pt(II) complexes: (a) Five-membered chelate ($\Phi_{lum} = 0.04$)¹⁰³ (b) Six-membered chelate ($\Phi_{lum} = 0.56$).¹²⁴

blue-shift in emission owing to stabilisation of the HOMO; the reverse was true for electron-donating substituents.¹²⁵ Functionalisation of the BPI backbone and the introduction of an N-heterocyclic ligand in the fourth coordination site led to slight distortions of the geometry, such that where crystal structures were obtained, the bite angles were ca. 170° .¹²⁶ Photophysical properties were comparable to the initial BPI series: $\Phi_{lum} = 0.00031$ – 0.026 and $\tau = 0.05$ – 2.98 . Thompson *et al.* continued research into Pt(BPI)-based compounds by exploring the effect of benzoannulation¹²⁷ on absorption and emission processes. Dependent on the site of benzoannulation, a blue-shift or a red-shift could be achieved and through DFT calculations, the electronic properties could be explained.

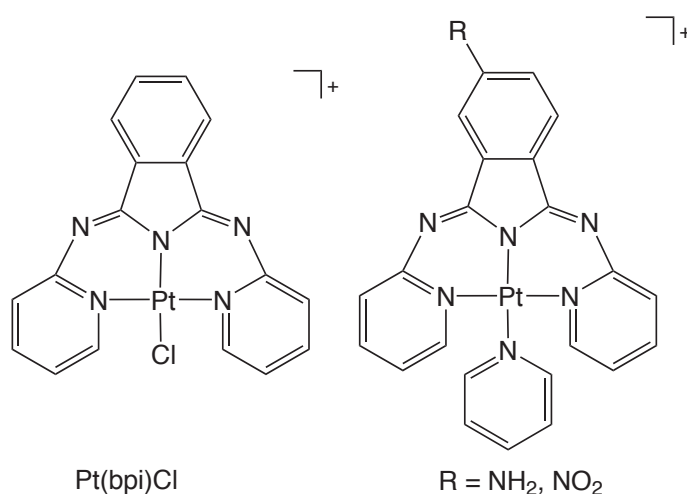


Fig. 1.31 Isoindoline-based Pt(II) complexes containing six-membered chelate rings.^{125,126}

Table 1.2 Photophysical data for [Pt(tpy)Cl]⁺, Pt(dpyb)Cl and representative complexes incorporating six-membered chelates at 298 K in CH₂Cl₂.

Complex	λ_{abs} /nm	λ_{max} /nm	$\Phi_{\text{lum}} \times 10^2$	τ /ns
[Pt(tpy)Cl] ⁺ ^a	305, 320, 340, 390, 403	500, 535, 590	0.04	<0.01
Pt(dpyb)Cl ^b	332, 380, 401, 454, 485	491, 524, 562	0.60	7200
[Pt(phenq)Cl] ⁺ ^c	395	555, 590, 660sh	0.20	310
[Pt(bpi)Cl] ⁺ ^d	249, 277, 347, 385, 468, 495 536	631	0.005	960
Pt(ppa)Cl ^f	330, 345, 372	g	g	g

^a Data from ref^{87,89}. ^b Data from ref¹⁰⁶. ^c Data from ref¹²².

^d Data from ref¹²⁵. ^e Data from ref¹²⁷. ^f Data from ref¹²³. ^g Non-emissive in solution.

1.4 Organic light-emitting devices (OLEDs)

One of the main applications of luminescent complexes is in organic light-emitting devices (OLEDs), also referred to as organic light-emitting diodes. These devices work on the principle of electroluminescence, a phenomenon first observed by Round in 1907 from silicon carbide (SiC) and then noted by Destriau¹²⁸ in 1936 who observed fluorescence from zinc sulphide (ZnS), but it was not until 1955 that an organic compound was found to exhibit fluorescence when Bernanose studied single crystals of anthracene.¹²⁹ Light emission from inorganic GaAsP semiconductor junctions was reported in 1962 by Bevacqua,¹³⁰ followed by the discovery of EL in organic semiconductors by Pope *et al.* in 1963.¹³¹ Several attempts to incorporate organic materials into light-emitting diode LED technology were made later during the decade by Helfrich and Schneider,¹³² Dresner¹³³ and Williams and Schadt,¹³⁴ but these thick film devices required large voltages of the order of 100 V. The first device to operate at a respectable driving voltage was produced in 1987 by Tang and VanSlyke working for the Eastman Kodak company. Their novel bilayer device was based on thin films (active zone of <1 μm), which prevents formation of pinholes that causes shorting out of the cell (as in Dresner's work¹³³ for example). It was discovered that inclusion of a hole-injection layer (HIL) alongside a luminescent layer comprising an electron-transporting compound greatly improved power conversion efficiency.

OLEDs have many advantages over both traditional and more modern display screen technology such as the cathode ray tube (CRT), liquid crystal displays (LCDs) and plasma display panels (PDPs). Fundamentally, they draw less power than these forms of display equipment due to the lack of a permanent backlight. Only the "active" molecules are lit at any one time and so the devices can be lit over a wide

area with a relatively low direct current, allowing them to be thinner and lighter than backlit screens. In the modern world, portability and flexibility of technology is in demand and OLEDs are robust enough to be deposited on a wide range of surfaces, including flexible substrates.^{135,136} They offer bright colours and retain high contrast images at wide viewing angles, with a fast (sub-microsecond) response time.

Organic LEDs are typically multi-layered structures, which can be tuned and improved by the addition of various enhancement layers but, nonetheless, they have a standard basic composition (Fig. 1.32). This consists of a transparent anode, usually indium tin oxide (ITO) to allow the photons to pass through, an emissive organic layer (usually doped into a host material) and a metallic cathode with a low work function, such as aluminium or calcium, or an alloy such as Mg/Ag or Li/Al. The most appropriate methods for OLED fabrication are evaporation under vacuum by resistive heating and spin-coating from solution onto an ITO glass substrate. For large substrates, organic vapour phase deposition (OVPD) has been employed successfully.¹³⁷ The latest developments in printing technology have enabled more accurate deposition of layers utilising techniques such as screen printing,¹³⁸ masked dye diffusion,¹³⁹ micro-contact printing¹⁴⁰ and inkjet printing.¹⁴¹

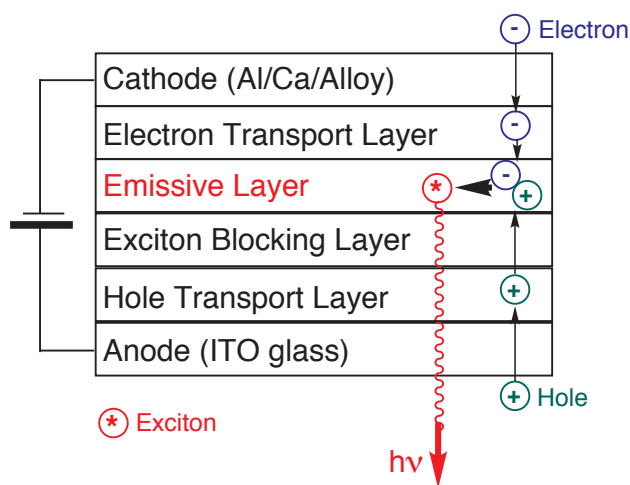


Fig. 1.32 Schematic diagram of the generic structure of a working OLED.

The principle of electroluminescence is the formation of excitons that decay by emitting energy in the form of light. An electric potential is applied across the organic material by injection of electrons from the cathode and holes (electron vacancies) from the anode. Under the influence of the applied field, the electrons and holes migrate through the device and on meeting an opposite charge recombination occurs to form an excited state, termed an exciton. The exciton can form in a singlet or triplet state and decays either by fluorescence or phosphorescence respectively,

releasing photons of light through the transparent anode. Different forms of recombination and, thus, population of the excited state can occur: one of the charge carriers is directly trapped on the emitter dopant so that recombination occurs on the molecular site, or the exciton is trapped on the host molecule with subsequent energy transfer to the triplet emitter.¹⁴² In the latter process, energy transfer may proceed *via* Dexter¹⁴³ or Förster¹⁴⁴ transfer. Dexter transfer is a short range process where excitons diffuse from donor (D) to acceptor (A) using intermolecular electron exchange, whereas Förster transfer is a long-range (ca. 40–100 Å) non-radiative dipole-dipole coupling of D and A molecules. Due to spin requirements, triplet-triplet energy transfer is likely to transpire *via* Dexter transfer, whilst singlet-singlet energy transfer is dominated by Förster transfer at low acceptor concentrations, so both processes are typically involved in host-dopant systems.¹⁴²

Devices performance is improved by the use of synergic layers that increase transport properties and hole and electron injection, to optimise exciton formation. Adjacent to the electrodes, an electron transport layer (ETL) and hole transport layer (HTL) increase charge mobility towards the emissive layer (EML). The most widely used compound for the ETL is tris(8-hydroxyquinolato)aluminium (Alq₃), with 3-phenyl-4-(1'-naphthyl)-5-phenyl-1,2,4-triazole (TAZ) another popular choice (Fig. 1.33a). For hole transport the most common materials are *N,N'*-diphenyl-*N,N'*-bis(3-methyl)-1,1'-biphenyl-4,4'-diamine (TPD), *N,N'*-bis(1-naphthyl)-*N,N'*-diphenyl-1,1'-biphenyl-4,4'-diamine (NPB) and 4,4'-[bis(1-naphthyl)(phenyl)amino]-1,1'-biphenyl (NPD) (Fig. 1.33b), which have glass transition temperatures below 100 °C, a desirable property for ease of manipulation and manufacture.¹⁴⁵ Additional materials can be included, such as electron or hole injection layers (EIL and HIL, respectively) and electron and hole blocking layers (EBL and HBL, respectively) to prevent exciton movement and quenching by confining electrons and holes to the EML (see Chapter 5 for further discussion of the materials used in this study).

OLED properties are described by a series of parameters,⁴ often to assess suitability for particular applications, such as WOLEDs for white lighting. The commonly quoted value to define efficiency of luminescence in a metal complex is the photoluminescent quantum yield, Φ_{lum} , which is the ratio of the number of photons emitted compared to the number of photons absorbed. For an EL device, efficiencies are related to the number of electrons injected; although the maximum theoretical internal efficiency is 100 % if triplet excitons can be harnessed through phosphorescence (*vide infra*), the external quantum efficiency (EQE), η_{ext} , is significantly lower because of internal reflection that traps photons inside the organic layer. The internal quantum efficiency, η_{int} , represents the ratio of the number of photons emit-

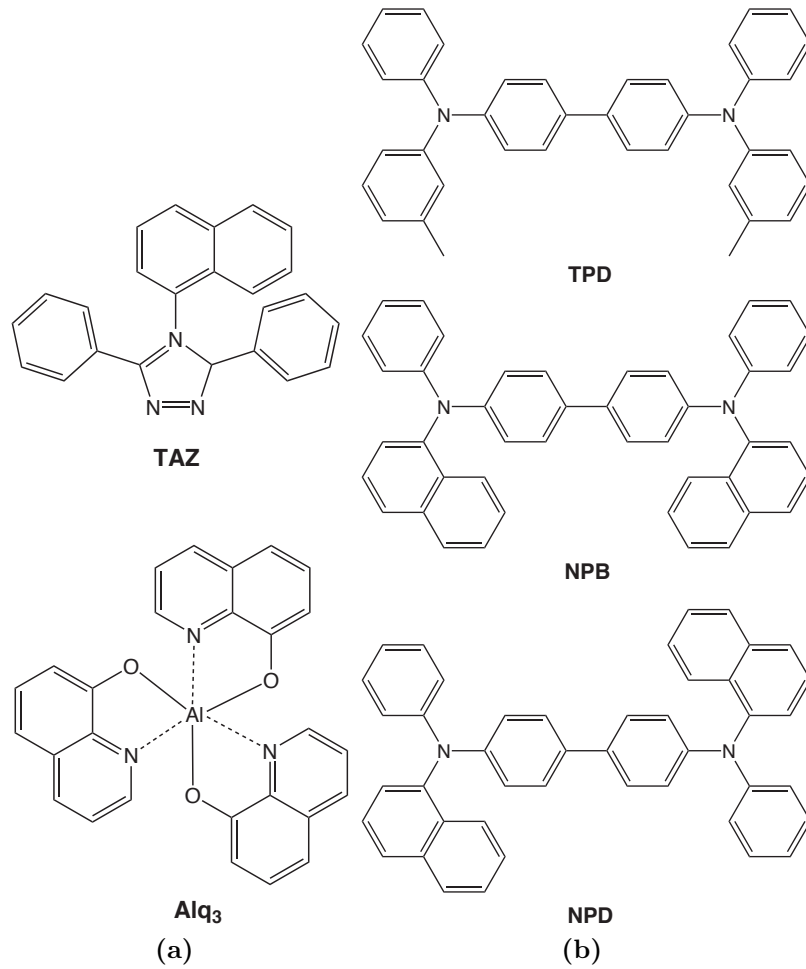


Fig. 1.33 Examples of common transport materials used in OLEDs for (a) Electron transport and (b) Hole transport.

ted to the number of electrons injected at the cathode and the relationship between the external and internal efficiency, η_{ext} and η_{int} , is given by either Equation 1.1 or Equation 1.2:

$$\eta_{\text{ext}} = \eta_{\text{int}}\eta_{\text{ph}} \quad (1.1)$$

$$\eta_{\text{ext}} = \gamma\eta_{\text{ex}}\phi_{\text{p}}\eta_{\text{ph}} \quad (1.2)$$

where η_{ph} is the light-out coupling efficiency, η_{ex} is the fraction of total excitons formed that result in radiative transitions, γ is the ratio electrons to holes injected (or *vice versa* to maintain $\gamma < 1$) and ϕ_{p} is the intrinsic quantum efficiency for radiative decay.¹⁴⁶ The internal efficiency can also be compared to the external efficiency in terms of n , the refractive index of the medium by considering Equation 1.3.

$$\eta_{\text{int}} = 2n^2\eta_{\text{ext}} \quad (1.3)$$

For technological purposes other parameters often reported are:

- Device brightness: measured in candela per unit area (cd m^{-2}),
- Luminous power efficiency, η_{pow} : ratio of the output light power to the input electric power, $\eta_{\text{pow}} = \eta_{\text{ext}}E_p/V$, measured in W W^{-1}
- Luminous efficiency, η_{lum} : the perceived radiant power (luminance) of the standard observer, measured in candela per amp (cd A^{-1}) or lumens per watt (lm W^{-1}) by a weighting parameter, S according to the sensitivity of the eye to colour
- CIE (Commission Internationale d’Eclairage) chromaticity coordinates, reported as x,y-coordinates to define the colour of emission on the CIE 1931 XYZ-colour space

1.4.1 Transition metal complexes in OLEDs

Statistically the ratio of singlets to triplets generated by recombination should be 1:3, such that the maximum internal quantum efficiency is limited to 25 % through spin-allowed fluorescence where only singlet decay leads to emission of light.¹⁴⁷ Although some research has explored the possibility of manipulating the fraction of excitons that form as singlets,¹⁴⁸ the majority of studies have focused on triplet harvesting by employing phosphorescent emitters as dopants in OLEDs. Early multilayered devices utilised fluorescent emitters, polyarenes and heterocycles;^{149,150} the first successful implementation of an organic phosphorescent dye in an OLED was in 1998 when Baldo *et al.*¹⁴⁷ constructed a device containing the red phosphor 2,3,7,8,12,13,17,18-octaethyl-21H,23H-porphine platinum(II) (PtOEP) (*Fig. 1.33a*). Following shortly afterwards a polymer light emitting device (PLED) containing poly(*p*-phenylenevinylene) (PPV) (*Fig. 1.34b*) was developed by Friend *et al.*^{151,152} Subsequently, OLEDs became more widespread and many review articles have since been published on the subject (see for example^{145,153,154,155,156,157}), so only a brief overview of some example OLEDs will be discussed here.

For full-colour displays, a combination of the three primaries of light, red, green and blue, is required. The central span of the visible spectrum is relatively easy to access, with green emitters the most commonly encountered colour for phosphorescent emission, but the outer reaches of the visible region, in particular the blue

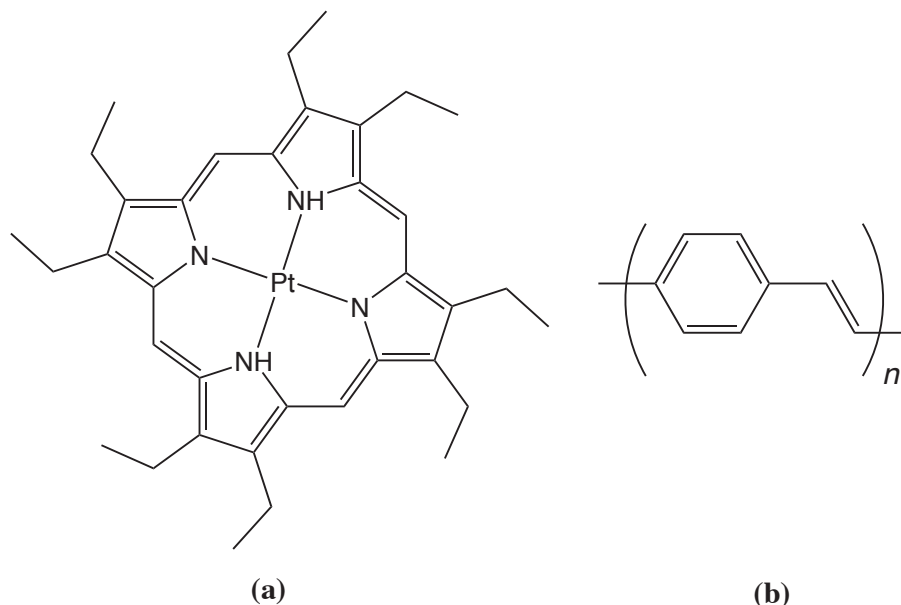


Fig. 1.34 Structure of (a) PtOEP, the first phosphor to be used in an OLED and (b) PPV, the first polymer to be used in a PLED.

high-energy region, have proven more impenetrable through the use of transition metal complexes. The first OLED based upon an organometallic complex, that of PtOEP doped into Alq₃, generated an internal efficiency of 23 %, corresponding to an external efficiency of 4 %¹⁴⁷ but had a long lifetime such that triplet-triplet annihilation occurred, especially at high currents. Ideally for OLED applications, phosphorescent complexes should have a short lifetime (ca. 1 μ s) to reduce annihilation,¹⁵⁸ therefore complexes that emit from a charge transfer state often exhibit better characteristics for OLEDs than LC emitters. Osmium and ruthenium compounds for use in OLEDs were the subject of a short review article,¹⁵⁹ which notes the tuneability of emission colour from red to blue through a wide variation of ligands.

As discussed in Section 1.2.5, rhodium(III) polypyridyl complexes are largely non-emissive at room temperature, with the exception of a select few diimine complexes published by von Zelewsky¹⁶⁰ and Lo,⁷⁵ so the use of Rh(III) complexes for OLED applications has not been explored. On the contrary, Ir(III)-based OLEDs have been widely investigated and, like ruthenium and osmium, a range of colours from red to blue has been obtained. Thompson *et al.* continued to be pioneers in the field, reporting a series of iridium-based OLEDs with internal efficiencies approaching 100 % and external efficiencies reaching up to 19 % (reported to ± 0.2 %). Initially, the archetypal iridium complex *fac*-Ir(ppy)₃ (Fig. 1.8a) was used to fabricate a green device reaching a maximum η_{ext} of 15.4 ± 0.5 %, followed shortly afterwards by a red-emitting OLED based upon bis[2-[2'-benzo(4,5-a)thienyl]pyridinato-N,C^{3'}]-

iridium(III)acetylacetonate, Ir(btp)(acac),¹⁶¹ and a highly efficient bright green device utilising bis(2-pyridinato-*N,C3'*)-iridium(III)acetylacetonate, Ir(ppy)₂(acac) (see Fig. 1.9 for ligand structures).^{2,162} The red device showed a distinct improvement over the PtOEP red emitter previously reported by the same group,¹⁴⁷ with its much shorter decay lifetime of 4 μ s diminishing triplet-triplet annihilation, resulting in an η_{ext} of 7 %. The green device displayed an excellent η_{ext} of 19% from a calculated internal efficiency of 87 ± 7 %.

Red emitters containing Ir(III) compounds with inductive F or CF₃ substituents, or extended conjugated frameworks¹⁶³ reached external efficiencies approaching that of the green emitters with the use of tris(bidentate) chelates; for example, the tris chelate containing 2-phenylisoquinoline reported by Tsuboyama showed an efficiency of 10.3 %. Fluorination of iridium complexes has been shown to reduce triplet-triplet annihilation and increases the tendency for the material to sublime, both of which are important in the manufacture of OLEDs. Additionally, an enhancement in phosphorescent quantum yield is typically seen.⁴ Fluorination can also blue-shift emission and the most famous blue phosphor for OLED applications is bis[(4,6-difluorophenyl)-pyridinato-*N,C2'*]picolinatoiridium, (FIrpic) (Fig. 1.35) which showed a maximum η_{ext} of 10.1 % in a layered device.¹⁶⁴ This compound has also been employed in many dual-emitter WOLEDs with successful results (*vide infra*).

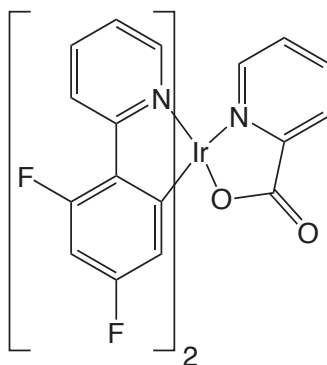


Fig. 1.35 Structure of the blue emitter FIrpic.

Platinum(II) compounds have also been successfully employed in a host of OLEDs spanning the colour range from red to blue, including as dopants in WOLEDs, aided by their square planar geometry permitting intermolecular effects, such as excimers and aggregates, which are not observed for octahedral d⁶ compounds.^{145,165,166} Improvements to the initial PtOEP-based red OLED were carried out by Carty *et al.*, who produced a device containing a Pt(II) complex incorporating indazolyloisoquinoline ligands (Fig. 1.36) that exhibits an η_{ext} of 7 %.¹⁶⁷ As discussed above (see

Section 1.3.1.2) colour-tuning is possible by variation of the ancillary ligand, and Che *et al.* created a range of red and orange Pt(II)-containing OLEDs with low turn-on voltages and η_{ext} values up to 4.2 cd A^{-1} , demonstrating that small changes in ligand environment could impact upon light emission from an OLED.^{99,103,119}

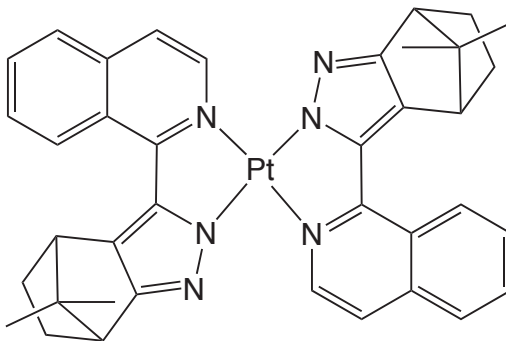


Fig. 1.36 Structure of the indazolyl-containing complex incorporated into a series of OLEDs by Carty *et al.*¹⁶⁷

1.4.2 White organic light-emitting devices (WOLEDs)

Iridium and platinum compounds have played key roles in white-emitting devices, both in single- EML and multi-EML devices.¹⁶⁸ The use of multi-layer WOLEDs, the concept of combining two or more phosphors in a single device, either in one emissive layer or in two adjacent layers, has proven a successful method to obtain white light suitable for solid-state lighting applications.^{168,169,170} The combination of highly emissive red and blue phosphors has led to external quantum efficiencies of up to 12 % and a maximum luminance efficiency of 18 cd A^{-1} in the case of a WOLED based upon an $\text{Ir}(\text{CF}_3\text{ppy})_2(\text{pic})/\text{Ir}(\text{btp})_2(\text{acac})$ pairing, where acac and pic are β -diketonato ligands (Fig. 1.37).¹⁷¹ Forrest *et al.* led the way in developing multi-layered WOLEDs with a series of devices containing iridium or platinum phosphors^{156,172,173} where Pt(II) compounds containing 2-(4,6-difluorophenyl)pyridine (dFppy) derivatives, (as seen in FIrpic, Fig. 5.14), as well as compounds based on $\text{Ir}(\text{btp})_2(\text{acac})$ (Fig. 1.37a) have proved particularly useful in aiding with high energy emission.

An alternative method of obtaining white light is *via* phosphor down-conversion, where a blue emitter, traditionally a gallium nitride-based inorganic LED, is combined with a green/yellow down-conversion phosphor, such as an organic phosphorescent dye.¹⁷⁴ Duggal *et al.* were the first to implement this technique in a white organic device with $\eta_{\text{pow}} = 3.8 \text{ lm W}^{-1}$, through the use of a blue fluorescent emitter and a phosphorescent dye.¹⁷⁵ A fluorescent rather than phosphorescent blue phosphor was employed to avoid the limiting factor of short phosphorescent lifetimes

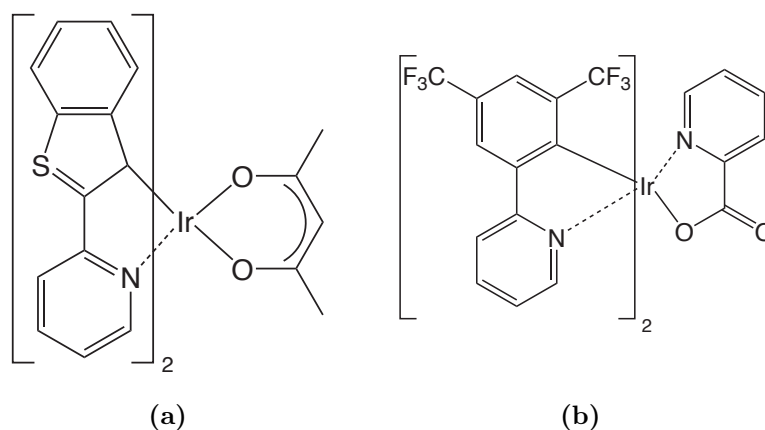


Fig. 1.37 Structure of Ir(III) complexes combined in a WOLED by Tokito *et al.*¹⁷¹ (a) Ir(btp)₂(acac) and (b) Ir(CF₃ppy)₂(pic).

of blue triplet emitters that can limit colour stability. Petty *et al.* also adopted this approach in a spin-coated FIrpic-based device,¹⁷⁶ producing a similar power efficiency of 3.4 lm W⁻¹. Krummacher *et al.* recently manufactured devices with an organic blue phosphorescent emitter, which exhibited efficiencies of 25 lm W⁻¹ and 39 cd A⁻¹, by combining the phosphor with an enhancing nitro-disilicate down-conversion layer, which absorbs a fraction of the photons emitted by the blue phosphorescent layer and re-emits them in the form of orange emission.¹⁷⁷

Platinum compounds show great potential for WOLEDs containing a single emissive layer due to their excimeric emission, which offers a contrasting colour of light to that of the monomer. Cocchi, Williams *et al.* have published extensive research on OLEDs based upon substituted Pt(dpyb)Cl motifs (Fig. 1.25). Red, green and blue devices with external efficiencies up to 18.3 ± 0.5 % have been fabricated by thermal evaporation,¹⁷⁸ with results dependent on substituent and dopant concentration, which affects the monomer/excimer ratio in WOLEDs.^{166,179,180,181}

Results published by Mröz *et al.* on 5-substituted members of the Pt(dpyb)Cl family, using spin-coating rather than the thermal evaporation technique used for the previous compounds, showed the lowest η_{ext} figures for the series (ca. 0.2 %), but were of an order of magnitude higher than those containing a 4,4'-stilbenoid-N[^]C[^]N) Pt(II) compound, also manufactured by spin-coating.¹⁸² A key issue with OLED performance is current roll-off, seen as a sharp drop in device efficiency at high currents, due to triplet-triplet annihilation. The 4-ester-substituted complex based on Pt(dpyb)Cl showed good white device characteristics of up to $\eta_{\text{ext}} = 15.5 \pm 0.2$ %, but the striking effect noted was the decrease in current roll-off observed.¹⁷⁹ The WOLED does not drop to half its peak value until application of a drive cur-

rent more than three times higher than that reported for similar single-dopant devices.^{169,172,183} Further examples of spin-coated devices were manufactured by Petty *et al.*, resulting in a maximum luminescent efficiency and brightness of 8 cd A⁻¹ and 3 lm W⁻¹, respectively.¹⁷⁰ Although the results for the device using FIrpic and Ir(piq)₂(acac) (Fig. 1.38) are not amongst the best WOLEDs reported, device fabrication is relatively straightforward owing to the simple blended-layer configuration, which can be tuned by varying the film thickness. In collaboration with Wang, the group also included Ir(piq)₂(acac) in a WOLED containing the blue fluorescent dye *N*-(4-((*E*)-2-(6-((*E*)-4-(diphenylamino)styryl)naphthalen-2-yl)vinyl)phenyl)-*N*-phenylbenzenamine (N-BDAVBi), which was found to exhibit much better device characteristics when a mixed transition layer (MTL) was included.¹⁷⁶ This layer consisted of the fluorescent dye doped into an ETL material, 4,7-diphenyl-1,10-phenanthroline (Bphen), and devices containing the MTL exhibited a maximum power efficiency of 11.3 lm W⁻¹, twice the value of the corresponding WOLED without the MTL.

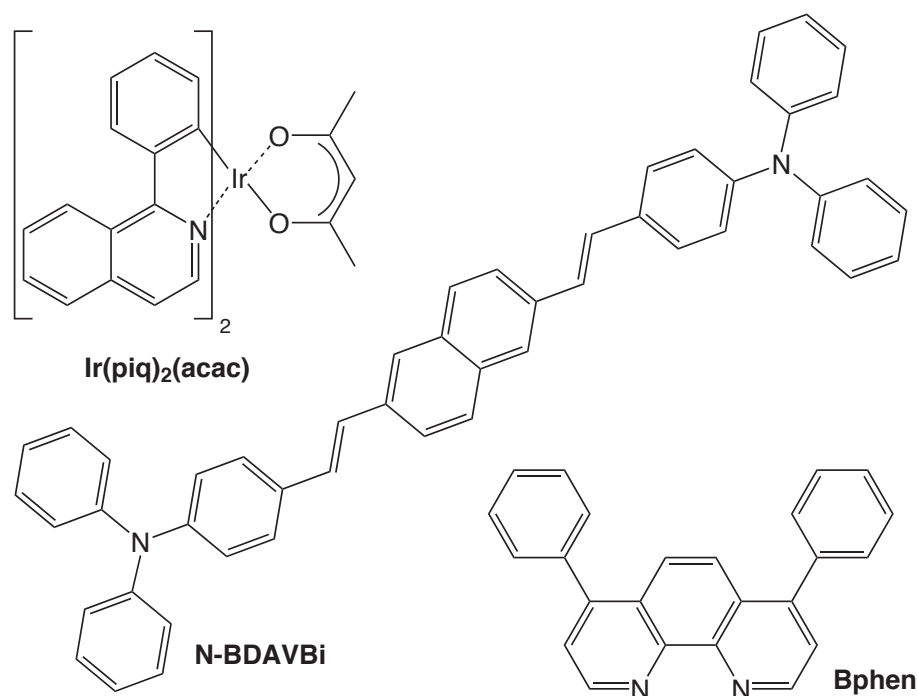


Fig. 1.38 Structure of the red phosphorescent emitter Ir(piq)₂(acac), the blue fluorescent emitter N-BDAVBi and the electron transport material Bphen incorporated into WOLEDs by Wang *et al.*¹⁷⁶

Chapter 2

Synthesis of iridium, rhodium and platinum complexes

2.1 Synthesis of ligands and precursors

The principal ligands studied in this work are terdentate ligands; the only bidentate ligands considered are those that are already well-established polypyridine ligands, which have been synthesised and used in metal complexation reactions for many years, consequently these will not be discussed in any detail. Terdentate ligands are desirable in attaining high quantum yields in platinum group complexes due to the inherent rigidity of the system, which discourages distortions that can quench luminescence (Fig. 2.1). Many terdentate ligands based upon a simple 2,2':6',2''-terpyridine system (henceforth abbreviated as tpy) show a strong preference for planarity, although, as described later, this is not always the case. Practically all previous research in the Williams group has focused on outer pyridyl units so it was hoped that the extended π -conjugated system offered by quinolyl frameworks would increase the likelihood of low-lying emissive charge-transfer states, as well as altering the steric bulk and, in some cases, the bite angles around the metal.

The majority of ligands synthesised were N⁺C⁻N cyclometallating ligands that coordinate through two neutral nitrogen donors and one formally anionic carbon donor, thus achieving a high ligand field about the metal centre (Scheme 2.1). This is an important factor in terms of phosphorescent quantum yield, owing to the energy of the d-d states increasing because of the strong field splitting induced by this class of ligands, thereby diminishing population of these deactivating states. A further advantage of using N⁺C⁻N ligands in conjunction with anionic donors as ancillary ligands is the reduction in overall charge on the complexes. In general, charge neutral complexes are more desirable for OLED fabrication because they tend

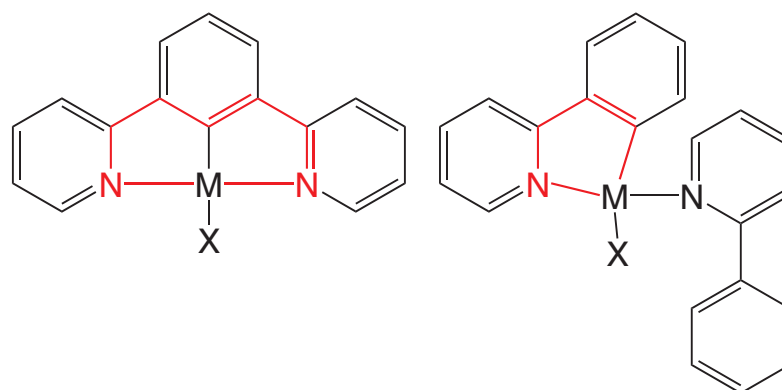
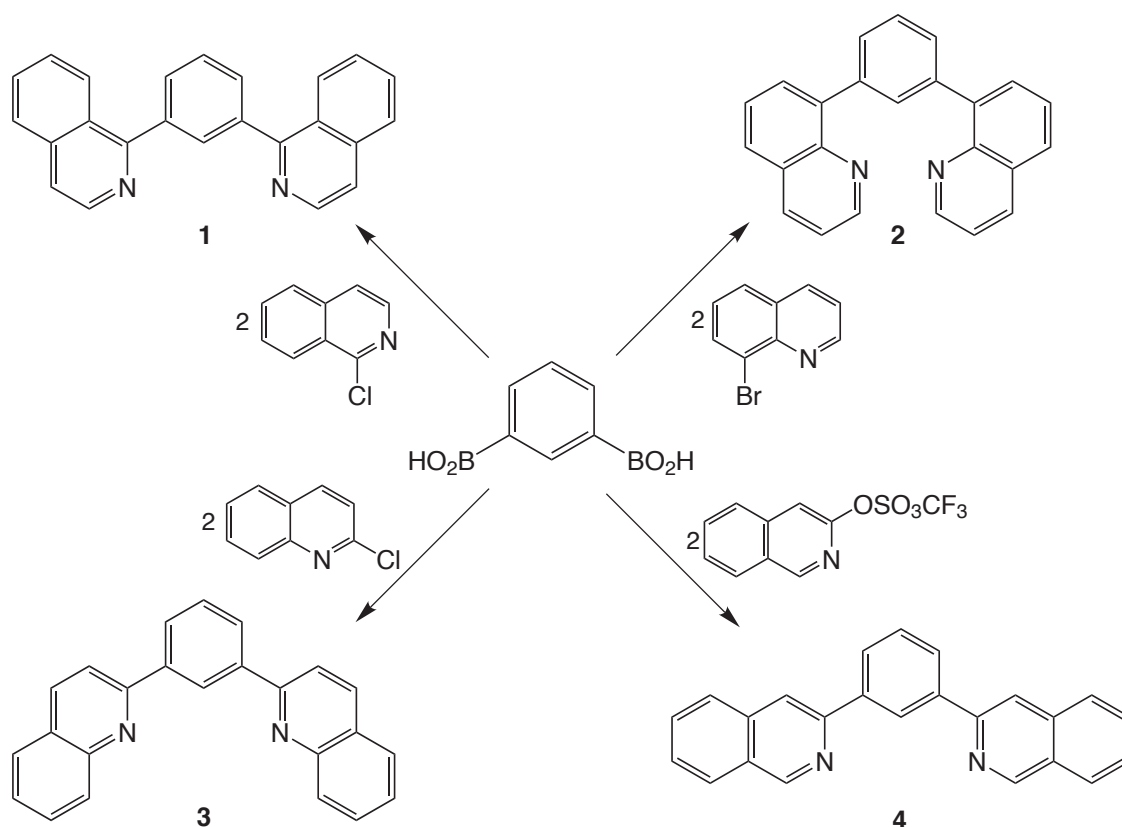


Fig. 2.1 Terdenticity favours rigidity, minimising distortions that occur more readily with bidentate ligands.

to offer greater device stability than their charged counterparts. Charged complex OLEDs also tend to have longer turn-on times (seconds to minutes) due to the need for charge redistribution, and suffer more rapid degradation due to ion migration towards the opposing electrode.



Scheme 2.1 Synthesis *via* Suzuki-Miyaura cross-coupling of the unsubstituted ligands 1-diqb, 1, 8-dqb, 2, 2-dqb, 3 and 3-diqb, 4, using a palladium catalyst and base.

A second class of ligands investigated is terpyridine-type N[^]N[^]N systems, binding through three nitrogen donor atoms, which traditionally offer less scope for high quantum yields; the archetypal complex [Pt(tpy)Cl]⁺ being virtually non-emissive at room temperature. Nonetheless, complexes based upon tpy typically have high stability with respect to dissociation, due to the polydentate nature of the ligand and synergic effect of the σ -donating nitrogen atoms and the π -accepting heterocycles. Recent work utilising a new quinoline-containing ligand, 1,3-di(8-quinolyl)pyridine (dqp), on a ruthenium centre, [Ru(dqp)₂]³⁺,^{34,184} showed promising results (*vide supra*), so it was a natural step to extend the scope of this work to include this ligand, given that the cyclometallated analogue and corresponding platinum complex had been prepared in our group previously. The present study explored whether a positive result could be achieved with different platinum group metals.

A slightly altered approach to synthesis for these all-nitrogen donating ligands was required, albeit based upon very similar chemistry. A crucial feature of the N[^]N[^]N and N[^]C[^]N 8-substituted quinolyl-based ligands is their ability to form six-membered chelate rings around the metal centre rather than the commonly encountered five-membered chelates seen for trivial terpyridine-type arrangements (Fig. 2.2). A six-membered chelating system permits a more linear architecture around the metal, allowing a bite angle very close to the ideal of 180° for a square planar complex. It is the improvement in bite angle that produces near-perfect octahedral symmetry in [Ru(dqp)₂]³⁺, which is thought to be largely responsible for the improved quantum efficiency of the ruthenium complex.³⁴

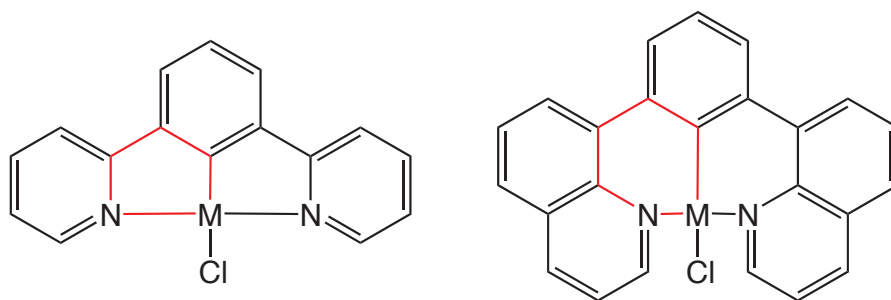


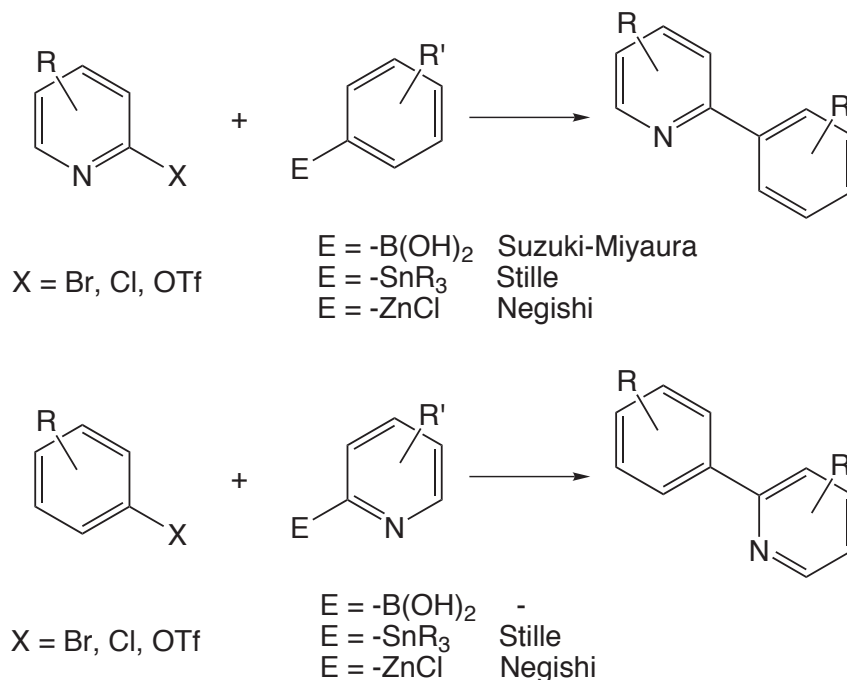
Fig. 2.2 Five-membered versus six-membered chelate rings in metal complexes incorporating terdentate ligands.

2.1.1 Cyclometallating terdentate N[^]C[^]N ligands

2.1.1.1 Synthesis of parent cyclometallating ligands

The advent of palladium-catalysed cross-coupling reactions in the 1970s and 1980s has greatly facilitated the reliable formation of aryl-aryl and aryl-heterocycle bonds.

Such methods are increasingly used by coordination chemists in the synthesis of new and previously established polypyridyl and arylpyridyl/quinolyl ligands. The Suzuki, Stille and Negishi reactions are most suitable for this purpose, and involve the coupling of aryl halides or triflates with, respectively, arylboronic acids, aryl stannanes or arylzinc reagents (Scheme 2.2).

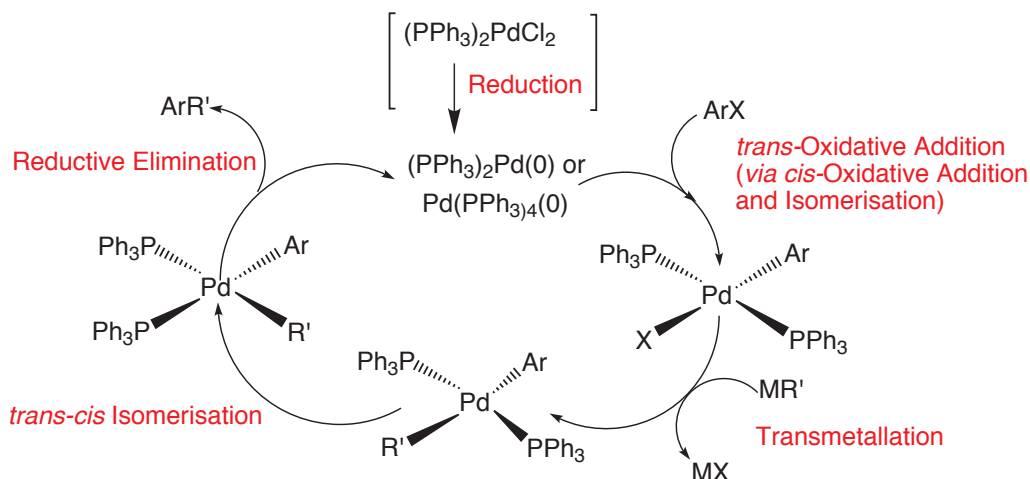


Scheme 2.2 Cross-coupling reactions showing the two approaches to synthesising arylpyridines/quinolines. Instability of *ortho* boronic acid groups in pyridyl rings prevents use of the Suzuki-Miyaura reaction in the second approach.

One limitation of the Suzuki-Miyaura reaction however, is that nitrogen heterocycles incorporating a boronic acid group *ortho* to the heteroatom are usually unstable with respect to carbon-boron bond cleavage and hydrodeboration. Thus, in the synthesis of 2-arylpyridines and 2-arylquinolines *via* the Suzuki-Miyaura reaction the boronic moiety must be in the aryl partner, not the heterocycle.

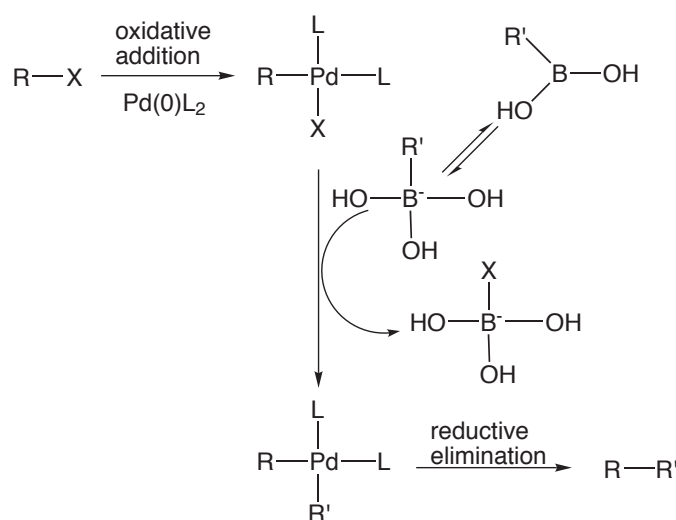
The general catalytic cycle for these reactions consists of oxidative addition to a coordinatively unsaturated Pd(0) centre, followed by transmetalation and then reductive elimination of the product (Scheme 2.3). Frequently there is an additional step involving a *cis-trans* isomerisation prior to the elimination, to form the most stable product. The catalyst used is a palladium(0) species, usually Pd(PPh₃)₄, or else a palladium(II) species, such as Pd(PPh₃)₂Cl₂ that reduces to Pd(0) *in situ*.

Suzuki-Miyaura reactions use organoboronates, which are quite mild nucleophiles with good stability in air and water, they generate benign borate side products and can be used with most functional groups, without the need to protect them. The



Scheme 2.3 General palladium-catalysed cross-coupling mechanism.

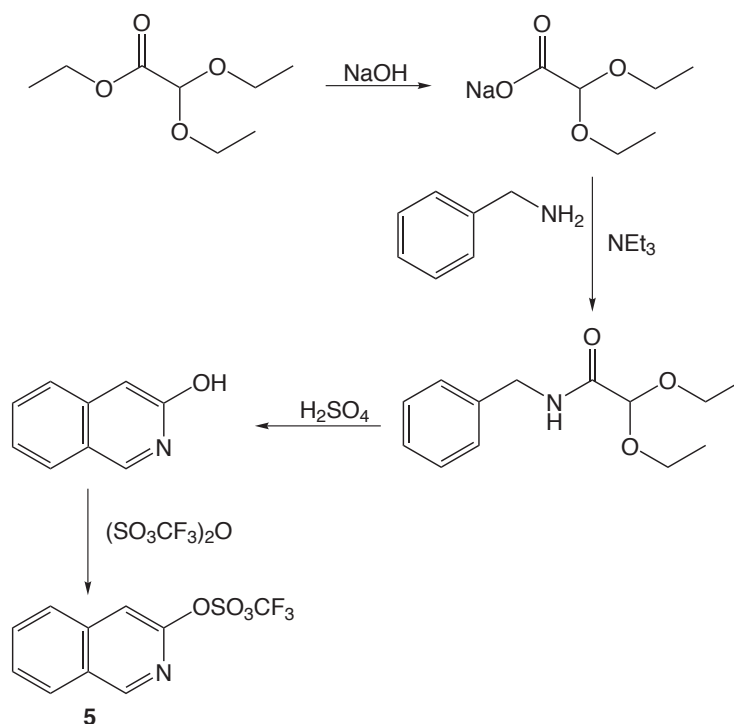
mechanism follows the general pathway of Scheme 2.3 but, unlike the Stille and Negishi reactions, the presence of a base is required to form a nucleophilic “ate” complex, $[B(OH)_3R]^-$ (Scheme 2.4).



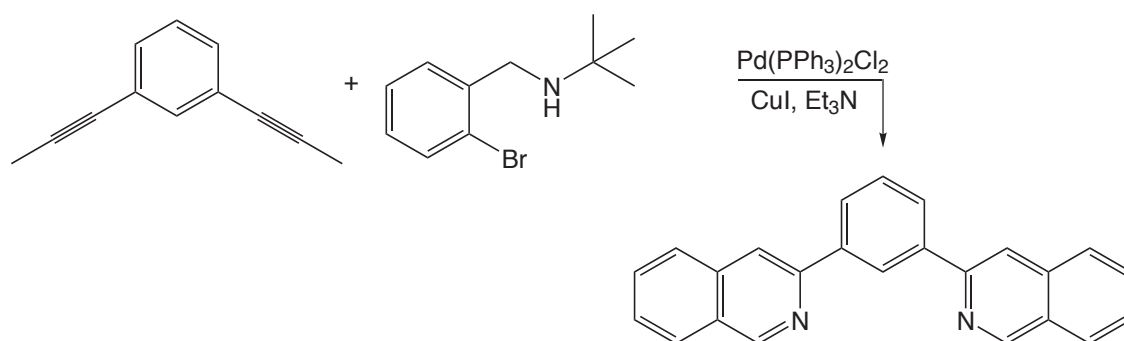
Scheme 2.4 General mechanism of Suzuki-Miyaura cross-coupling.

In the present work, a range of 1,3-diquinolyl benzene ligands were prepared in this way, by Suzuki-Miyaura coupling of an aryl diboronic acid with two equivalents of quinolyl halides or triflate (Scheme 2.1). The reactions were carried out using $Pd(PPh_3)_4$ as a catalyst in a mixed solvent system of toluene/ethanol/aqueous sodium carbonate solution (2 M) (3:3:1 by volume). All reagents, except the catalyst, were degassed *via* four freeze-pump-thaw cycles, prior to addition of the catalyst under nitrogen. The mixture was then heated at reflux for 72 h. All three halogenated quinolines in Scheme 2.1 were commercially available. However, for the preparation of 3-diqb, **4**, a 3-substituted isoquinoline was required. The 3-position

of isoquinoline is notoriously unreactive to both electrophilic and nucleophilic substitution, therefore 3-isoquinolyl triflate, **5** was synthesised by a procedure involving cyclisation to generate the heterocyclic ring and the intermediary of isoquinolin-3-ol, as shown in Scheme 2.5.¹⁸⁵ Towards the end of the work carried out herein, the same ligand was reported by Li *et al.*,¹¹⁰ prepared *via* an annelation reaction of the type pioneered by Larock (Scheme 2.6)^{186,187}



Scheme 2.5 Synthesis of 3-isoquinolyl triflate.

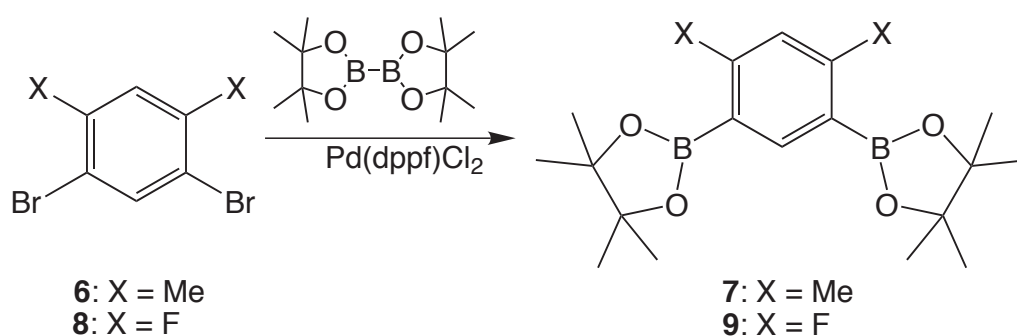


Scheme 2.6 Synthesis of 1,3-di(3-isoquinolyl)benzene by Li *et al.*, based upon work by Larock.^{186,187}

2.1.1.2 Substituted N^C^N ligands

As discussed in Chapter 1, a problem encountered when working with terdentate ligands is competitive bidentate binding (Fig. 1.12), therefore it was of interest to synthesise 4,6-disubstituted systems, using either methyl or fluorine substituents as blocking groups. For this purpose, disubstituted precursors were required and as 4,6-disubstituted boronic acids are not readily available, suitable equivalents, namely diboronic esters, were prepared. This route to boronic functionality proceeds by the method of Miyaura,¹⁸⁸ and involves the cross-coupling of the aryl halide with an alkoxydiboron, such as bis(pinacolato)diboron, (Me₄C₂O₂)B–B(Me₄C₂O₂) (B₂pin₂) adapted to suit a disubstituted system.¹⁸⁹ The most effective catalyst for this process is [1,1'-bis(diphenylphosphino)ferrocene]dichloropalladium(II), Pd(dppf)Cl₂, which is used in conjunction with potassium acetate, KOAc, to facilitate the reaction. Alkoxydiborons are mild reagents that are stable in air, although the preclusion of moisture in the reaction was found to be important for achieving high yields. B₂pin₂, catalyst and base were combined and the apparatus thoroughly degassed, before addition of the appropriate dibromo precursor and dry dimethylsulfoxide (DMSO) under nitrogen. The mixture was then heated at 80 °C for 24 h (Scheme 2.7).

Employing 1,3-dibromo-4,6-dimethylbenzene, **6** and B₂pin₂ in the boronate reaction following Scheme 2.7 led to the synthesis of 1,3-di(pinacolatoboron)-4,6-dimethylbenzene, **7** in 69 % yield after recrystallisation. Combining 1,3-dibromo-4,6-dimethylbenzene, **8** and B₂pin₂ using the same method resulted in isolation of 1,3-di(pinacolatoboron)4,6-di-fluorobenzene, **9** in a 94 % yield following recrystallisation.



Scheme 2.7 Synthesis of dimethyl- and difluoro-substituted boronate esters.

The diboronates were employed in Suzuki-Miyaura cross-coupling reactions to produce the desired disubstituted N^C^N ligands with either methyl or fluoro substituents in the 4'- and 6'-positions. The reaction conditions were identical to that of the unsubstituted ligands, and the ligands shown in Table 2.1 were synthesised in good yields (58–91 %), after purification by column chromatography.

Table 2.1 Disubstituted cyclometallating ligands: precursors and yields.

Number	Boronate	Halide/Triflate	Ligand	Yield
10				76 %
11				91 %
12				58 %
13				79 %
14				63 %

2.1.1.3 Synthesis of an asymmetric ligand: 1,3-(8-quinolyl)(2-pyridyl)-benzene

The success of a Suzuki-Miyaura cross-coupling is dependent on matching the reactivity of the coupling partners (Scheme 2.2) and for 1,3-disubstituted arylpyridines, this can only be achieved successfully using a halopyridine and a boronic arene, due to the instability of *ortho*-boronic functionalities. In contrast, the reverse functionality can be employed to create 1,3-disubstituted ligands containing quinolines. This is due to the nitrogen atom in the quinolyl moiety not being *ortho* to the boron, as it would be in the 2-pyridyl-based compounds. 8-dqb, **2**, was prepared *via* the established methodology of coupling 8-bromoquinoline with benzene-1,3-diboronic acid (Scheme 2.1), however, the reverse method, *via* 8-quinoline boronic acid and 1,3-dibromobenzene, was also tested. The desired ligand was not obtained from this reaction; instead, a useful precursor was isolated in high yield (95 %), in the form of the monosubstituted compound 3-bromo(8-quinolyl)benzene, **15** (Fig. 2.3). This product allows further functionalisation to be carried out to produce new ligands containing two different heterocycles for coordination.

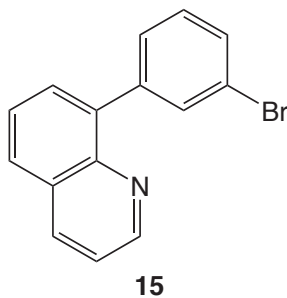
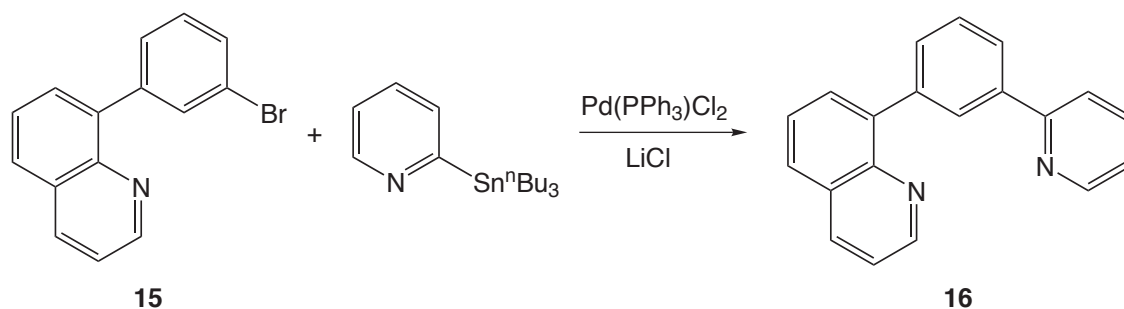


Fig. 2.3 3-bromo(8-quinolyl)benzene, **15**.

Since previous work in the Williams group has focused largely on pyridyl-based side units, it was a natural choice to investigate the synthesis of a terdentate ligand containing one quinolyl constituent and one pyridyl constituent. Incorporation of a pyridyl ring into the system required a change in methodology, as a 2-functionalised pyridine was required. Stille coupling using 2-*n*-butylstannylpyridine, a commonly used precursor in our group, was employed to effect this process. Stille coupling follows the general palladium-catalysed cross-coupling cycle (Scheme 2.3), using an organostannane with the addition of lithium chloride to increase reactivity by chloride binding to the Pd(PPh₃)₂Cl₂ catalyst. The reaction mixture was degassed *via* four freeze-pump-thaw cycles and heated for 45 h, then quenched with a saturated solution of aqueous potassium fluoride, and tin residues removed by filtration (Scheme 2.8).



Scheme 2.8 Stille coupling to create an asymmetric ligand, 1-(8-quinolyl)-3-(2-pyridyl)benzene, qpyb, **16**.

2.1.2 Terdentate N[^]N[^]N ligands

Owing to the lack of room temperature emission observed for all-nitrogen-donor ligands, one quinolyl-based N[^]N[^]N ligand only was chosen for its ability to form six-membered chelates with metal centres. 1,3-di(8-quinolyl)pyridine, dqp, **17** was synthesised following the literature procedure published by Hammarström *et al.*,³⁴ based upon a method pioneered by Buchwald and co-workers.¹⁹⁰ 8-quinolineboronic acid and 2,6-dibromopyridine were combined with bis(benzylidene)acetone palladium(0), Pd(dba)₂, K₃PO₄ and (2-dicyclohexyl-phosphino-2,6-dimethoxybiphenyl), S-Phos (Fig. 2.4), which together provide a catalytic palladium species *in situ* to promote the reaction. After three degassing cycles, dry degassed toluene was added under nitrogen and the reaction heated for 24 h (Scheme 2.9).

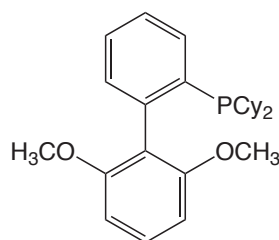
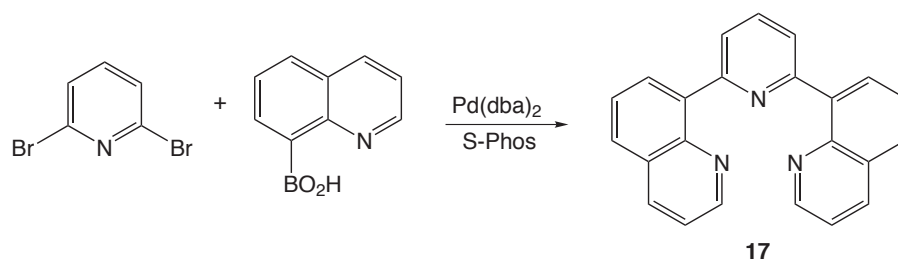


Fig. 2.4 Structure of the sterically hindered phosphine S-Phos used in the preparation of an *in situ* Buchwald catalyst.

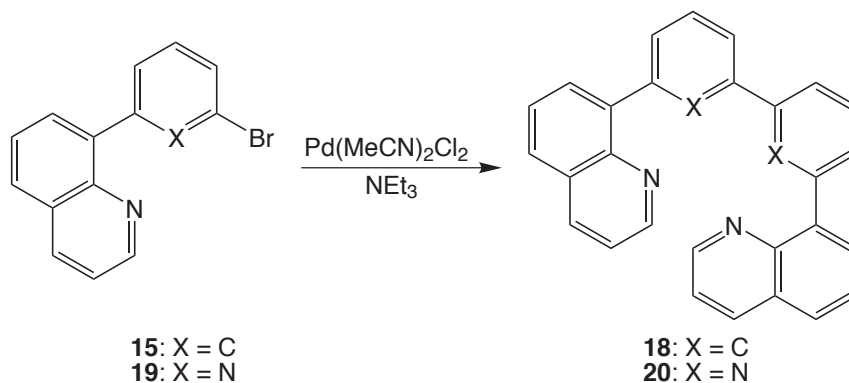


Scheme 2.9 Synthesis of 1,3-di(8-quinolyl)pyridine, dqp, **17**.

2.1.3 Tetradentate ligands

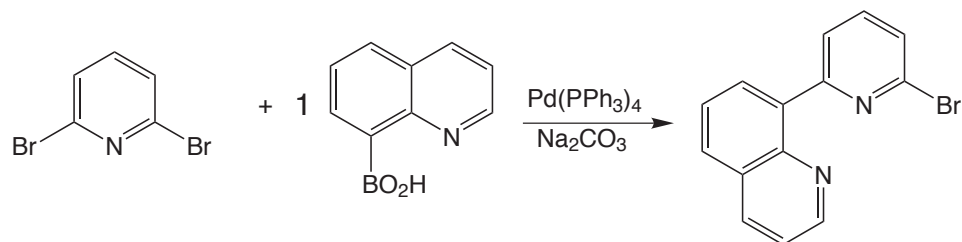
In light of the fact that terdentate ligands offer potential for highly rigid systems and less excited state quenching due to distortions compared to complexes containing bidentate ligands, an obvious further route to explore is synthesis and complexation of tetradentate ligands. Complexation with platinum in a square planar, or pseudo-square planar complex induces a chelating effect where the ligand effectively encompasses the metal centre in a ligand pocket; with the right design, a highly rigid complex should be produced.

Synthesis of tetradentate ligands containing quinolines was undertaken by joining two identical precursors in a homocoupling reaction. Analogously to the terdentate ligands, an $N^{\wedge}C^{\wedge}C^{\wedge}N$ and an $N^{\wedge}N^{\wedge}N^{\wedge}N$ ligand were prepared in order to compare the effect of cyclometallation and neutral donors in an encapsulating ligand. The required precursor **15** (Fig. 2.3), for the cyclometallating ligand 3,3'-bis(8-quinolyl)-biphenyl, bqbph, **18** (Scheme 2.10, X = C) had previously been prepared en route to the asymmetric ligand, qpyb, **16**. Employing this reagent, homocoupling conditions were taken from work by Tanaka *et al.*¹⁹¹ and the reaction was heated overnight in *N,N*-dimethylformamide (DMF) using dry triethylamine and dichlorobis(acetonitrile)palladium, $Pd(MeCN)_2Cl_2$ under an inert atmosphere.



Scheme 2.10 Homocoupling to synthesise tetradentate ligands bqbph, **18** and bqbpy, **20**.

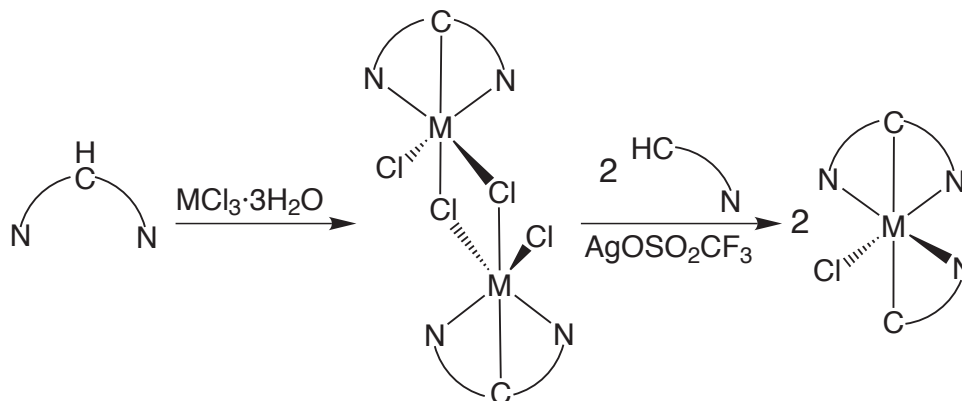
In order to compare the cyclometallated and non-cyclometallated ligands, the analogous tetra-nitrogen ligand was synthesised from a homocoupling of 3-bromo(8-quinolyl)pyridine, qBrpy, **19**. This precursor was prepared from a Suzuki-Miyaura cross-coupling of 2,6-dibromopyridine with one equivalent of 8-quinoline boronic acid (Scheme 2.11), using the standard Suzuki-Miyaura conditions used throughout. The $N^{\wedge}N^{\wedge}N^{\wedge}N$ ligand 6,6'-bis(8-quinolyl)-2,2'-bipyridine, bqbpy, **20** was then isolated in high yield (89 %) after reaction of **20** using the homocoupling conditions described above (Scheme 2.10, X = N).



Scheme 2.11 Synthesis of mono-substituted precursor, qBrpy, **19** using one equivalent of 8-quinolineboronic acid.

2.2 Synthesis of d⁶ iridium(III) and rhodium(III) complexes

Synthesis of the octahedral metal complexes is a two-step process: initially a chloro-bridged metal dimer is formed, followed by cleavage of the dimer to produce two equivalents of the desired complex (Scheme 2.12). Dimer formation proceeds by an established reaction, combining the ligand with a slight excess of the metal trichloride hydrate, IrCl₃ · nH₂O or RhCl₃ · nH₂O, in 2-ethoxyethanol and water (7:3, v/v) and heating at 80 °C overnight. Further product was obtained in several cases by heating the recovered reaction solution for an additional 24 h.



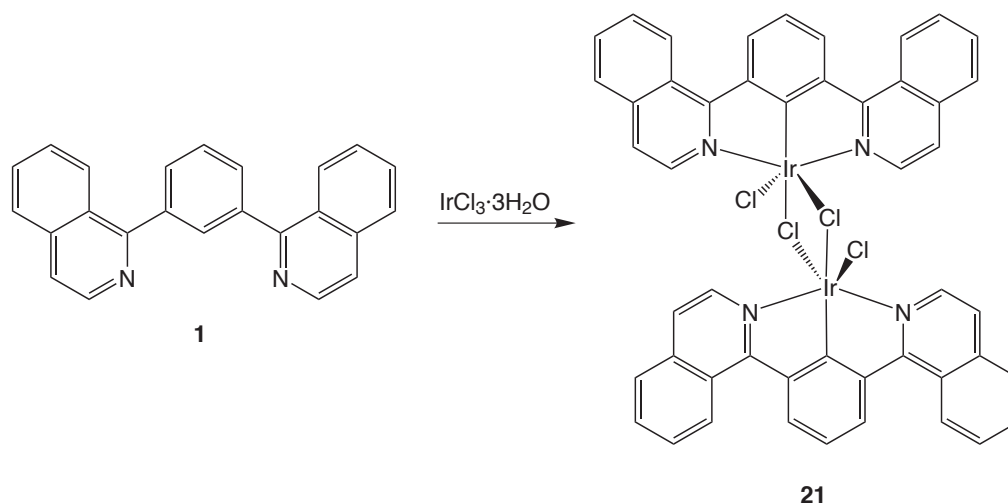
Scheme 2.12 General scheme for synthesis of a d⁶ complex: chloro-bridged dimer formation followed by cleavage with a bidentate ligand to give two equivalents of the metal complex. M = Ir or Rh, N[^]C[^]N and N[^]C represent a terdentate and bidentate cyclometallating ligand, respectively.

Chloro-bridged dimers are frequently insoluble and therefore difficult to purify and characterise. This issue is exacerbated when a mixture of products ensues from competitive binding modes. For the dimers synthesised in this study the precipitate obtained in each case was collected by centrifuge and washed with water, ethanol and diethyl ether to remove unreacted starting materials and aid drying of the prod-

uct. Purification and characterisation of the combination of products was unfeasible due to insolubility. Heating the dimers in deuterated DMSO led to several very weak multiplets in the aromatic region of the nuclear magnetic resonance (NMR) spectrum. Analysis by mass spectrometry (MS) using the atmospheric solids analysis probe (ASAP) showed a range of peaks, affirming the various binding modes. Confirmation of the successful synthesis of the dimers in this work was only obtained subsequently, by preparing and fully characterising the target complex (the second step in Scheme 2.12), verifying the dimer as the intermediate reaction stage.

2.2.1 Cyclometallated N[^]C[^]N iridium(III) complexes

Dimer preparation was attempted for the unsubstituted ligands **1**, **2**, **3** and **4**, and the disubstituted ligands **10**, **11**, **12**, **13** and **14**. Success or failure of the dimer synthesis was confirmed upon addition of the bidentate ligand ppyH (the second step in Scheme 2.12). From these further reactions it could be shown that dimer formation with regard to the unsubstituted ligands was successful only in the case of **1**, to form [Ir(1-diqb)(μ -Cl)Cl]₂, **21** (Scheme 2.13). Terdentate binding to a metal is most favourable for **1** because the isoquinolyl units are oriented away from the terdentate binding site and are in the proximity of the alternative bidentate position as in binding mode II (see Fig. 1.12).



Scheme 2.13 Synthesis of [Ir(1-diqb)(μ -Cl)Cl]₂, **21**.

Attempts to bind iridium to the remaining three unsubstituted ligands were unsuccessful as the subsequent complexation step did not produce the desired iridium complex. It was hoped that the disubstituted ligands would force binding in the desired mode; an unexpected result was the lack of successful dimer formation from 1-diqMeb, **10**, despite successful binding of the unsubstituted parent ligand **1**. It

could be hypothesised that the potential binding of **10** in a terdentate manner is disfavoured by steric interactions between the isoquinolyl groups and the methyl groups (Fig. 2.5). In work published by Li *et al.*¹⁹² the difluorinated analogue of this ligand was complexed to platinum but the dimethyl complex was not reported. Hydrogen bonds to the fluorine substituents may help to stabilise this complex, whereas the methyl to C-H interactions do not have this stabilisation effect. Efforts to produce the platinum complex of **10** were also unable to isolate a clean sample, which may reinforce a steric issue in pseudo-planar binding of this ligand.

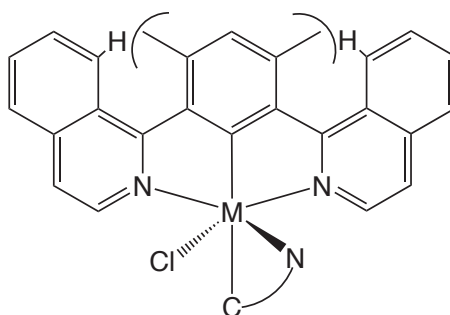


Fig. 2.5 Representation of unfavourable steric interactions affecting binding of **10** to a metal centre.

Steric hindrance increases around the terdentate binding pocket on moving from the lateral isoquinolines in 3-diqMeb, **11** to successively more sterically congested systems through 2-dqFb, **13**, to the two ligands based on 8-quinolines: 8-dqMeb, **12** and 8-dqFb, **14**. Indeed, attempts to synthesise an iridium complex containing **12** or **14** proved futile, as was the case with the unsubstituted ligand. An insoluble red solid could be isolated from each of the reactions, suggesting formation of some dimeric species had taken place and attempts were made to cleave the dimers with ppyH but pure product was not isolable in each case. In contrast, syntheses of $[\text{Ir}(3\text{-diqMeb})(\mu\text{-Cl})\text{Cl}]_2$, **22** and $[\text{Ir}(2\text{-dqFb})(\mu\text{-Cl})\text{Cl}]_2$, **23** were successful, as verified by the preparation thereafter of the ppy complexes (Fig. 2.6).

A solventless method was employed for the cleavage of the dimers with 2-ppyH (second step of Scheme 2.12) as this permits a more facile extraction of the product. The crude dimer was heated at 110 °C with silver triflate (to act as a chloride scavenger) in 2-ppyH for 16 h in an inert atmosphere (example shown for $\text{Ir}(1\text{-diqb})(\text{ppy})\text{Cl}$, **25** in Scheme 2.14). Synthesis of the ppy adducts led to formation of a small amount of the triply cyclometallated complex iridium tris(2-phenylpyridine), $\text{Ir}(\text{ppy})_3$, which could be removed easily by column chromatography on silica, using CH_2Cl_2 /methanol as the eluant. When using bpy or 2-(4,6-difluorophenyl)pyridine, dFppyH, **21** (prepared by the literature method¹⁹³) as the bidentate ligand, the reaction was performed in ethylene glycol and heated at 298 °C for 2 h.

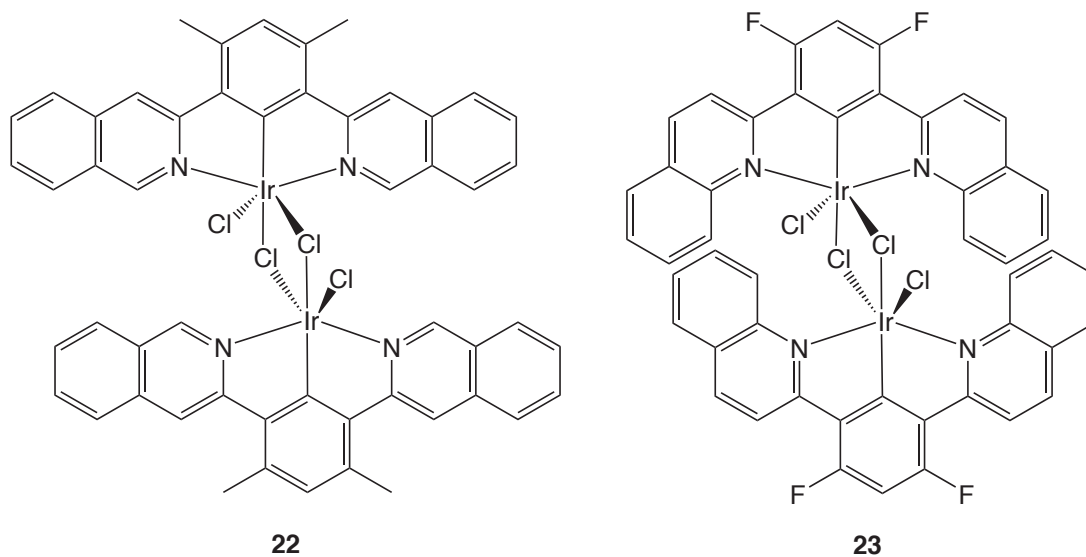
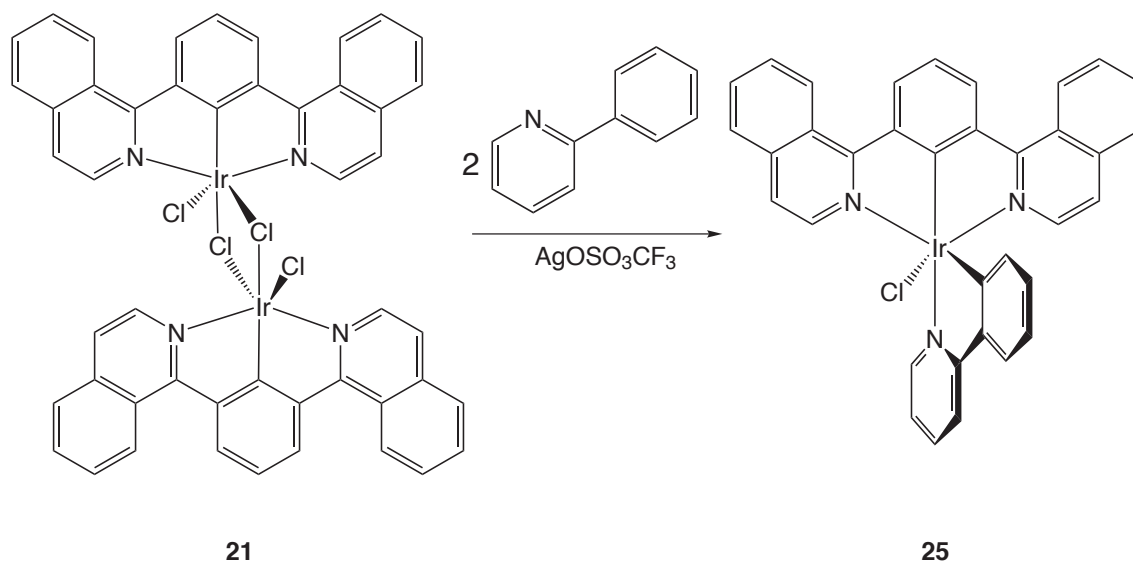


Fig. 2.6 Chloro-bridged dimers from disubstituted ligands: $[\text{Ir}(3\text{-diqMeb})(\mu\text{-Cl})\text{Cl}]_2$, **22** and $[\text{Ir}(2\text{-dqFb})(\mu\text{-Cl})\text{Cl}]_2$, **23**.



Scheme 2.14 Example of cleavage of the iridium dimer **21** *via* a solventless reaction with a chloride scavenger to synthesise $\text{Ir}(1\text{-diqb})(\text{ppy})\text{Cl}$, **25**.

Characterisation of iridium complexes was carried out by NMR spectroscopy and electrospray (ES) or ASAP mass spectrometry. ^1H NMR spectra for cyclometallated complexes show characteristic high-field aromatic peaks for the protons adjacent to the site of cyclometallation, and for this series of complexes, low-field doublets for the protons adjacent to the binding nitrogen sites are also observed (Fig. 2.7). In all metal complexes prepared in this study, a downfield shift of proton resonances was observed on binding of the ligand to the metal. This was accompanied by loss of the $\text{H}^{2'}$ resonance at the site of cyclometallation for the cyclometallated complexes.

The shift to lower field that occurs is in line with decreased electron density in the aromatic rings with M–C or M–N bond formation upon binding. A similar trend has been reported for cyclometallated complexes of 1,3-di(2-pyridyl)benzenes, although upfield shifts are also seen for certain protons in these cases.^{106,108,109,178}

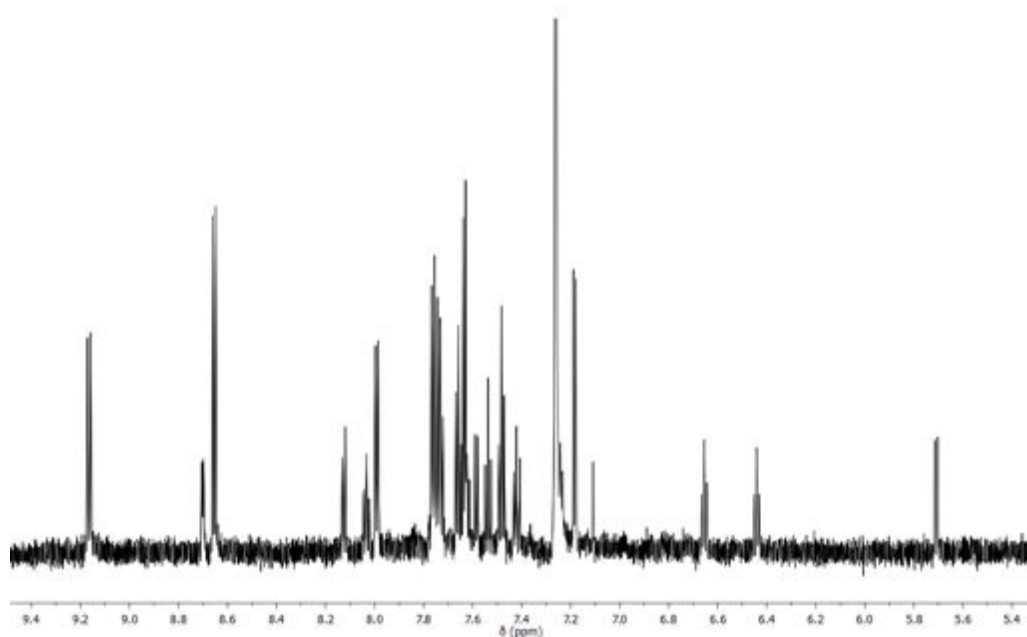
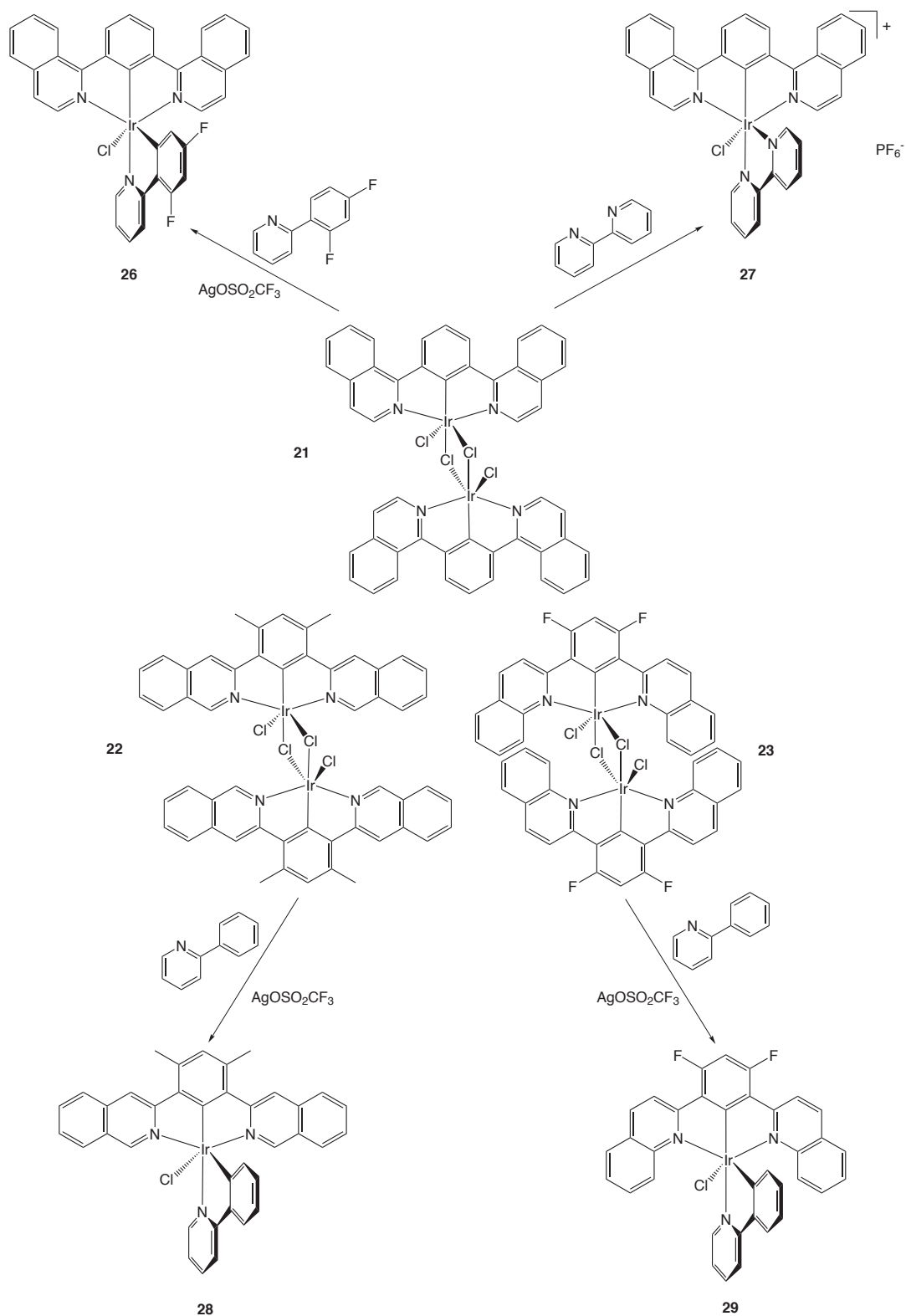


Fig. 2.7 Expansion of the aromatic region of the NMR spectrum of Ir(1-diqb)(ppy)Cl, **25** in CDCl_3 at 700 MHz showing high-field peaks.

For mass spectrometry the ES^+ technique frequently returned a mass/charge (m/z) peak for the complex without the chloride ligand, which is labile under this technique. However, use of the QToF-ASAP (quadrupole time-of-flight-ASAP) technique ensured that there was minimal solvent contact (solely through the injection process) and spectra showing the molecular ion peak inclusive of chloride were obtained. Unfortunately, accurate elemental analyses proved difficult to obtain for the majority of complexes reported herein, as has been discovered for similar platinum group complexes,¹⁹⁴ which has been suggested to be due to the propensity for these complexes to retain solvent molecules. This effect has been observed in vapochromic studies of platinum complexes,^{195,196} in mass spectrometry data as m/z peaks including solvent, and also in the crystal structures of the complexes presented here (*vide infra*).

Ir(1-diqb)(ppy)Cl, **25** was produced as a red solid as in Scheme 2.14, following on from which, two further complexes were prepared from the 1-diqb-based dimer, **21**, by incorporation of alternative bidentate ligands dFppy, **24** and bpy. **21** was

combined with the desired ligand and silver triflate in ethylene glycol and after degassing, the reaction was heated under nitrogen at 196 °C for 2 h. A work-up identical to that of the ppy complex, afforded Ir(1-diqb)(dFppy)Cl, **26** as a red solid. For the cationic compound, [Ir(1-diqb)(bpy)]Cl, an ion-exchange was performed by drop-wise addition to a saturated solution of aqueous KPF₆ to yield [Ir(1-diqb)(bpy)]PF₆, **27** as an orange solid (Scheme 2.15).

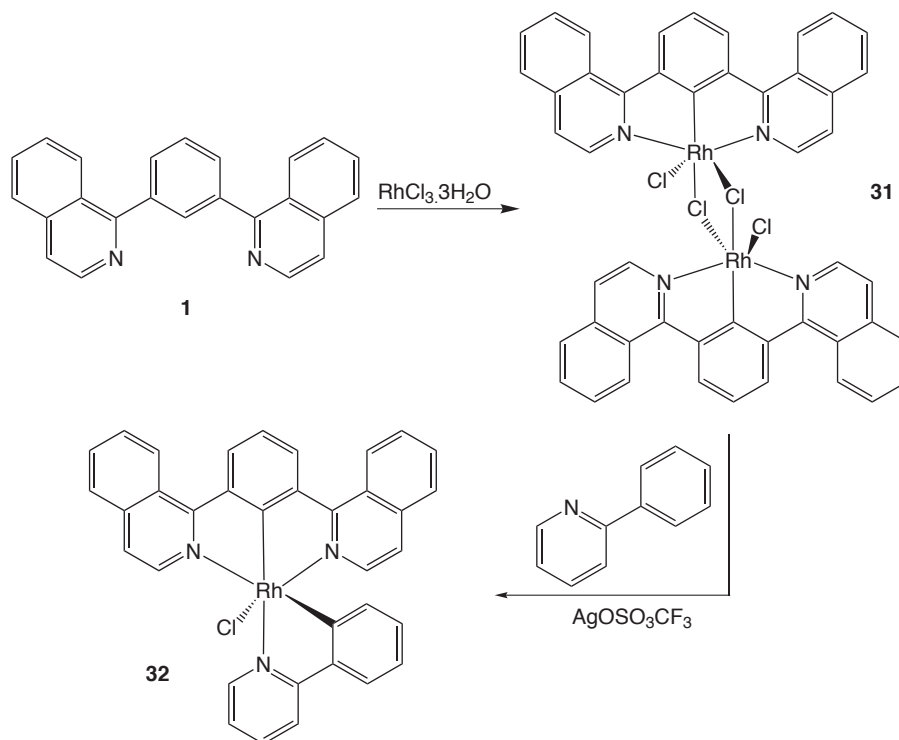


Scheme 2.15 $\text{Ir}(\text{1-diqb})(\text{dFppy})\text{Cl}$, **26**, $[\text{Ir}(\text{1-diqb})(\text{bpy})\text{Cl}]\text{PF}_6$, **27**, $\text{Ir}(\text{3-diqMeb})(\text{ppy})\text{Cl}$, **28** and $\text{Ir}(\text{2-dqFb})(\text{ppy})\text{Cl}$, **29**.

As shown in (Scheme 2.15), the dimers of the disubstituted ligands $[\text{Ir}(3\text{-diqMeb})(\mu\text{-Cl})\text{Cl}]_2$, **22** and $[\text{Ir}(2\text{-dqFb})(\mu\text{-Cl})\text{Cl}]_2$, **23** could be cleaved with 2-ppyH utilising a solvent-free method, as before, to yield a yellow complex, $\text{Ir}(3\text{-diqMeb})(\text{ppy})\text{Cl}$, **28** and a bright orange complex, $\text{Ir}(2\text{-dqFb})(\text{ppy})\text{Cl}$, **29**, respectively.

2.2.2 Cyclometallated N^C^N rhodium(III) complexes

Two chloro-bridged dimer syntheses were attempted with rhodium(III) chloride: those of ligands **1** and **2**. As found for iridium, the dimer based upon 1-diqb, **1** was formed successfully to give $[\text{Rh}(1\text{-diqb})(\mu\text{-Cl})\text{Cl}]_2$, **31**, whilst that based upon **2** was not. Employing the same method as for iridium dimers, heating in 2-ethoxyethanol and water (7:3, v/v) produced **31** from **1** as an insoluble solid that was washed with water, ethanol and diethyl ether and used in its crude state for complexation. Corroboration of dimeric binding was provided in the successful synthesis thereafter of $\text{Rh}(1\text{-diqb})(\text{ppy})\text{Cl}$, **32** as a yellow solid that was purified by column chromatography on silica as for the Ir(III) species. Confirmation of the identity of the complex was provided by NMR spectroscopy with low-field and high-field signals indicating cyclometallation had occurred, together with observation of the desired m/z peak from mass spectrometry.

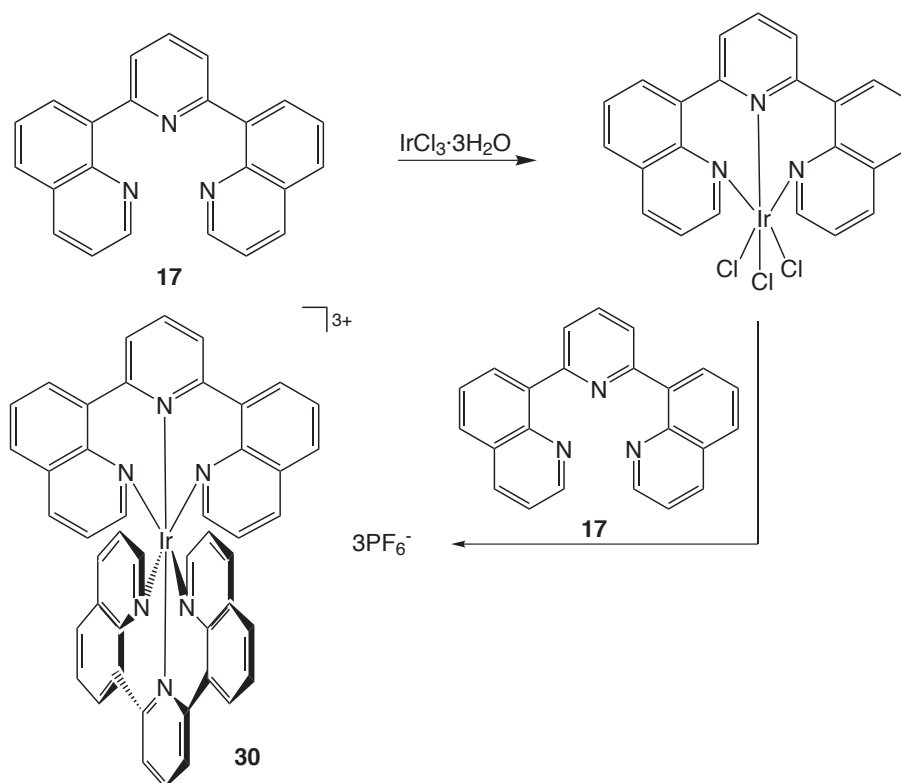


Scheme 2.16 Synthesis of a rhodium chloro-bridged dimer, **31** and complex $\text{Rh}(1\text{-diqb})(\text{ppy})\text{Cl}$ **32**.

2.2.3 Synthesis of an N^N^N iridium(III) complex

The synthesis of iridium complexes containing terdentate all-nitrogen donor ligands has been well documented as being challenging and difficult^{26,40,41,197} due to the kinetic inertness of the Ir(III) ion coordination sphere and the harsh reactions required to overcome this.

To attach two N^N^N ligands to an iridium centre, a two-step procedure was necessary (Scheme 2.17). Firstly, dqp, **17** was suspended in degassed ethylene glycol and heated under an inert atmosphere at 160 °C for 30 minutes, forming an iridium(N^N^N)trichloride intermediate.⁴¹ The second stage involved the addition of another equivalent of the ligand in degassed ethylene glycol, as before, but with heating for 2 h at 196 °C to drive the reaction to completion. Purification was carried out *via* extensive column chromatography and an ion-exchange with a saturated solution of aqueous KPF₆. The yellow precipitate was collected and washed in the standard way (water/ethanol/diethyl ether) and on characterisation by NMR spectroscopy and mass spectrometry it was concluded that the target molecule had been synthesised successfully.



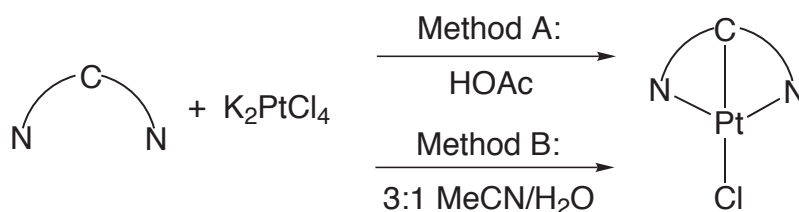
Scheme 2.17 Synthesis of $[\text{Ir}(\text{dqp})_2][\text{PF}_6]_3$.

2.3 Synthesis of d⁸ platinum(II) complexes

2.3.1 Terdentate cyclometallated platinum(II) N[^]C[^]N complexes

Two main reaction methods (Scheme 2.18) were employed to synthesise cyclometallated Pt(II) complexes, both involving stringent degassing and reflux under nitrogen at relatively high temperatures for 2–4 days. The final work-up varied according to the solubility of the precipitate obtained. Method A proceeded in glacial acetic acid, a procedure first published by Cárdenas *et al.* in 1999,¹⁰⁵ consisting of combining the ligand and K₂PtCl₄ in a small amount of the acid (2–4 mL) and degassing *via* four freeze-pump-thaw cycles. The reaction was then heated under nitrogen at reflux, typically for 3 d. After cooling and collection by centrifuge, the precipitate was washed successively with methanol, water, ethanol and diethyl ether. Characterisation was performed using the same techniques as for the octahedral complexes; ¹H NMR spectra showed a downfield shift upon complexation, with the added aid of the appearance of ¹⁹⁵Pt satellites for the highest frequency proton signal (H²) when run at low frequencies (see Section 2.6 for further discussion of satellites in NMR spectra).

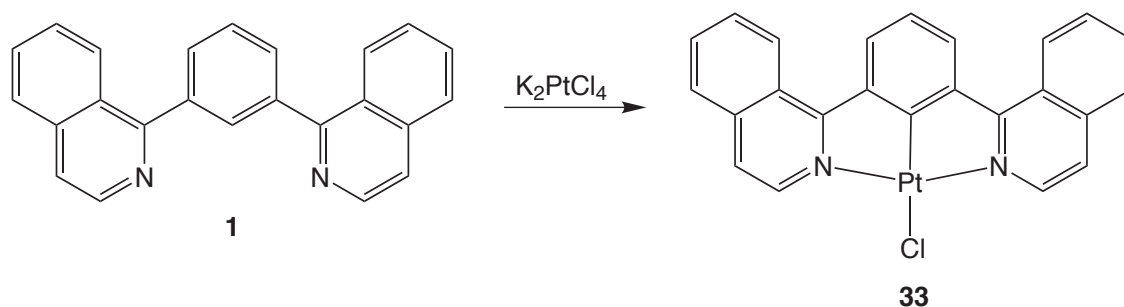
Method B was a procedure used for similar reactions by Williams *et al.*¹⁰⁶ based upon previous work by Constable *et al.*⁹⁶ The methodology consisted of preparing separate solutions of the ligand in MeCN and K₂PtCl₄ in water in a 3:1 (v/v) ratio and degassing each *via* three freeze-pump-thaw cycles before transferring the aqueous solution into the organic solution under positive pressure of nitrogen. The reaction was heated at reflux under nitrogen for 3 d and work-up performed as for method A.



Scheme 2.18 Two routes to cyclometallated platinum complexes.

Preparation of the platinum complex of the unsubstituted ligand, 1-diqb, **1**, was previously effected by another member of our group using method A to produce Pt(1-diqb)Cl, **33** as an orange solid (Scheme 2.19), and this was repeated to enable further measurements to be performed. Successful complexation to platinum was confirmed by a downfield shifting of the proton peaks in the ¹H NMR spectrum,

together with loss of the $H^{2'}$ signal from the cyclometallating carbon. Further validation of complexation was provided in the mass spectrometry data obtained for all the platinum complexes. As seen for the octahedral complexes, the *trans*-effect of the cyclometallating carbon in $N^{\wedge}C^{\wedge}N$ ligands can cause ligand substitution of the chloride with solvent molecules so solid ASAP-MS analysis was used to ensure retention of the chloride at the fourth coordination site.

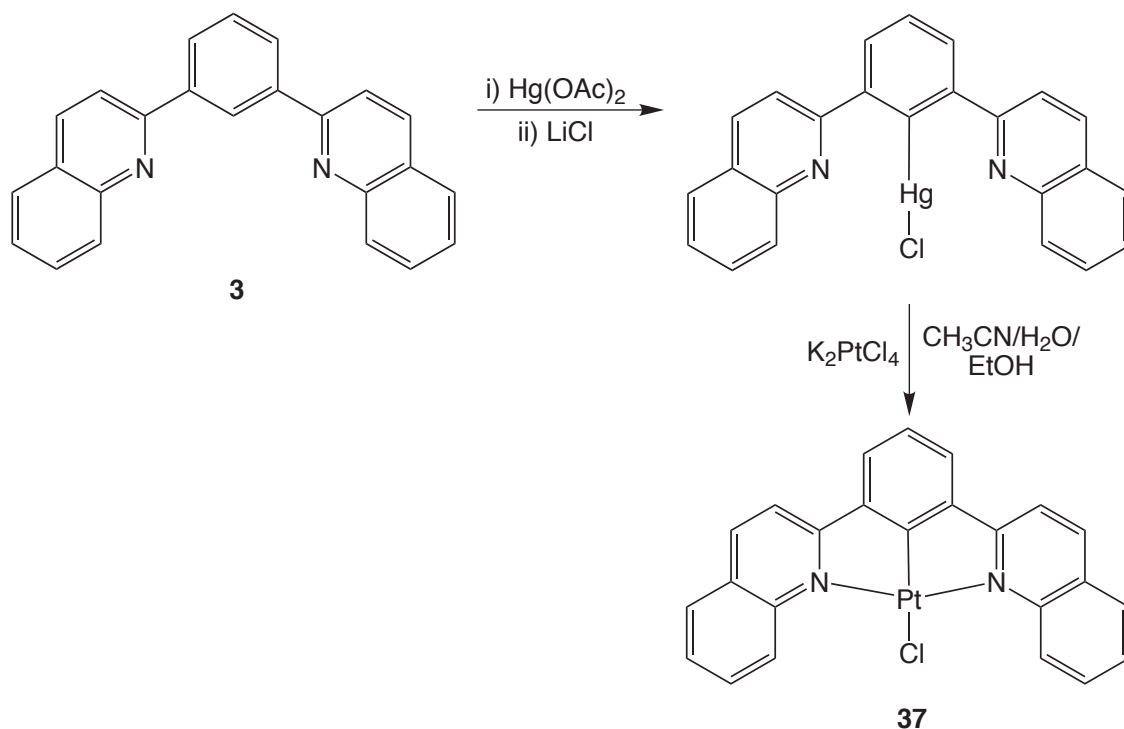


Scheme 2.19 Synthesis of Pt(1-diqb)Cl.

The platinum complex of 2-dqb, **3**, was prepared previously in the group, although neither method A or B was successful in obtaining the complex. Instead a route *via* mercuration was required,¹⁹⁸ where a transmetallation step was necessary to effect the transformation from the mercury(II) complex to the dark yellow platinum(II) species Pt(2-dqb)Cl, **36** (Scheme 2.20). The transmetallation step was carried out using method B, with added absolute ethanol to solubilise the mercury compound.

For the difluorinated ligand 2-dqFb, **13**, it was envisaged that the presence of blocking groups in the 4- and 6-positions of the central phenyl ring might enable complexation to be carried out *via* method A. A sparingly soluble yellow solid that glowed very bright orange under long-wave UV light was obtained using this method, and NMR spectroscopy and (ASAP⁺) mass spectrometry were suggestive of the presence of the desired complex Pt(2-dqFb)Cl, **37**. However, the NMR spectrum showed additional peaks, which remained after further washings, and recrystallisation was hindered by insolubility.

Synthesis of the platinum(II) complex of the unsubstituted 3-isoquinolyl ligand, 3-diqb, **4** was effected *via* method A to yield Pt(3-diqb)Cl, **34** as a yellow solid (Fig. 2.8). Additionally, synthesis of the platinum complex Pt(3-diqMeb)Cl, **35** containing the dimethyl substituted ligand **11** was attempted using the same method. **35** proved to be less soluble, and therefore difficult to characterise. A yellow solid that glowed bright orange under long-wave UV light was isolable and MS showed the desired molecular ion peak, yet upon the basis of NMR spectroscopy



Scheme 2.20 Synthesis of $\text{Pt}(2\text{-dqb})\text{Cl}$ *via* mercuration.

it was presumed that a mixture of emissive platinum species were produced.

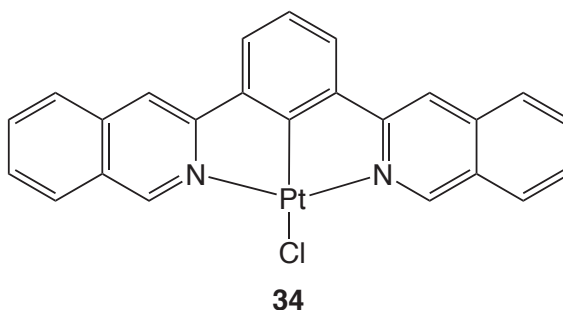


Fig. 2.8 Structure of $\text{Pt}(3\text{-diqb})\text{Cl}$.

The last group of cyclometallated platinum complexes explored were those based upon the 8-quinolyl unit (Fig. 2.9). The di(8-quinolyl) parent ligand extends around the metal centre in a chelating mode with an increased bite angle compared to tpy-based ligands. Complexation of the parent unsubstituted ligand was carried out *via* method B in an MeCN/water solvent mixture, and repeated to yield a grey-green solid that was sparingly soluble in CH_2Cl_2 and so was dried *in vacuo* after washing. Characterisation showed that the target complex, $\text{Pt}(8\text{-dqb})\text{Cl}$, **38** had been formed confirming that a square planar arrangement with six-membered chelate rings is tenable for this system. NMR spectroscopy showed a shift to higher frequency for most of the quinoline resonances upon complexation, in particular H^2 ($\Delta\delta$ 0.8 ppm

in CDCl₃), which also displays well-resolved platinum satellites ($^3J = 44$ Hz) in low resolution ^1H NMR spectroscopy.

In order to synthesise the dimethyl-substituted complex from 8-dqMeb, **12**, method A could be used, as the ligand was soluble in glacial acetic acid. Platinum 1,3-dimethyl-4,6-di(8-quinolyl)benzene chloride, **39**, was obtained as a yellow solid in moderate yield (43 %). Attempts to obtain the difluorinated species using 8-dqFb, **14** were unsuccessful; whilst an off-white solid was obtained in high yield, its identity could not be fully confirmed. Mass spectrometry showed a molecular ion peak but through NMR spectroscopy, an unambiguous assignment of a pure compound was not possible and low solubility hindered further attempts at purification.

To complete the series of 8-quinolyl based platinum complexes, the asymmetric ligand qpyb, **16** was complexed using method B. The product, Pt(qpyb)Cl, **40**, which contains one six-membered and one five-membered ring, was afforded as a pale yellow solid in 40 % yield.

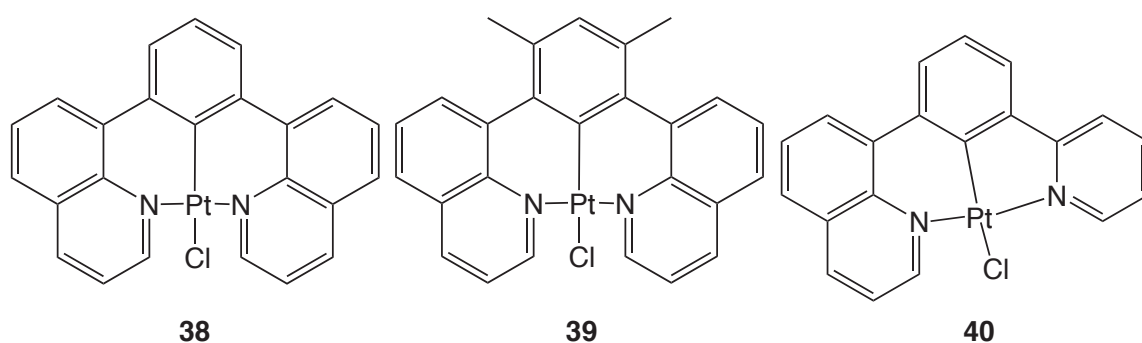


Fig. 2.9 Structures of cyclometallated 8-quinolyl-based complexes Pt(8-dqb)Cl, Pt(8-dqMeb)Cl and Pt(qpyb)Cl

2.3.2 Terdentate platinum(II) N[^]N[^]N-coordinated complexes

Complexation of the terdentate N[^]N[^]N-coordinating ligand using K₂PtCl₄ proceeded in low yield and a different approach was sought. By using an alternative platinum source, Cl₂Pt(DMSO)₂, which has good solubility in alcohols and eliminates the need for water as a co-solvent, the reaction could be performed in methanol to increase solubility of the ligand. The platinum precursor¹⁹⁹ is facile to make by stirring K₂PtCl₄ with DMSO in water at room temperature under nitrogen overnight. Complexation to dqp, **17** was then readily achieved upon treatment of the ligand with Cl₂Pt(DMSO)₂ in refluxing methanol for 3 d, after degassing *via* the freeze-pump-thaw method. A lower temperature than for the cyclometallated complexes is sufficient for synthesis using methanol instead of an acetic acid/water

mix as no C-H activation is required. The chloride salt of the N[^]N[^]N complex [Pt(dqp)Cl]Cl, **41** was first isolated by centrifuge, then an ion-exchange performed by dissolution in minimal DMSO and addition to a saturated solution of aqueous KPF₆ to convert to the more soluble hexafluorophosphate salt, [Pt(dqp)Cl]PF₆, **42**.

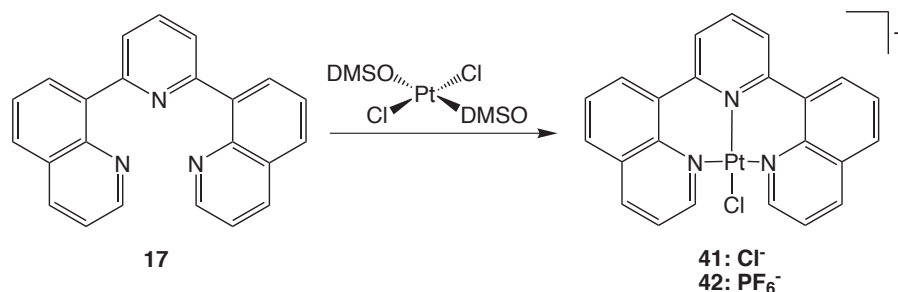


Fig. 2.10 Synthesis of [Pt(dqp)Cl]⁺ using Cl₂Pt(DMSO)₂ as a platinum source.

Despite repeated attempts to crystallise this complex using a variety of solvent systems, counter-anions and crystallisation techniques, it has not hitherto proved possible to obtain crystals of sufficient quality for an X-ray diffraction study. As noted earlier, the use of DFT calculations to optimise structural geometry has proved very successful³⁴ in predicting solid state geometries and so this technique was used to study this complex (*vide infra*).

The complexation of dqp, **17** to platinum results in shifts to higher frequencies of all the ¹H NMR signals as typically observed for C-H aromatic protons when ligands form cationic complexes with square planar geometry. As seen for the complexation of terpyridine to platinum(II) the protons *para* to the coordinating nitrogen atoms experience a significant deshielding effect ($\Delta\delta$ ca. 0.5 ppm in *d*₆-DMSO). However, the position which experiences the largest perturbation is H⁷ of the quinoline, *ortho* to the interannular bond ($\Delta\delta$ ca. 0.68 ppm in *d*₆-DMSO).

2.3.3 Tetradentate-coordinated platinum(II) complexes

Following the logic that terdentate ligands produce more rigid frameworks than bidentate ligands, the next step is to move on to tetradentate ligands, which, for a square planar platinum complex, enables full encapsulation of the metal in the centre of the molecule. Complexation of the two tetradentate ligands prepared was attempted by the same methodology as for the terdentate complexes. The tetradentate cyclometallated complex utilising bqbph, **18** was carried out *via* Method A to yield an insoluble yellow precipitate. Characterisation was very difficult due to insolubility, so definitive proof of a pure sample of Pt(bqbph), **43** could not be obtained. Confirmation of platinum binding was obtained using the MS(ASAP⁺) technique,

which showed the desired molecular mass peak for the platinated species (Fig. 2.11) but elemental analysis did not produce the desired results. From the complexation of bqbpy, **20**, a grey-yellow solid was ion-exchanged with a saturated solution of aqueous KPF_6 but, as with the neutral compound, the solid collected was very insoluble in common solvents and a suitable NMR spectrum was not obtained. Mass spectrometry showed only the peak for the unbound ligand with no molecular mass peak for the complex visible.

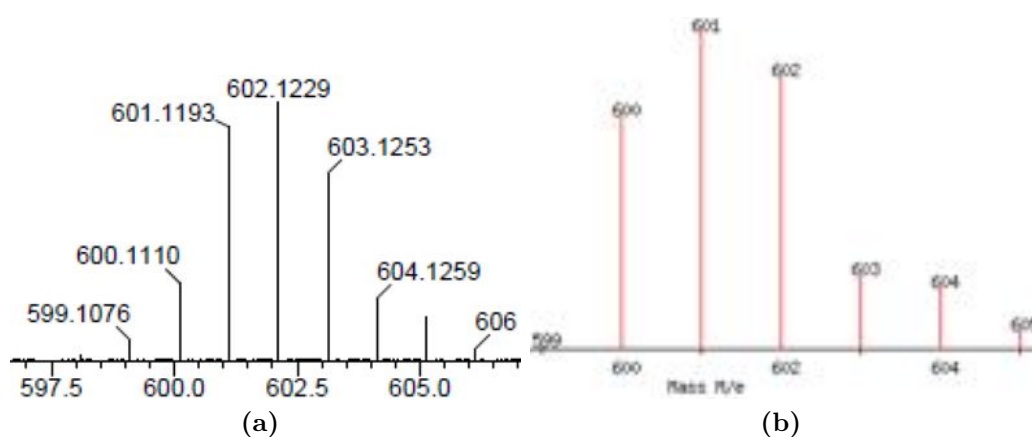


Fig. 2.11 Comprison of (a) experimental $[\text{M} + \text{H}]^+$ and (b) simulated mass spectra of $\text{Pt}(\text{bqbph})$, **43** (QtoF-ASAP⁺)

2.4 Metathesis reactions with alkynes

Once complexes have been formed, further chemistry can be performed on the complex itself with the aim of modulating the phosphorescent properties of the complex. Typically, chloride is the ancillary ligand seen in the majority of platinum group coordination complexes due to the availability of chloride metal salts as starting materials. As a weak-field ligand, chloride takes virtually no part in promoting luminescent emission, but it does, nonetheless, offer scope for chemical transformation, being a relatively labile donor. This is particularly true in the case of cyclometallated complexes where the metal-chloride bond is labilised by the presence of the strongly donating cyclometallating carbon centre, notably when *trans* to the metal-chloride bond. Loss of chloride is frequently observed in the electrospray mass spectra or high performance liquid chromatography (HPLC) chromatograms of such complexes. This feature enables facile displacement of the chloride ligand by another donor, requiring relatively mild reaction conditions, *i.e.* the reaction proceeds at ambient temperature.

A common method of improving the luminescent efficiency of heavy metal complexes, especially in square planar platinum(II) complexes, is incorporation of a strong donor ligand in the fourth coordination site. Successful strategies include replacement of the weak-field halide with a strong-field ligand, frequently one containing a formally anionic carbon donor. The standard literature procedure for metathesis reactions with alkynes is a variation on Sonogashira cross-coupling,²⁰⁰ which involves the coupling of an alkyne reagent with an aryl halide (predominantly an aryl iodide). The organic Sonogashira reaction is catalysed by palladium and copper(I) iodide, CuI, in the presence of an arylamine, typically either diethylamine or triethylamine, and metathesis proceeds *via* the same route.

The acetylide products Ir(1-diqb)(ppy)CC-tfp, **44** and Rh(1-diqb)(ppy)CC-tfp, **45** of the unsubstituted iridium and rhodium complexes, Ir(1-diqb)(ppy)Cl, **25** and Rh(1-diqb)(ppy)Cl, **32** were synthesised under nitrogen in methanol, utilising a catalytic amount of CuI in the presence of triethylamine. Ethynyl-3,5-bis(trifluoromethyl)benzene, was first stirred for 1 h with sodium hydroxide before addition of the degassed complex, triethylamine and CuI, and the reaction proceeded at room temperature to yield a precipitate in each case. Confirmation of the successful isolation of the desired acetylide complexes was provided by accurate mass spectrometry and the appearance of three protons in the ¹H NMR spectrum, although the chemical shifts of the terdentate and ppy protons are very close to those of the starting chloro complexes, ($\Delta\delta = ca. + 0.05$ ppm).

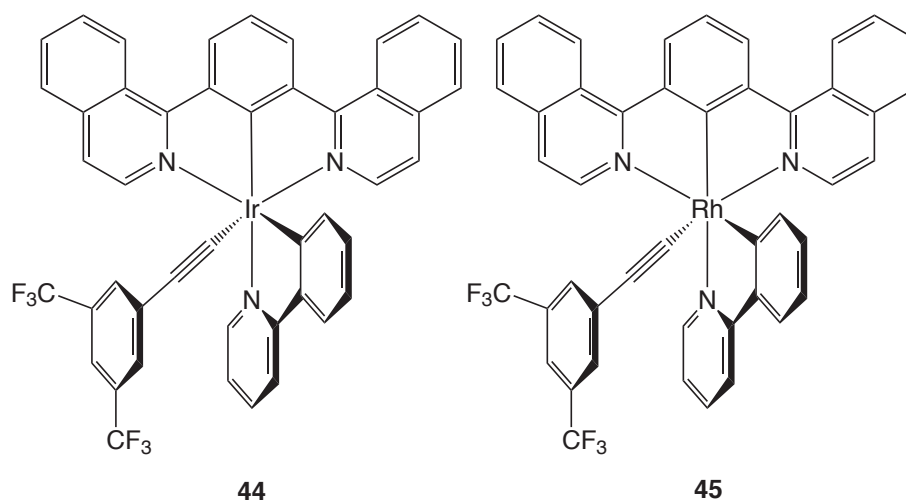


Fig. 2.12 Ir(1-diqb)(ppy)(CC-tfp), **44** and Rh(1-diqb)(ppy)(CC-tfp), **45**.

The N[^]N[^]N-coordinated compound, [Pt(dqp)Cl]PF₆, **42** was treated with ethynyl-3,5-bis(trifluoromethyl)benzene in the same two-step manner as for the cyclometalated complexes. However, on first stirring at ambient temperature in the presence

of CuI and sodium hydroxide in methanol, an additional metathesis reaction was observed, in the appearance of a bright yellow precipitate. After an ion-exchange was performed with a saturated solution of aqueous KPF_6 to give a more soluble product, characterisation showed the product to be the methoxide adduct, $[\text{Pt}(\text{dqp})\text{OMe}]\text{PF}_6$, **46**.

Addition of the alkyne to a fresh sample of **42** under the same conditions produced the desired acetylide adduct. A large change in deshielding of the H^2 protons of the dqp ligand was observed on metathesis ($\Delta\delta = +0.5$ ppm) but no other significant shifts were noted, so this is likely a through-space effect, arising from the proximity of the $\text{C}-\text{H}^2$ bonds, which are parallel to the $\text{C}\equiv\text{C}$ triple bond of the acetylide.

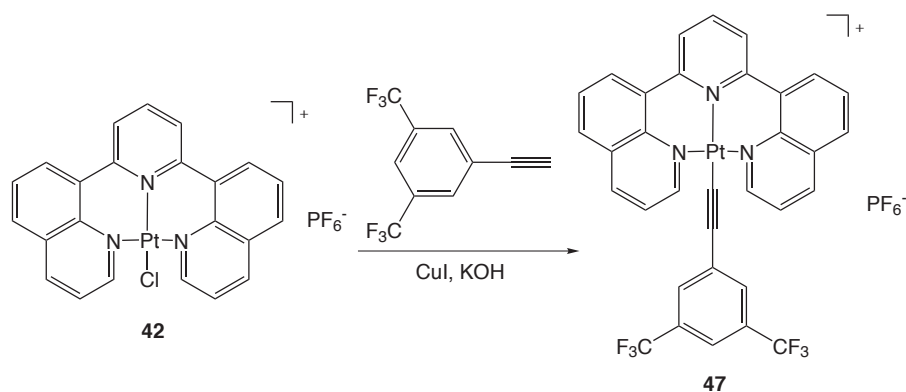


Fig. 2.13 Metathesis of $[\text{Pt}(\text{dqp})\text{Cl}]\text{PF}_6$, **42** with an acetylide.

2.5 Crystal structure elucidation by X-ray diffraction

Several precursors, ligands and complexes synthesised in this work were crystallised by slow evaporation of product solutions. Their structures could be elucidated by X-ray diffraction; refinement data are presented in Appendix A and full crystallographic data in the accompanying information.

2.5.1 Organic precursors and ligands

The precursors dMeBpin, **7** and qBrpy, **19** and ligands 1-diqb, **1**, 8-dqb, **2**, 2-dqFb, **13** and dqp, **17** were crystallised from a variety of solvents. Each shows the expected connectivity and physical data for the structures are presented in Table 2.2. Molecular structures for related $\text{N}^{\wedge}\text{C}^{\wedge}\text{N}$ -coordinating ligands have been obtained

previously by Williams *et al.*^{109,111,201}, and show similar non-planar structures to diminish steric repulsions. These studies found different geometrical arrangements for the pyridyl rings: either the nitrogen atoms were positioned towards the terdentate binding site or else a head-to-tail disposition of the nitrogen atoms was displayed. The crystal structures for the quinoline-containing ligands show a variety of geometries so there appears to be no definitive geometry that minimises steric repulsions for these tpy-based ligands.

Table 2.2 Crystal structure data for organic precursors and ligands

		Solvent	Colour	Interplane angle cen-lat ₁ /° ^a	Interplane angle cen-lat ₂ /°
1-diqb	1	MeCN	pale yellow	49.19	–
8-dqb	2	hex/Et ₂ O	colourless	53.84	117.21
dMeBpin	7	hex/Et ₂ O	colourless	17.00	–
2-dqFb	13	hex/Et ₂ O	colourless	38.93	–32.41 ^b
dqp	17	hex/EtOAc ^c	colourless	48.28	–
qBrpy	19	hex/EtOAc	pale yellow	39.44	–

^a lat₁ and lat₂ indicate that each of the quinolines lies at a different angle to the central ring ^b A difference in sign denotes that the plane of the quinoline is on the opposing side of the plane of the central ring

^c This ligand also crystallised readily from CDCl₃

1,3-di(1-isoquinolyl)benzene, 1-diqb, 1

The pale yellow crystals of 1-diqb (Fig. 2.14) shows a structure with isoquinolyl units related by a mirror plane that are offset from the plane of the benzene-derived ring by 49.19°. Selected bond lengths and angles are presented in Table 2.3.

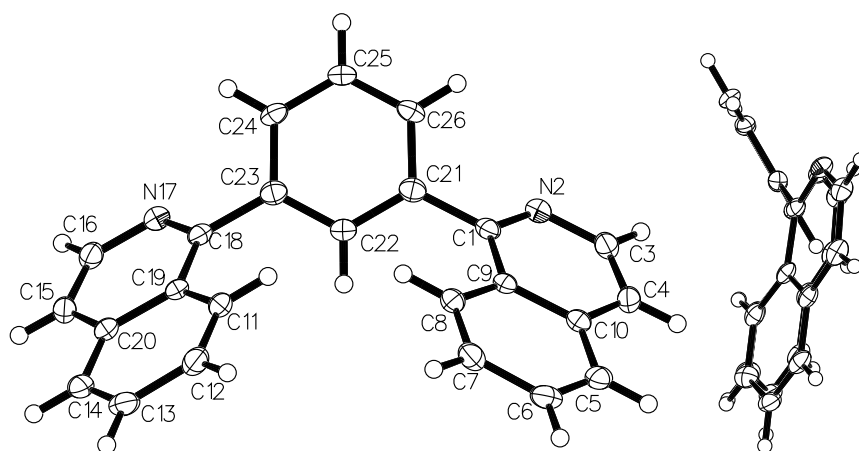


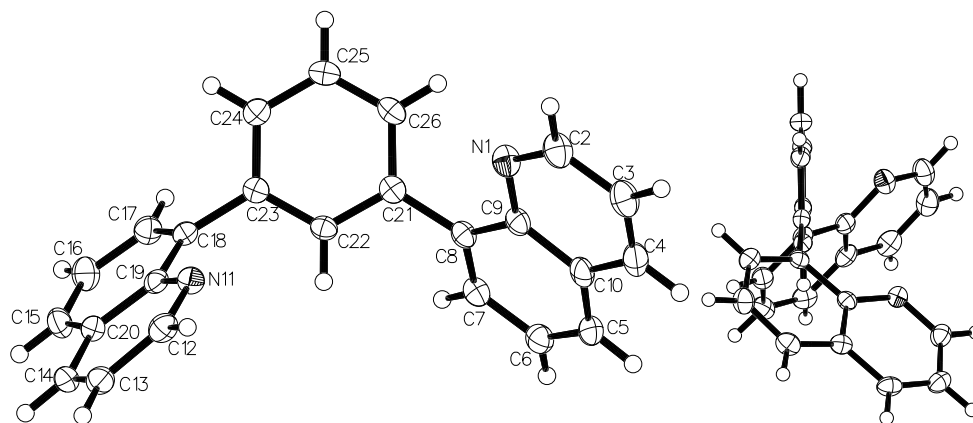
Fig. 2.14 Molecular structure of 1-diqb, **1**, with ellipsoids at the 50 % probability level.

Table 2.3 Selected bond lengths and bond angles of 1-diqb, **1**.

Bond Lengths/Å		Bond Angles/°	
N(2)–C(1)	1.327(4)	C(1)–N(2)–C(3)	118.4(3)
N(2)–C(3)	1.358(5)	C(21)–C(22)–C(23)	121.3(4)
C(21)–C(22)	1.397(4)	C(1)–C(21)–C(22)	122.1(3)
C(1)–C(21)	1.487(5)	N(2)–C(1)–C(21)	115.4(3)

1,3-di(8-quinolyl)-benzene, 8-dqb, 2

The structure of the colourless crystals of 8-dqb (Fig. 2.15; Table 2.4) displays a clear difference from that of the crystal structure of **1**. Whereas the quinolyl groups of **1** are related by a mirror plane, no such symmetry is seen for **2**. The torsional angles between the isquinolyl rings and the central benzene ring are 53.84° and 117.21°.

**Fig. 2.15** Molecular structure of 8-dqb, **2**, with ellipsoids at the 50 % probability level.**Table 2.4** Selected bond lengths and angles of 8-dqb, **2**.

Bond Lengths/Å		Bond Angles/°	
N(1)–C(2)	1.318(2)	C(2)–N(1)–C(9)	117.7(2)
N(1)–C(9)	1.370(2)	C(9)–C(8)–C(21)	121.59(16)
C(8)–C(21)	1.491(2)	C(8)–C(21)–C(22)	118.50(16)
C(21)–C(26)	1.398(3)	C(21)–C(22)–C(23)	121.72(17)

1,3-di(pinacolatoboron)-4,6-dimethylbenzene, dMeBpin, 7

Two forms of colourless crystals were obtained for dMeBpin, one stable in air (structure and data shown in Fig. 2.16 and Table 2.5) and the other unstable, such that opening of the sample vial caused them to degrade over several hours. Unfortunately data cannot be presented for the second form as full data could not be collected and multiple attempts to obtain crystals of the unstable form again resulted only in the air-stable triclinic form.

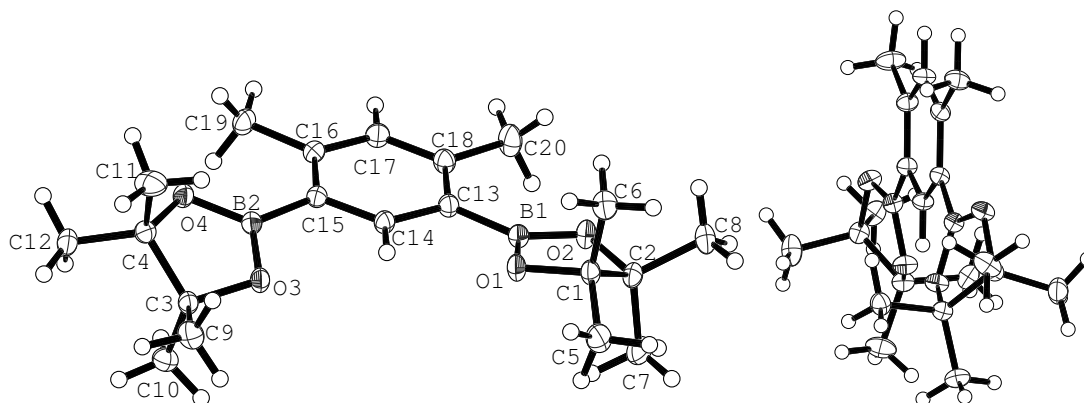


Fig. 2.16 Molecular structure of dMeBpin, **7**, with ellipsoids at the 50 % probability level.

Table 2.5 Selected bond lengths and angles of dMeBpin, **7**.

Bond Lengths/Å		Bond Angles/°	
B(1)–C(13)	1.5617(13)	C(15)–B(2)–O(3)	119.38(8)
B(2)–C(15)	1.5579(14)	C(13)–B(1)–O(1)	120.03(8)
B(1)–O(1)	1.3700(12)	B(2)–C(15)–C(16)	126.06(8)
B(2)–O(3)	1.3772(13)	B(1)–C(13)–C(18)	126.00(8)

1,3-di(2-quinolyl)-4,6-difluorobenzene, 2-dqFb, 13

2-dqFb crystallised very readily (Fig. 2.17; Table 2.6) and proved different in geometry to either of the other N[^]C[^]N-coordinating ligands. The two quinolyl units are oriented in opposing directions from the plane of the central ring, at 38.93° and 34.21°.

2,6-di(8-quinolyl)pyridine, dqp, 17

This ligand crystallised readily (Fig. 2.18; Table 2.7). The solid-state structure resembles that of **1** rather than that of **2** where the quinolines lie on the same side of the plane of the central pyridine ring, inclined at an angle of 48.28°.

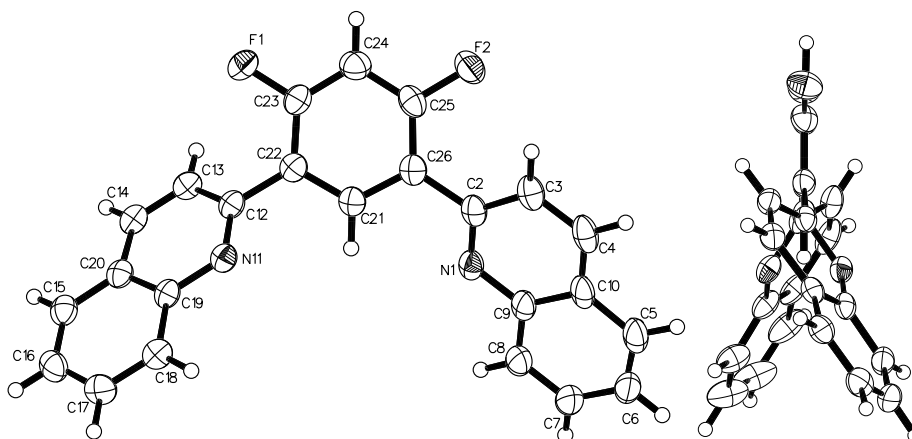


Fig. 2.17 Molecular structure of 2dqFb, **13**, with ellipsoids at the 50 % probability level.

Table 2.6 Selected bond lengths and angles of 2dqFb, **13**.

Bond Lengths/Å		Bond Angles/°	
N(1)–C(2)	1.324(2)	N(1)–C(2)–C(3)	122.64(18)
N(1)–C(9)	1.369(2)	C(2)–C(26)–C(21)	119.07(16)
C(2)–C(26)	1.434(3)	N(1)–C(2)–C(26)	115.01(16)
C(23)–F(1)	1.354(2)	N(1)–C(9)–C(8)	118.16(18)

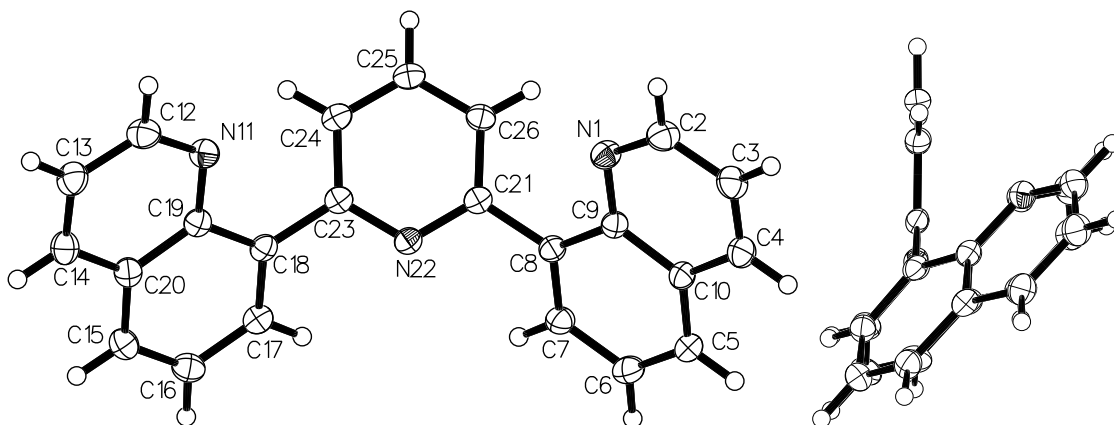


Fig. 2.18 Molecular structure of dqp, **17**, with ellipsoids at the 50 % probability level.

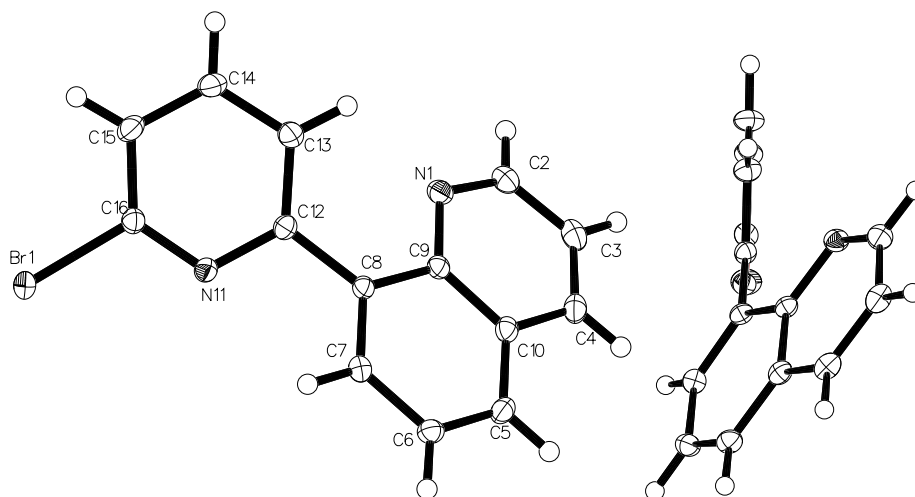
3-bromo(8-quinolyl)pyridine, qBrpy, 19

The ligand precursor qBrpy (Fig. 2.19; Table 2.8) confirmed the twist about the interannular bond typically seen for biaryls. The interplanar angle for **19** is 38.66°, which is comparable with that of the disubstituted ligands, whilst the bromine atom lies in the plane of the pyridine ring. As may be predicted, owing to its less hindered

Table 2.7 Selected bond lengths and angles of dqP, **17**.

Bond Lengths/Å		Bond Angles/°	
N(22)–C(21)	1.351(2)	C(8)–C(21)–N(22)	116.28(15)
N(22)–C(23)	1.348(2)	C(21)–N(22)–C(23)	118.60(15)
C(21)–C(8)	1.487(3)	N(1)–C(8)–C(9)	119.17(16)
N(1)–C(2)	1.319(3)	C(9)–C(8)–C(21)	121.54(16)
N(1)–C(9)	1.368(2)	C(18)–C(23)–N(22)	115.79(16)

structure this precursor has the lowest twist angle of any of the molecular structures, being closest to that of 2-dqFb, **13**, (39.44°).

**Fig. 2.19** Molecular structure of qBrpy, **19** with ellipsoids at the 50 % probability level.**Table 2.8** Selected bond lengths and angles of qBrpy, **19**.

Bond Lengths/Å		Bond Angles/°	
C(16)–Br(1)	1.911(14)	Br(1)–C(14)–N(2)	115.35(10)
N(11)–C(16)	1.314(17)	C(12)–N(11)–C(16)	117.61(12)
N(11)–C(12)	1.354(18)	N(11)–C(12)–C(8)	114.20(12)
C(8)–C(12)	1.489(18)	N(1)–C(9)–C(8)	119.77(12)

2.5.2 Complexes

*Iridium (1,3-di(1-isoquinolyl)benzene- $N, C^{2'}$, N)(2-phenylpyridine- $N, C^{2'}$) chloride, Ir(1-diqb)(ppy)Cl, **25***

Slow evaporation of a chloroform solution of **25** led to the formation of small needle-like crystals that were suitable for X-ray diffraction (Fig. 2.20, Table 2.9). The complex crystallised with 1.5 molecules in the unit cell with 2.5 solvent molecules also present; no $\pi - \pi$ interactions exist between molecules. The structure shows an approximately octahedral geometry about iridium with the anticipated arrangement of the terdentate and bidentate ligands approximately orthogonal to one another (interplane angle between the planes of the bidentate ligand and the central phenyl ring of the terdentate ligand = 84.1°). The terdentate ligand remains largely planar on binding with a small amount of deviation for the two isoquinoline groups in opposite directions from the plane of the central ring. The other key feature shown in the solid-state structure is the *trans* disposition of the cyclometallating carbon atom and the nitrogen atom of the phenylpyridine ligand. This *trans* disposition is seen often for square planar and octahedral complexes containing ligands with carbon and nitrogen donor atoms,²⁰² owing to the strong *trans* influence of the cyclometallating carbon donor, which causes a lengthening of the opposing Ir–N bond. The Ir–N(ppy) bond length is 2.132(14) Å for this complex in comparison with the lateral C–N bonds of the terdentate ligand (2.070(12) Å and 2.045(9) Å), an effect that replicates that seen in the literature, for example in work by Thompson *et al.* and Scandola *et al.*, who noted a lengthening of bonds *trans* to phenyl groups in comparison to those opposing heterocyclic groups.^{51,56,58}

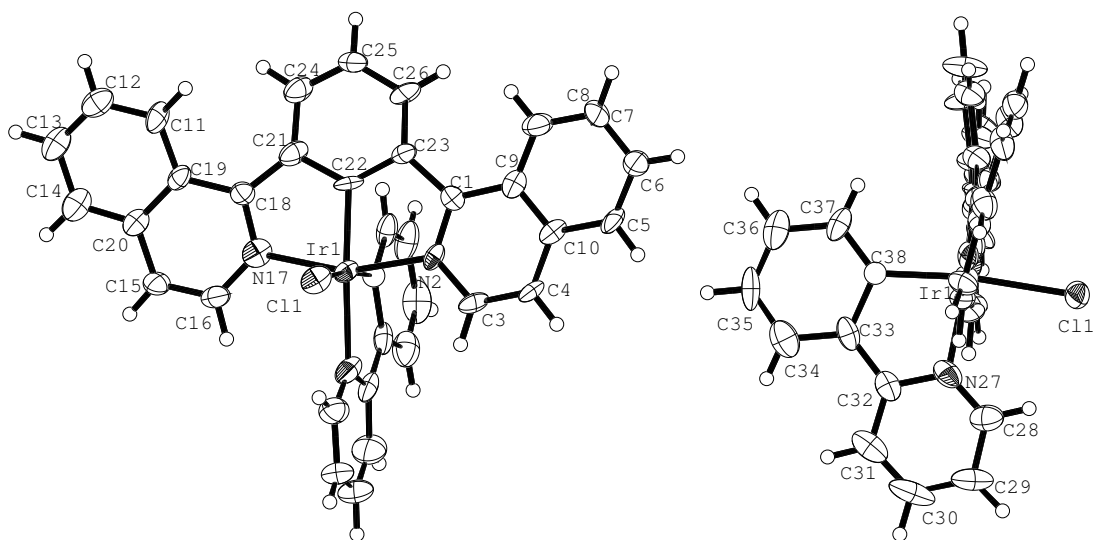


Fig. 2.20 Molecular structure of Ir(1-diqb)(ppy)Cl, **25**, with ellipsoids at the 50 % probability level; solvent molecules omitted for clarity.

Table 2.9 Selected bond lengths and bond angles of Ir(1-diqb)(ppy)Cl, **25**.

Bond Lengths/Å		Bond Angles/°	
Ir–C(22)	1.941(12)	C(22)–Ir–N(27)	173.1 (5)
Ir–N(2)	2.070(12)	N(2)–Ir–N(17)	159.7(4)
Ir–N(17)	2.045(9)	C(22)–Ir–N(2)	80.2(4)
Ir–C(38)	2.025(16)	C(22)–Ir–N(27)	79.5(5)
Ir–N(27)	2.132(14)	C(22)–Ir–Cl	95.0(4)
Ir–Cl(1)	2.462(5)	N(27)–Ir–Cl	91.9(3)
C(1)–C(21)	1.501(17)	C(38)–Ir–Cl	172.8(4)

*Rhodium (1,3-di(1-isoquinolyl)benzene- $N,C^{2'}$, N)(2-phenylpyridine- $N,C^{2'}$) chloride, Rh(1-diqb)(ppy)Cl, **32***

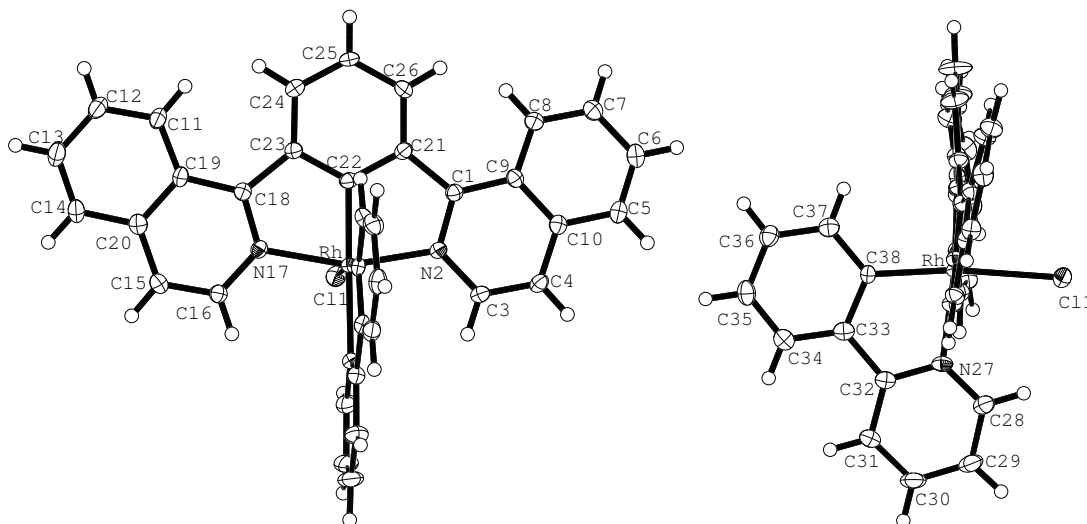


Fig. 2.21 Molecular structure of Rh(1-diqb)(ppy)Cl, **32**, with ellipsoids at the 50 % probability level; solvent molecules omitted for clarity.

Slow evaporation of a CH_2Cl_2 solution of **32** led to the formation of fine crystals that were suitable for an X-ray diffraction study, confirming the molecular structure of the species (Fig. 2.21, Table 2.10). The structure shows a close analogy with that of the iridium species, **25** with the same pseudo-octahedral geometry and near-orthogonal arrangement of the rings of the terdentate and bidentate ligands (interplane angle between the plane of the bidentate ligand and that of the central phenyl ring = 91.36°). A *trans* disposition of the cyclometallating carbon of the terdentate ligand and the nitrogen donor of the phenylpyridine ligand is seen, as for

25. The Rh-N(ppy) bond length is 2.180(3) Å, longer than the lateral bonds to the terdentate nitrogen atoms (2.049(3) Å and 2.051(3) Å) and slightly longer than that of the corresponding Ir-N(ppy) bond (2.132(14) Å).

Table 2.10 Selected bond lengths and bond angles of Rh(1-diqb)(ppy)Cl, **32**.

Bond Lengths/Å		Bond Angles/°	
Rh–C(22)	1.907(4)	C(22)–Ir–N(27)	174.15(16)
Rh–N(2)	2.049(3)	N(2)–Ir–N(17)	160.57(13)
Rh–N(17)	2.051(3)	C(22)–Ir–N(2)	80.02(15)
Rh–C(38)	1.995(4)	C(22)–Ir–N(27)	80.56(15)
Rh–N(27)	2.180(3)	C(22)–Ir–Cl	92.40(12)
Rh–Cl(1)	2.4791(10)	N(27)–Ir–Cl	93.44(10)
C(1)–C(21)	1.483(5)	C(38)–Ir–Cl	172.99(11)

Platinum (1,3-di(8-quinolyl)-4,6-dimethylbenzene) chloride, Pt(8-dqMeb)Cl, 39

Orange orthorhombic crystals of **39** were grown from slow evaporation of an ethanol sample (Fig. 2.22, Table 2.11). X-ray diffraction confirmed that the structure has very similar metal-ligand bond lengths to those of the unsubstituted dipyriddy complex Pt(dpyb)Cl.¹⁰⁵ The angles around the platinum centre total 360° indicating square planar geometry with the ligand distorted significantly from planarity to achieve this geometry. It is intuitive that the platinum centre is too large to bind to the ligand in a planar conformation, for which the bite angle would be inappropriate. By rotation of the lateral heterocyclic rings relative to that of the central cyclometallating ring, the d⁸ centre can achieve its preferred square planar coordination. Significantly, the angles about the metal centre are very close to 90°, and the C(22)–Pt–Cl angle is 180°, displaying linear coordination geometry. More importantly, the bite angle, N(1)–Pt–N(11), is 177.8°, amongst the most linear coordination geometries seen in platinum complexes, suggesting that the strategy of utilising six-membered chelates proved successful in relieving the ring strain associated with the more acute angles subtended by five-membered chelate-forming ligands such as tpy. A comparison of the structural data with computational results from DFT calculations will be presented in Chapter 4.

Crystal structures of transition metal complexes composed of terpyridyl-based ligands tend to show planarity of the tpy ligands but twisted geometries have been observed for those containing alternative terdentate heterocyclic ligands^{203,204}. A simi-

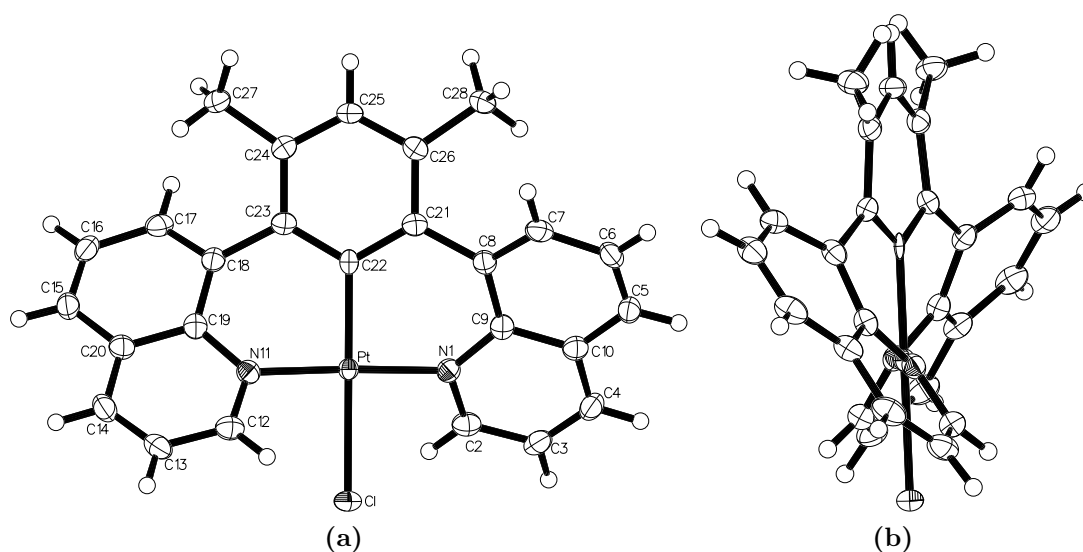


Fig. 2.22 Molecular structure of Pt(8-dqMeb)Cl, **39**, with ellipsoids at the 50 % probability level.

Table 2.11 Selected bond lengths and bond angles of Pt(8-dqMeb)Cl, **39**.

Bond Lengths/Å		Bond Angles/°	
Pt–C(22)	1.992(5)	C(22)–Pt–N(1)	91.11(8)
Pt–N(1)	2.035(3)	C(22)–Pt–N(11)	91.11(8)
Pt–N(11)	2.035(3)	Cl–Pt–N(1)	88.89(8)
Pt–Cl	2.451(1)	Cl–Pt–N(11)	88.89(8)
C(21)–C(22)	1.410(4)	C(8)–C(21)–C(22)	122.5(3)
C(8)–C(9)	1.418(5)	N(1)–C(8)–C(9)	120.9(3)
C(8)–C(21)	1.485 (5)	C(22)Pt–Cl	180.0
N(1)–C(9)	1.331(5)	N(1)–Pt–N(11)	177.79(16)

lar angle and twisting of the ligands was seen in the ruthenium complex $[\text{Ru}(\text{dqp})_2]^{2+}$ (see Chapter 1) synthesised by Hammarström *et al.*,³⁴ leading to a near-perfect octahedral environment around the ruthenium centre with a N–Ru–N angle of 179.6°. Near-perfect square planar geometries have been observed previously for platinum complexes containing chelating ligands that form six-membered chelate rings as opposed to five-membered chelate rings. Work by Huo *et al.* has very recently investigated the creation of six-membered chelating rings with platinum; bite angles approaching 180° were achieved in both terdentate²⁰⁵ (N–Ru–N of 173.18(6)° and 174.82(6)°) and tetradentate¹²⁴ (N–Ru–N of 171.75(1)° and 173.8(3)°) square planar platinum complexes.

2.6 NMR studies of $[\text{Pt}(\text{dqp})\text{Cl}]\text{PF}_6$

Whilst characterising $[\text{Pt}(\text{dqp})\text{Cl}]\text{PF}_6$, **42** an interesting phenomenon was noted in the ^1H NMR spectra at differing frequencies. Having initially obtained an NMR spectrum at 400 MHz the complex was run at 700 MHz to garner higher resolution data for characterisation and assignment purposes. As is expected, the peaks appear narrower at higher frequency relative to the chemical shift separation, with slightly less overlap, but the noticeable feature of the spectrum was the absence of platinum satellites usually observed for the H^2 signal of complexes in this study, which appear at ca. 9.4 ppm in this case. To explore the frequency dependence further, an NMR spectrum was also taken at 200 MHz under the same conditions (d_6 -acetone, 298 K). The satellites are clearly visible in the spectrum taken at 200 MHz, appearing more distinctly than in the spectrum taken at 400 MHz, completing the trend from high to low frequency. The three spectra are shown in Fig. 2.23, clearly showing the disappearance of the platinum satellites (which are widely displaced from the central peak at 200 MHz) on moving to higher frequency.

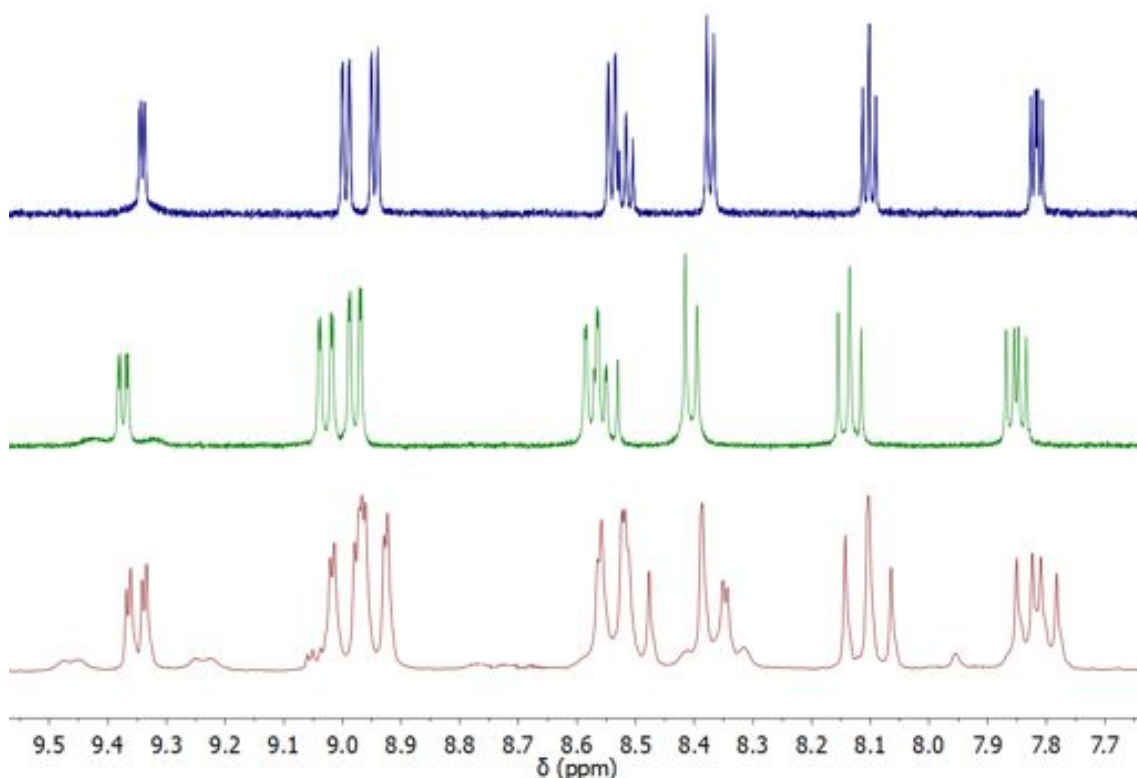


Fig. 2.23 ^1H NMR spectra of $[\text{Pt}(\text{dqp})\text{Cl}]\text{PF}_6$ in d_6 -acetone (298 K) at 700 MHz (top), 400 MHz and 200 MHz (bottom).

Platinum satellites arise due to the fact that 33.8 % of naturally occurring platinum nuclei are magnetically active ^{195}Pt nuclei, with spin, $I = \frac{1}{2}$. Other nuclei in

platinum-containing compounds will thus interact in different ways with the magnetically active and inactive platinum nuclei, giving rise to splitting patterns that are more complex than simple splitting due to one active type of nucleus. Owing to the spin-spin coupling present from interaction of the measured nuclei (^1H in the present case) with the active species (^{195}Pt), a weaker sub-spectrum is detected. Platinum satellites are each about a quarter of the intensity of the central proton peaks and so are easily detected.

2.6.1 Chemical shift anisotropy-induced relaxation

The disappearance of the ^{195}Pt satellites in high frequency solution NMR spectra is a relaxation effect related to the fact that the relaxation of the nuclei is heavily influenced by the chemical shift anisotropy (CSA) of the ^{195}Pt resonance and, in particular, by its frequency and field dependence, which is generally not the case for other forms of relaxation. On application of an external magnetic field to a sample, the spins interact with the field, giving rise to orientation dependent splittings, *i.e.* anisotropic interactions, which may be a cause of spin relaxation in molecules.²⁰⁶ The key feature to note here is that when this relaxation mechanism is active, only the magnetically active ^{195}Pt nuclei are affected by the CSA-dependent relaxation time, and therefore only satellites are broadened; the width of the main peak, corresponding to the inactive platinum nuclei, remains unchanged.

Two types of relaxation need to be considered: longitudinal relaxation and transverse relaxation. Longitudinal relaxation (also called spin-lattice relaxation), termed T_1 , is the time constant for the growth towards equilibrium of the z-component of nuclear spin, M_z , *i.e.* the component of magnetisation in the same direction as the applied magnetic field, B_0 . Transverse relaxation (also called spin-spin relaxation), termed T_2 , is the decay constant for the rate of decay towards zero of the transverse component of the magnetisation vector, M_{xy} , *i.e.* the component of magnetisation at 90° to the applied magnetic field, B_0 .

Anisotropic interactions are directionally dependent interactions that comprise CSA, dipolar coupling and anisotropic J -coupling. Chemical shift, δ , is a measure of electron screening and is often referred to as a screening constant, $\sigma = -\delta$. Screening constants are characterised by three directional components, σ_{xx} , σ_{yy} and σ_{zz} which are not usually equal so the screening constant is anisotropic,²⁰⁷ and is given by the following equation:

$$\Delta\sigma = \frac{2\sigma_{zz} - (\sigma_{xx} + \sigma_{yy})}{3} \quad (2.1)$$

In non-viscous, isotropic solution the fast molecular motions average out these components and the only observable components remaining are the isotropic parts of the J -coupling and the chemical shift:

$$\sigma_{\text{ISO}} = \frac{(\sigma_{xx} + \sigma_{yy} + \sigma_{zz})}{3} \quad (2.2)$$

Relaxation is produced by rapid fluctuation in the anisotropic interactions due to molecular reorientation. In most molecules in solution, in the absence of paramagnetic species, the dominant relaxation effect is due to fluctuation in dipolar coupling, since this is generally bigger than the CSA or anisotropy in J -coupling. However, the unusually large CSA of platinum²⁰⁸ dictates the T_1 relaxation of $[\text{Pt}(\text{dqp})\text{Cl}]\text{PF}_6$, even at 200 MHz, since it is considerably larger than the dipolar couplings present. Molecules in solution undergo fast thermal motions which contribute to nuclear relaxation times, with the time necessary for a molecule to rotate through one radian termed the correlation time, τ_c (also known as the ‘tumbling time’):²⁰⁷

$$\tau_c = \tau_0 \exp \frac{E_a}{RT} \quad (2.3)$$

where τ_0 is the correlation time constant and E_a is the activation energy for the molecular motions (reorientations, translations and rotations). For a large complex such as $[\text{Pt}(\text{dqp})\text{Cl}]\text{PF}_6$ a good approximation for τ_c is 200 ps (2×10^{-10} s). On application of this approximation to the equations concerning anisotropy, a trend appears that validates the NMR spectroscopic observations without the need for a rigorous mathematical treatment, therefore this approximation is sufficient to prove the theory.

Both T_1 and T_2 relaxation constants due to CSA for a site with axial symmetry are inversely proportional to the square of the magnetic field and the square of the anisotropy,²⁰⁹ with the longitudinal relaxation given by Equation 2.4:

$$\frac{1}{T_1}(\text{CSA}) = \frac{\gamma^2 B_0^2 \Delta\sigma^2}{30} \frac{\tau_c}{1 + \tau_c^2 \omega^2} \quad (2.4)$$

where $\Delta\sigma$ is the chemical shift anisotropy (CSA) of the ^{195}Pt nuclei, γ is the nuclear magnetogyric ratio, B_0 is the magnetic field strength, ω is the resonance frequency of the nucleus and τ_c is the correlation time, as above. The $\gamma B_0 \Delta\sigma$ term can be defined as AS , working on the assumption that the platinum complex is axially symmetric.

$$AS = \gamma B_0 \Delta\sigma \quad (2.5)$$

This relaxation mechanism is dependent on molecular motions that cause fluctuations in local magnetic fields and it is particularly effective for nuclei such as ^{195}Pt that have large CSA values.²⁰⁷ As a consequence of equation 2.4, such molecules undergoing fast molecular motion (*i.e.* $\omega^2\tau_c^2 \ll 1$), have CSA as the dominant relaxation mechanism, and therefore have field-dependent nuclear relaxation. This varies with $(B_0)^2$ (see Equation 2.4) and is borne out in this case by the frequency dependence of the platinum satellites. The Stokes-Einstein-Debye theory of the liquid state shows that the correlation time, τ_c , is dependent on volume (size) of the molecule and the bulk viscosity of the solvent. τ_c can be estimated for molecules according to Equation 2.6.

$$\tau_c = \frac{4\pi r^3 \eta}{3kT} \phi C + \tau_0 \quad (2.6)$$

where r is the radius of the molecule, η is the bulk viscosity, ϕ is a shape parameter (1 for a sphere) and τ_0 is the inertial contribution to the reorientation time, which is negligible in liquids and so is usually ignored. C is the calculated slip coefficient, which measures the hindrance to rotation of a molecule in a liquid.²¹⁰ The equation can be simplified by setting ϕ and C to 1 (known as the ‘stick condition’) and disregarding τ_0 :

$$\tau_c = \frac{4\pi r^3 \eta}{3kT} \quad (2.7)$$

The J -coupling in a series of thallium complexes was reported by Parkin *et al.*²¹¹ to be strongly influenced by the relaxation rate of the thallium nucleus *via* a mechanism resulting from the large chemical shift anisotropy of thallium. As a consequence, the $J_{\text{Tl-C}}$ and $J_{\text{Tl-H}}$ coupling constants are strongly dependent on the magnetic field strength and frequency, as is the case with $[\text{Pt}(\text{dqp})\text{Cl}]\text{PF}_6$, owing to the extremely large CSA of the platinum nucleus (as evidenced by its wide CSA range ca. 1370–12000 ppm). This effect has been noted for various thallium pyrazolylborates²¹² and scorpionates,²¹³ as well as in mercury²¹⁴ and platinum compounds.^{215,216,217} Some studies into this effect have merely alluded to contribution of the CSA of platinum to spin-lattice relaxation, whilst others give a more detailed analysis. Chottard *et al.*²¹⁵ noted the lack of ^1H - ^{195}Pt coupling at higher frequencies in simple chloro-bridged platinum phosphine dimers and obtained an approximate value for $\Delta\sigma$ of ca. 900 ppm, whilst Fontaine *et al.*²¹⁷ reported a solid state NMR (ss-NMR) spectroscopic study detailing the methods used to obtain satisfactory spectra (see Section 2.6.2), from which quantitative data could be extracted.

By taking into account Equations 2.2 and 2.4, the $(1/T_1)$ relaxation rate for

[Pt(dqp)Cl]PF₆ can be approximated as follows:^{206,207}

$$\left(\frac{1}{T_1}\right) = \frac{AS^2}{30} \left(\frac{\tau_c}{1 + \tau_c^2 \omega^2}\right) \quad (2.8)$$

AS can then be expressed in terms of Ani , the anisotropy of the system, which can be determined experimentally using solid state NMR spectroscopy (*vide infra*, Section 2.6.2).

$$AS = 2A_{zz} - (A_{xx} + A_{yy} + A_{zz}) + (A_{zz}) \quad (2.9)$$

$$= 3A_{zz} - 3ISO \quad (2.10)$$

$$= 3Ani \quad (2.11)$$

The A terms in Equation 2.9 denote the chemical shift tensor with components having definite values in a frame bound to the molecule (anisotropic tensor elements).²¹⁸ Substituting the Ani term into Equation 2.8 produces Equation 2.12:

$$\left(\frac{1}{T_1}\right) = \frac{(3Ani)^2}{30} \left(\frac{\tau_c}{1 + \tau_c^2 \omega^2}\right) \quad (2.12)$$

From the value of Ani for [Pt(dqp)Cl]PF₆, determined by ssNMR spectroscopy to be 140 kHz at 400 MHz (see Section 2.6.2), and estimating τ_c to be 200 ps, as explained previously, the $(1/T_1)$ relaxation rate can be calculated using 400 MHz as the example solution state NMR frequency:

$$\left(\frac{1}{T_1}\right) = \frac{9 \cdot 4 \pi^2}{30} (140,000 \text{ s}^{-1})^2 \left(\frac{\tau_c}{1 + \tau_c^2 \omega^2}\right) \quad (2.13)$$

$$= 2.32 \times 10^{11} \text{ rad s}^{-1} \left(\frac{2 \times 10^{-10} \text{ s}^{-1}}{1 + (2 \times 10^{-10} \text{ s}^{-1})^2 (2\pi \cdot 8.6 \times 10^7 \text{ rad s}^{-1})^2}\right) \quad (2.14)$$

$$= 46.4 \text{ s}^{-1} \quad (2.15)$$

where $\omega = 2\pi\nu$ and the anisotropy, Ani , contains a 2π term in order to convert the units to rad s^{-1} . Applying these equations to give values for 200 MHz and 700 MHz produces the following values for relaxation rates, and, accordingly, the values for the T_1 relaxation time at each frequency can be obtained:

200 MHz:	$(1/T_1)$	11.6 s^{-1}	$T_1 = 86.4 \text{ ms}$
400 MHz:	$(1/T_1)$	46.4 s^{-1}	$T_1 = 21.5 \text{ ms}$
700 MHz:	$(1/T_1)$	137 s^{-1}	$T_1 = 7.28 \text{ ms}$

This demonstrates how the rate of relaxation, T_1 increases with increasing resonance frequency for **42**. Appearance of the ^{195}Pt satellites is dependent on T_1 because coupling is not observed if the relaxation rate (in s^{-1}) is faster than the magnitude of the J -coupling (in $\text{Hz} \equiv \text{s}^{-1}$), which is the reason for the general lack of J -coupling observed to quadrupolar nuclei such as ^{14}N and ^{11}B . For $[\text{Pt}(\text{dqp})\text{Cl}]\text{PF}_6$ the ^1H - ^{195}Pt J -coupling is 45 Hz, hence it lies within the range of calculated value for the relaxation times. At 200 MHz the rate of relaxation of 10.9 s^{-1} , is much faster than the J -coupling (45 s^{-1}) and so the nuclei relax slowly enough for satellites to be clearly observed. At 400 MHz the relaxation rate of 37.1 s^{-1} is of a similar magnitude to the J -coupling but slow enough that weak satellites can be seen, whereas at 700 MHz the rate is greater and relaxation occurs on a much faster timescale than the J -coupling, thus satellites are not observed.

2.6.2 Solid state NMR spectroscopy

To explore this phenomenon further, a solid state NMR spectroscopic study was undertaken to investigate the anisotropy of the system, so that estimates for the CSA-dependent relaxation time constants can be produced (Section 2.6.1). In solution the rapid tumbling motion of molecules averages out anisotropic interactions, which produces sharp lined spectra, but the disadvantage is loss of anisotropic (orientation-dependent) information. The shape of ssNMR spectra reflects the probability of molecules having a particular orientation and gives information about the components of the screening constant (Fig. 2.24). Certain anisotropic interactions can be controlled by use of the magic angle spinning (MAS) technique,²¹⁹ which involves spinning the sample in a rotor whose axis is inclined at an angle of 54.74° to the magnetic field direction, the so-called ‘magic angle’.

However, for platinum compounds the extremely broad spectra due to the high CSA, and the low signal-to-noise ratio, S/N, present more of a challenge, resulting in the need for alternative methods. As had been found previously for platinum amino- and iminophosphines,²¹⁷ a signal enhancement and repeated echo acquisition method proved successful in attaining suitable ssNMR spectra. The Carr-Purcell-Meiboom-Gill (CPMG) method²²⁰ is a modification of the Carr-Purcell scheme²²¹ originally published in 1954, where a 90° radiofrequency (RF) pulse was followed by a succession of 180° pulses to obtain an echo train for measurement of T_2 , and a 180° pulse followed by a succession of 90° pulses was used for measurement of T_1 . The modifications to the system are to combat the need for such highly accurate pulses, which otherwise leads to cumulative errors. CPMG pulse sequences are identical to that of Carr-Purcell, but the successive pulses are coherent, and the phase of the

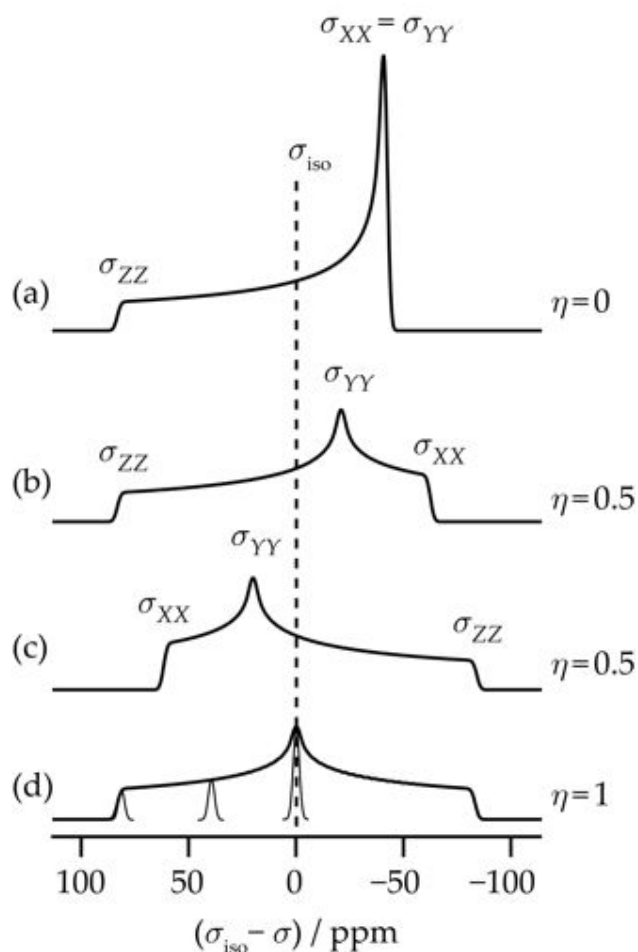


Fig. 2.24 Schematic powder patterns of shielding for (a) an axially symmetric case, (b) a case with negative shielding anisotropy, (c) an analogous case with positive shielding anisotropy, and (d) a case with an asymmetry of one. The bottom spectrum also shows the narrow lines obtained from three particular crystallite orientations.

RF of the 90° pulse is shifted by 90° relative to the 180° pulse.

[Pt(dqp)Cl]PF₆, **42** was analysed as a powder by using a static rather than spinning strategy, in order to enhance S/N. To minimise broadening of the signals and simplify the experiment, a frequency-stepped piecewise CPMG approach was adopted. With MAS the pulse sequence timing is critical, but this is less true for a static sample. Piecewise accumulation was necessary due to the broad chemical shift range of platinum, which cannot be uniformly excited, therefore the transmitter frequency was altered to record each piece of the spectrum separately (Fig. 2.25) and the sub-spectra co-added to provide the full spectrum (Fig. 2.26). Although this method increases acquisition time drastically, owing to the need for many sub-spectra, the technique can provide precise chemical shielding tensor information, free from the effects of incomplete excitation or variable sideband intensities.

A sample of [Pt(tpy)Cl]Cl was synthesised for comparison purposes in utilising this technique (Fig. 2.27), owing to the difficulty in obtaining good quality spectra for **42**. The spectrum obtained for [Pt(tpy)Cl]Cl shows a very similar profile to **42**, as expected for a closely related system, and shows improved resolution, verifying reliability of the additive methodology. For both compounds the ^{195}Pt observation frequency was ca. 85.8 MHz, and the duration of the pulses was 3.6 μs for the 90° pulse and, consequently, 7.2 μs for the 180° pulse. The recycle delay was 300 s for [Pt(dqp)]PF₆ and 30 s for [Pt(tpy)Cl]Cl with a frequency step of 50 kHz in both instances.

The chemical shift extremities of the spectra correspond to extremes in orientation and the anisotropic components of the screening constant. Referring to Fig. 2.24a, it can be seen that the systems are axially symmetric, and the combination of axial symmetry with anisotropy confirms the square planarity of the structures. For these complexes the high-field, shielded peripheral corresponds to the σ_{zz} component, and the low-field, deshielded peripheral corresponds to the σ_{xx} and σ_{yy} components. This suggests that σ_{zz} is most different by symmetry and is therefore likely to be oriented in a direction perpendicular to the square planar platinum centre, whilst σ_{xx} and σ_{yy} are likely to be oriented in the plane of the molecules. This assessment correlates well with findings for platinum compounds in the literature, *e.g.* in hexadentate platinum amino- and iminophosphines²¹⁷ and in simpler compounds such as Pt[(¹Pr₂PSe)₂]₂ and (cod)PtI₂.²²² The greater chemical shift range for [Pt(tpy)Cl]Cl, which displays a greater difference between the σ_{zz} component and the components in the plane of the molecule compared to [Pt(dqp)Cl]PF₆, is likely due to the higher planarity for [Pt(tpy)Cl]Cl, in comparison with the geometry seen for **42**, where the ligand is highly distorted from planarity.

Applying Equation 2.2 for a system with axial symmetry, one can take η (σ_{yy} - σ_{zz} /anisotropy) to be equal to zero, thereby the anisotropic centre σ can be calculated. This corresponds to ca. 1650 ppm for [Pt(dqp)]PF₆ and ca. 2800 ppm for [Pt(tpy)Cl]Cl, with the anisotropic shielding, $\sigma_{zz} - \sigma_{\text{ISO}}$ having the opposite sign to that of the chemical shift, so the chemical shifts for the complexes are equal to -1650 ppm (ca. -140 kHz) and -2800 ppm (ca. -240 kHz), respectively. These values can be applied to calculate relaxation rates, as shown previously (Section 2.6.1)

2.7 Concluding remarks

This chapter has addressed the synthesis and characterisation of a series of new terdentate ligands and platinum group metal complexes containing quinolyl and

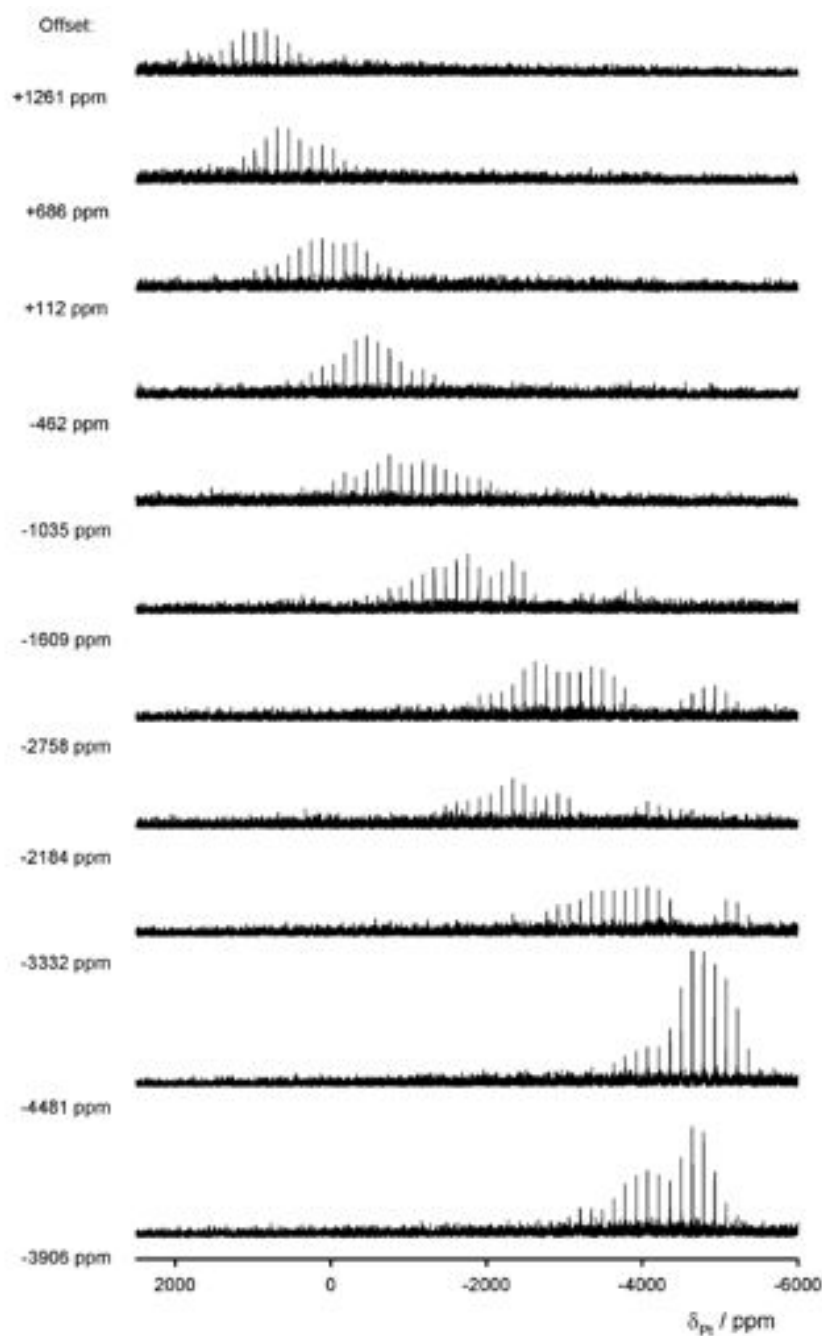


Fig. 2.25 Solid state NMR sub-spectra of $[\text{Pt}(\text{dqp})\text{Cl}]\text{PF}_6$, showing piecewise accumulation by separate excitation at 11 different frequencies.

isoquinolyl units. Following on from the preparation of new cyclometallating, terdentate quinoline-based ligands utilising cross-coupling methodologies, a series of iridium and rhodium complexes were synthesised, by a two-step process *via* a chloro-bridged dimer intermediate. Cleavage of the dimer with a bidentate ligand produced

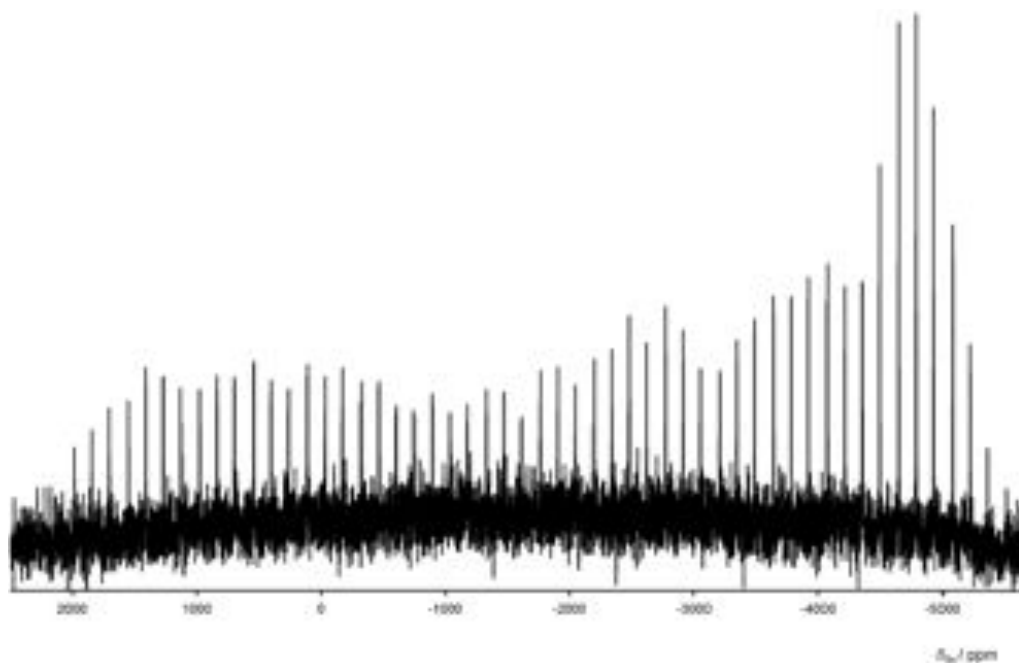


Fig. 2.26 Full solid state NMR spectrum of $[\text{Pt}(\text{dqp})\text{Cl}]\text{PF}_6$, produced by co-addition of the subspectra in Fig. 2.25.

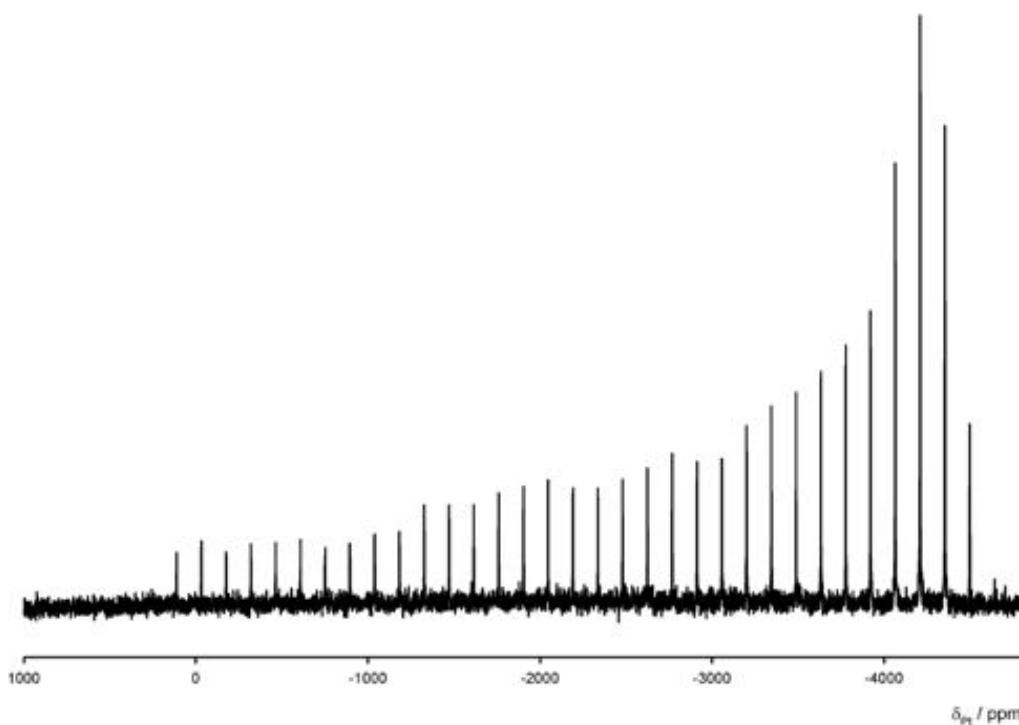


Fig. 2.27 Full solid state NMR spectrum of $[\text{Pt}(\text{tpy})\text{Cl}]\text{Cl}$, acquired in the same piecewise manner as for $[\text{Pt}(\text{dqp})\text{Cl}]\text{PF}_6$.

a range of new species, the electronic properties of which will be discussed in the forthcoming chapters. Subsequent functionalisation of these compounds was carried out *via* metathesis of the chloride ligand with strong σ -donor acetylide ligands. A

tricationic complex containing all nitrogen-donor atoms was also synthesised using a two-step approach.

Two series of platinum compounds were prepared: one comprising Pt(II) complexes containing ligands that form traditional five-membered rings with the metal centre, and the other displaying rarer six-membered chelate rings through the use of 8-quinoline-based ligands which provide a large bite angle. This permits a square planar geometry that is less strained than more distorted five-membered chelated compounds. The former series includes cyclometallating N[^]C[^]N-coordinating ligands around a platinum(II) centre, whilst the latter grouping contains either N[^]C[^]N-cyclometallating ligands or neutral N[^]N[^]N-coordinating ligands. The physical properties of each type of complex will be discussed from Chapter 4 onwards.

It has been shown that the disappearance of ¹⁹⁵Pt satellites in [Pt(dqp)Cl]PF₆, **42** can be rationalised with reference to the effect of CSA on the relaxation time, T₁ of the molecule [Pt(dqp)Cl]PF₆. The large CSA has an effect on the solution state and solid state NMR spectra, which can be used in tandem to provide a detailed picture of sample structure, from evidence of the timescales involved in relaxation of platinum complexes, and information about their anisotropic components.

Chapter 3

Photophysical, electrochemical and computational studies of d⁶ complexes

A variety of terdentate polypyridine iridium compounds have been studied to date, as discussed in Chapter 1, although compounds incorporating terdentate cyclometallating ligands, in particular, remain very much unexplored in comparison with Ir(III) compounds containing bidentate ligands. Luminescent properties are very much dependent on the number and location of cyclometallating or anionic donor sites in the ligands. The archetypal luminescent iridium complex is the (tris)bidentate green emitter *fac*-tris(2-phenylpyridine)iridium, Ir(ppy)₃, originally reported as having a quantum yield of 0.4 and a lifetime of 2.0 μ s at room temperature,⁴⁷ but more recently found to possess a quantum yield approaching 1.0.^{158,223} [Ir(tpy)₂]³⁺, meanwhile, exhibits only weak emission with a quantum yield of 0.025 and a lifetime of 1.0 μ s.^{40,41} Study of the physical properties of complexes discussed in this work comprises a computational, electrochemical and photophysical investigation into the complexes synthesised, in order to establish the nature of the excited state in each case.

3.1 Complexes based upon 1,3-di(1-isoquinolyl) benzene, 1-diqb, **1**

Iridium and rhodium complexes discussed in this section are those incorporating 1-diqb, **1**. Structures of the iridium complexes Ir(1-diqb)(ppy)Cl, **25**, Ir(1-diqb)(dFppy)Cl, **26**, [Ir(1-diqb)(bpy)Cl]⁺, **27** and Ir(1-diqb)(ppy)CC-tfp, **44** are

shown in Fig. 3.1; results for the rhodium complexes Rh(1-diqb)(ppy)Cl, **32** and Rh(1-diqb)(ppy)CC-tfp, **45** (analogues of **25** and **44**) will also be presented.

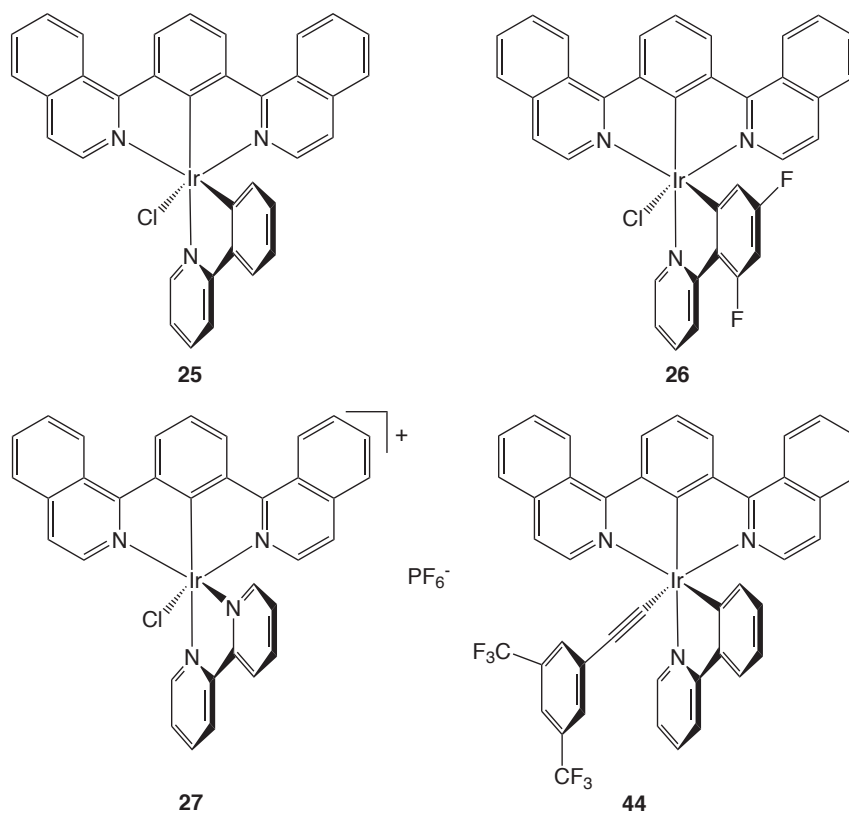


Fig. 3.1 Iridium complexes based upon 1-diqb, **1**.

3.1.1 Computational studies

Computational studies can be used to give an insight into the photophysical properties of phosphorescent complexes. Density functional theory (DFT) calculations are the method of choice for heavy transition metal complexes with many atoms due to the failures of *ab initio* methods, such as Hartree-Fock (HF), when dealing with large systems. These present a challenge due to the need to account for correlation and relativistic effects.²²⁴ The ‘hybrid’ density functionals include ‘exact exchange’,^{225,226} and the hybrid functional B3LYP is frequently employed for calculations of the magnitude encountered here, therefore it was used for all calculations performed in this study. DFT calculations have proved highly successful in predicting geometries for transition metal complexes,²²⁷ as emphasised when crystal structures are available to confirm the theoretical predictions.^{34,123}

Calculations in this study were carried out using an approach that is well established for structure optimisation of third row transition metal complexes. B3LYP was employed in conjunction with double- ζ basis sets: 6-311G for ligands and

LanL2DZ (Los Alamos relativistic basis set) for metals.²²⁸ The inner core electrons of the metal were replaced by a relativistic core potential, as is routinely used for large systems to reduce calculation times. All calculations were carried out as energy minimisations for gas-phase molecules at 0 K.

Optimisations were performed for all of the complexes synthesised and a comparison can be made with the single crystal X-ray structures obtained for the parent iridium and rhodium complexes, Ir(1-diqb)(ppy)Cl, **25** and Rh(1-diqb)(ppy)Cl, **32**. The optimised geometries are in good agreement with the two solid state crystal structures for these compounds (Fig. 2.20 and Fig. 2.21, respectively), correctly predicting the orthogonal nature of the terdentate and bidentate ligands (as discussed in Chapter 2) and modelling the small deviations from planarity noted for the terdentate ligand.

The optimised geometry for the parent complex Ir(1-diqb)(ppy)Cl, **25**, (Fig. 3.2a and 3.2b), is representative of the geometries of all the 1-diqb structures, which are predicted to adopt almost identical structures. The terdentate ligand is mostly planar, with small deviations from the plane of the molecule in opposing directions for the two quinolyl groups on either side of the central phenyl ring. The bidentate ligand lies planar with the chloride ancillary ligand. For the metathesis products **44** and **45**, the phenyl ring of the acetylide lies roughly perpendicular to both the plane of the terdentate and the bidentate ligands (Fig. 3.2).

Time-dependent DFT (TD-DFT) calculations were also performed on the compounds to gather further information about the nature of the lowest-energy transitions. Oscillator strengths for the transitions can be extracted from the results and the lowest-energy singlet excited state determined. For the majority of complexes examined, the lowest singlet state transition occurs between the HOMO and the LUMO, although in some cases it can be seen that the HOMO-1 and LUMO+1 are more important, and orbitals ranging from the HOMO-6 to LUMO+6 are seen to be involved in the absorption and emission processes. As is typically seen for d⁶ metal complexes, the HOMO for many of the complexes synthesised in this study has a high degree of metal-based character, comprising the 5d orbitals of iridium or the 4d orbitals of rhodium. However, in addition to their strong σ donor properties, there is a notable π -contribution from the cyclometallating ligands, which lends an LC/LLCT component to the photophysical properties. The LUMO is, in turn, largely ligand based, with a strong terdentate constituent, emphasising the LC and LLCT character often seen for these compounds, which often makes clear-cut assignments unfeasible. Compounds such as these are best described using a mixed orbital description, involving excited states with varying amounts of metal-

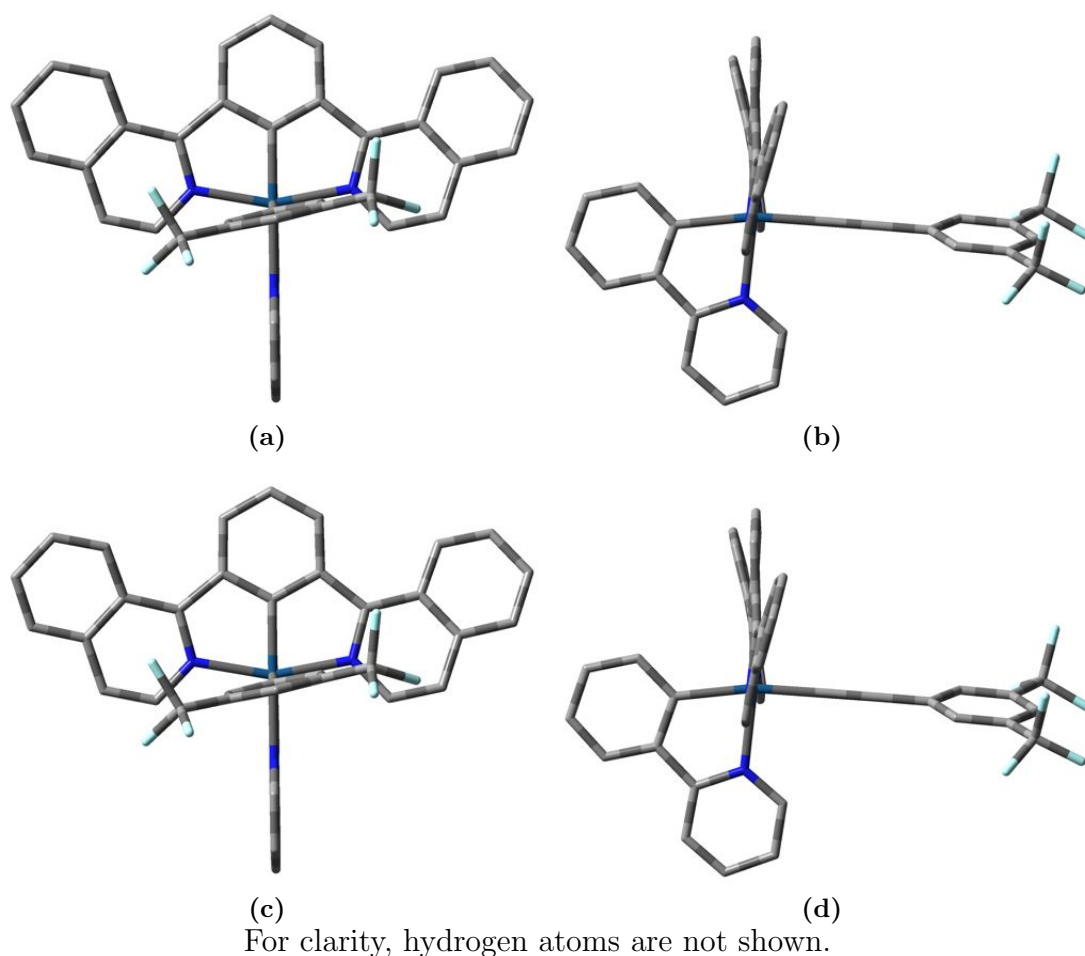


Fig. 3.2 Optimised structure of Ir(1-diqb)(ppy)CC-tfp, **44**, as predicted by energy minimisation using DFT, showing (a) the three approximately perpendicular planes of the molecular configuration and (b) the deviations from planarity of the terdentate ligand.

and ligand-based character together with charge transfer components.

Frontier orbital plots of Ir(1-diqb)(ppy)Cl, **25** and related compounds **26** and **27** are shown in Fig. 3.3. The plots for **25** and **26** bear a striking resemblance to one another, as would be expected, with the overall density regions largely the same in each case. The LUMO comprises primarily terdentate orbital contributions, whereas the HOMO lies over the metal centre, the bidentate ligand and the central phenyl ring of the terdentate ligand. In contrast, the cationic complex [Ir(1-diqb)(bpy)Cl]⁺, **27**, has a very different electron density distribution, with a LUMO that is highly bpy-based and a HOMO that has a lower metal contribution and more terdentate character. This suggests a much higher degree of LC/LLCT character and less SOC promotion of emission through metal participation, both factors that influence emission quantum yield (*vide infra*).

The rhodium analogue of the parent iridium complex **25**, Rh(1-diqb)(ppy)Cl,

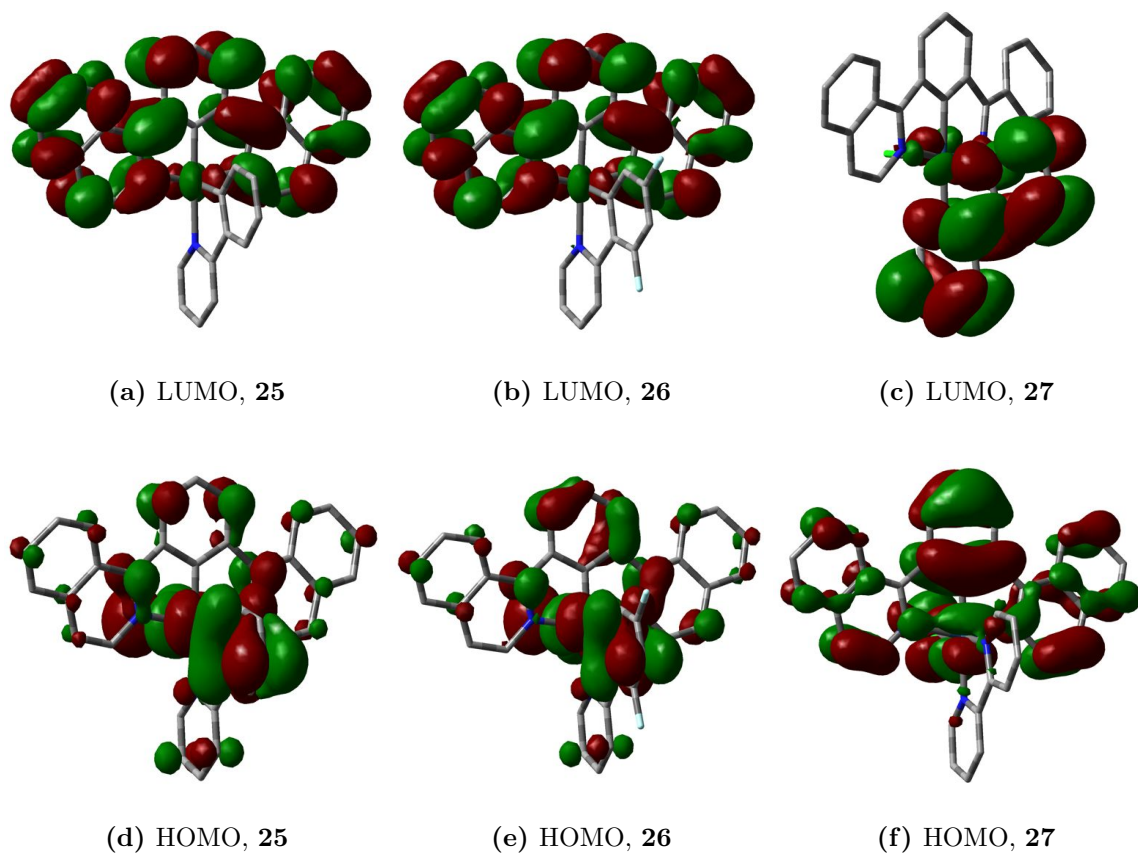


Fig. 3.3 Frontier orbital plots of **25**, **26** and **27** calculated by TD-DFT.

32, closely resembles the iridium species (Fig. 3.4a and Fig. 3.4d), with a similar percentage density distribution (Table 3.1). On considering the acetylide adducts of these two compounds, the optimisation in each case shows a higher contribution from the co-ligand to the HOMO than is seen for the chloride counterparts but virtually no contribution to the LUMO.

3.1.2 Electrochemistry

Cyclic voltammetry measurements were performed on 1-diqb-containing complexes in dilute CH_2Cl_2 solution using Bu_4NPF_6 (0.1 M) as the supporting electrolyte. Data are reported relative to the standard ferrocene couple Fc/Fc^+ ($E_{1/2}^{\text{ox}} = 0.40$ V vs the saturated calomel electrode (SCE))²²⁹ under the same conditions. Consistent results were difficult to obtain for a number of compounds studied, with poor reproducibility of peaks, therefore the voltammograms must be taken as a qualitative observation of the trends to reinforce the photophysical observations, rather than as a quantitative study. Electrochemical data are presented for all d^6 complexes in Table 3.7 at the end of this chapter.

Table 3.1 Molecular orbital (MO) characteristics of 1-diqb-based complexes, as calculated by TD-DFT; figures represent the percentage proportion of electron density residing at that site.

Complex	Constituent	HOMO-1	HOMO	LUMO	LUMO+1 ^a
Ir(1-diqb)(ppy)Cl 25	Ir	53	57	4	7
	Ter ^b	36	17	95	90
	Bi ^c	7	22	1	2
	Anc ^d	5	6	0	1
Ir(1-diqb)(dFppy)Cl 26	Ir	48	49	4	7
	Ter	41	31	95	90
	Bi	6	14	1	2
	Anc	4	6	0	1
[Ir(1-diqb)(bpy)Cl] ⁺ 27	Ir	39	38	5	4
	Ter	54	56	3	95
	Bi	3	4	92	1
	Anc	4	3	0	0
Rh(1-diqb)(ppy)Cl 32	Rh	52	54	3	6
	Ter	29	9	97	92
	Bi	7	20	0	1
	Anc	13	18	0	1
Ir(1-diqb)(ppy)CC-tfp 44	Ir	52	41	4	5
	Ter	14	22	94	88
	Bi	16	6	1	4
	Anc	17	32	1	3
Rh(1-diqb)(ppy)CC-tfp 45	Rh	49	38	3	4
	Ter	16	19	96	91
	Bi	15	3	0	2
	Anc	19	40	1	3

^a Percentages rounded to nearest integer, therefore totals do not always equal 100.

^b Ter denotes a terdentate ligand. ^c Bi denotes a bidentate ligand.

^d Anc denotes an ancillary ligand.

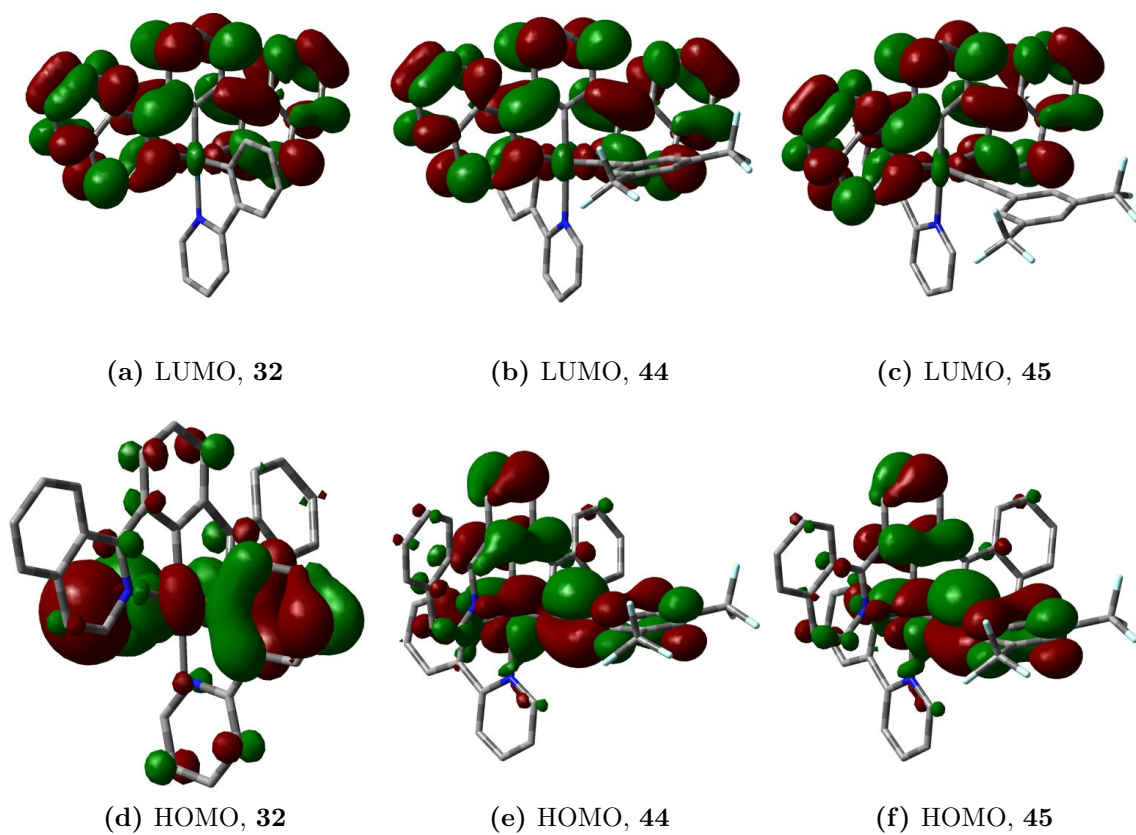


Fig. 3.4 Frontier orbital plots of **32**, **44** and **45** calculated by DFT.

Values for the peak positions for irreversible processes are less accurate than for reversible processes due to the variation of peak position with changing scan rate. Where reduction processes are present they are typically ligand-based, whilst the location of oxidations is dependent on the donor atoms of the ligands: complexes containing anionic donors such as chloride and cyclometallating carbons display metal-centred oxidations, whereas for charged complexes containing neutral donors or those that show LC emission, metal-based oxidation is not observed. It has been suggested that adsorption of the heavy metal species is the reason for the lack of reversibility of processes for third row transition metals complexes.⁴¹

All oxidations and reductions reported as $E_{1/2}$ values are pseudo-reversible; they do not fulfill the criteria for full reversibility but it can clearly be seen that there are two processes occurring. Examples of the pseudo-reversible forward and reverse oxidation waves for the iridium complexes Ir(1-diqb)(ppy)Cl, **25** and Ir(1-diqb)(ppy)CC-tpf, **44** are shown in Fig. 3.5. Pseudo-reversible oxidations are seen solely for these two complexes out of the series of complexes based upon 1-diqb, occurring at 0.69 V and 0.83 V for **25** and **44**, respectively. The value for **25**, together

with data from DFT calculations suggests that oxidation can be assigned to the loss of an electron from a HOMO spanning the metal ion and the 2-ppy moiety, due to an almost identical value seen for $\text{Ir}(\text{ppy})_3$ (0.70 V).^{145,230} These complexes are significantly easier to oxidise than the $\text{Ir}(\text{N}^{\wedge}\text{C}^{\wedge}\text{N})(\text{N}^{\wedge}\text{N}^{\wedge}\text{C})$ complex $[\text{Ir}(\text{dpyx})(\text{dppy})]^+$ (Fig. 1.11b, $E_{1/2} = 1.21$ V),⁶⁰ which is consistent with the quinoline systems being charge-neutral and more electron-rich than compounds based on pyridyl rings. Oxidation could be described as metal-based to a moderate extent, with the HOMO composed of ca. 50 % metal character for these two complexes but, as noted previously,²³¹ due to the covalent nature of the cyclometallating carbon–metal bonds, a purely metal-based picture cannot be assumed. From DFT studies, the portion of density appropriated to the HOMO by the ligands for all of the 1-diqb-based complexes confirms this observation. An irreversible oxidation process is seen for $\text{Ir}(1\text{-diqb})(\text{dFppy})\text{Cl}$, **26** (1.29 V) akin to that of $[\text{Ir}(\text{dpyx})(\text{dppy})]^+$,⁶⁰ although the latter shows a reversible oxidation wave. No oxidation process is observed for the cationic complex $[\text{Ir}(1\text{-diqb})(\text{bpy})\text{Cl}]^+$, **27** within the scanned range of the solvent window, -2.3 V– 1.3 V, as it is a less electron-rich charged species and has a lower metal contribution to the HOMO.

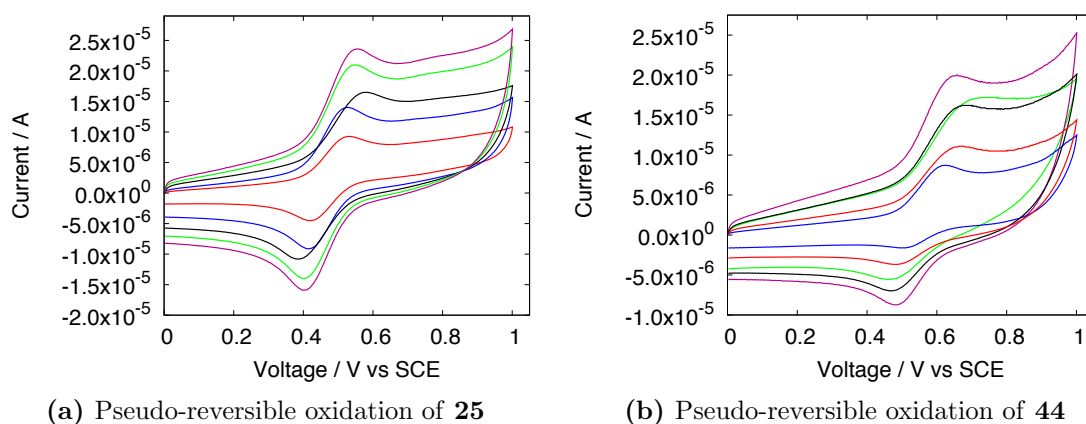


Fig. 3.5 Example of pseudo-reversible forward and reverse oxidation CV waves for 1-diqb-based iridium complexes at scan rates from 100 mV s^{-1} to 500 s^{-1} .

Irreversible oxidation processes are seen for the two rhodium compounds at 1.07 V and 1.01 V for $\text{Rh}(1\text{-diqb})(\text{ppy})\text{Cl}$, **32** and $\text{Rh}(1\text{-diqb})(\text{ppy})\text{CC-tfp}$, **45**, respectively, with the acetylide adduct also showing a wave at 0.78 V; this position is inline with the oxidation peak observed for the acetylide-containing iridium species, $\text{Ir}(1\text{-diqb})(\text{ppy})\text{CC-tfp}$, **44** (0.76 V). The more positive potential for **32** compared to its iridium analogue **25** is consistent with previous studies that have reported rhodium complexes to be more difficult than iridium species to oxidise and re-

duce.^{232,233} However, the first oxidation of **45** at 0.78 V is at a less positive potential than for the iridium analogue, suggestive of a higher energy HOMO. On comparing the DFT results for the two acetylide adducts, one can see that the contribution to the HOMO for the rhodium complex is composed of metal and acetylide character in almost equal parts, thus there is an increased LC nature to the oxidation process, so stabilising the orbital away from the highly charged metal centre more effectively than in the iridium complex.

The three chloride-containing iridium complexes, Ir(1-diqb)(ppy)Cl, **25**, Ir(1-diqb)(dFppy)Cl, **26** and [Ir(1-diqb)(bpy)Cl]⁺, **27** do not display clear-cut reduction peaks within the solvent window to -2.3 V. The acetylide adducts **44** and **45** display an irreversible reduction at -1.61 V, suggestive of the addition of an electron to the LUMO based upon 1-diqb or, perhaps more likely, on the acetylide, as a reduction is not seen in the chloride counterparts. This value is more negative than reductions seen for tpy-based complexes such as [Ir(tpy)₂][PF₆]⁴¹ and Ir(Brp-tpy)(dtpy) (see Fig. 1.14),⁵⁶ but is comparable with results found for a series of cyclometallated bis(terdentate) d⁶ complexes previously studied in our group.⁶⁰ The results concur with a more electron-rich character than for tpy-based compounds, due to the cyclometallating carbon donor.

3.1.3 Absorption spectroscopy

The absorption spectra show the expected profile for transition metal compounds: a series of high intensity bands at high energy (< 330nm), moderate intensity bands in the UV region of the spectrum (330 – 400 nm) and a long tail of well-resolved absorption bands into the visible region (> 400 nm). Absorption spectra for the iridium 1-diqb complexes Ir(1-diqb)(ppy)Cl **25**, Ir(1-diqb)(dFppy)Cl, **26**, [Ir(1-diqb)(bpy)Cl]⁺, **27** and the rhodium complex Rh(1-diqb)(ppy)Cl, **32** in dilute CH₂Cl₂ solution at room temperature are shown in Fig. 3.6. The spectra are very similar in nature and with reference to previous terdentate platinum group metal chemistry,^{50,52,85,234} the high energy bands can be assigned to spin-allowed $\pi-\pi^*$ LC transitions. Any high-energy d-d transitions due to increased splitting of the d-d states in comparison with compounds comprising neutral-donor ligands only, would be expected to be much weaker than LC transitions in this region of the spectrum. TD-DFT shows that the predominant lowest energy transition in most cases is that of the HOMO to LUMO transition, therefore the frontier orbitals can be utilised to provide a good description of the electron density distribution involved in the emission processes observed.

Absorption data are presented for the complexes in Table 3.5, highlighting the

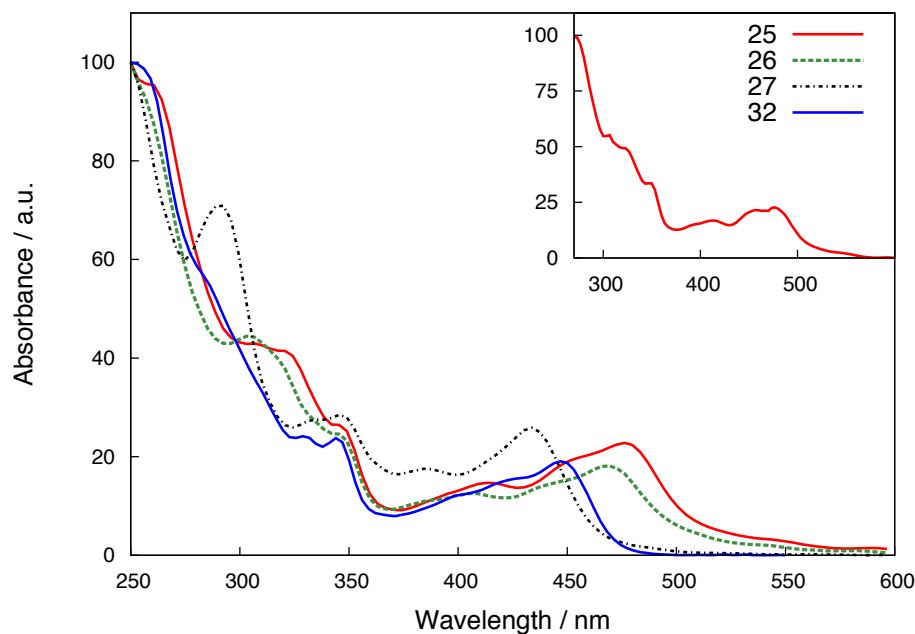


Fig. 3.6 UV-visible absorption spectra of 1-diqb-based complexes **25**, **26**, **27** and **32** in CH_2Cl_2 at 298 K; each is normalised to set the maximum intensity to 100. Inset: Excitation spectrum of **25**.

similarity in peaks for the 2-phenylpyridine derivatives of the 1-diqb-based compounds. The high-energy LLCT bands represent transitions from the ppy ligand to the terdentate ligand in the case of **25** and **26**, but for **27** the opposite may be true. Taking into consideration the bpy-based LUMO (92 % of the LUMO density) for the cationic complex, the likelihood is that the LLCT transition occurs from the bpy ligand to the terdentate 1-diqb ligand. Care must be taken when assigning lower energy bands as MLCT bands using a localised orbital description for MOs and transitions, because there is often significant delocalisation across the molecule, with a proportion of electron density based upon the ligands, thus necessitating a mixed-orbital description.^{51,56} This is especially true of cyclometallated complexes where the strong-field donor properties of the ligand induce a destabilisation of the 5d orbitals on the iridium centre, which can then mix more efficiently with the ligand and π^* orbitals. The lower energy absorption bands can therefore be ascribed to a mixture of LC and CT character, involving ^3LC , $^1\text{MLCT}$ and $^3\text{MLCT}$ transitions, as described for comparable iridium complexes.^{51,54,58} The weak band stretching into the red region, seen in particular for the iridium complexes containing moderate charge transfer character, likely corresponds to direct absorption from the singlet to triplet state, $\text{T} \leftarrow \text{S}$, which is formally spin-forbidden and therefore occurs with weak intensity. The tail is not as visible for the rhodium complex due to the lower SOC coefficient for the second row transition metal, thus direct absorption to the

triplet is less favourable.

On metathesis of the parent iridium and rhodium complexes with an acetylide, the absorption spectra retain the key features of the chloride compounds (Fig. 3.7). Both acetylide complexes, Ir(1-diqb)(ppy)CC-tfp, **44** and Rh(1-diqb)(ppy)CC-tfp, **45**, possess much higher ϵ values than their chloride counterparts (shown for **44** and **45** compared to chloride-containing equivalents **25** and **32** in Table 3.5) and appear darker red and orange in colour, respectively, than their chloride counterparts. Transitions are expected to be of the same origins as discussed above.

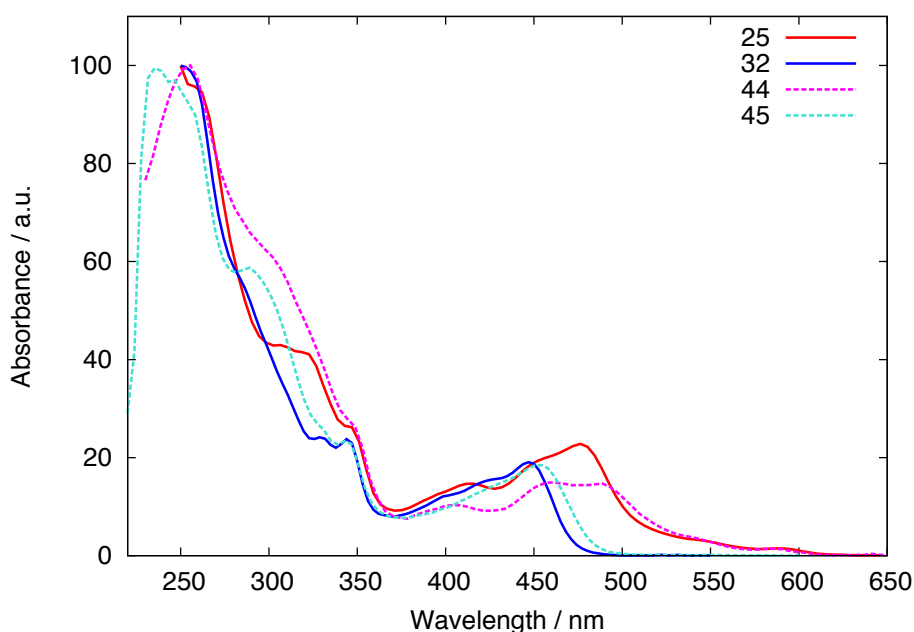


Fig. 3.7 UV-visible absorption spectra of 1-diqb-based chloride and acetylide complexes **25**, **32**, **44** and **45** in CH_2Cl_2 at 298 K; each is normalised to set the maximum intensity to 100.

Table 3.2 Ground state UV-visible absorption properties in CH_2Cl_2 at 298 K.

Complex	abs $\lambda_{\text{max}}/\text{nm}$ ($\epsilon/\text{M}^{-1} \text{cm}^{-1}$)
25	308 (12 239), 346sh (7 328), 414 (4 118), 477 (6 616)
26	305 (8 687), 345 (7 238), 407 (2 550), 469 (3 556)
27	290 (17 643), 347 (6 822), 386 (4 197), 433 (6 534)
32	330 (6 352), 344 (6 296), 430br (6 358), 444 (6 196)
44	251 (49 775), 305 (30 479), 345sh (16 239), 405 (6 228), 461 (9 359), 486 (8 951)
45	289 (28 025), 327 (10 315), 344 (11 018), 451 (9 494)

3.1.4 Emission spectroscopy

All compounds based upon 1-diqb, **1**, are luminescent at both room temperature and 77 K, with **25**, **26** and **44** showing particularly intense luminescence. These compounds have a significant contribution (ca. 40–60 %) to the HOMO from the iridium(III) ion, which facilitates spin-orbit coupling and increases the MLCT character of the excited state. This improves the quantum yield of phosphorescence by relaxing the spin selection rules (see Section 1.1) and allowing emission from the triplet state, which ensures that internal efficiency can theoretically reach a maximum of 100 %. Lifetimes for the three iridium 1-diqb chloride species are of the order 1–3 μs , which is ideal for use in OLED applications. Short lifetimes on the microsecond scale are preferable to reduce the probability of quenching and annihilation in the device.¹ The emission decay time for the rhodium parent complex, **32** is substantially longer at 16.2 μs , which is remarkably long-lived emission for a rhodium species. Lo *et al.* reported τ values of 4.2 – 8.7 μs for bidentate cyclometalated species, but similar Rh(III) compounds containing bidentate ligands typically show decay lifetimes on the nanosecond timescale. For example, $[\text{Rh}(\text{ppy})_2(\text{bpy})]^+$ and $[\text{Rh}(\text{bzq})_2(\text{phen})]^+$, where Hbzq is 7,8-benzoquinoline, have emission lifetimes of less than 10 nanoseconds.^{160,232,235}

Table 3.3 Luminescence data of 1-diqb-based complexes in CH_2Cl_2 at 298 K, and in an EPA glass at 77 K.

Complex	$\lambda_{\text{max}}/\text{nm}^{\text{a}}$	298 K		77 K	
		$\tau/\mu\text{s}$ deg(aer) ^b	$\Phi_{\text{lum}} \times 10^2$ ^c	$\lambda_{\text{max}}/\text{nm}$	$\tau/\mu\text{s}$
25	*610, 653sh	1.6 (0.58)	0.41	*594, 647, 705	2.8
26	*602, 646sh	1.9 (0.62)	0.50	*590, 640, 697br	3.0
27	583, *623	3.0 (0.69)	0.22	*576, 627, 679	4.9
32	*579, 620	16.2 (0.13)	0.10	*561, 608, 663	53
44	*604	1.7 (0.38)	0.51	*586, 635, 697	3.2
45	*575, 619	12 (1.0)	0.02	*564, 611, 667	49

^a λ_{max} value denoted by *. ^b Lifetimes in degassed and aerated solution.

^c Quantum yields measured using $[\text{Ru}(\text{bpy})_3]^{2+}$ as a standard.

Complexes **25** and **26** exhibit very similar emission profiles (Fig. 3.8), with a broad unstructured band at approximately 600 nm and a shoulder at lower energies. Broad featureless luminescence spectra originating predominantly from charge transfer states mixed with some ligand centred character are well-established in the literature. The seminal luminescent iridium complex *fac*-Ir(ppy)₃ is believed to emit from a mixed LC-MLCT state^{47,51,52,232,234,236} and many related compounds

feature this mixing of states.^{45,163,237} Emission for the present complexes can therefore be tentatively assigned as having ¹MLCT and ³MLCT excited state character, originating from $d(\text{Ir})/\pi(\text{Cl}) \rightarrow \pi^*$ ($\text{N}^-\text{C}^-\text{N}$) transitions, with possible mixing of LC/LLCT character. Support for this assessment is found in the appearance of low-energy MLCT bands seen both in the absorption and excitation spectra (see inset of Fig. 3.6). The λ_{max} value for the difluorinated complex **26** has a slight hypsochromic shift due to the electron-withdrawing effect of the fluorine atoms, which stabilises the HOMO and causes a blue-shift. Quantum yields of emission are very good for these two complexes, $\Phi = 0.41$ and 0.50 for **25** and **26**, respectively; amongst the highest quantum yields of the complexes studied herein and favourable in comparison with the numerous luminescent iridium complexes published.

The cationic complex containing bpy, **27**, and the rhodium species, **32**, have spectra that resemble one another (Fig. 3.8), though differ from **25** and **26**. The vibrational structure is somewhat more pronounced in these spectra, suggestive of increased LC character in the excited state,^{41,42} which is consistent with the DFT calculations that predict a smaller metal contribution to the HOMO (38 % for each). A lower metal influence also dictates the amount of SOC occurring and, consequently, less efficient singlet-triplet mixing results in lower quantum yields for these two species ($\Phi = 0.22$ and 0.10 for **27** and **32**, respectively). Nevertheless, a 10 % quantum yield for a rhodium complex is unprecedented in the literature, amongst the few luminescent rhodium compounds published.^{73,74,75} Bidentate complexes of the form $[\text{Rh}(\text{R-ppy})(\text{bpy})]^+$, synthesised by Lo *et al.*, emit from a mixed ³IL-³MLCT at room temperature with quantum yields ranging from 0.015–0.032 but these remain the most emissive rhodium compounds yet reported.⁷⁵ The shift to higher energy for the rhodium emission compared to its iridium counterpart, **25**, is in agreement with more stabilisation occurring for the d_π -orbitals on Rh(III) than on Ir(III). Electrochemical potentials also reinforce this point since a reduction process is seen for the iridium complex at -0.32 V, whereas no reduction wave is seen within the range to -2.3 V for the rhodium analogue.

The decay constants k_r and Σk_{nr} shown in Table 3.8 at the end of the chapter represent the decay constants for the radiative decay (Equation 3.1) and the sum of the non-radiative decay pathways (from Equation 3.2), respectively, which can be estimated from the quantum yield and lifetimes of the emission. This does, however, make the assumption that the excited state is formed with unitary efficiency. Although recently, unitary efficiency has been shown to be improbable from zero-time fluorescence of rhenium and iridium complexes,^{238,239} it is, nonetheless, a reasonable approximation for the present species, due to the good match between

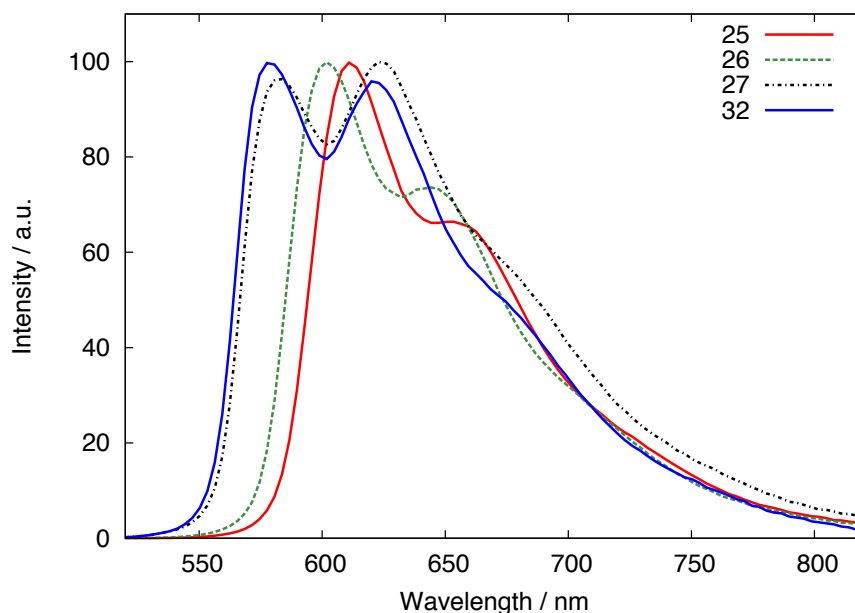


Fig. 3.8 Luminescence emission spectra of 1-diqb-based complexes **25**, **26**, **27** and **32** in CH_2Cl_2 at 298 K; each is normalised to set the maximum intensity to 100.

the absorption and excitation spectra.

$$k_r = \frac{\Phi}{\tau} \quad (3.1)$$

$$k_{nr} = \frac{1}{\tau} - k_r \quad (3.2)$$

The majority of the d^6 complexes discussed here have radiative and non-radiative rate constants of the order of 10^5 s^{-1} , comparable to those found in the literature for platinum group metal complexes. It can be seen that the value of the radiative constant k_r for the cationic complex **27** is roughly one fifth the value for the neutral complexes **25** and **26**, although the value for Σk_{nr} is also lower, hence its quantum yield remains moderate (0.22). The rhodium complex **32**, meanwhile, has a k_r value of $6.2 \times 10^3 \text{ s}^{-1}$ and a Σk_{nr} of $5.6 \times 10^4 \text{ s}^{-1}$, which explains its lower quantum yield, as justified above.

As observed for the absorption spectra, substitution of the ancillary chloride for an acetylide has little effect on the spectral profile shape (Fig. 3.9), only a small blue-shift due to stabilisation of the HOMO. The quantum yields for $\text{Ir}(1\text{-diqb})(\text{ppy})\text{CCtfp}$ **44** and $\text{Rh}(1\text{-diqb})(\text{ppy})\text{CCtfp}$ **45** are 0.51 and 0.02, respectively. The values are not dissimilar to those seen for the chloride-containing complexes (0.40 and 0.10 for **25** and **26**, respectively), although it is interesting to note that metathesis has had opposite effects on the quantum efficiencies for the two. The

higher k_r values, presumably owing to the effect of the additional cyclometallating carbon, is counteracted by the increased non-radiative constant for the Rh(III) complex, **45**, whilst in the case of the Ir(III) analogue **44**, a reduction in Σk_{nr} , results in an increase over **25**.

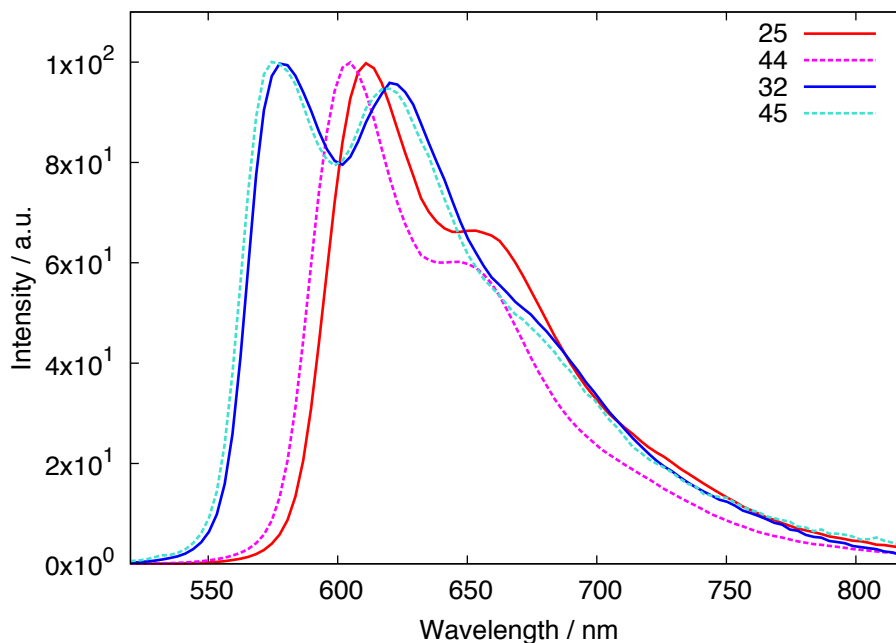


Fig. 3.9 Luminescence emission spectra of chloride and acetylide complexes of 1-diqb-based species **25**, **32**, **44** and **45** in CH_2Cl_2 at 298 K; each is normalised to set the maximum intensity to 100.

Photophysical characterisation was also performed at low temperatures by taking luminescence measurements at 77 K in a frozen EPA glass (EPA = diethyl ether/isopentane/ethanol, 2:2:1, v/v). The spectra display much more vibrational structure than at room temperature, the 0–0 band having the highest intensity (Fig. 3.10 and Fig. 3.11). The spectra are all slightly blue-shifted compared to the spectra taken at 298 K but they follow the same trend in emission energy.

3.2 Iridium(III) complexes based upon further isomers of terdentate quinolyl ligands

Three further iridium complexes were studied by computational, electrochemical and photophysical means: the cyclometallated compounds $\text{Ir}(3\text{-diqMeb})(\text{ppy})\text{Cl}$ **28**, $\text{Ir}(2\text{-dqFb})(\text{ppy})\text{Cl}$ **29**, and the bis(terdentate) species $[\text{Ir}(\text{dqp})_2]^{3+}$, **30**, which contains two $\text{N}^{\wedge}\text{N}^{\wedge}\text{N}$ -coordinating ligands (Fig. 3.12).

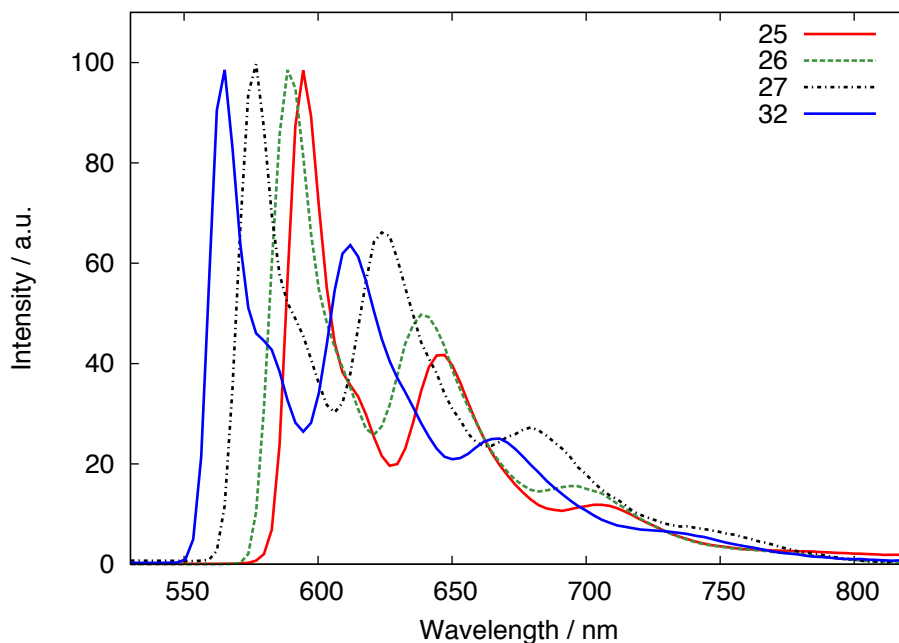


Fig. 3.10 Luminescence emission spectra of 1-diqb-based complexes **25**, **26**, **27** and **32** in an EPA glass at 77 K; each is normalised to set the maximum intensity to 100.

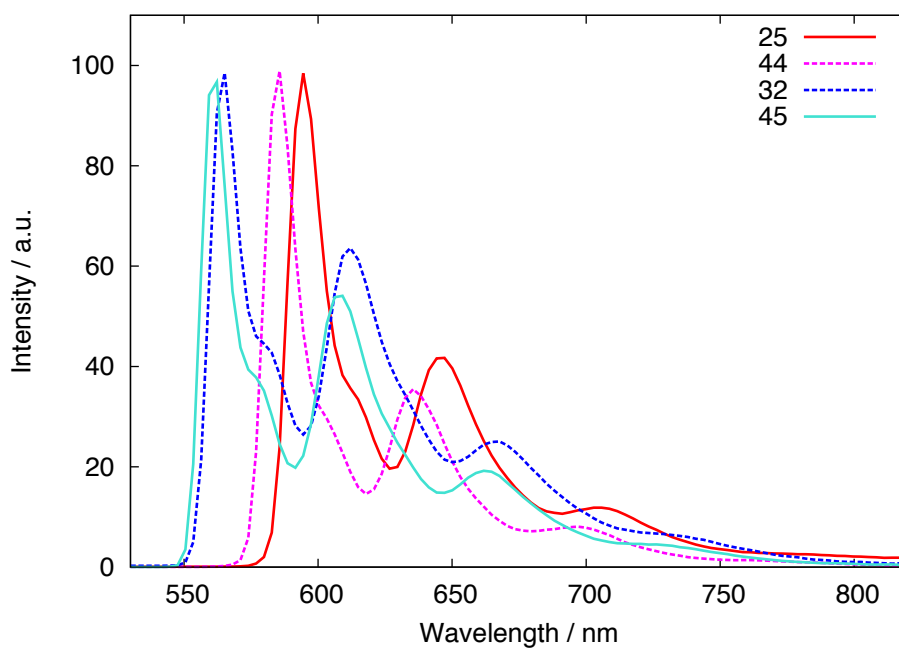


Fig. 3.11 Luminescence emission spectra of 1-diqb-based complexes **25**, **26**, **44** and **45** in an EPA glass at 77 K; each is normalised to set the maximum intensity to 100.

3.2.1 Computational studies

DFT and TD-DFT calculations were performed on the three complexes shown in Fig. 3.12 and the optimised structures are presented in Fig. 3.13. Initially, it can be

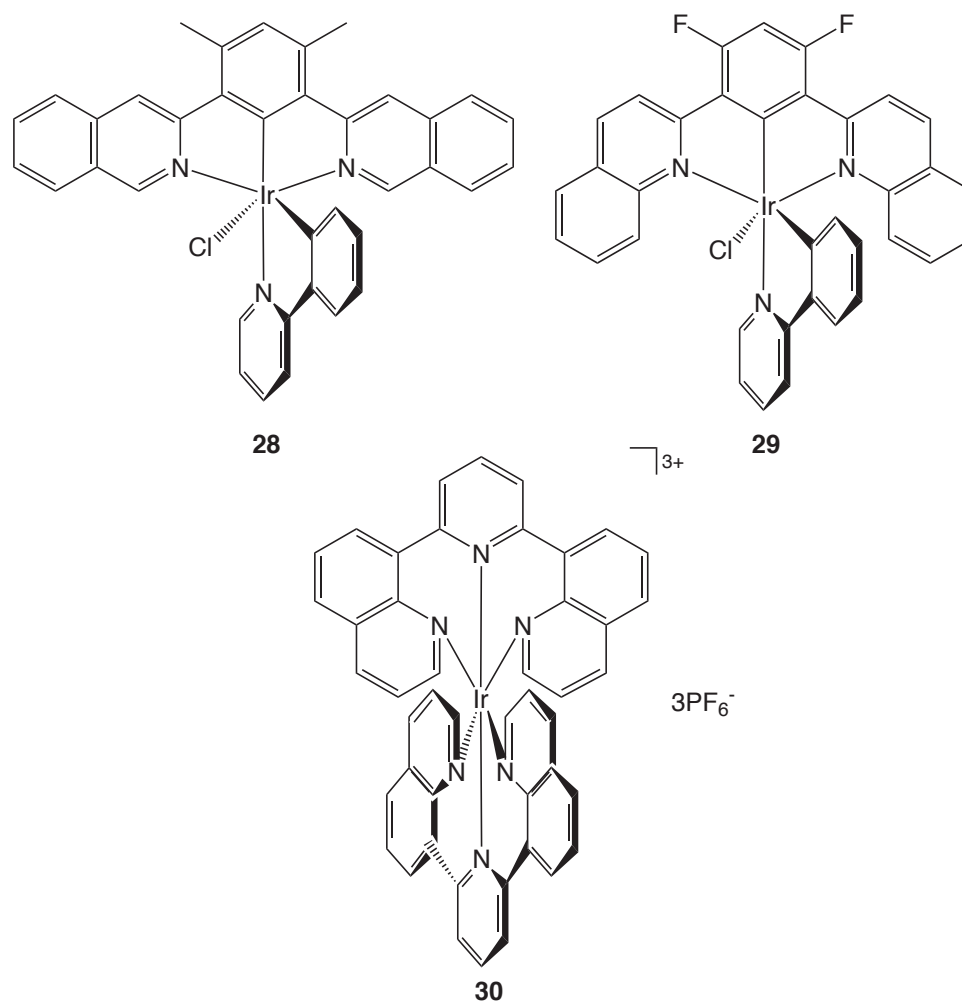


Fig. 3.12 Structures of iridium complexes **28**, **29** and **30**.

seen that of all the octahedral complexes discussed, **28** has the most planar geometry, with only a slight deviation from planarity for the terdentate ligand 3-diqMeb. The quinoline moieties are distorted very slightly, both in the same direction away from the plane of the central phenyl ring and the bidentate ligand is orthogonal to this ligand. The 2-quinolyl-based complex **29** is more twisted in nature, indicating the increased steric hindrance around the metal centre. The optimised structure of the $\text{N}^+\text{N}^+\text{N}$ -coordinated species, $[\text{Ir}(\text{dqp})_2]^{3+}$, **30**, demonstrates a twisted geometry, whereby the ligand must distort to obtain its preferred geometry around the iridium centre. By forming six-membered chelates, this ligand achieves a favourable bite angle of close to linearity (176.8° and 177.0°), as has been reported for the crystal structure of the ruthenium analogue (176.3° and 177.6°), which allows a near-perfect octahedral metal coordination environment.³⁴

Frontier-orbital plots for the three compounds are presented in Fig. 3.14 and percentage densities by location are given in Table 3.4. It can be seen that the

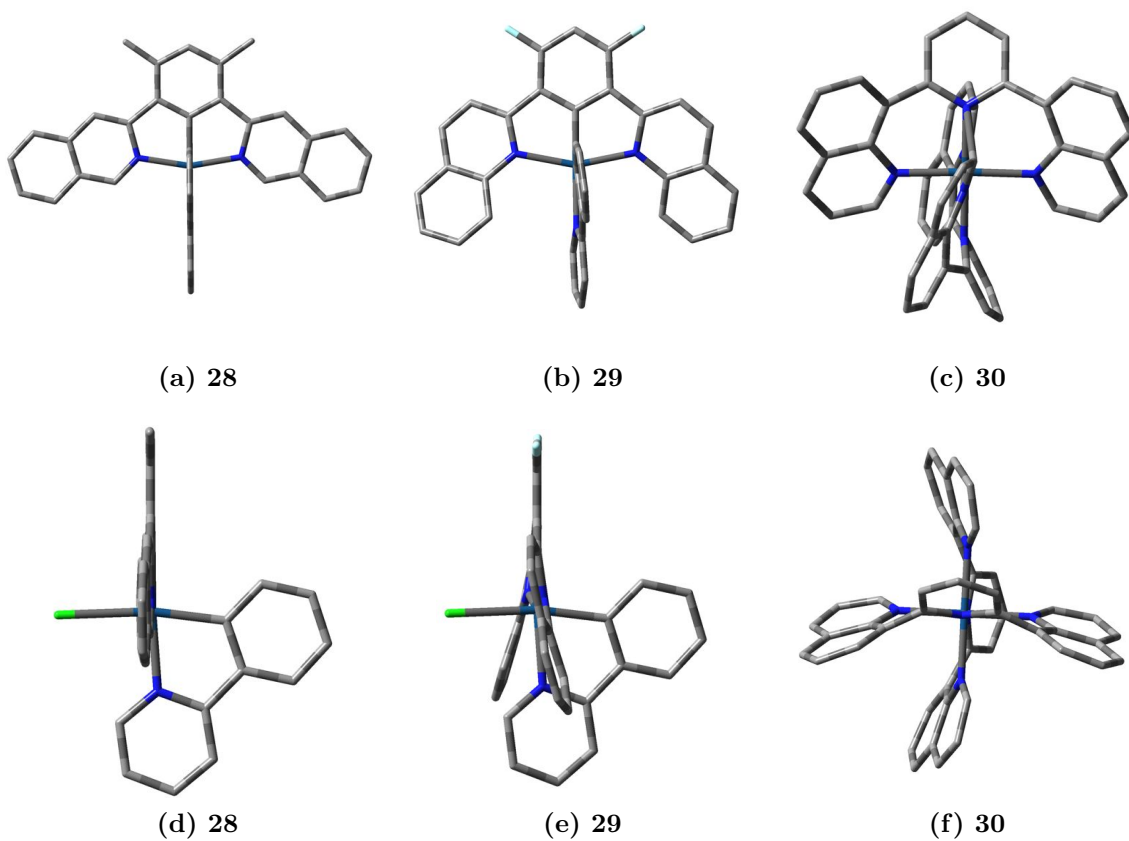


Fig. 3.13 Optimised structures of **28**, **29** and **30** with perpendicular views shown top and bottom, as predicted by energy minimisations using DFT (for clarity, hydrogen atoms are not shown).

overall picture for the cyclometallated complexes is much the same as for the 1-diqb-based compounds. The LUMO comprises predominantly terdentate orbitals, although there is a slightly increased contribution from the ppy ligand in the case of **29**, whilst the HOMO resides largely upon the central segment of the molecules. There is, however, a clear difference between the specific localisations of the HOMO: an increased ppy-contribution is observed for **29** with little density on the central phenyl ring, resembling that of the neutral 1-diqb compounds **25** and **26** (Fig. 3.3d and Fig. 3.3e), whereas **28** mirrors the cationic complex $[\text{Ir}(\text{1-diqb})(\text{ppy})\text{Cl}]^+$, **27** (3.3f) most closely in its electron distribution, with a significant contribution from the bidentate ligand.

The tricationic iridium complex, **30** is most distinctive of all, owing to its two terdentate ligands that encompass the metal. The frontier orbitals are widely dispersed over the entire molecule, displaying an identical distribution on each of the two ligands. The HOMO has a large ligand component, in contrast to all other complexes studied in this work, suggesting less metal character, and therefore less

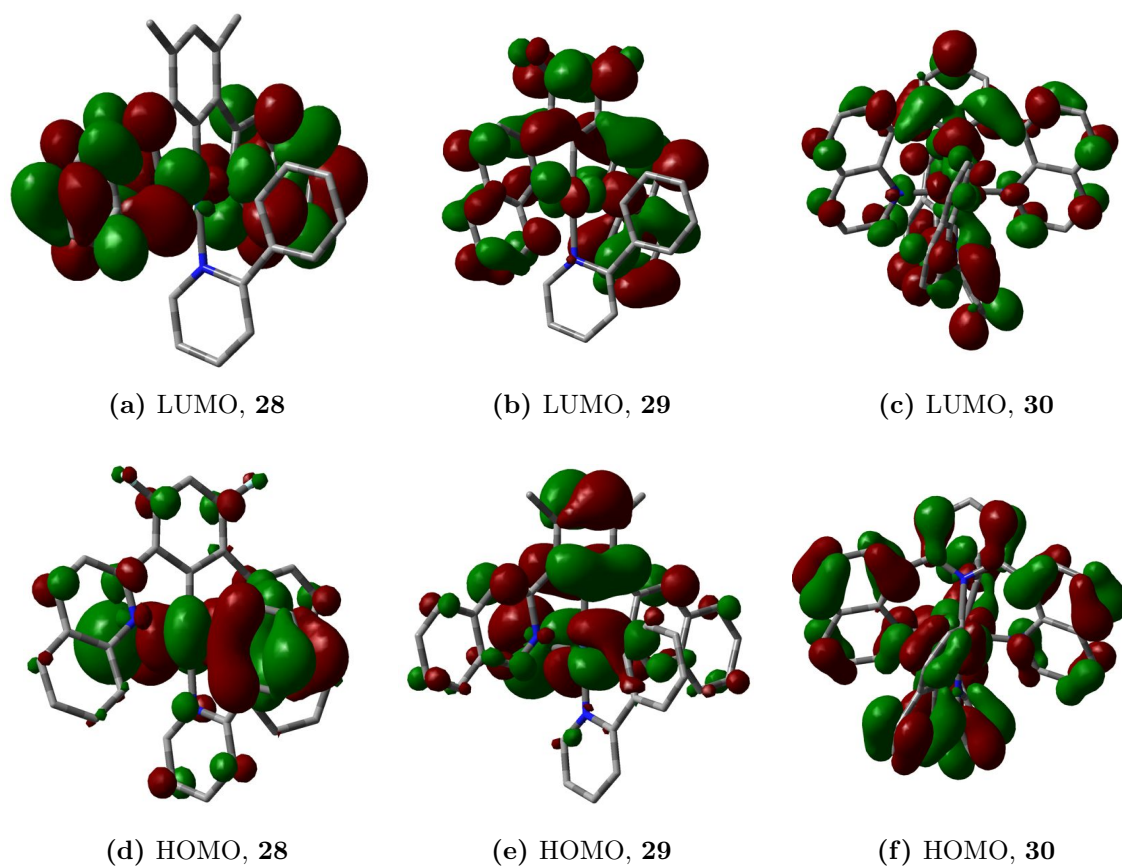


Fig. 3.14 Frontier orbital plots of **28**, **29** and **30** calculated by TD-DFT.

likelihood of MC or CT excited states. The LUMO is widely dissociated over the ligands (88 % ligand-based).

3.2.2 Electrochemistry

Electrochemical measurements were performed as in Section 3.1.2, using Bu_4NPF_6 (0.1 M) as the supporting electrolyte, in CH_2Cl_2 for the neutral compounds and MeCN for the cationic compound, using ferrocene as a standard couple (Fc/Fc^+ , $E_{1/2}^{\text{ox}} = 0.40 \text{ V vs SCE}$)²²⁹. The compounds containing cyclometallating ligands, $\text{Ir}(\text{3-diqMeb})(\text{ppy})\text{Cl}$, **28** and $\text{Ir}(\text{2-dqFb})(\text{ppy})\text{Cl}$, **29** each display a pseudo-reversible oxidation wave as seen for $\text{Ir}(\text{1-diqb})(\text{ppy})\text{Cl}$, **25** and $\text{Ir}(\text{1-diqb})(\text{ppy})\text{CCtfp}$, **44**. **28** is the easiest of all the six-coordinate compounds to oxidise, with an approximate $E_{1/2}$ value of 0.51 V, suggesting a more accessible HOMO. As suggested for the 1-isoquinolyl-containing complexes, oxidation can be tentatively termed a metal-based process but with a moderate ligand contribution. No oxidation wave is observed within the scanning range (up to 1.3 V) for the cationic complex **30**.

A single reduction wave is seen for both **28** and **29**, although it is irreversible

Table 3.4 Molecular orbital (MO) characteristics of **28**, **29** and **30** as calculated by TD-DFT; figures represent the percentage proportion of electron density residing at that site.

Complex	Component	HOMO-1	HOMO	LUMO	LUMO+1 ^a
Ir(3-diqMeb)(ppy)Cl 28	Ir	62	53	2	2
	Ter ^b	15	36	96	96
	Bi ^c	19	8	2	2
	Anc ^d	5	3	0	0
Ir(2-dqFb)(ppy)Cl 29	Ir	58	59	4	7
	Ter	23	15	88	79
	Bi	12	20	8	15
	Anc	6	5	0	0
[Ir(dqp)] ₂ ³⁺ 30	Ir	2	28	12	3
	Ter	98	72	88	97

^a Percentages rounded to nearest integer, therefore totals do not always equal 100. ^b Ter denotes a terdentate ligand. ^c Bi denotes a bidentate ligand.

^d Anc denotes an ancillary ligand.

in the case of the dimethyl-substituted complex, **28**, in addition to being shifted to a more negative potential. These are ligand-based reductions with the LUMOs comprising ligand orbitals and the values are consistent with those observed for iridium complexes containing cyclometallating ligands (see Table 3.7), occurring at more cathodic values than for tpy complexes. Two irreversible reduction waves are apparent in the cyclic voltammogram of [Ir(dqp)]₂³⁺ at -0.88 V and -1.67 V. These peaks are well separated, suggesting that it is unlikely they represent the first reduction of each of the ligands, as was seen in the work of Mamo *et al.* for example²⁴⁰, and which occur at -0.77 V and -0.93 V in [Ir(tpy)₂]³⁺,²³¹ instead it can be inferred that they may coincide with the first and second reduction processes of one of the ligands, as was noted for [Ir(bpy)₃]³⁺²⁴¹ and [Ir(tpy)₂]³⁺.²³¹

3.2.3 Absorption spectroscopy

The absorption spectra of Ir(3-diqMeb)(ppy)Cl, **28** and Ir(2-dqFb)(ppy)Cl, **29** display similar profiles with a maximum around 250 nm and a series of weaker bands in the lower energy region as for the complexes with unsubstituted phenyl rings (Fig. 3.15). By comparison with published literature^{51,54,58} the low energy bands can be assigned as a mixture of LC and CT transitions involving both singlet and triplet states. Absorption extends past 420 nm for both, with the weak bands representing direct (formally spin-forbidden) singlet to triplet excitation (S→ T),

promoted by SOC of the iridium centre.

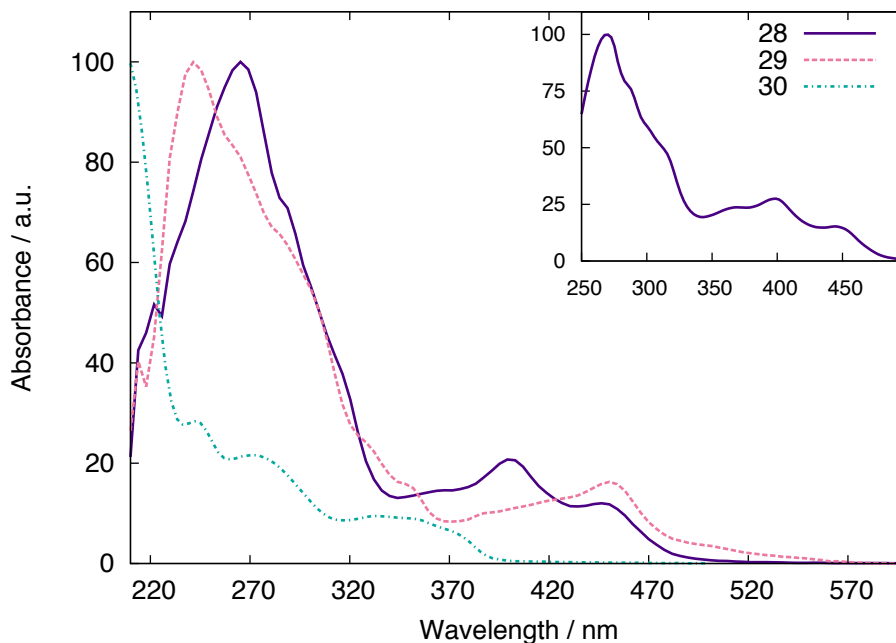


Fig. 3.15 UV-visible absorption spectra of iridium complexes Ir(3-diQMeb)(ppy)Cl, **28** and Ir(2-dqFb)(ppy)Cl, **29** in CH_2Cl_2 , and $[\text{Ir}(\text{dqp})_2]^{3+}$, **30** in MeCN. Inset: Excitation spectrum of **28**.

In contrast, the UV-visible spectrum for $[\text{Ir}(\text{dqp})_2]^{3+}$ at low concentrations extends much less into the longer wavelength region, being curtailed at approximately 400 nm. Observation of less CT character for iridium complexes containing neutral all-nitrogen donor ligands is not unexpected, since there are no anionic ligands present to raise the energy of the metal orbitals. In contrast to the rest of the iridium series, a concentration dependence emerged on altering concentration of $[\text{Ir}(\text{dqp})_2]^{3+}$. The absorption band at 272 nm that is apparent as a low intensity band in the spectra for the more concentrated solutions (where $\lambda_{\text{max}} = 215$ nm), increases in intensity so that it becomes the λ_{max} value (Fig. 3.16). This phenomenon occurred at concentrations below ca. 3×10^{-5} M, and an ϵ value at this point can only be obtained from the weaker solutions due to non-linear data above this concentration. Due to the occurrence at lower concentrations it could be tentatively suggested that it is due to a solvent effect. The system is very strained due to the enforced geometry necessary for binding of two six-membered chelate-forming ligands in an octahedral structure. DFT structure optimisation shows an orthogonal arrangement with a cross-like disposition when viewed from above (see Fig. 3.13c and Fig. 3.13f).

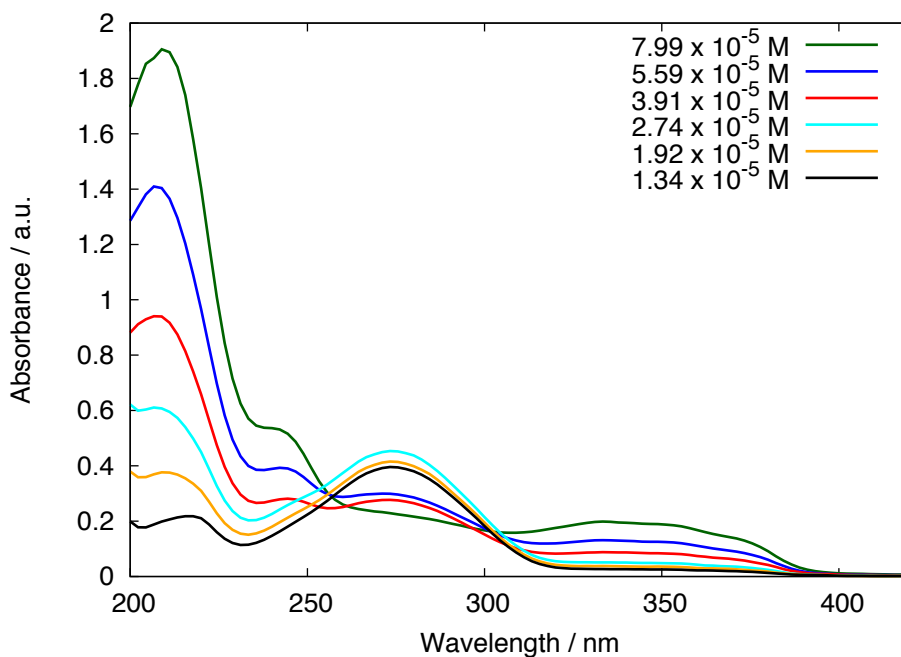


Fig. 3.16 UV-visible absorption spectra of $[\text{Ir}(\text{dqp})_2]^{3+}$, **30** in MeCN, highlighting the concentration dependence, as shown by the grow-in of a new band.

Table 3.5 Ground state UV-visible absorption properties of **28** and **29** in CH_2Cl_2 , and **30** in MeCN at 298 K.

Complex	$\lambda_{\text{max}}/\text{nm}$ ($\epsilon/\text{M}^{-1} \text{cm}^{-1}$)
28	256 (30 200), 400 (10 888), 447 (6 285)
29	242 (77 734), 347 (13 360), 450 (14 568)
30	215 (23 926) 242 (5 465), 272 (4 212) ^a , 334br (1 901)

^a ϵ value taken from measurements at high concentrations due to non-linearity at low concentrations.

3.2.4 Emission spectroscopy

The three compounds **28**, **29** and **30** are luminescent at room temperature and at 77 K (Fig. 3.17). $\text{Ir}(2\text{-dqFb})(\text{ppy})\text{Cl}$, **29** matches well with that of the neutral 1-diqb-based complexes discussed in the first part of this chapter, exhibiting a maximum at 604 nm and a shoulder to higher energy. $\text{Ir}(3\text{-diqMeb})(\text{ppy})\text{Cl}$, **28** displays two maxima of similar intensity (555 nm and 587 nm) so resembles the cationic species $[\text{Ir}(1\text{-diqb})(\text{bpy})\text{Cl}]^+$, **27**. The luminescence spectrum for the tricationic compound, $[\text{Ir}(\text{dqp})_2]^{3+}$, **30**, shows more a more structured nature.

The dimethylated species **28** is yellow in colour and emits brightly in the yellow region of the spectrum whilst the difluorinated species **29** is bright orange and emits orange luminescence. Complex **28** is highly emissive with a quantum yield of 0.67 and a lifetime of 5.1 μs , whilst **29** is much less efficient with a quantum

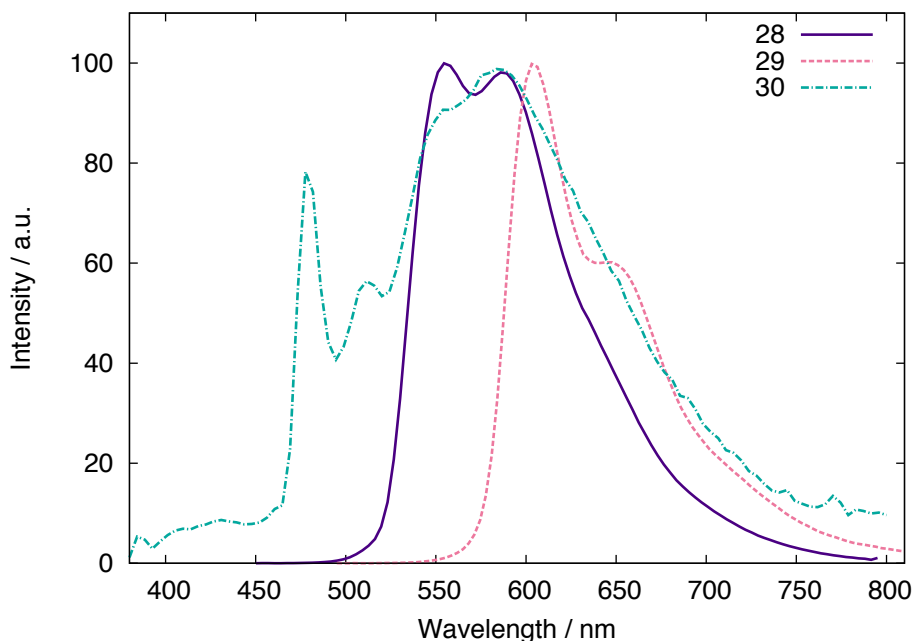


Fig. 3.17 Luminescence emission spectra of complexes **28** and **29** in CH_2Cl_2 , and **30** in MeCN at 298 K; each is normalised to set the maximum intensity to 100.

yield of 0.018 and a short lifetime of 220 ns, despite its bright colour in the solid state. The broad featureless emission spectra for both compounds are indicative of charge transfer character in the emitting state and DFT calculations support this assessment, exhibiting metal-based HOMOs and ligand-based LUMOs.

Table 3.6 Luminescence data of Ir complexes in CH_2Cl_2 at 298 K, and in an EPA glass at 77 K, except where stated otherwise.

Complex	$\lambda_{\text{max}}/\text{nm}^{\text{a}}$	298 K		77 K	
		$\tau/\mu\text{s}$ deg(aer) ^b	$\Phi_{\text{lum}} \times 10^{2\text{c}}$	$\lambda_{\text{max}}/\text{nm}$	$\tau/\mu\text{s}$
28	555, 587	5.1 (0.15)	0.67	*527, 568, 618	13
29	*604, 646sh	0.22 (0.16)	0.0018	*596, 634	11
30	*479, 510,	2.3 (0.28) ^d	0.0077 ^d	533, *576, 612sh ^e	260 ^e

^a λ_{max} value denoted by *. ^b Lifetimes in degassed and aerated solution.

^c Quantum yields measured using $[\text{Ru}(\text{bpy})_3]^{2+}$ as a standard.

^d In MeCN. ^e In ethanol.

Emission emanating from the tricationic iridium complex $[\text{Ir}(\text{dqp})_2]^{3+}$, **30** displays a more structured profile than any of the other octahedral compounds, which concurs well with ligand-centred luminescence observed for terpyridyl-based iridium complexes^{40,41,44,45,56} and the tris(bidentate) analogue $[\text{Ir}(\text{bpy})_3]^{3+}$.³⁹ LC emission is intuitive for neutral donor ligands since there is no formal charge donation to the metal centre to help stabilise CT states. This assignment is also reinforced by the

DFT calculations which predict a large percentage density localised on the ligands for both the HOMO and LUMO and a more minor metal contribution (28 %) to the HOMO than the other octahedral complexes. Consequently the quantum yield is much lower for this iridium species, $\Phi = 0.0077$, comparable with that of tpy-based Ir(III) complexes ($[\text{Ir}(\text{tpy})_2]^{3+}$ has a quantum yield of 0.025, for example).⁴¹

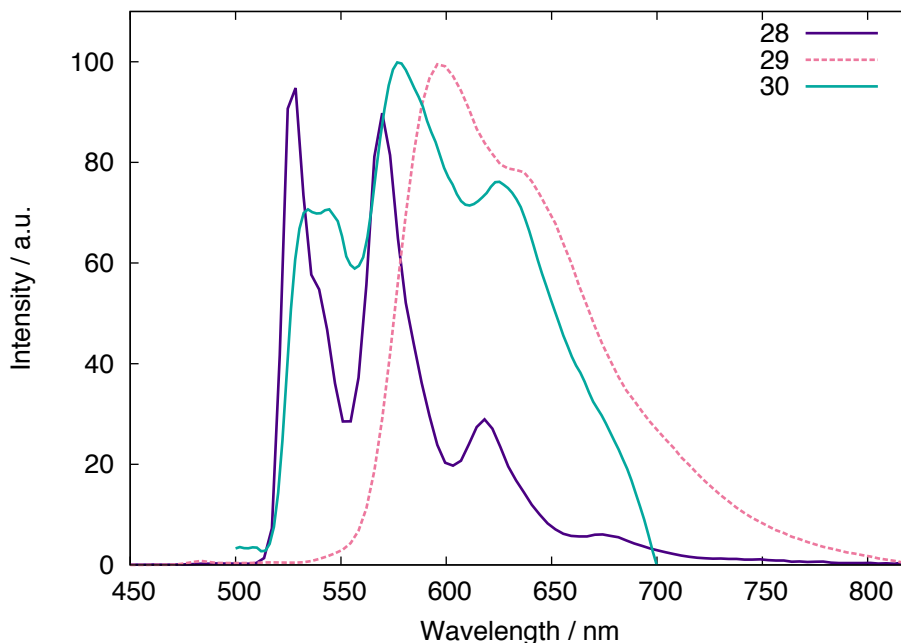


Fig. 3.18 Luminescence emission spectra of **28**, **29** and **30** in an EPA glass at 77 K; each is normalised to set the maximum intensity to 100.

3.2.5 Concluding remarks

Intensely luminescent Ir(III) complexes have been shown to possess a high degree of charge transfer character, predominantly involving $^1\text{MLCT}$ and $^3\text{MLCT}$ states, though admixtures with higher-lying singlet states are likely, which lend a mixed orbital picture to the assignment. Luminescence is observed for all iridium complexes in solution at room temperature and in a frozen glass at 77 K, and somewhat unusually, this is also the case for the two rhodium(III) complexes. The iridium complexes show a wide range of quantum yields from 0.018 to 0.67, for both cyclometallated systems and the bis($\text{N}^{\wedge}\text{N}^{\wedge}\text{N}$)-coordinated complex. Lifetimes are largely of the order of several microseconds, which is in the ideal region for applications in OLEDs, where short lifetimes reduce quenching by triplet-triplet annihilation.

The rhodium(III) complexes have quantum yields of 0.1 and 0.02, which are amongst the highest reported in the literature for Rh(III) complexes. This is likely to originate from the high metal contribution to the HOMO in each case, and the

low non-radiative decay constants. Metathesising the chloride species with acetylide-containing ancillary ligands does not have substantial effect on absorption or emission properties, and has opposing effects on the quantum yield: although diminished in the case of the Rh(III) complex, **45**, there is a slight improvement for the Ir(III) analogue from 0.40 to 0.50, for these deep red iridium emitters.

Table 3.7 Electrochemical data and the predominant character and energy of the lowest-lying singlet states of all d^6 complexes as determined by TD-DFT. CV measurements performed in CH_2Cl_2 using Bu_4NPF_6 as an electrolyte unless stated otherwise.

Complex	Lowest S state E/eV [λ/nm]	E_{ox}^0/V ^a	$E_{\text{red}}^0/V(\Delta/mV)$ ^a
$[\text{Ir}(\text{tpy})_2]^{3+\text{b}}$	HOMO \rightarrow LUMO 4.27 [291]	–	–0.77, –0.93
$\text{Ir}(\text{dpyx})(\text{dppy})^{\text{c}}$	HOMO \rightarrow LUMO 3.29 [377]	1.21 (83)	–1.39 (86)
$\text{Ir}(\text{Brptpy})(\text{tdppy})^{\text{d}}$	e	1.08	–1.27
$[\text{Ir}(\text{NNN})(\text{NNC})]^{2+\text{f}}$	e	g	–0.67, –1.04, –1.37, –1.91 ^h
$[\text{Ir}(\text{NNC})_2]^{+\text{f}}$	e	1.40	–1.11, –1.36, –2.01, –2.13 ^h
25 , $\text{Ir}(1\text{-diqb})(\text{ppy})\text{Cl}$	HOMO \rightarrow LUMO 2.47 [503]	0.69 (159)	g
26 , $\text{Ir}(1\text{-diqb})(\text{dFppy})\text{Cl}$	HOMO–1 \rightarrow LUMO 2.50 [496]	1.29	g
27 , $[\text{Ir}(1\text{-diqb})(\text{ppy})\text{Cl}]^+$	HOMO \rightarrow LUMO 2.31 [538]	g	g
28 , $\text{Ir}(3\text{-diMeqb})(\text{ppy})\text{Cl}$	HOMO \rightarrow LUMO 2.55 [487]	0.51 (284)	–1.53
29 , $\text{Ir}(2\text{-dqb})(\text{ppy})\text{Cl}$	HOMO \rightarrow LUMO 2.43 [510]	0.92 (213)	–1.13 (490)
30 , $[\text{Ir}(\text{dqp})_2]^{3+\text{+}}$	HOMO \rightarrow LUMO 2.90 [428]	g	–0.88, –1.67 ⁱ
32 , $\text{Rh}(1\text{-diqb})(\text{ppy})\text{Cl}$	HOMO \rightarrow LUMO 2.64 [470]	1.07	g
44 , $\text{Ir}(1\text{-diqb})(\text{ppy})\text{CC-tfp}$	HOMO \rightarrow LUMO ^j	0.83 (176)	–1.61
45 , $\text{Rh}(1\text{-diqb})(\text{ppy})\text{CC-tfp}$	HOMO \rightarrow LUMO ^j	0.78, 1.01	–1.61

^a Peak potentials are given for irreversible waves; for the pseudo-reversible waves, values refer to approximate $E_{1/2}$ values and the peak-to-peak separation is given in parentheses. ^b Data from ref⁴¹; in MeCN.

^c Data from ref⁶⁰; in MeCN. Data unavailable for the related compound $\text{Ir}(\text{dpyx})(\text{ppy})\text{Cl}$.

^d Data from ref⁵⁶; in MeCN. ^e Data unavailable. ^f Data from ref⁵⁵; in MeCN using Et_4NPF_6 as an electrolyte.

^g No defined peak was observed within the scanning range (–2.3–1.3 V).

^h $E_{1/2}$ values presented for reversible reductions. ⁱ In MeCN. ^j Values not obtained by TD-DFT calculations.

Table 3.8 Luminescence data in CH₂Cl₂ at 298 K, except where stated otherwise.

Complex	$\lambda_{\max}/\text{nm}^{\text{a}}$	$\tau/\mu\text{s}$ deg(aer) ^b	Φ_{lum}	$k_{\text{O}_2}^{\text{Q}}/10^8$ $\text{M}^{-1}\text{s}^{-1}$ ^c	$k_{\text{r}}/10^5$ s^{-1} ^d	$k_{\text{nr}}/10^5$ s^{-1} ^d
<i>fac</i> -Ir(ppy) ₃ ^e	510	1.9	0.40	e	2.1	3.2
<i>mer</i> -Ir(ppy) ₃ ^e	512	0.15	0.036	e	2.4	65
[Ir(tpy) ₂] ^{3+f}	458	1.0	0.025	0.76	0.25	9.8
[Ir(dpyx)(dppy)] ^{+g}	585	3.8 (0.077)	0.21	67	0.55	2.1
[Ir(dpyx)(ppy)Cl] ^{+g}	508	1.6 (<0.1)	0.76	>49	4.8	1.5
Ir(Brptpy)(tdppy) ^h	690	0.032	1.70	20	0.19	5.7
[Ir(NNN)(NNC)] ²⁺ⁱ	620	0.33	0.005	-	0.15	30
[Ir(NNC) ₂] ⁺ⁱ	630	2.3	0.066	-	0.29	4.0
25 , Ir(1-diqb)(ppy)Cl	*610, 653sh	1.6 (0.58)	0.41	5.0	2.7	3.6
26 , Ir(1-diqb)(dFppy)Cl	*602, 646sh	1.9 (0.62)	0.50	4.9	2.6	2.6
27 , [Ir(1-diqb)(bpy)Cl] ⁺	583, *623	3.0 (0.69)	0.22	9.3	0.50	1.8
28 , Ir(3-diqMeb)(ppy)Cl	*555, 587	5.1 (0.15)	0.67	27	1.3	0.65
29 , Ir(2-dqFb)(ppy)Cl	*604, 646sh	0.22 (0.16)	0.018	6.3	4.5	1.3
30 , [Ir(dqp) ₂] ³⁺	479, 514, 554sh, *584 ^j	2.3 (0.28) ^j	0.24 ^j	14	1.0	3.4
32 , Rh(1-diqb)(ppy)Cl	*579, 620	160 (0.13)	0.10	3.4	0.06	0.56
44 , Ir(1-diqb)(ppy)CC-tfp	*604	2.2 (0.48)	0.51	0.41	3.0	2.9
45 , Rh(1-diqb)(ppy)CC-tfp	*575, 619	12 (1.0)	0.020	4.1	1.7	8.1

^a λ_{\max} value denoted by *. ^b Lifetimes in degassed and aerated solution. ^c $k_{\text{O}_2}^{\text{Q}}$ is the bimolecular rate constant for quenching by molecular oxygen at 298 K, estimated from the lifetimes in degassed and aerated solutions, assuming [O₂] at 1 atm pressure of air = 2.2 mmol dm⁻³. ^d Rate constants k_{r} and k_{nr} estimated from Φ_{lum} and τ values at 298 K. ^e Data from ref⁵¹; full data unavailable. ^f Data from ref⁴¹; in MeCN. ^g Data from ref⁶⁰; in MeCN. ^h Data from ref⁵⁶; in MeCN. ⁱ Data from ref⁵⁵; in MeCN. ^j In MeCN.

Chapter 4

Photophysical, electrochemical and computational studies of d^8 complexes

In the study of the photophysics of square planar d^8 platinum(II) complexes, a difference exists between cationic complexes based upon the neutral donor ligand tpy, and those of cyclometallating ligands, of which the latter are typically more luminescent due to increased ligand field strength. Nevertheless, there is no clear-cut distinction, and there are many non-luminescent cyclometallated species, whilst some N[^]N[^]N-coordinated complexes do show emission at room temperature. In this chapter, physical properties of Pt(II) complexes based upon both types of ligand will be discussed and comparisons made.

4.1 Platinum complexes containing five-membered chelate rings

Platinum(II) complexes based upon ligands that form five-membered chelate rings with the metal centre are well-established in both bidentate^{81,242,243,244} and terdentate systems.^{90,105,121,245,246,247} It is most convenient to compare the complexes discussed in this section (Fig. 4.1) with the archetypal terdentate Pt(II) complexes [Pt(tpy)Cl]⁺ and Pt(dpyb)Cl. In the structured absorption spectrum of [Pt(tpy)Cl]⁺, weak bands are observed at 433 nm and 463 nm, corresponding to LC $^3\pi - \pi^*$ absorption.⁸⁷ Pt(dpyb)Cl, meanwhile, shows intense $^3\pi - \pi^*$ bands at higher energies (below 300 nm) and a series of intense bands between 320–430 nm, corresponding to both LC $^3\pi - \pi^*$ and metal influenced transitions, including MCLT transitions such

as the S_1 peak for the $S_0 \rightarrow S_1$ transition.¹⁰⁶ A lower energy tail is often present in such systems, which is due to direct excitation from the singlet to the triplet state ($S_0 \rightarrow T_1$).

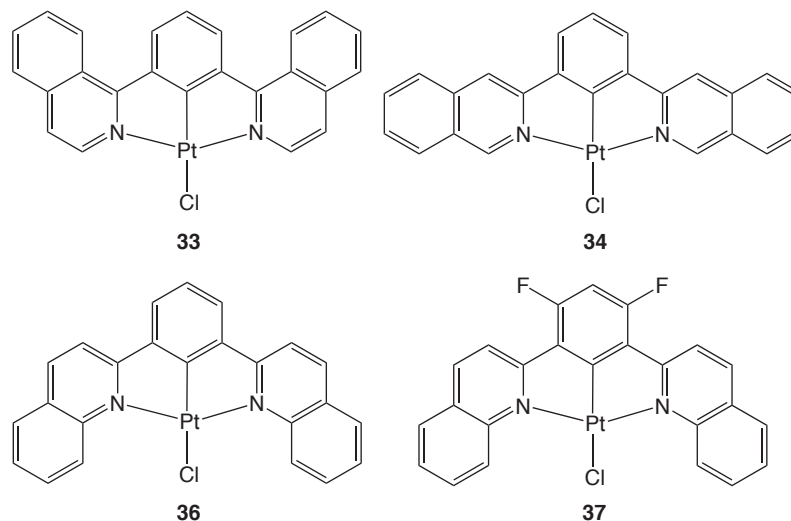


Fig. 4.1 N[^]C[^]N-coordinated Pt(II) complexes forming five-membered chelate rings that were investigated during this study.

There is a sharp contrast in the emission properties of the two complexes: $[\text{Pt}(\text{tpy})\text{Cl}]^+$ is non-emissive in solution at room temperature whilst $\text{Pt}(\text{dpyb})\text{Cl}$ is one of the most luminescent platinum complexes reported and emits with a quantum yield of 0.60 and a lifetime of 7.2 μs . Peaks are reported at 491 nm, 524 nm and 562 nm,¹⁰⁶ and were postulated initially to be of LC $^3\pi - \pi^*$ character, due to the very small Stokes shift, relatively long lifetime and lack of solvatochromism. However, more recent work applying computational calculations to this and related complexes has put forth the notion of an LC-MLCT admixture.^{107,108}

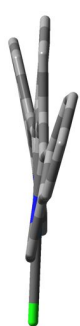


4.1.1 Computational studies

Computational calculations were carried out for the complexes $\text{Pt}(1\text{-diqb})\text{Cl}$, **33**, $\text{Pt}(3\text{-diqb})\text{Cl}$, **34** and $\text{Pt}(2\text{-dqFb})\text{Cl}$, **37** by employing the same methods as used in Chapter 3 (Section 3.1.1). The optimised structures show a distorted square planar geometry due to the bite angle of the terdentate ligand. The smaller bite angle (Table 4.1) does not necessitate the geometric distortion seen for the 8-quinolyl-based complexes (*vide infra*), as the ideal linear coordination geometry about the metal centre is not achievable for these ligand frameworks. Small distortions from a planar structure are seen for $\text{Pt}(1\text{-diqb})\text{Cl}$, **33** and $\text{Pt}(2\text{-dqFb})\text{Cl}$, **37**, but the complex containing lateral aryl rings, $\text{Pt}(3\text{-diqb})\text{Cl}$, **34**, shows perfect planarity, with an interplanar angle between the central benzene ring and the quinolyl side

groups of 0.0° . A notable feature of the more sterically hindered complex, **37**, is the non-linearity of the carbon-platinum-chloride fragment; the chloride is bent at an angle away from the plane of the structure to minimise steric interactions with the quinolyl units.

Whilst nearing completion of this project, a publication reporting the synthesis of a series of pyridyl- and quinolyl-based platinum compounds, presented the crystal structure of a related complex, namely platinum(1,3-di(1-isoquinolyl)-4,6-difluorobenzene) chloride,¹⁹² the difluorinated analogue of **33**. Comprising the same basic components, it is likely that the geometry about the metal centre would be much the same, and results from DFT optimisations are in good agreement with the molecular structure reported by Li *et al.*¹⁹² In addition to showing the slight deviation of the quinolyl groups from the plane of the central ring, an extremely accurate value is found for the platinum-carbon bond at the site of cyclometallation; the values are the same to within experimental error (1.94 Å). The calculated bite angle of approximately 160° for these ligands mirrors that found in the molecular structure of the difluorinated compound, and other related complexes such as those incorporating pyridyl and pyrazolyl heterocycles,^{109,111,112} as well as platinum(II) tpy compounds.^{87,105}

Table 4.1 Optimised structures of the N[^]C[^]N complexes with five-membered chelate rings as predicted by energy minimisations using DFT (for clarity, hydrogen atoms are not shown).

Complex	33	34	37
			
Interplanar angle/ $^\circ$	11.6	0.0	4.8
Trans N-Pt-N angle/ $^\circ$	161.2	161.9	159.1
Lateral N-Pt bond length/Å	2.05	2.06	2.11
Central Pt-C bond length/Å	1.92	1.94	1.93

The frontier orbital plots for **33**, **34** and **37** are presented in Fig. 4.2, with plots for HOMO-1 and LUMO+1 shown in Appendix B. In comparison with calculations for the well-studied pyridyl-containing compound, Pt(dpyb)Cl,^{107,108,248}

the overall density distribution follows the same pattern. The HOMO is located predominantly on the central core of the molecule comprising largely metal and ancillary ligand orbitals, with only a small proportion originating from the terdentate ligand. Conversely, the LUMO in each case is widely distributed over the terdentate ligand, with the percentage proportion of electron density situated on the cardinal ligand being $\geq 90\%$ for each of the complexes (Table 4.2). The lowest-energy spin-allowed singlet excited state for Pt(1-diqb)Cl, **33** and Pt(3-diqb)Cl, **34** is composed of HOMO \rightarrow LUMO character, whereas the lowest singlet excited state for the difluorinated complex **37** represents the HOMO-1 \rightarrow LUMO transition. There is a moderate contribution to the HOMO from the central phenyl ring for the three complexes (48–64%), which also plays a variable part in the LUMO in each case.

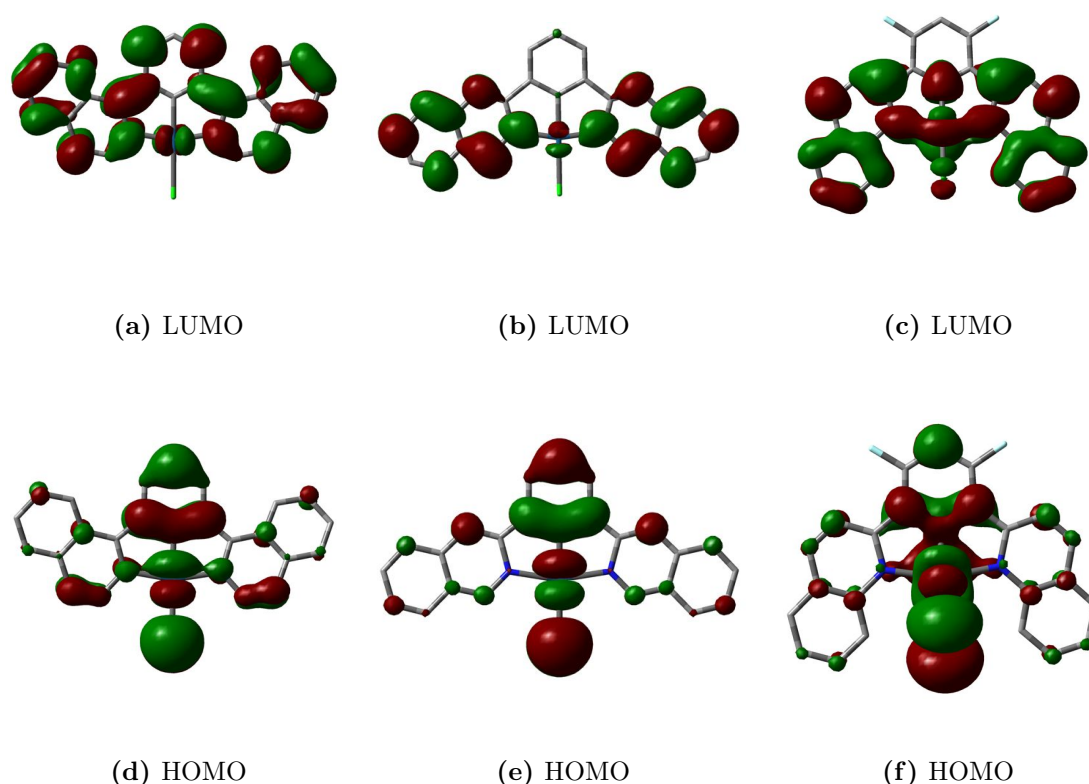


Fig. 4.2 Frontier orbital plots of **33**, **34** and **37** calculated by TD-DFT.

4.1.2 Electrochemistry

The isoquinolyl-based complexes Pt(1-diqb)Cl, **33** and Pt(3-diqb)Cl, **34** were investigated by cyclic voltammetry (CV) using Bu_4NPF_6 (0.1 M) as the supporting

Table 4.2 Molecular orbital characteristics of **33**, **34** and **37**, as calculated by TD-DFT; figures represent the percentage proportion of electron density residing at that site.

Complex	Constituent	HOMO-1	HOMO	LUMO	LUMO+1 ^a
Pt(1-diqb)Cl 33	Pt	42	48	4	1
	Ter ^b	27	41	96	99
	Anc ^c	31	12	0	0
Pt(3-diqb)Cl 34	Pt	37	57	3	1
	Ter	44	35	97	99
	Anc	19	8	0	0
Pt(2-dqFb)Cl 37	Pt	40	64	9	4
	Ter	47	27	91	96
	Anc	13	8	0	0

^a Percentages rounded to nearest integer, therefore totals do not always equal 100. ^b Ter denotes a terdentate ligand.

^c Anc denotes an ancillary ligand.

electrolyte and CH₂Cl₂ as the carrier solvent (Table 4.3). Complex **37** was not isolated as a pure sample so its electrochemical and photophysical properties will not be discussed. Data are reported relative to the standard ferrocene couple Fc/Fc⁺ ($E_{1/2}^{\text{ox}} = 0.40$ V vs SCE)²²⁹ under the same conditions. Like the octahedral complexes, consistent results were difficult to obtain, with reproducibility presenting a challenge, therefore the results must be taken as a qualitative rather than quantitative study. In general, platinum(II) complexes containing imines and related ligands do not show clear-cut oxidations, or at best, show irreversible ill-defined peaks due to the reactivity at the vacant axial sites,²⁴⁹ causing them to be intrinsically variable. For comparison purposes, cyclic voltammetry data for all platinum compounds are presented in Table 4.13 at the end of this chapter.

An irreversible oxidation peak is seen for **33** and **34** (0.37 V and 0.27 V respectively) close to the $E_{1/2}^{\text{ox}}$ value for Pt(dpyb)Cl (0.35 vs Fc/Fc⁺). This concurs with metal based oxidation, as reported for many platinum complexes,⁸⁵ which is largely independent of the ligands present. Fig. 4.3, corresponding to the voltammograms for Pt(3-diqb)Cl, **34**, is shown as an example of the irreversible oxidation peak at varying scan rates, from which it can be seen that a forward and a reverse wave occurs, but that the site of the peak maximum is not constant.

A reversible reduction wave is seen for **33**, whilst no defined process is present for **34**. Reduction is ligand-based, as emphasised by the almost exclusive localisation of the LUMO on the terdentate ligand. The increased conjugation present in these quinoline-containing complexes in comparison with related pyridyl- and pyrazolyl-

Table 4.3 Electrochemical data and the predominant character and energy of the lowest-lying singlet states as determined by TD-DFT.

Complex	Lowest S state	E/eV [λ/nm]	$E_{\text{ox}}^0/V^{\text{a}}$	$E_{\text{red}}^0/V(\Delta/mV)^{\text{a}}$
Pt(dpyb)Cl	HOMO→LUMO	2.64 [471] ^b	0.35 ^c	-2.14 ^c
33	HOMO→LUMO	2.58 [481]	0.37 (89)	-1.59 (280), -2.19 (170)
34	HOMO→LUMO	2.64 [469]	0.27 (90)	^d

^a In CH_2Cl_2 using Bu_4NPF_6 as an electrolyte. Peak potentials are given for the irreversible oxidations and second reductions (ill-defined return wave). For the pseudo-reversible reductions, values refer to $E_{1/2}$ and the peak-to-peak separation is given in parentheses. ^b Data from ref¹⁰⁸. ^c Data from ref¹⁰⁶.

^d No defined peak was observed within the scanning range (-2.3–1.3 V).

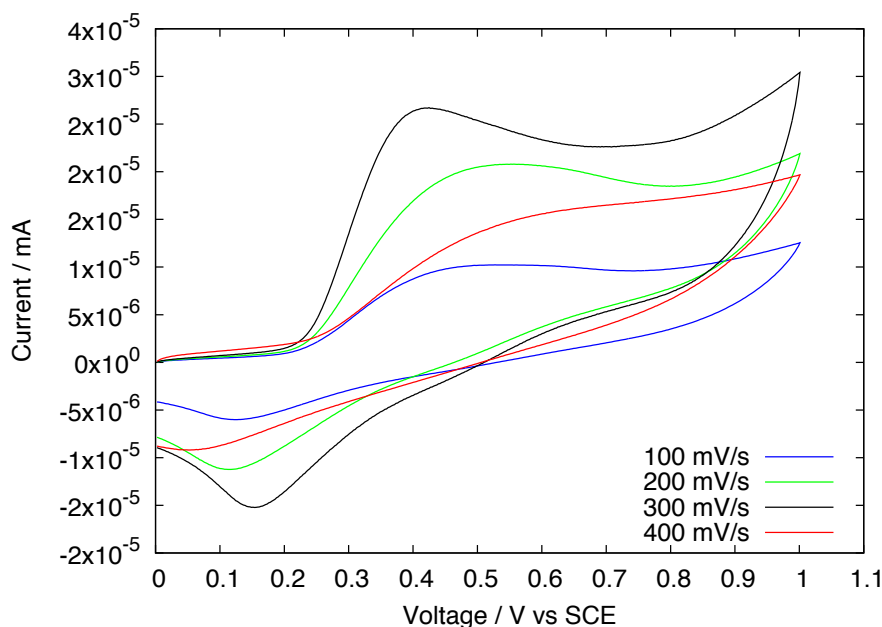


Fig. 4.3 Example of irreversible oxidation process for Pt(3-diqb)Cl, **34** at scan rates of 100 mV s^{-1} to 400 mV s^{-1} .

based platinum(II) complexes shifts reduction potentials to less negative values due to a stabilised LUMO level.

4.1.3 Absorption spectroscopy

Absorption spectra for **33** and **34** in dilute CH_2Cl_2 solution are shown in Fig. 4.4 and data are presented in Table 4.4; each adheres to the Beer-Lambert law, $A(\lambda) = \epsilon(\lambda)cl$, at low concentrations. Both complexes display a set of high-energy bands ($<280 \text{ nm}$), which can, in part, be attributed to LC $\pi\text{-}\pi^*$ transitions, in addition to several lower energy features, consistent with an increase in electron density on

the metal from cyclometallation. It can be inferred that there may be some degree of mixing of excited states (LC and CT), owing to the structured profiles shown. MLCT and LLCT character may feature, due to a dispersion of the frontier orbitals over both ligands as well as the metal centre.

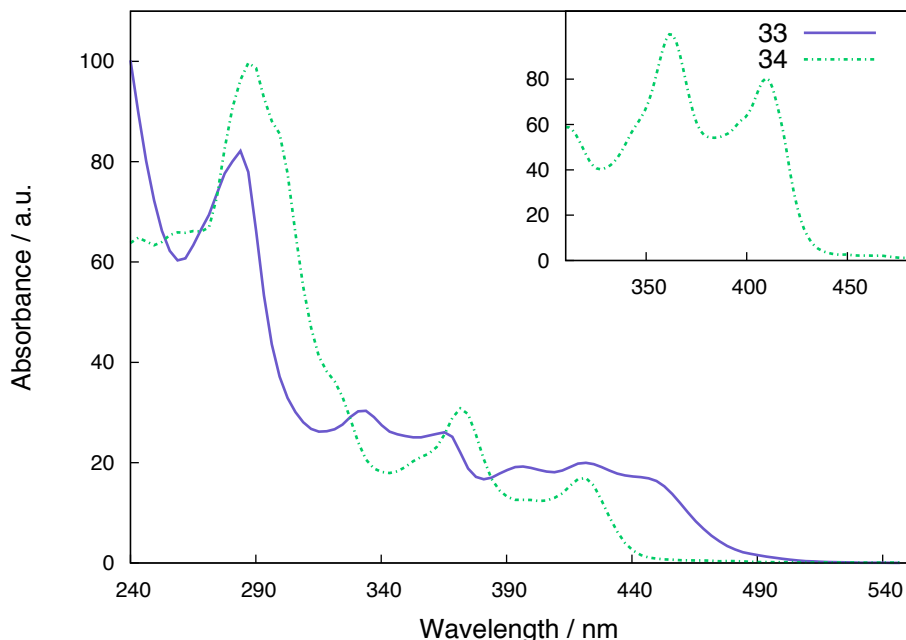


Fig. 4.4 UV-visible absorption spectra of the Pt(N[^]C[^]N) complexes **33** and **34** in CH₂Cl₂ at 298 K, following excitation into the lowest energy absorption band; each is normalised to set the maximum intensity to 100. Inset: Excitation spectrum of **34**.

The complex containing the lateral isoquinoline units, Pt(3-di**iqb**)Cl, **34**, shows two defined peaks, rather than a series of bands in the red region of the spectrum. The planar geometry of this complex would imply that of all of the complexes in this study, this would be the most likely to form aggregates; however, this phenomenon is not observed in the absorption spectrum because the profile does not alter with changing concentration and the bands also appear in the luminescence excitation spectrum (see inset of Fig. 4.4).

DFT calculations show the lowest-lying spin-allowed singlet state to be composed of HOMO→LUMO character for **33** and **34**, although for the difluorinated species **36** the lowest singlet state is HOMO–1→LUMO (*vide supra*, Table 4.3). The calculated energies for the lowest transition for the three complexes are very similar (ca. 2.60 eV), as expected from the same conjugation present in the systems and the cyclometallating carbon donation. The calculations underestimate the experimental absorption wavelengths for **33** and **34** but the qualitative comparison between the two is accurate, as is also seen for the six-membered chelate-containing compounds

Table 4.4 Ground state UV-visible absorption properties at 298 K in CH₂Cl₂.

Complex	λ_{\max}/nm ($\epsilon/\text{M}^{-1} \text{cm}^{-1}$)
33	232 (35 054), 284 (24 577), 332 (7 821), 366 (7233), 395 (5435), 420 (5 211)
34	278 (71 352), 287sh (60 351), 307sh (27 494) 363 (22 893), 410 (12 612)
36	267 (41 790), 288 (15 521), 332 (8 814), 429 (1 036) ^a

^a Data from ref²⁵⁰

(*vide infra*).

4.1.4 Emission spectroscopy

The two complexes Pt(1-diqb)Cl, **33** and Pt(3-diqb)Cl, **34** are emissive at room temperature in dilute CH₂Cl₂ solution (Fig. 4.5), as is the unsubstituted 2-quinolyl compound, Pt(2-dqb)Cl, **36**, previously studied by another group member. Bright orange emission was observed for Pt(2-dqFb)Cl, **37** when naked eye observations were made using a UV lamp; if this originates from the desired complex then potential for room temperature luminescence from this complex exists. Further work to isolate a pure sample through an alternative method (*via* mercuration, for example) is necessary to investigate whether this is the case.

Emission profiles for the two emissive compounds show different features; Pt(1-diqb)Cl, **33** displays two maxima of similar intensity at 595 nm and 642 nm, whilst Pt(3-diqb)Cl, **34** shows one main broad band centred at 668 nm, with much weaker peaks at 559 nm and 520 nm (Table 4.5). The quantum yield for **33** is 0.09 with a lifetime in degassed solution of 4.3 μs , whilst **34** shows concentration-dependent figures. At a concentration of $1.8 \times 10^{-5} \text{ mol dm}^{-3}$ the quantum yield is 0.28 with a lifetime of 30 μs , but much higher quantum yields are found for more dilute solutions (*vide infra*).

In order to explain the difference in photophysics for **33** and **34**, the frontier orbitals for each can be considered. DFT calculations exhibit a clear difference between the distribution of the calculated frontier orbitals; for Pt(1-diqb)Cl, **33**, the LUMO is evenly distributed over the entire terdentate ligand, whereas for **34** the density is concentrated on the outer quinolyl units with virtually no localisation on the central phenyl ring. This ensures much better overlap of the frontier orbitals in **33** and a very distinct separation of the HOMO and LUMO for **34**, producing different photophysical characteristics. The higher quantum yield for **34** can be explained by the increased metal contribution to the HOMO (see Table 4.2), which

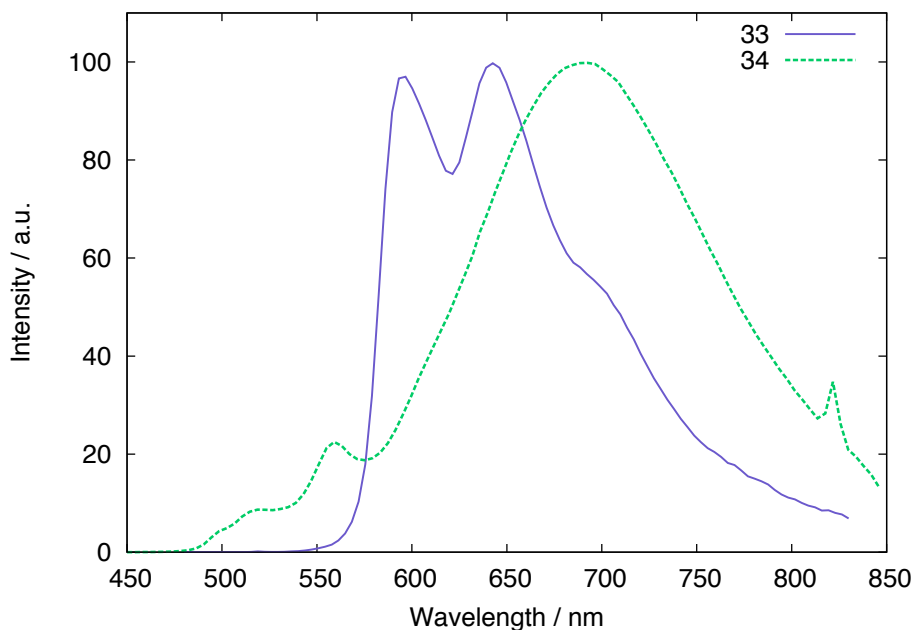


Fig. 4.5 Luminescence emission spectra of the Pt(N[^]C[^]N) complexes **33** in CH₂Cl₂ at 298 K, following excitation into the lowest energy absorption band; Excimeric behaviour can be seen for **34** (*vide infra*). Each spectrum is normalised to set the maximum intensity to 100.

Table 4.5 Luminescence data for N[^]C[^]N-coordinated complexes containing five-membered chelates at 298 K in CH₂Cl₂ and 77 K in an EPA glass.

Complex	298 K			77 K	
	$\lambda_{\max}/\text{nm}^a$	$\tau/\mu\text{s}$ deg(aer) ^b	$\Phi_{\text{lum}} \times 10^2$ ^c	λ_{\max}/nm	$\tau/\mu\text{s}$
33	595, *642	4.3 (3.6)	9.0	*586, 604sh, 635, 695	5.8
34	559, *668	30 (0.67)	28	412, 527, *556, 598, 655br	132
36^d	585sh, *612	5.5	–	–	–

^a λ_{\max} value denoted by *. ^b Lifetimes in degassed and aerated solution.

^c Quantum yields measured using [Ru(bpy)₃]²⁺ as a standard.

^d Data from ref²⁵⁰; full data unavailable.

leads to higher SOC that promotes phosphorescence.

In contrast with the remainder of the platinum(II) compounds, concentration-dependent behaviour is observed for Pt(3-diqb)Cl, **34** (Fig. 4.6). Excimeric effects, as described in Chapter 1, are likely in flat molecules such as **34**, as they are more likely to undergo dimeric interactions due to their ability to align themselves in stacks with $\pi - \pi$ interactions between molecules. Two distinct emission bands are seen on varying the concentration of **34** in CH₂Cl₂; monomer emission is seen in all spectra, appearing as a peak at 559 nm, and at low concentrations (0.34×10^{-5} mol

dm⁻³ and 0.2×10^{-5} mol dm⁻³), only monomeric peaks are seen. As concentration increases an excimer forms and grow-in of a broad band centred at ca. 668 nm occurs. The effect can be assigned as excimeric emission owing to concentration-independent absorption and emission decay kinetics. The decay measured at the site of monomeric emission occurs almost instantaneously (dependent only on the spectral response of the detector), whilst the decay measured at the site of excimeric emission shows an initial grow-in before decay occurs (Fig. 4.7). This delay corresponds to the time taken for formation of the excimer once excitation has taken place.²⁵¹

Self-quenching causes the emissive lifetime to increase as concentration decreases, such that for the most dilute solution (0.2×10^{-5} mol dm⁻³) $\tau = 83 \mu\text{s}$, and the quantum yield of 0.67 measured at this concentration is much higher than seen for the more concentrated samples. In aerated dilute solution the lifetime is 775 ns for **34**, therefore such a large difference between the two values suggests there could be potential for use as an oxygen sensor.^{252,253}

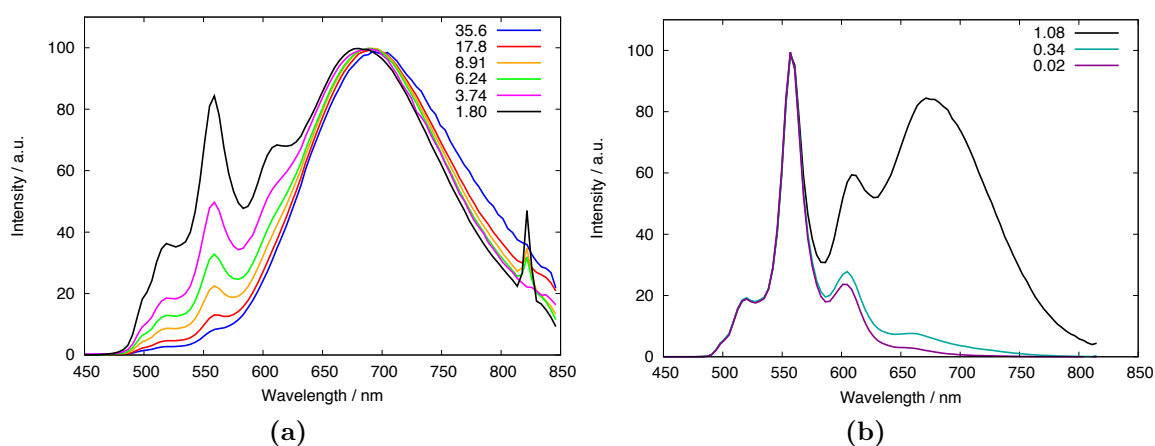


Fig. 4.6 Luminescence emission spectra of Pt(3-diqb)Cl, **34** in CH₂Cl₂ at 298 K at differing concentrations to illustrate monomer ($\lambda_{\text{max}} = 559$ nm) and excimer ($\lambda_{\text{max}} = 668$ nm) emission. Concentrations $\times 10^{-5}$ mol dm⁻³, $\lambda_{\text{ex}} = 411$ nm. (a) spectra normalised to set the maximum intensity to 100 and (b) Low concentration spectra exhibit monomer emission only (0.34 and 0.2×10^{-5} mol dm⁻³).

Emission spectra at 77 K are highly structured (Fig. 4.8), with emission for **34** resembling the monomeric emission seen at low concentrations rather than that of the excimer. Emission decay lifetimes are $5.8 \mu\text{s}$ and $132 \mu\text{s}$ for **33** and **34**, respectively, which are in line with values reported very recently by Li *et al.*¹⁹² ($5.7 \mu\text{s}$ and $109 \mu\text{s}$, respectively). Long lifetimes of over $100 \mu\text{s}$ are also seen for the majority of the six-membered complexes discussed hereafter (Section 4.2.4).

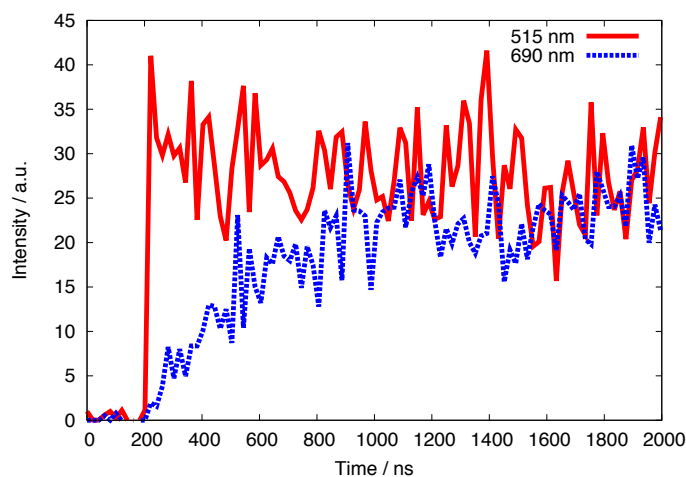


Fig. 4.7 Temporal evolution of intensity of monomeric (red) and excimeric (blue) for Pt(3-diqb)Cl, **34** at a concentration of $3 \times 10^{-4} \text{ mol dm}^{-3}$. Delayed emission is seen for the excimeric region (690 nm) due to non-instantaneous formation of the excimer

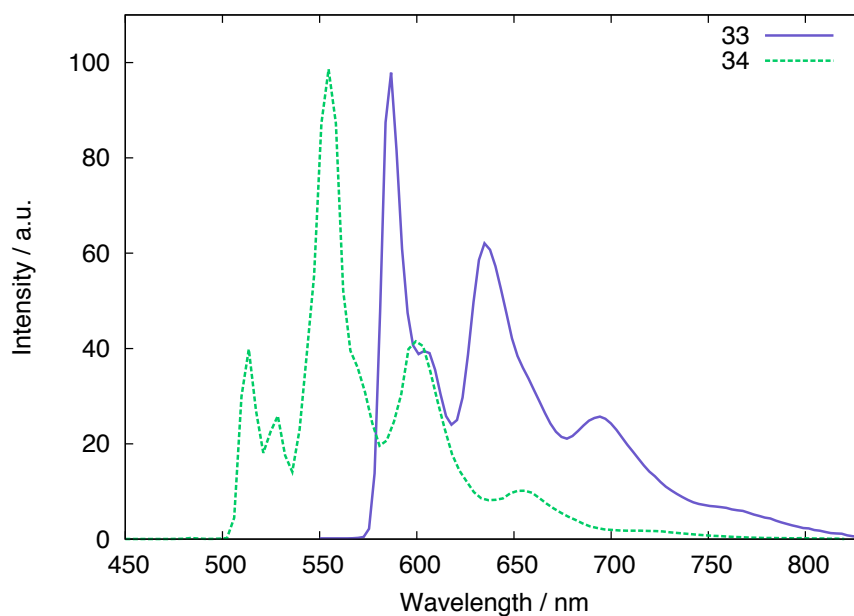


Fig. 4.8 Luminescence emission spectra of the Pt(N[^]C[^]N)Cl complexes **33** and **34** in an EPA glass at 77 K; each is normalised to set the maximum intensity to 100.

4.2 Platinum complexes containing six-membered chelate rings

As discussed in Chapter 1, Thummel *et al.* reported the complex [Pt(phenq)Cl]⁺ (4.9a), containing a ligand based upon 1,10-phenanthroline (phen), that could form six-membered rings with platinum(II). This compound displayed much higher quan-

tum yields than standard tpy complexes.¹²² Platinum complexes with terdentate bis(2-pyridylimino)isoindolate derivatives published by Chen *et al.*¹²⁵ and Thompson *et al.*¹²⁷ (based upon the motif in Fig. 4.9b), exhibit relatively weak luminescence or are non-emissive in solution at room temperature, as is $[\text{Pt}(\text{tpy})\text{Cl}]^+$, but acetylide adducts and substituted systems have quantum yields reaching several percent. Cyclometallated platinum complexes published by Huo *et al.* containing six-membered chelate rings show impressive quantum yields (up to 0.56) and longer lifetimes for the acetylide adducts of their compounds in solution, but the chloride complexes are emissive only in the solid state (4.9c).¹²³

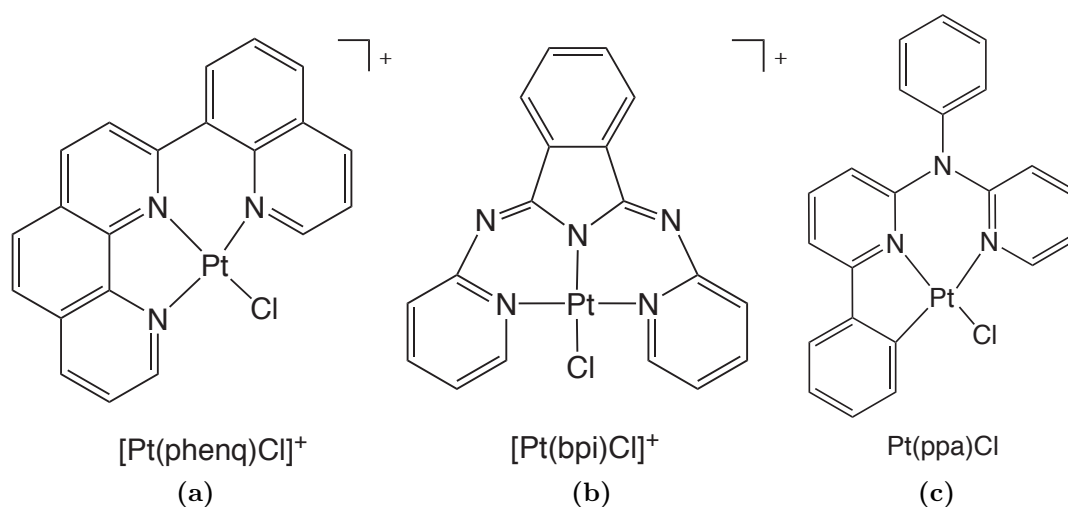


Fig. 4.9 Pt(II) complexes reported in the literature that contain six-membered chelate rings.^{122,123,125,127}

This section will discuss complexes synthesised in this work that are based upon 8-quinoline-containing ligands, which are able to form Pt(II) complexes incorporating six-membered chelates. A series containing cyclometallating $\text{N}^+\text{C}^-\text{N}^-$ and $\text{N}^+\text{C}^+\text{C}^-\text{N}^-$ -coordinating ligands (Fig. 4.10), and a second series incorporating neutral $\text{N}^+\text{N}^+\text{N}^-$ -coordinating ligands (Fig. 4.11), will be presented.

4.2.1 Computational studies

Computational calculations were carried out using the methods described in Chapter 3 (Section 3.1.1) and the results compare favourably with those presented in the literature for similar square planar platinum compounds containing six-membered chelated structures.^{123,125} The most notable feature of the optimised geometries is the significant twist of the ligands to maintain a square planar geometry about the metal centre. This observation is reinforced in physical data, in the form of the

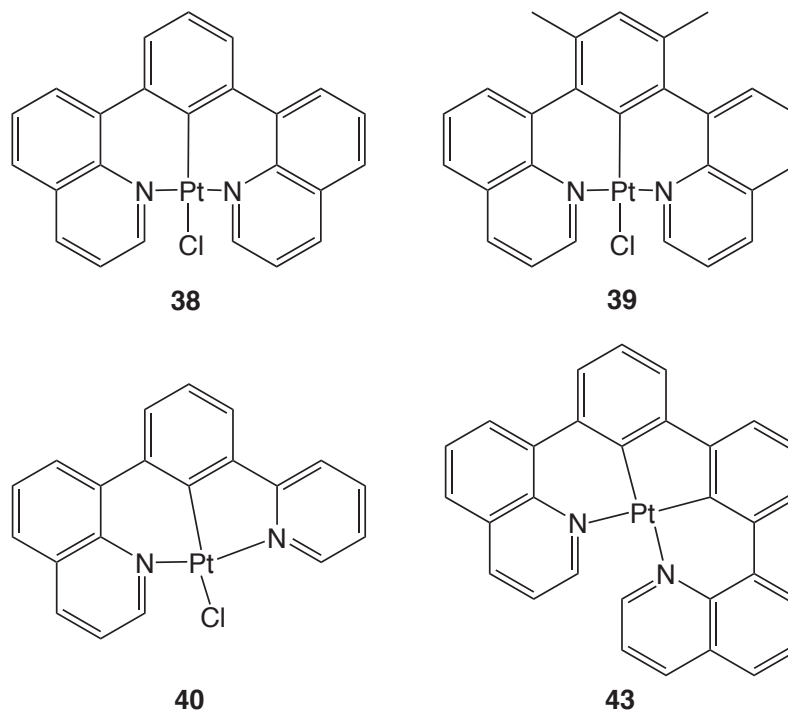


Fig. 4.10 Structures of the cyclometallated platinum complexes containing six-membered chelate rings prepared during this work.

molecular crystal structure of Pt(8-dqMeb)Cl, **39**, (Fig. 2.22), which aptly demonstrates the helical twist of the terdentate ligand to coordinate with angles approaching 90° about the Pt(II) centre. A direct comparison of the calculated optimised structure by energy minimisation, and the solid-state structure as determined by X-ray diffraction, can be made, indicating the accuracy of the DFT calculations in predicting the distortion of the terdentate ligands (Fig. 4.12c). Bond lengths for the calculated structure compare favourably with the molecular structure.

The calculated structures of the cyclometallated complexes are similar to one other in nature (Table 4.6), although the asymmetry present in **40** forces the lateral rings of the ligand to twist in a different manner to that of the symmetric compounds, so as to achieve the favoured linear binding. The pyridine is displaced only slightly from the plane of the central phenyl ring, as is found in calculations for the five-membered chelate species, with the result that the *trans* N-Pt-N bite angle is not so favourable. The complex containing the tetradentate ligand bqbpH, **43**, has the lowest interplanar twist angle of this series, and due to the geometry constraints enforced by the six-membered–five-membered–six-membered chelate arrangement, the *trans* N-Pt-N angle is significantly less, at 167.3° , than the species containing two six-membered chelate rings only (178.5° , therefore very close to the ideal of 180°).

Optimised structures for the N[^]N[^]N-coordinated Pt(II) systems containing six-

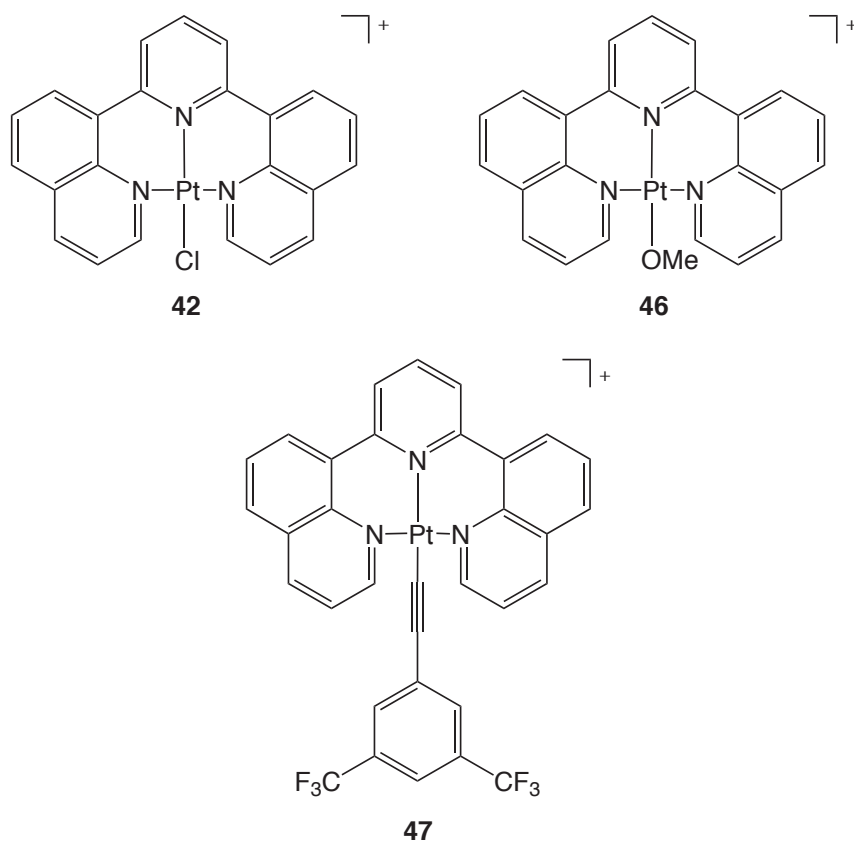


Fig. 4.11 Structures of the $N^{\wedge}N^{\wedge}N$ -coordinated platinum complexes containing six-membered chelate rings prepared during this work.

membered chelate rings were calculated using energy minimisation and are shown in Table 4.7, together with geometric data. These complexes are all based upon dqp, **17** and are calculated to be highly twisted to attain square planar geometry, as demonstrated in the crystal structure of $Pt(dqMeb)Cl$, **39** (Fig. 2.22). Fundamentally, it can be seen that in each case, the bite angle of the ligand is very close to the ideal of 180° , implying that the strategy of utilising ligands that form six-membered rings to achieve a square planar platinum system is a successful one. For the complexes in which significant deviation from linearity of the $N-Pt-N$ bite angle occurs, *i.e.* $Pt(qpyb)Cl$, **40**, $Pt(bqbph)$, **43** and $[Pt(dqp)OMe]^+$, **46**, this is caused by a displacement of the metal ion towards the central ring, such that $N^{cen}-Pt-N^{lat} > 90^\circ$ (denoting central and lateral respectively) in contrast to the effect seen for terpyridyl compounds.⁸⁷

Essentially the results present the same picture as for the compounds discussed in Section 4.1, showing a similar dispersion of the frontier orbitals, with the HOMO largely residing on the central core of the molecule and the LUMO delocalised over the terdentate ligand (Table 4.8). The HOMO is composed largely of metal and ancillary ligand orbitals, with only a small proportion originating from the terden-

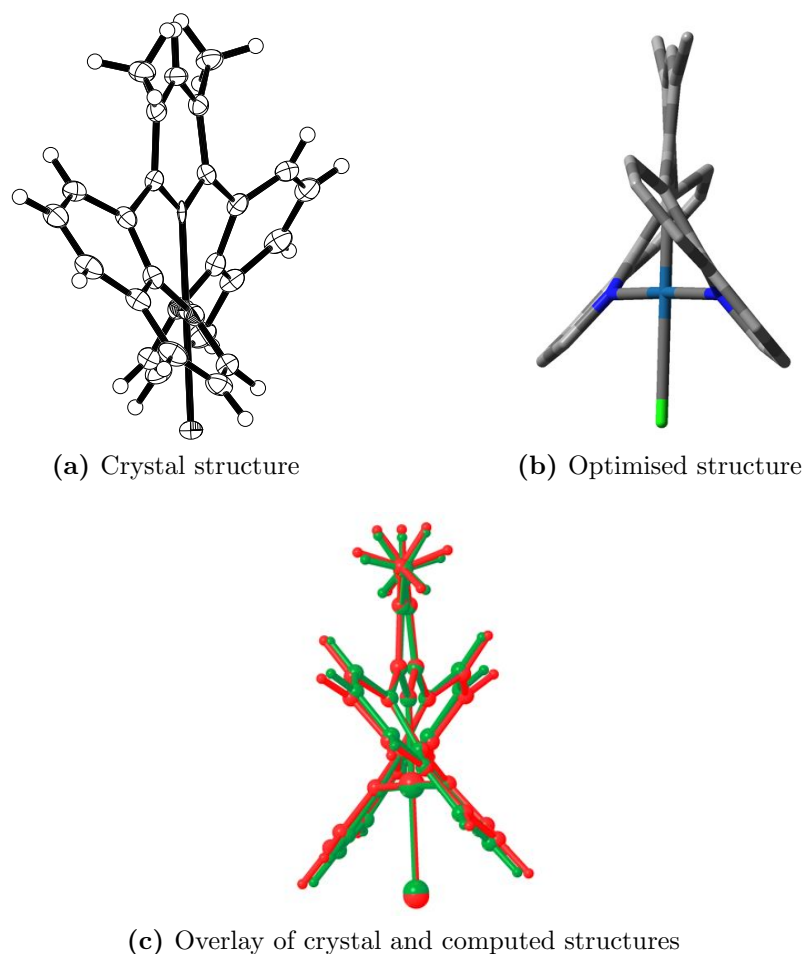
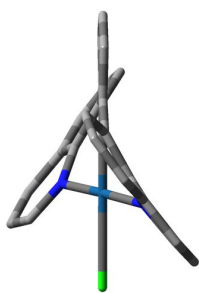

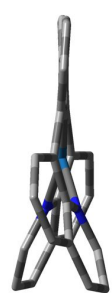


Fig. 4.12 Comparison of the crystal structure of Pt(8-dqMeb)Cl, **39** and the optimised structure by energy minimisation DFT calculations.

tate/tetradentate ligand. Conversely, the LUMO in each case is widely distributed over the cardinal ligand, as is typical of this class of compounds, with the percentage proportion of electron density situated on the terdentate or tetradentate ligand being $\geq 90\%$ for each of the complexes. Orbital plots showing the HOMO-2, HOMO-1, LUMO+1 and LUMO+2 orbital contributions are presented in Appendix B.

Orbital plots for the HOMO and LUMO of the terdentate N[^]C[^]N-coordinated complexes **38**, **39** and **40** are shown in Fig. 4.13. As would be expected, given that DFT studies frequently disregard minor substituents when optimising structures, the HOMO and LUMO plots for **38** and its dimethylated analogue **39** are virtually indistinguishable, with the methyl groups playing no role in these orbitals, although they do impart a contribution to other frontier orbitals. The localisation of the HOMO on the central portion of the complexes and the dispersion of the LUMO over the dqb ligand resembles that of the related complex Pt(dpyb)Cl.^{107,108,248} For the case of Pt(qpyb)Cl, **40**, a marked difference is observed owing to the asymmetry

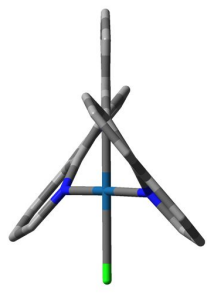
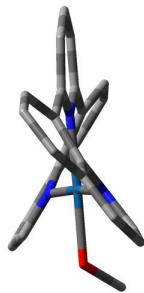
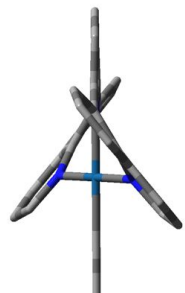
Table 4.6 Optimised structures of the N[^]C[^]N complexes as predicted by energy minimisations using DFT, oriented to best show the twist in the ligand and the planarity at the metal centre (for clarity, hydrogen atoms are not shown).

Complex	38	40	43
			
Interplanar angle / °	33.4	81.6 ^a 92.2 ^b	22.4 ^a
Trans N–Pt–N angle °	178.5	173.2	167.3
Lateral N–Pt bond length / Å	2.06	2.05	2.16
Central Pt–N bond length / Å	1.99	1.97	2.00

^aData for planes of lateral quinoline and central phenyl rings

^bData for planes of lateral pyridine and central phenyl rings

Table 4.7 Optimised structures of the N[^]N[^]N complexes as predicted by energy minimisations using DFT, oriented to best reveal the twist in the ligand and the planarity at the metal centre; **47** is cropped to focus on the square planar segment (for clarity, hydrogen atoms are not shown).

Complex	42	46	47
			
Interplanar angle/°	38.5	30.4	35.1
Trans N–Pt–N angle/°	178.8	174.9	179.7
Lateral N–Pt bond length/Å	2.05	2.05	2.06
Central Pt–N bond length/Å	2.03	2.05	2.08

of the complex, although the same basic principles apply. The striking difference is the lack of orbital contribution from the pyridyl fragment of the terdentate ligand, particularly in the LUMO, where a notable contribution would be predicted based upon previous findings for pyridyl systems such as Pt(dpyb)Cl¹⁰⁶ and the asym-

metric pyridyl/pyrazolyl-containing complex published by our group (Fig. 1.26b) whereby the LUMO is localised on the pyridyl fragment as opposed to the pyrazole.¹¹²

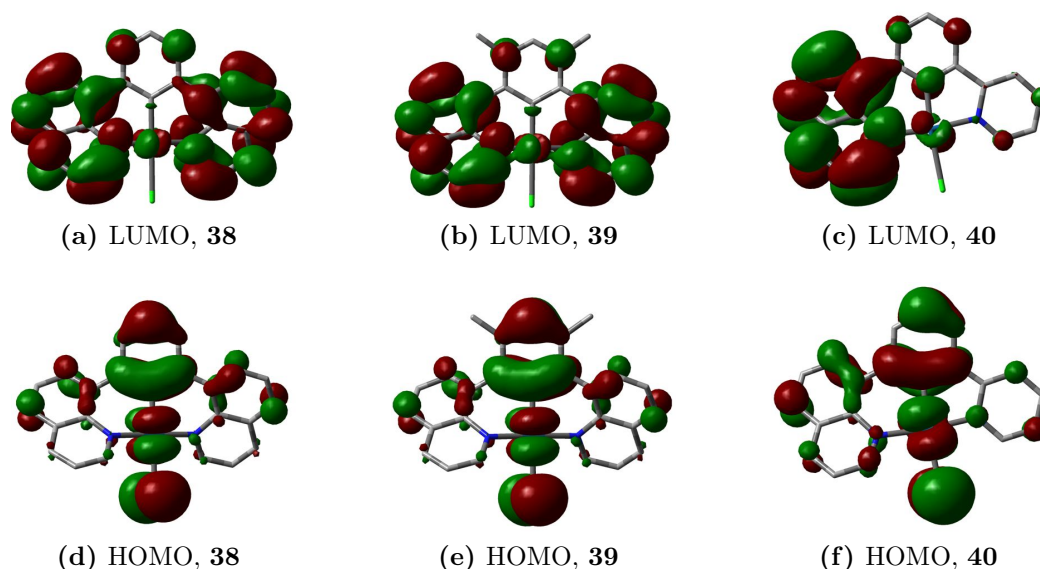


Fig. 4.13 Frontier orbital plots of **38**, **39** and **40** calculated by TD-DFT.

DFT calculations for the complex containing the terdentate ligand bqbp, **43**, present a somewhat different picture to that of the complexes with terdentate ligands (Fig. 4.14). At the basic level, the LUMO comprises ligand orbitals, with only a 1 % contribution from the metal centre whereas the HOMO is composed of a combination of metal and ligand orbitals, as seen previously. However, the platinum(II) ion is less involved in the HOMO than for the other six-membered chelated complexes, due to a higher contribution from the two central phenyl rings of the ligand. This suggests a movement of electrons resulting in creation of a dipole, which would be borne out in a solvatochromic shift of the optical bands. Unfortunately however, owing to purification and solubility problems with this complex, a thorough treatment of its physical properties could not be carried out.

Frontier orbital plots for the N[^]N[^]N[^]-coordinated platinum complexes are shown in Fig. 4.15. The percentage densities for the HOMO and, even more obviously, the HOMO–1, for these species differ according to the ancillary ligand. A much higher degree of electron density is proportioned on the ancillary ligands of **46** and **47** than in the chloride complex. A key difference between the frontier orbitals calculated for the neutral and charged complexes is the participation of the central phenyl ring of the cyclometallated species, compared to the pyridine ring of the dqp complexes. In cyclometallated complexes this central ring has a contribution towards the HOMO

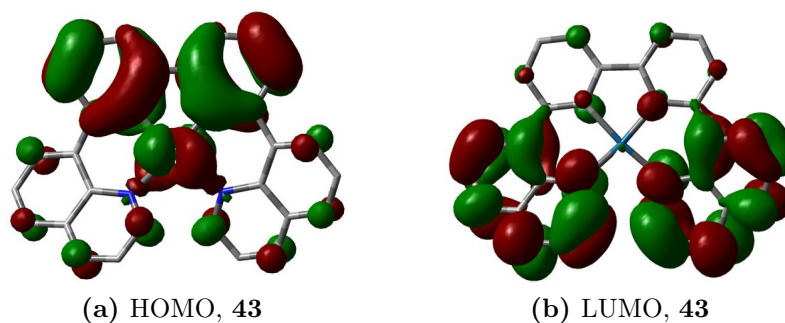


Fig. 4.14 Frontier orbital plots of the tetradentate-bound complex **43**.

not observed for the cationic complexes, due to the increased electron density available on deprotonation of the cyclometallating carbon. Conversely, as seen in studies of Pt(dpyb)Cl and its derivatives,^{107,108} the phenyl fragment contributes little to the LUMO, with electron density localised on the quinoyl units.

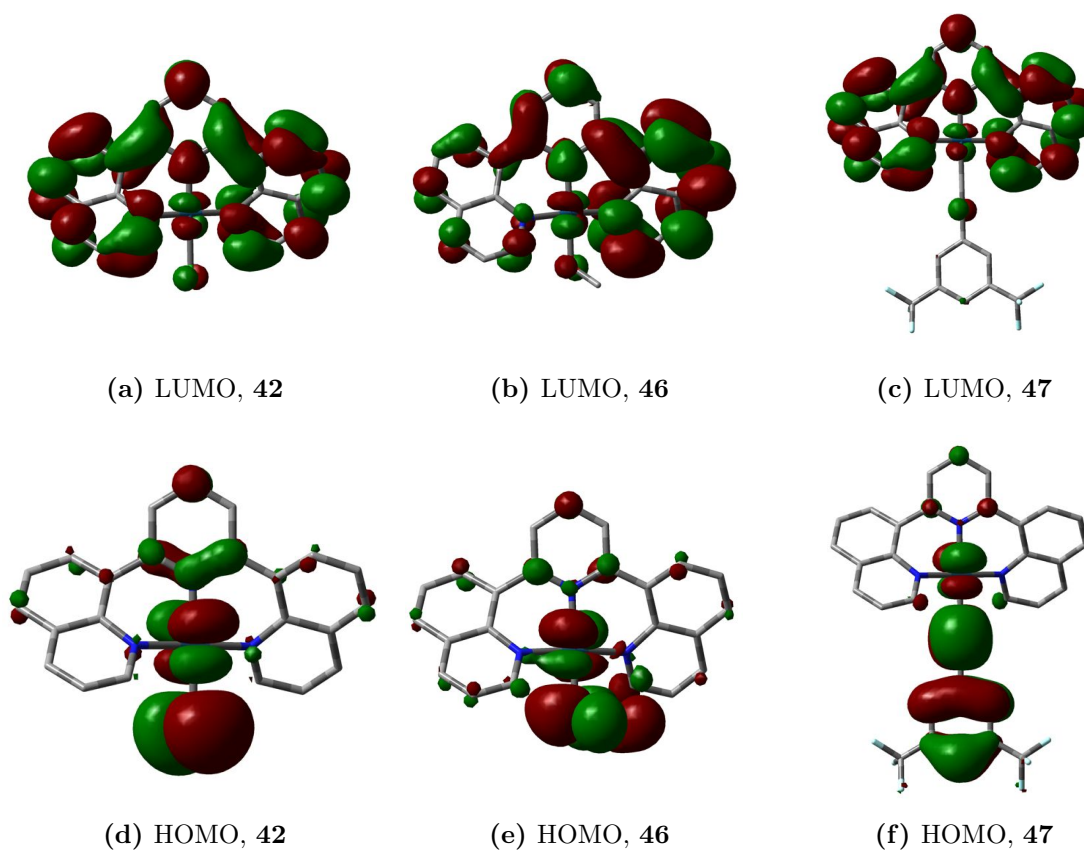


Fig. 4.15 Frontier orbital plots of **42**, **46** and **47** calculated by TD-DFT.

TD-DFT calculations were also performed on the complexes to abstract information about the transitions between ground and excited states. The electron densities for the three highest-energy occupied orbitals and the three lowest-energy unoccu-

pied orbitals are summarised in Table 4.8. These confirm the MLCT nature of the transitions between these key orbitals, as will be demonstrated by the photophysical measurements. These results provide the oscillator strengths for transitions to the lowest-energy excited states, and it can be seen that the HOMO-LUMO transition is the most important transition for these complexes, though there are notable contributions from the range of orbitals between the HOMO-5 and LUMO+5, as is typically seen for complexes with mixed LC and CT excited states.

Table 4.8 Molecular orbital characteristics of complexes containing six-membered chelate rings, as calculated by TD-DFT; figures represent the percentage proportion of electron density residing at that site.

Complex	Constituent	HOMO-1	HOMO	LUMO	LUMO+1
[Pt(8-dqb)Cl] 38	Pt	76	55	4	4
	Ter ^a	24	40	96	96
	Anc ^b	0	5	0	0
Pt(8-dqMeb)Cl 39	Pt	64	44	4	4
	Ter	36	52	96	96
	Anc	0	4	0	0
Pt(qpyb)Cl 40	Pt	87	58	3	4
	Ter	11	37	97	96
	Anc	2	5	0	0
Pt(bqbph) 43	Pt	45	39	1	8
	Tet ^c	55	61	99	92
[Pt(dqp)Cl] ⁺ 42	Pt	21	20	2	2
	Ter	79	55	98	98
	Anc	0	25	0	0
[Pt(dqp)OMe] ⁺ 46	Pt	54	24	4	3
	Ter	12	15	95	96
	Anc	34	61	1	1
[Pt(dqp)CC-tfp] ⁺ 47	Pt	34	29	3	4
	Ter	9	7	92	89
	Anc	57	34	5	7

^a Ter denotes a terdentate ligand. ^b Anc denotes an ancillary ligand. ^c Tet denotes a tetradentate ligand.

4.2.2 Electrochemistry

Cyclic voltammetry measurements were performed on the neutral complexes **38**, **39** and **40**, and on cationic complexes **42**, **46** and **47**, under the same conditions as before: Bu₄NPF₆ (0.1 M) as the supporting electrolyte and CH₂Cl₂ or MeCN as the

carrier solvent, dependent on solubility of the complex. Data are reported relative to the standard ferrocene couple Fc/Fc^+ ($E_{1/2}^{\text{ox}} = 0.40 \text{ V vs SCE}$)²²⁹ under the same conditions (Table 4.9). Peaks for the dimethylated complex **39** and the asymmetric complex **40** were poorly defined and not clearly identifiable, so are not presented here. The data for the remaining six-membered chelated complexes are presented in Table 4.9, together with TD-DFT data for this series of complexes. Each complex shows an irreversible oxidation in the region 0.6–0.8 V, tentatively attributed to a metal-based oxidation process. DFT supports the notion that the metal is involved in the oxidation process since the HOMO is composed largely of metal and ancillary ligand orbitals.

Table 4.9 Electrochemical data and the predominant character and energy of the lowest-lying singlet states as determined by TD-DFT.

Complex	Lowest S state	E/eV [λ/nm]	E_{ox}^0/V ^a	$E_{\text{red}}^0/V(\Delta/mV)$ ^a
$[\text{Pt}(\text{tpy})\text{Cl}]^+$	–	–	–	–1.24(70), –1.82(70) ^b
$\text{Pt}(\text{dpyb})\text{Cl}$	–	–	0.35 ^c	–2.14 ^{c,d}
38	HOMO→LUMO	2.61 [475]	0.62 ^d	–1.57 (80), –2.26 (160)
39	HOMO→LUMO	2.53 [490]	d ^e	d ^e
40	HOMO→LUMO	2.54 [488]	e	e
42	HOMO→LUMO	2.99 [415]	0.67	–1.27 (70), –1.82 (70)
43	HOMO→LUMO	2.06 [603]	f	f
46	HOMO→LUMO	2.44 [508]	0.77	–1.41 (120), –1.98
47	HOMO→LUMO	2.45 [506]	0.78	–1.49 (100), –1.66

^a In MeCN except where stated otherwise, using Bu_4NPF_6 as an electrolyte. Peak potentials are given for the irreversible oxidations and second reductions (ill-defined return wave). For the pseudo-reversible reductions, values refer to $E_{1/2}$ and the peak-to-peak separation is given in parentheses.

^b Data from refs⁸⁷ and⁸⁹. ^c Data from ref¹⁰⁶; in CH_2Cl_2 , using Bu_4NPF_6 as an electrolyte. ^d In CH_2Cl_2 . ^e No defined peak was observed within the scanning range (–2.3–1.3 V). ^f Computational data presented only, due to difficulty obtaining a pure sample for CV.

Voltammograms of the cyclometallated species were difficult to obtain due to ill-defined peaks. Reproducible CV waves for **38**, the analogue of the parent $\text{N}^-\text{N}^-\text{N}$ complex, were obtained in CH_2Cl_2 , owing to poor solubility in MeCN. An irreversible oxidation and two reduction waves were observed. A quantitative comparison of the complexes is undermined by the use of a different solvent but the overall trend can be noted. All the potentials are shifted to more negative values, consistent with the more electron-rich character of a neutral complex containing a formally anionic donor.

Terpyridine-based reduction is well-established^{87,89,254} and the cationic complexes

42, **46** and **47** display two pseudo-reversible reductions in the cyclic voltammograms similar to that seen for $[\text{Pt}(\text{tpy})\text{Cl}]^+$. TD-DFT calculations establish that the LUMO and LUMO+1 are based almost exclusively on the terdentate ligands, with virtually no contribution from the platinum(II) ion, suggesting that the reduction processes involve π^* orbitals of dqp.

4.2.3 Absorption spectroscopy

All Pt(II) complexes adhere to the Beer-Lambert law at low concentrations. Each complex displays a set of high-energy bands (<280 nm), which can, in part, be attributed to LC π - π^* transitions. This assignment is based on analogy with related polypyridyl complexes as well as the appearance of these bands in the same region of the spectrum for each complex, inclusive of **47** and **48**, and therefore regardless of the ancillary ligand present. The profile at lower energies is dependent on the ligands present and they can be categorised accordingly. Data for all six-membered chelate-containing complexes are presented in Table 4.10

4.2.3.1 N[^]C[^]N-coordination: Pt(8-dqb)Cl, **38**, Pt(8-dqMeb)Cl, **39** and Pt(qpyb)Cl, **40**.

The absorption spectra for Pt(dqb)Cl, **38** and the disubstituted derivative **39** are structured in nature, with a prominent band at lower energy ($\lambda_{\text{max}} = 416$ nm and 423 nm, respectively) that is not observed for the N[^]N[^]N-coordinated complexes (Fig. 4.16). This agrees with computational data which predicts a higher energy HOMO due to increased electron density on the central cyclometallating ring, and also with TD-DFT calculations that predict a lower S_1 energy, and therefore a shift towards absorption in the red region of the visible spectrum. This band also displays a larger degree of negative solvatochromism than for the other bands seen, both in these, and the cationic compounds.

Notably, there is no evidence for any direct S \rightarrow T transition bands at lower energies, corresponding to direct (formally forbidden) triplet excitation, as is seen in Pt(dpyb)Cl and its derivatives.¹⁰⁶ The dpyb-based complexes show weak low-energy bands (ϵ ca. $200 \text{ M}^{-1} \text{ cm}^{-1}$) due to spin-orbit coupling (SOC) enhanced by the presence of the heavy metal ion. Absorption for the asymmetric complex Pt(qpyb)Cl, **40** is a shallower curve with less defined peaks. It was hypothesised that it should resemble an admixture of the symmetric compounds containing 2-pyridyl and 8-quinolyl groups, Pt(dpyb)Cl and Pt(8-dqb)Cl respectively, which is true to some extent: **40** absorbs at approximately the same wavelengths as the

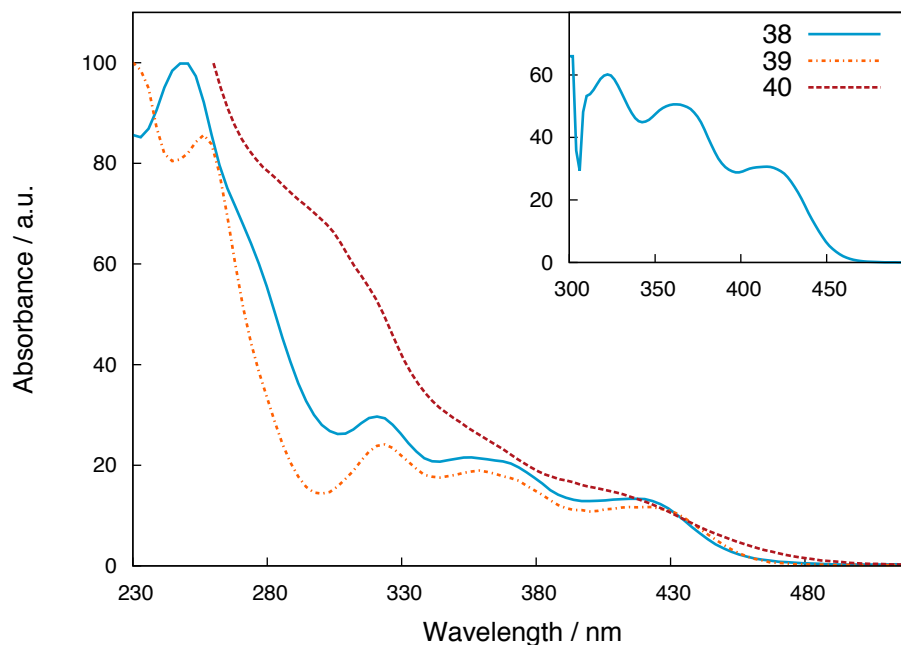


Fig. 4.16 UV-visible absorption spectra of the Pt(N[^]C[^]N) complexes **38**, **39** and **40** at 298 K in CH₂Cl₂; each is normalised to set the maximum intensity to 100. Inset: Excitation spectrum of **38**.

compounds incorporating symmetric ligands and the opposing peaks and troughs cancel to produce a shallow wave with little definition (Fig. 4.17).

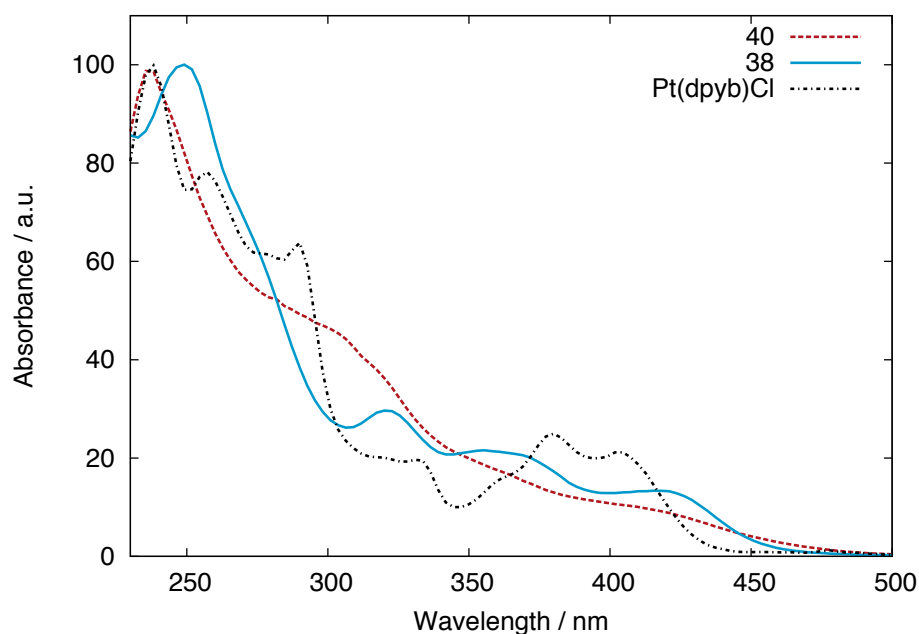


Fig. 4.17 UV-visible absorption spectra of the asymmetric complex **40** compared to the symmetric species; all spectra recorded in CH₂Cl₂ at 298 K; each is normalised to set the maximum intensity to 100.

4.2.3.2 N[^]N[^]N-coordination: [Pt(dqp)Cl]⁺, **42**, [Pt(dqp)OMe]⁺, **46** and [Pt(dqp)CC-tfp]⁺ **47**.

The N[^]N[^]N-bound Pt(II) complexes display an envelope of absorption bands at ca. 350 nm, which shows very little negative solvatochromism. This is likely attributable to charge-transfer (CT) transitions involving metal and/or ancillary ligand orbitals, as reinforced by DFT studies and comparison with similar platinum imine compounds.^{89,255,256} TD-DFT calculations support the assignment of a mixture of LC and CT transitions, by revealing the lowest excited singlet state to be that of the HOMO→LUMO transition for all the six-membered chelate-containing complexes (Table 4.9), therefore it is appropriate to consider the frontier orbitals as being the key orbitals concerned with regard to emission spectroscopy. The electron density representations computed by DFT studies infer a large CT component from d(Pt)/π(X)→π*(N[^]N[^]N), which concurs with the lack of solvatochromism observed, as charge transfer for this transition is in an outward motion from the central core of the molecule to the outer quinolyl units, as opposed to in a dipolar moment across the molecule.

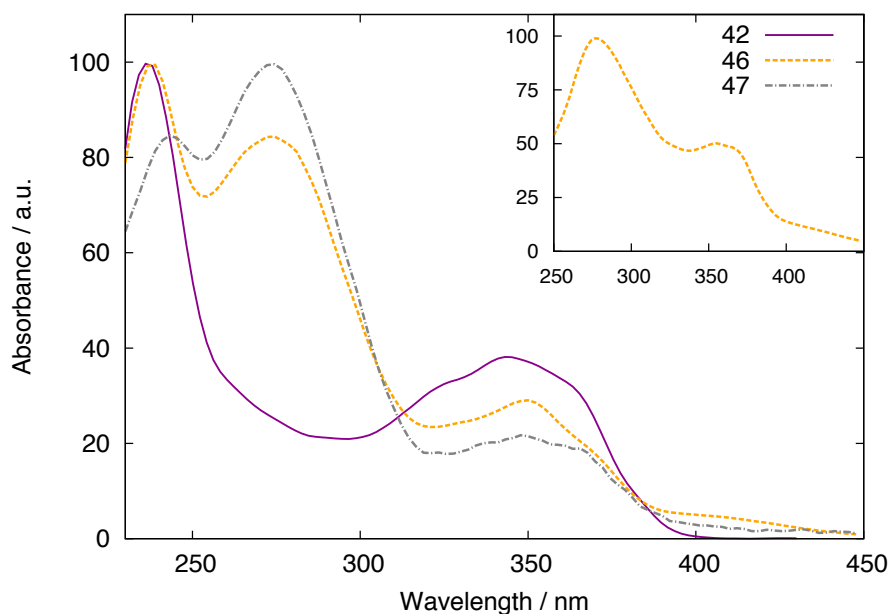


Fig. 4.18 UV-visible absorption spectra of the Pt(N[^]N[^]N) complexes **42**, **46** and **47** in CH₂Cl₂ at 298 K; each is normalised to set the maximum intensity to 100. Inset: Excitation spectrum of **46**.

The absorption spectra of the methoxide and acetylide derivatives, **46** and **47**, have similar profiles to each other, with a more structured profile than the parent compound. An additional band is seen in the high energy region of the absorption spectrum for **46** and **47**. The lowest energy bands extend further into the red region

for the metathesis products, with an obvious tail present for **46**, and, although less clear-cut for **47**, there is a suggestion of an extension of the absorption into longer wavelengths for this compound too, as would be expected for the two stronger σ -donor ancillary ligands. The energy of the CT states will be lowered, and the maximum of the main band is shifted by 7 nm, from 343 nm for **42**, to 350 nm for both **46** and **47**.

The energies of the lowest excited singlet states (S_1) are given in Table 4.9, which are underestimated compared to the experimental values, but the qualitative trends are informative. For example, the difference between the lowest energy bands for the methoxide derivative, **46** (a shoulder at $\lambda = 405$ nm) and the parent complex **42** ($\lambda = 347$ nm), is equivalent to an energy difference of 4400 cm^{-1} , corresponding exactly to the calculated energy difference of the lowest singlet state of 0.54 eV , (4400 cm^{-1}). The possibility of the low energy band for these species being due to a dimer or aggregate can be discounted for two reasons: firstly, the profile of the absorption spectrum is not concentration dependent, and secondly, the bands also appear in the luminescence excitation spectrum (see inset of Fig. 4.18), which closely resembles the absorption spectrum.

Table 4.10 Ground state UV-visible absorption properties at 298 K in CH_2Cl_2 .

Complex	$\lambda_{\text{max}}/\text{nm}$ ($\epsilon/\text{M}^{-1}\text{ cm}^{-1}$)
$[\text{Pt}(\text{tpy})\text{Cl}]^+$	305, 320, 340, 390, 403 ^a
$\text{Pt}(\text{dpyb})\text{Cl}$	332 (6 510), 380 (8 690), 401 (7 010), 454 (270), 485 (240) ^b
38	249 (228,813), 320 (67 500), 356 (49 900), 420 (31 500)
39	232 (19 810), 257 (15 848), 323 (5 469), 359 (4 263), 419 (2 656)
40	302 (10,885), 349 (5 769), 405 (3,377)
42	240 (67 200), 327sh (23 200), 347 (26 100)
46	274 (81 400), 350 (28 500), 405 (4 860)
47	239 (64 700), 271 (34 300), 349 (24 200), 364 (21 500)

^a Data from ref^{87,89}. ^b Data from ref¹⁰⁶.

4.2.4 Emission spectroscopy

4.2.4.1 N[^]C[^]N-coordination: $\text{Pt}(\text{8-dqb})\text{Cl}$, **38**, $\text{Pt}(\text{8-dqMeb})\text{Cl}$, **39** and $\text{Pt}(\text{qpyb})\text{Cl}$, **40**.

All three cyclometallated complexes show room temperature luminescence in CH_2Cl_2 solution at 298 K with broad emission profiles (Fig. 4.19). Complexes **38** and **39** follow the same shaped curve very closely, with little deviation found due to the methyl groups, although **39** is blue-shifted with a λ_{max} value of 637 nm compared to

645 nm for the unsubstituted complex (Table 4.11, with further information in Table 4.14). Both complexes are red-shifted, in comparison to the N[^]N[^]N-coordinated complexes, whilst the asymmetric complex **40** has an emission maximum intermediate between the N[^]N[^]N-coordinated complexes and the cyclometallated complexes **38** and **39** (613 nm). Complex **38** shows a hint of vibrational structure, in the form of a shoulder, but the emission does not show the structure seen in cyclometallated species such as Pt(dpyb)Cl. The shifts between the complexes are more distinct at 77 K, where the spectral shape is very similar (Fig. 4.20). This shift can be ascribed to a lower excited state energy resulting from the destabilisation of the HOMO upon cyclometallation, as was seen for the absorption spectra.

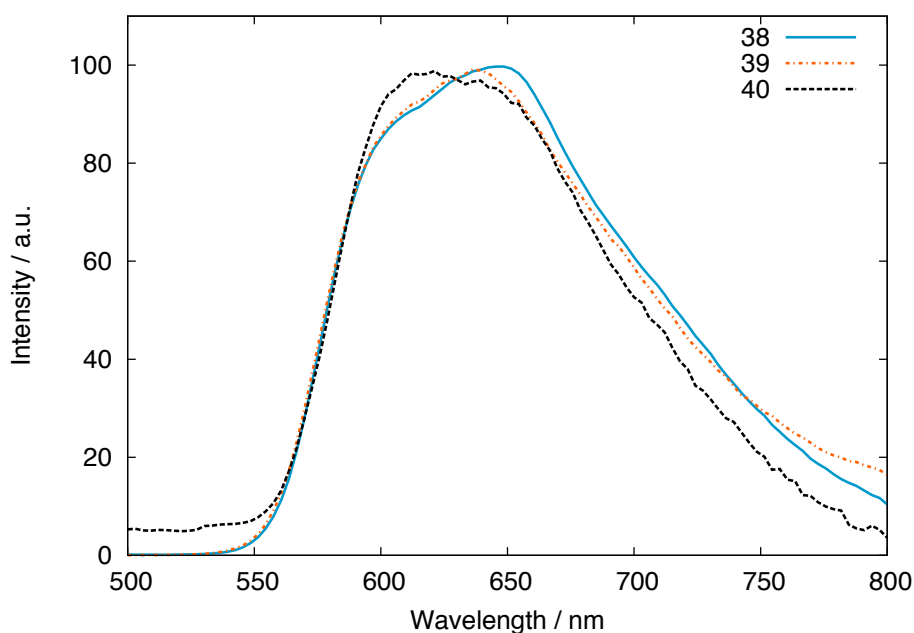


Fig. 4.19 Luminescence emission spectra of the Pt(N[^]C[^]N) complexes: **38**, **39** and **40** in CH₂Cl₂ at 298 K, following excitation into the lowest energy absorption band; each is normalised to set the maximum intensity to 100.

Quantum yields for the three cyclometallated compounds are very similar: 0.016, 0.012 and 0.012 for **38**, **39** and **40**, respectively, in degassed CH₂Cl₂. In comparison with the five-membered chelated complex Pt(dpyb)Cl, the quantum yields are substantially lower and lifetimes are longer at room temperature, owing to the decreased radiative decay constant, k_r , which is approximately two orders magnitude lower (0.8–1.2 cf. 83 for Pt(dpyb)Cl, see Table 4.14). Despite the seemingly low quantum yields found here, comparative complexes reported by Huo *et al.*, containing one six-membered and one five-membered ring were found to be non-emissive in solution at room temperature.¹²³

Preliminary DFT results from ongoing studies in our group examining a range

Table 4.11 Luminescence data for N[^]C[^]N-coordinated complexes containing six-membered chelates in CH₂Cl₂ at 298 K and in an EPA glass at 77 K.

Complex	$\lambda_{\max}/\text{nm}^{\text{a}}$	298 K		$\Phi_{\text{lum}} \times 10^{2\text{c}}$	77K	
		$\tau/\mu\text{s}$	deg(aer) ^b		λ_{\max}/nm	$\tau/\mu\text{s}$
38	611sh, *645	14 ^d	1.6		575, *626, 676sh	28
39	637	10 (0.69)	1.2		570, 585, *619, 670sh	18
40	613	15 ^d	1.2		555sh, *570	103

^a λ_{\max} value denoted by *. ^b Lifetimes in degassed and aerated solution.

^c Quantum yields measured using [Ru(bpy)₃]²⁺ as a standard.

^d Aerated emission too weak to be detected.

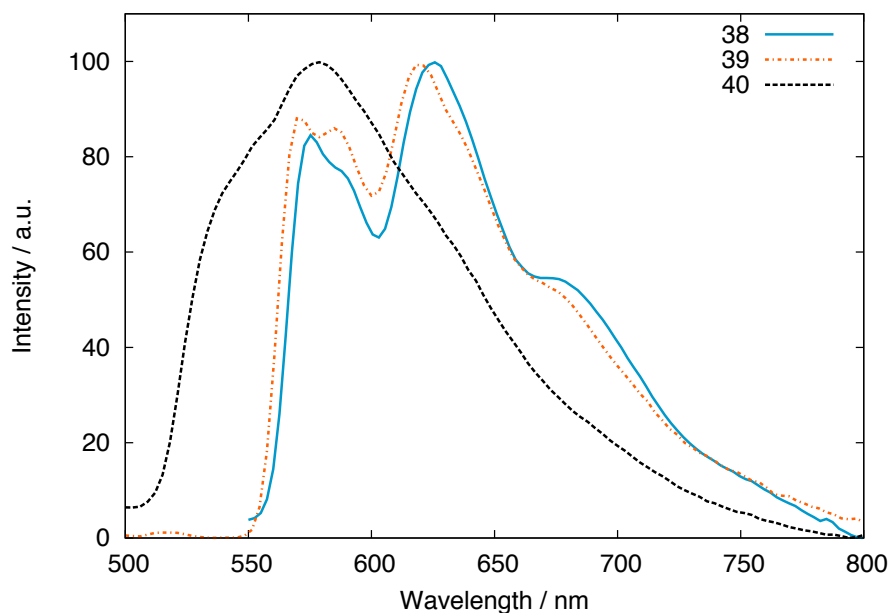


Fig. 4.20 Luminescence emission spectra of the Pt(N[^]C[^]N) complexes based on dqp: **38**, **39** and **40** in an EPA glass at 77 K; each is normalised to set the maximum intensity to 100.

of complexes containing terdentate ligands, have shown that complexes tending to lower radiative rate constants have lower spatial overlap between the frontier orbitals, and this is apparent for the cyclometallated complexes discussed here. There is a higher degree of overlap between the HOMO and the LUMO for [Pt(dqp)Cl]⁺, **42** than for Pt(dqb)Cl, **38**, which would support this observation. Orbital overlap is important when considering optical properties as spatial overlap between initial and final states is necessary for transitions to occur (Franck–Condon principle, see Chapter 1).

4.2.4.2 N[^]N[^]N–coordination: [Pt(dqp)Cl]⁺, **42**, [Pt(dqp)OMe]⁺, **46** and [Pt(dqp)CC-tfp]⁺ **47**.

All three dqp-based complexes display a broad unstructured emission profile, with λ_{max} values of 600 nm, 612 nm and 593 nm for [Pt(dqp)Cl]⁺, **42**, [Pt(dqp)OMe]⁺, **46** and [Pt(dqp)CC-tfp]⁺ **47**, respectively (Fig. 4.21). The emission shows no significant solvatochromism in THF, chloroform and MeCN with the spectra being virtually identical to that measured in CH₂Cl₂ under the same conditions. This is consistent with an outward movement of electron density from the central core to the quinolyl units, which does not result in a dipolar moment, as opposed to being from one side of the molecule to the other. Lifetimes in degassed CH₂Cl₂ at 298 K span an order of magnitude from 1.3 μs for **46**, through 16 μs for the parent compound **42**, to 33 μs for the acetylide derivative **47**.

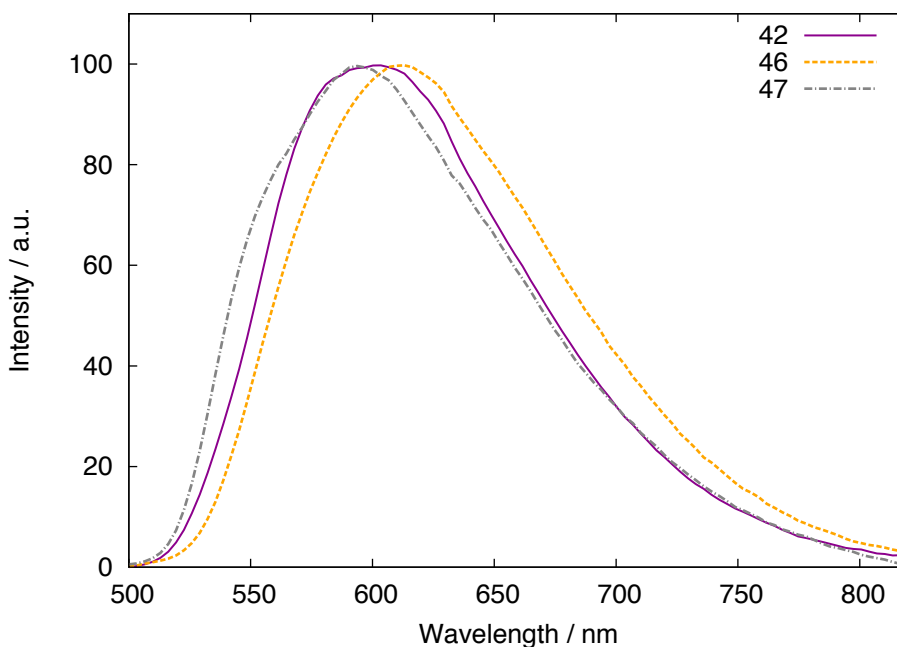


Fig. 4.21 Luminescence emission spectra of the Pt(N[^]N[^]N) complexes based on dpq: **42**, **46** and **47** in CH₂Cl₂ at 298 K, following excitation into the lowest energy absorption band; each is normalised to set the maximum intensity to 100.

Quantum yields for the complexes are in the range 0.0007–0.042 (degassed CH₂Cl₂, 298 K) and lifetimes are in the μs region for measurements both at 298 K and 77 K (Table 4.12). The quantum yield of luminescence for the parent complex [Pt(dqp)Cl]⁺, **42** is 0.036, a value comparable to that of [Ru(bpy)₃]²⁺,²⁵⁷ commonly used as a standard for calculating quantum yields, and contrasting with the lack of room temperature luminescence for [Pt(tpy)Cl]⁺ in solution at 298 K.⁸⁹ The lifetime of decay for **42** is 16 μs and no significant self-quenching was observed upon varying concentration in the range 5×10^{-6} to 10^{-4} M. The improvement in quantum yield

compared to $[\text{Pt}(\text{tpy})\text{Cl}]^+$ confirms that the inclusion of favourable six-membered chelates in $\text{N}^{\wedge}\text{N}^{\wedge}\text{N}$ -coordinated compounds has a positive impact on emission, due to increased ligand field strength and reduced non-radiative decay pathways from removal of the d-d states to higher energies.

Notably, an interesting observation with regard to $[\text{Pt}(\text{dqp})\text{Cl}]^+$, **42**, is that the quantum yield for this complex (0.036) is higher than that of the cyclometallated analogue, $\text{Pt}(\text{dqb})\text{Cl}$, **38** (0.016). However, previous investigations within our group into a six-membered chelate-containing $[\text{Pt}(\text{N}^{\wedge}\text{N}^{\wedge}\text{N})\text{Cl}]^+$ complex show that an improved bite angle leading to relief of ring strain is not the only factor to consider when looking to improve luminescent efficiency of $(\text{N}^{\wedge}\text{N}^{\wedge}\text{N})$ -coordinated species. Containing azaindolyl units instead of quinolines, platinum(7-aza-indolyl) chloride, $[\text{Pt}(\text{azai})\text{Cl}]^+$, failed to emit at room temperature and only emits weakly at 77 K. The long lifetime seen for the 77 K luminescence suggests a lower radiative constant k_r , than for the quinolyl-based complexes. DFT calculations predict a longer bond length, 2.11 Å compared to 2.05 Å for the lateral Pt–N bonds of $[\text{Pt}(\text{dqp})\text{Cl}]^+$, **42**, plausibly reducing the ligand field strength and rigidity of the system. Optimised structures are shown for $[\text{Pt}(\text{azai})\text{Cl}]^+$ in Appendix 2.

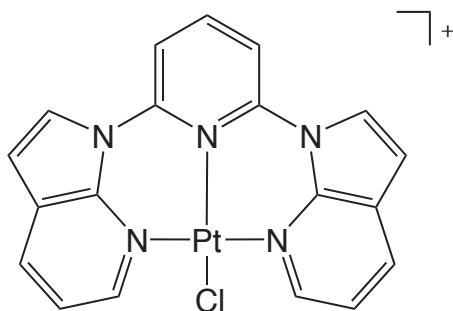


Fig. 4.22 Structure of $[\text{Pt}(\text{azai})\text{Cl}]^+$, a six-membered chelate-containing complex that does not show room temperature luminescence.

The values of k_r and Σk_{nr} obtained using the equations given in Chapter 3 (see Section 3.1.4) suggest that it is the value of the radiative decay constant, $k_r = 2.3 \times 10^3 \text{ s}^{-1}$, which limits the efficiency of luminescence, since Σk_{nr} is comparable to that of the highly emissive $\text{Pt}(\text{dpyb})\text{Cl}$ ($6.0 \times 10^4 \text{ s}^{-1}$ and $5.6 \times 10^4 \text{ s}^{-1}$, respectively). The non-radiative rate constant is, nevertheless, far lower than simple tpy based $\text{N}^{\wedge}\text{N}^{\wedge}\text{N}$ -coordinated complexes; $[\text{Pt}(\text{tpy})\text{Cl}]^+$, for example, has a Σk_{nr} value of 10^4 s^{-1} .⁸⁹ The value for k_r and the lack of low-energy absorption bands in **42**, which suggest a low oscillator strength for the lowest singlet–triplet transition $\text{S} \rightarrow \text{T}$, may be indicative of a low metal participation in the excited state. This is a common feature of complexes with a large degree of $\text{LC } ^3\pi - \pi^*$ excited state character and is reinforced in the DFT results that designate only a 20 % contribution

Table 4.12 Luminescence data for N[^]N[^]N-coordinated complexes containing six-membered chelates at 298 K in CH₂Cl₂ and 77 K in an EPA glass.

Complex	298 K			77 K	
	λ_{\max}/nm	$\tau/\mu\text{s}$ deg(aer) ^b	$\Phi_{\text{lum}} \times 10^2$ ^c	λ_{\max}/nm	$\tau/\mu\text{s}$
42	600	16 (1.1)	3.6	538, *579, 623sh	130
46	612	1.3 (0.58)	0.7	544, *587, 628sh	70
47	593	33 (0.69)	4.2	537, *578, 622sh	135

^a λ_{\max} value denoted by *.

^b Lifetimes in degassed and aerated solution.

^c Quantum yields measured using [Ru(bpy)₃]²⁺ as a standard.

to the HOMO from the metal orbitals.

The methoxide and acetylide adducts, **46** and **47**, respectively, show very similar emission profiles at 298 K to **42**. Emission of **46** is slightly red-shifted in comparison to the parent complex, **42** and has a lower quantum yield of 0.007, whilst **47** is very similar to the spectral shape of **42**, with a slight blue-shift and an improved quantum yield of 0.042. The similarity of the spectra, together with the lack of solvatochromism, supports a LC basis for the luminescence, predominantly from the terdentate ligand, owing to the lack of influence from the ancillary ligand. The principal effect of the monodentate ligand is on the radiative lifetime, which is longer for the acetylide complex at 33 μs , suggesting a reduction in both radiative and non-radiative decay. The shortened lifetime of 1.3 μs for the methoxide adduct (compared to 16 μs for the parent compound), together with the lowest quantum yield of the series reflects an increase in non-radiative decay. This may be partially attributable to an increased geometric distortion on going from the ground to the excited state, which favours non-radiative decay pathways, as the methoxide ligand could lead to more distortion on rotation than a simple chloride co-ligand. DFT studies into triplet state geometries would be needed to confirm whether there is a significant distortion on moving to the excited state.

Luminescence measurements were also taken in a frozen EPA glass at 77 K and the three complexes display structured emission with longer lifetimes (70–135 μs , Table 4.12). The spectra of **42** and **47** at 77 K are virtually indistinguishable, with **46** again displaying a slight red-shift (Fig. 4.23). Emission at 77 K is shifted by approximately 40 nm to the blue for the N[^]N[^]N-coordinated compounds in comparison with the N[^]C[^]N-coordinated compounds composed of six-membered chelate rings. The long lifetimes at 77 K, for **42** and **46** in particular (130 μs and 135 μs respectively), are of a similar duration to Pt(3-diqb)Cl, **34** (132 μs). These life-

times are suggestive of emission from triplet origins (*e.g.* $^3\pi-\pi^*$ states); lifetimes of this length are too long to be of predominantly MLCT character. These results for this set of complexes shows the importance of quenching *via* thermally-activated non-radiative transitions, which are absent at low temperatures.

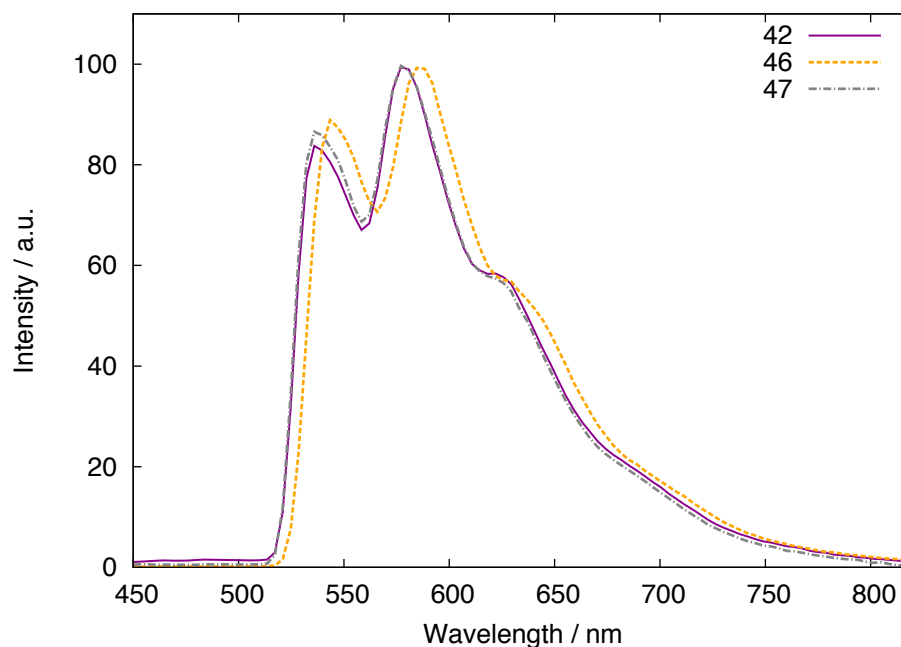


Fig. 4.23 Luminescence emission spectra of the Pt(N^NN)-coordinated complexes based on dq_p: **42**, **46** and **47** in an EPA glass at 77 K; each is normalised to set the maximum intensity to 100.

Table 4.13 Electrochemical data and the predominant character and energy of the lowest-lying singlet states as determined by TD-DFT of the d⁸ complexes. CV measurements performed in acetonitrile using Bu₄NPF₆ as an electrolyte unless stated otherwise.

Complex	Lowest S state E/eV [λ /nm]	$E_{\text{ox}}^0/V^{\text{a}}$	$E_{\text{red}}^0/V(\Delta/mV)^{\text{a}}$
[Pt(tpy)Cl] ^{+b}	–	–	–1.24(70), –1.82(70)
Pt(dpyb)Cl ^c	HOMO→LUMO 2.64 [471] ^d	0.35 ^e	–2.14 ^e
33 , Pt(1-diqb)Cl ^c	HOMO→LUMO 2.58 [481]	0.37 (89)	–1.59 (280), –2.19 (170)
34 , Pt(3-diqb)Cl ^c	HOMO→LUMO 2.64 [469]	0.27 (90)	^f
38 , Pt(8-dqb)Cl ^c	HOMO→LUMO 2.61 [475]	0.62	–1.57 (80), –2.26 (160)
39 , Pt(8-dqMeb)Cl ^c	HOMO→LUMO 2.53 [490]	^f	^f
40 , Pt(qpyb)Cl	HOMO→LUMO 2.54 [488]	^f	^f
42 , [PtdqpCl]PF ₆	HOMO→LUMO 2.99 [415]	0.67	–1.27 (70), –1.82 (70)
43 , Pt(bqbph)	HOMO→LUMO 2.06 [603]	^g	^g
46 , [PtdqpOMe]PF ₆	HOMO→LUMO 2.44 [508]	0.77	–1.41 (120), –1.98
47 , [PtdqpCC-tfp]PF ₆	HOMO→LUMO 2.45 [506]	0.78	–1.49 (100), –1.66

^a Peak potentials are given for the irreversible oxidations and second reductions (ill-defined return wave). For the pseudo-reversible reductions, values refer to $E_{1/2}$ and the peak-to-peak separation is given in parentheses. ^b Data from refs⁸⁷ and⁸⁹.

^c In CH₂Cl₂. ^d Data from ref¹⁰⁸. ^e Data from ref¹⁰⁶.

^f No defined peak was observed within the scanning range (–2.3–1.3 V).

^g Computational data presented only, due to difficulty obtaining a pure sample for CV.

Table 4.14 Luminescence data in CH₂Cl₂ at 298 K, except where stated otherwise.

Complex	$\lambda_{\max}/\text{nm}^{\text{a}}$	$\tau/\mu\text{s}$ deg(aer) ^b	$\Phi_{\text{lum}} \times 10^2$ ^c	$k_{\text{O}_2}^{\text{Q}}/10^8$ M ⁻¹ s ⁻¹ ^b	$k_{\text{r}}/10^3$ s ⁻¹ ^d	$k_{\text{nr}}/10^4$ s ⁻¹ ^e
[Pt(tpy)Cl] ⁺	500, 535, 590 ^f	<0.01	0.04	–	40	10 ⁴
Pt(dpyb)Cl ^g	491, 524, 562	7.2 (0.5)	60	9.1	83	5.6
Pt(bpqb)Cl ^h	603	2.8	14	–	50	31
Pt(1-diqb)Cl ⁱ	592	3.5	7.2	–	0.21	2.7
Pt(3-diqb)Cl ⁱ	520sh, *558	40	20	–	0.05	0.2
33 , Pt(1-diqb)Cl	595, *642	4.3 (3.6)	9.0	0.2	25	25
34 , Pt(3-diqb)Cl	559, *668	30 (0.67)	28	5.3	16	40
36 , Pt(2-dqb)Cl ^j	585sh, *612	5.5	–	–	–	–
38 , Pt(8-dqb)Cl	611(sh), *645	14 ^j	1.6	–	1.1	7.0
39 , Pt(8-dqMeb)Cl	637	10 (0.69)	1.2	6.1	1.2	9.9
40 , Pt(qpyb)Cl	613	15 ^k	1.2	–	0.8	6.6
42 , [Pt(dqp)Cl]PF ₆	600	16 (1.1)	3.6	3.8	2.3	6.0
46 , [Pt(dqp)OMe]PF ₆	612	1.3 (0.58)	0.7	4.3	5.4	76
47 , [Pt(dqp)CC-tfp]PF ₆	593	33 (0.69)	4.2	6.4	1.3	2.9

^a λ_{\max} value denoted by *. ^b Lifetimes in degassed and aerated solution.

^c Quantum yields measured using [Ru(bpy)₃]²⁺ as a standard. ^d $k_{\text{O}_2}^{\text{Q}}$ is the bimolecular rate constant for quenching by molecular oxygen at 298 K, estimated from the lifetimes in degassed and aerated solutions, assuming [O₂] at 1 atm pressure of air = 2.2 mmol dm⁻³.

^e Rate constants k_{r} and k_{nr} estimated from Φ_{lum} and τ values at 298 K. ^f Data from ref⁸⁹.

^g Data from ref¹⁰⁶. ^h Data from ref²⁵⁸. ⁱ Data from ref¹⁹². ^j Data from ref²⁵⁰; full data unavailable. ^k Aerated emission too weak to be detected using available instrumentation.

4.2.5 Concluding remarks

From the study of the physical properties of a series of platinum(II) complexes, it can be concluded that both steric and electronic effects are clearly extremely important in determining luminescent properties of a platinum-group metal complex. Luminescence in solution at room temperature and in a frozen glass at 77 K is observed for all complexes studied, and DFT calculations were used to aid with assignment of excited state character. The effect of increasing the conjugation framework of the terdentate ligands by the usage of quinoline groups does not produce an increase in quantum yield in comparison to terdentate N[^]C[^]N-coordinated Pt(II) species containing pyridine rings. Recent studies at cryogenic temperatures (1.2–4 K) confirm the presence of efficient spin-orbit coupling pathways in Pt(dpyb)Cl, despite the previous assessments of LC-like emission.²⁵⁹ Spin-orbit coupling appears to be less efficient for quinolyl-based systems than for pyridyl-based ones, as demonstrated by studies at cryogenic temperature (*vide infra*).

The use of 8-quinoline-based N[^]N[^]N-coordinating ligands that provide a six-membered coordination geometry about the platinum(II) centre permits room temperature luminescence, in contrast to simple tpy-based compounds containing five-membered chelates. Metathesis of the chloride-substituted compounds with a σ -donating methoxide or acetylide ligand proceeds successfully, but does not produce an increase in the quantum yield of luminescence. This can be ascribed to a significantly enhanced LLCT influence on the excited state, due to a lower metal contribution to the frontier orbitals and increased contribution from the ancillary ligand.

Chapter 5

Iridium versus platinum: cryogenic studies and OLED fabrication

5.1 Cryogenic spectroscopy

A more detailed investigation into the nature of excited states in phosphorescent complexes can be performed by exploring the extent of spin orbit coupling (SOC) in heavy metal complexes. SOC facilitates efficient intersystem crossing to the emitting triplet state and promotes the radiative transition $T_1 \rightarrow S_0$, so has a large effect on quantum yield and emission lifetime.^{1,52,260,261,262} Typically the 3MLCT state splits into three substates as a result of orbital symmetry constraints, denoted I, II and III, a phenomenon which is termed the zero-field splitting (ZFS). A large body of data suggests that the magnitude of the ZFS provides an indication of the efficiency of SOC, with a large ZFS showing that SOC is effective. This entails mixing of the MLCT states derived from different d-orbitals as a consequence of SOC selection rules.²⁶³ A large ZFS value can produce an emitter with a short decay lifetime, which is favourable in OLEDs, but very large values could diminish thermal population of the highest substate, and so may be a limiting factor in reducing the lifetime.¹⁵⁸ Yersin *et al.* have devised a scale ordering triplet emitters according to zero field splitting, thereby classifying them by SOC efficiency and their resulting character (LC or MLCT).^{1,263}

In order to compare the SOC present for iridium and platinum complexes, a study of the ZFS was carried out by high resolution optical spectroscopy at cryogenic temperatures (down to 1.2 K). A direct comparison was made between the two third-row transition metals by measuring spectra of the two complexes containing

the 1-diqb ligand, **1**: Ir(1-diqb)(ppy)Cl, **25** and Pt(1-diqb)Cl, **33** (Fig. 5.1). Since the excited state in both cases essentially involves the 1-diqb ligand, with the ppy and chloride ligands acting as spectators only, a direct comparison can be made between the influence of the two metals. According to previous studies by Yersin *et al.*, more efficient SOC is observed for a distorted octahedral system than a distorted square planar system.^{263,264,265} This prediction is based on the smaller separation between the highest occupied d-orbitals in a six-coordinate system, which results in a smaller separation between the lowest ³MLCT state and the next ¹MLCT state involving a different d-orbital, enabling SOC between the states to be more efficient.

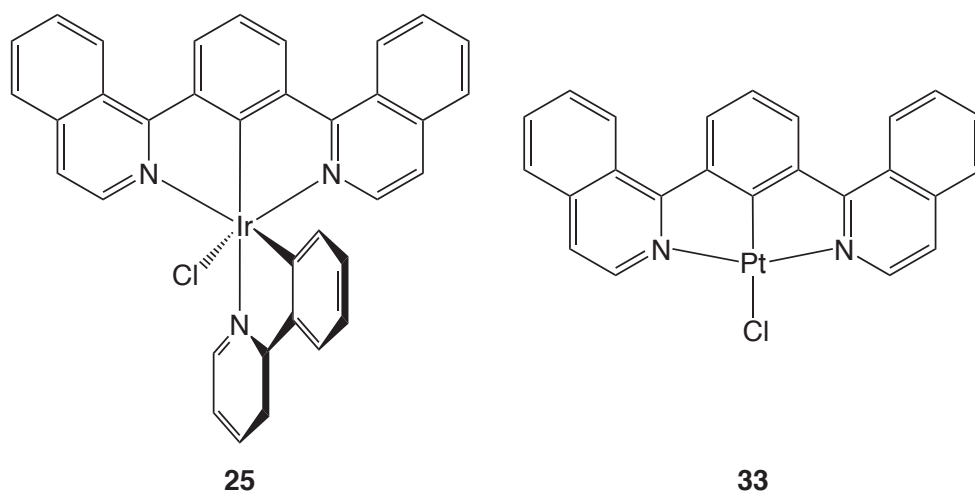


Fig. 5.1 Structures of the complexes Ir(1-diqb)(ppy)Cl, **25** and Pt(1-diqb)Cl, **33** studied by cryogenic spectroscopy

A sample of each complex was dissolved in CH₂Cl₂ and cooled using liquid helium to obtain a polycrystalline Shpol'skii matrix,⁸⁴ in which the emissive “guest” molecules lie at well-defined positions in the host solvent matrix.²⁶² This technique can result in highly resolved spectra with line widths of only a few cm⁻¹ due to a residual inhomogeneity.^{262,266} Ir(III) complexes tend to exhibit a more intense inhomogeneously broadened background than Pt(II) complexes, even at low temperatures, but resolution is far greater for both than for spectra recorded at 298 K or 77 K (where halfwidths are several hundred cm⁻¹). The spectra obtained in the matrix cage frequently represent a superposition of spectra stemming from several sites (orientations in the matrix) so site-selective excitation is performed by using a tunable dye laser to assess one particular site.

5.1.1 Cryogenic studies of Ir(1-diqb)(ppy)Cl

Emission and excitation measurements were taken at a range of temperatures down to 1.2 K for the two complexes. For Ir(1-diqb)(ppy)Cl, **25**, the three triplet substates could not be determined from the highly resolved spectra, so an alternative method was used to obtain further information. The zero-field splitting and the decay lifetimes of the three substates can be obtained from the temperature dependence of the emission decay time in THF from broadband spectra (Fig. 5.2a). At 1.2 K the decay time of the lowest substate can be measured directly since only this substate emits at that temperature. At higher temperatures only the thermalised emission decay time and the spin-lattice relaxation (SLR) components from higher-lying substates to substate I can be measured, so an indirect method must be employed by plotting the measured values of τ versus temperature.²⁶³ The values of τ determined for the substates were as follows:

$$\tau_{\text{I}} = 40 \mu\text{s}$$

$$\tau_{\text{II}} = 15 \mu\text{s}$$

$$\tau_{\text{III}} = 0.4 \mu\text{s}$$

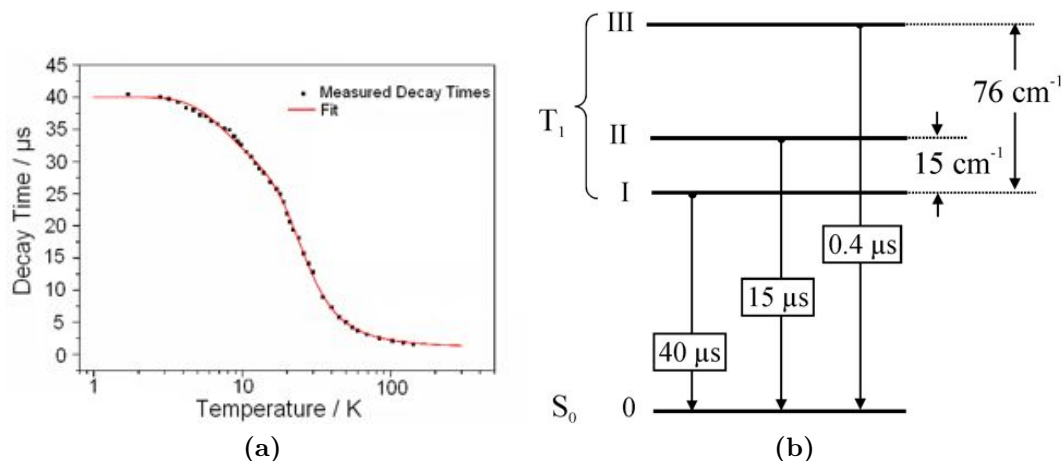


Fig. 5.2 (a) Thermalised emission decay of **25** in CH_2Cl_2 versus temperature; emission was detected at the electronic 0–0 transition $\text{I} \rightarrow 0$. The solid line represents a fit of Equation 5.2 to the experimental data. (b) Energy level diagram depicting the separation and decay lifetimes of triplet substates of **25**.

To assess the zero field splitting, a fit function must be applied to this data, assuming a system under fast thermalisation between excited substates. In this

instance, occupation dynamics are governed by the following expression:

$$\frac{dN}{dt} = -k_{\text{therm}}N = -\sum_i k_i n_i \quad (5.1)$$

where n_i denotes the Boltzmann occupation number, k_i is the total rate constant for the depopulation of state i ($i = \text{I, II, III}$), N is the total occupation number of excited states and k_{therm} is the rate constant for the depopulation for the thermally equilibrated states. Introducing Boltzmann factors produces an equation that can be applied to determine the ZFS parameters:

$$\tau_{\text{therm}}(T) = \frac{1 + \exp\left(\frac{-\Delta E_{\text{II-I}}}{k_{\text{B}}T}\right) + \exp\left(\frac{-\Delta E_{\text{III-I}}}{k_{\text{B}}T}\right)}{\frac{1}{\tau_{\text{I}}} + \frac{1}{\tau_{\text{II}}} \cdot \exp\left(\frac{-\Delta E_{\text{II-I}}}{k_{\text{B}}T}\right) + \left(\frac{1}{\tau_{\text{III}}}\right) \cdot \exp\left(\frac{-\Delta E_{\text{III-I}}}{k_{\text{B}}T}\right)} \quad (5.2)$$

where $k_i = 1/\tau_i$ and $\Delta E_{\text{II-I}}$ and $\Delta E_{\text{III-I}}$ represent the energy separation between the respective substates. The rate constant k_{therm} represents the inverse of the measured decay time τ_{therm} , and applying Equation 5.2 as a fit function to the thermalised emission decay generates the values for ZFS, which were calculated to be as follows:

$$\begin{aligned} \Delta E_{\text{III-I}} &= 76 \text{ cm}^{-1} \\ \Delta E_{\text{II-I}} &= 15 \text{ cm}^{-1} \end{aligned}$$

The total zero field splitting $\Delta E_{\text{III-I}}$ of 76 cm^{-1} (Fig. 5.2b) for the iridium complex is sufficiently large to suggest a high degree of $^3\text{MLCT}$ triplet state character. This splitting is induced by very efficient SOC, which signifies mixing of MLCT states derived from different d-orbitals.²⁶³ Assignment of emission from Ir(1-diqb)(ppy)Cl, **25** as derived largely from charge transfer is supported by DFT calculations (*vide supra*, see 3.1.1) and fits well with observations of large ZFS values for pseudo-octahedral compounds that are adjudged to contain excited states comprising a significant amount of MLCT character.^{263,264,265}

5.1.2 Cryogenic studies of Pt(1-diqb)Cl

For Pt(1-diqb)Cl, **33** a slightly different situation arises. The triplet substates I and II can be clearly identified from the cryogenic emission and excitation spectra (Fig. 5.3) but the exact location of substate III remains ambiguous. At 1.2 K only one band at $17\,067 \text{ cm}^{-1}$ is seen in the emission spectrum, which is assigned to the purely electronic 0–0 transition of substate I→0 (to the ground singlet state S_0) due to its resonant appearance in the excitation spectrum. On increasing temperature

up to 20 K, an intense band at $17\,070\text{ cm}^{-1}$ is observed, corresponding to the purely electronic 0–0 transition from substate II to the ground state (also resonant with the excitation peak). The weak additional lines occurring at ca. 20 cm^{-1} lower energy in the emission spectrum and ca. 20 cm^{-1} higher in the excitation spectrum with respect to the 0–0 transition are assigned to local phonon satellites, which stem from vibrations of the dopant in its matrix cage.

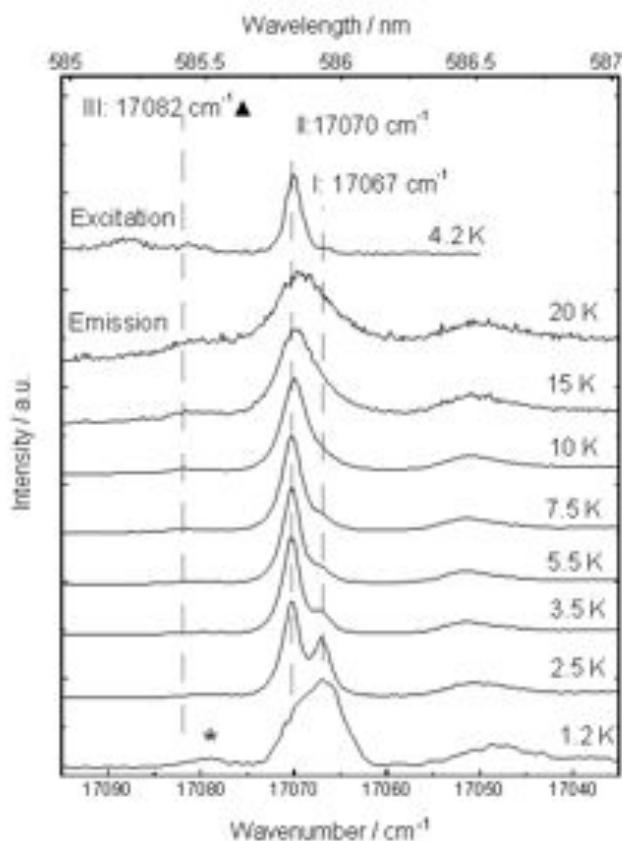


Fig. 5.3 Emission and excitation spectra of Pt(1-diqb)Cl in CH_2Cl_2 at selected temperatures. \blacktriangle denotes estimated location of substate III, * denotes another site.

Usually three triplet substates of platinum group compounds can be distinguished from the spectra at temperatures below 10 K but in certain cases the cryogenic data obtained do not provide enough information to classify the three 0–0 transitions.²⁶³ For Pt(1-diqb)Cl, **33** it can be proposed that the weak band at $17\,082\text{ cm}^{-1}$, which becomes slightly more prominent at temperatures above 7.5 K, correlates to the III→0 transition but an explicit assignment is not possible.

The II→0 electronic 0–0 transition exhibits the highest intensity in the excitation, whilst the other two substates are very weak in comparison. This indicates that the II→0 transition is much more allowed (by direct SOC processes and spin-vibronic Herzberg–Teller coupling) with a higher oscillator strength. It can therefore be

suggested that there is a significant degree of singlet-triplet admixture associated with this transition, whereas the I and III substates represent a higher degree of “forbiddenness” due to less mixing of singlet and triplet states. The ZFS between states were determined as follows:

$$\begin{aligned}\Delta E_{\text{III-I}} &= 15 \text{ cm}^{-1} \\ \Delta E_{\text{II-I}} &= 3 \text{ cm}^{-1}\end{aligned}$$

This evaluation of oscillator strength is confirmed in the thermalised emission decay, where the application of the fitting technique used for the Ir(III) compound (Equation 5.2), to the temperature-dependent decay data for **33**, can be used to calculate the decay times for the three substates (Fig. 5.4). Due to the uncertainty in the position of substate III, its decay lifetime is also approximate. The values obtained from the fit are as follows:

$$\begin{aligned}\tau_{\text{I}} &= 20 \text{ } \mu\text{s} \\ \tau_{\text{II}} &= 3.1 \text{ } \mu\text{s} \\ \tau_{\text{III}} &= 5.0 \text{ } \mu\text{s}\end{aligned}$$

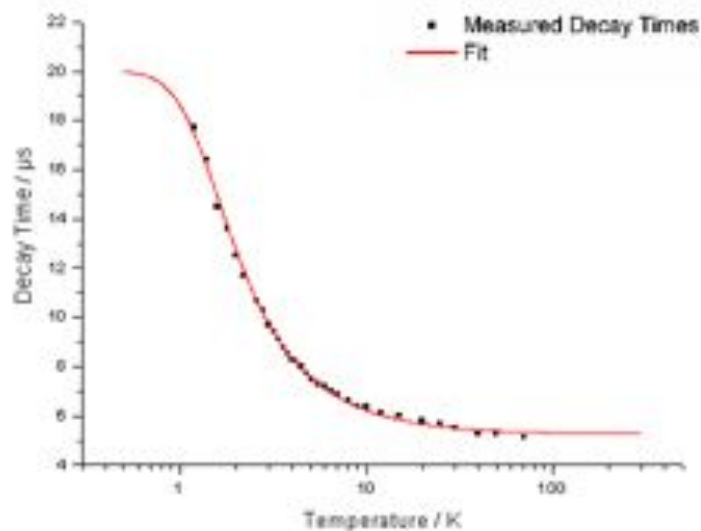


Fig. 5.4 Thermalised emission decay of **33** in CH_2Cl_2 versus temperature; emission was detected at the electronic 0–0 transition $\text{II} \rightarrow 0$. The solid line represents a fit of Equation 5.2 to the experimental data.

The value for τ_{I} of 20 μs corresponds to the measured decay time at 1.2 K,

indicating that at this temperature, the occupation of the higher lying substates II and III is negligible. The much longer decay time for this substate is suggestive of a higher degree of triplet character, whilst the shorter lifetimes for substates II and III show that these contain significant admixtures of higher-lying singlet states; a conclusion reinforced in the higher “allowedness” of the transitions in comparison with substate I.²⁶³

Regarding the scale devised by Yersin *et al.* to order triplet emitters according to ZFS,^{1,263} it can be clearly seen that geometry has a profound effect on SOC. In general, when considering metal complexes of approximately similar nuclear charge (*i.e.* those in the same row of the periodic table), four-coordinate systems have a tendency towards lower $\Delta E(\text{ZFS})$ values ($\lesssim 40 \text{ cm}^{-1}$), than six-coordinate systems, which largely possess higher values of $\Delta E(\text{ZFS})$ (predominantly $\gtrsim 40 \text{ cm}^{-1}$ with several exceptions). The findings from this work are in agreement with these previous observations: $\Delta E(\text{ZFS})$ values for Ir(1-diqb)Cl, **25** and Pt(1-diqb)Cl, **33** are 76 cm^{-1} and 15 cm^{-1} , respectively, underlining the trend that the pseudo-octahedral compound exhibits far greater splitting. With reference to the comparison made by Yersin *et al.* between Ir(4,6-dFppy)₂(acac) and Pt(4,6-dFppy)(acac),^{120,263} a similar contrast has emerged for the 1-diqb-based compounds. The high ZFS value, together with photophysical characterisation and DFT calculations discussed previously (Chapters 3 and 4), suggests that the excited triplet state of the iridium(III) complex is largely composed of MLCT character, with significant admixtures of higher-lying singlet states. The mixing of states induces highly efficient SOC, resulting in a high quantum yield and short decay lifetime. Conversely, the much lower ZFS observed for the platinum(II) species indicates less effective SOC, pointing to a possible LC triplet state with less mixing of states. Accordingly, Pt(1-diqb)Cl is a much less intense emitter with a longer decay lifetime, as determined experimentally.

5.2 Organic light-emitting device (OLED) fabrication

The platinum group metal complexes reported in this study represent a class of compounds that are ideally suited to applications in light-emitting devices. Preparing organic light-emitting devices (OLEDs) utilising triplet emitters as dopants can lead to a theoretical maximum of 100 % internal efficiency by harnessing light from both singlet and triplet excitons. The effective spin-orbit coupling, high quantum yields and short microsecond decay lifetimes of the complexes studied herein are desired attributes for efficient devices. Ir(1-diqb)(ppy)Cl, **25** and Pt(1-diqb)Cl, **33** are

therefore potentially ideal candidates for red-emitting OLEDs and were incorporated into multilayered OLEDs.

Two different techniques were employed to fabricate multilayered architectures, employing materials with good transport properties to enhance device efficiency. Initial collaborative work with the Institute for Organic Synthesis and Photoreactivity (ISOF) in Bologna, Italy, utilised sublimation under high vacuum to construct the layers but it was found that the two complexes were susceptible to degradation on sublimation, the Ir(III) species in particular. A novel collaboration was therefore initiated with the Department of Engineering at Durham University to prepare OLEDs *via* spin-coating from solution to investigate whether an improved light output was possible. Further studies were carried out using this technique and for comparison purposes, the rhodium analogue Rh(1-diqb)(ppy)Cl, **32** was also tested in a spin-coated device.

5.2.1 OLEDs fabricated by thermal evaporation under vacuum

The seven-layered structure of the OLEDs produced at Bologna ISOF is based upon an optimised system¹⁸¹ to enhance electron and hole injection, and provide a large recombination zone for exciton formation (Fig. 5.5). The OLEDs were prepared by deposition of a sequence of thin layers onto an indium tin oxide (ITO) glass substrate, which constitutes the anode layer from which holes are injected. *N,N'*-diphenyl-*N,N'*-bis(3-methyl)-1,1'-biphenyl-4,4'-diamine (TPD) blended with a bisphenolpol-*A*-polycarbonate (PC) binder is spin-coated directly onto the ITO to act as a hole transport layer (HTL). This blend prevents molecular diffusion and crystallisation, whilst its poor electron transport properties confine recombination of holes and electrons to the emitting layer (EML).

The remaining layers were deposited, in succession, by sublimation under vacuum at a pressure of 0.05 mPa. A 10 nm-thick layer of 4,4',4''-tris(*N*-carbozolyltriphenylamine) (TCTA) acts as a further HTL in addition to blocking triplet exciton transfer from the emissive layer. The 30 nm-thick EML consisted of the required complex doped into TCTA (5 % wt of complex), upon which a 30 nm-thick layer of 3-phenyl-4-(1'-naphthyl)-5-phenyl-1,2,4-triazole (TAZ) was deposited as an electron transfer layer (ETL). This acts in a similar manner to that of TPD in preventing exciton movement and quenching, whilst also blocking hole transport. The synergy of the layers forces recombination to occur in the emitting layer and minimises quenching of excitons by non-radiative processes. Inclusion of a very thin (0.5 nm) layer of lithium fluoride, LiF, between the ETL and the aluminium cathode enhances

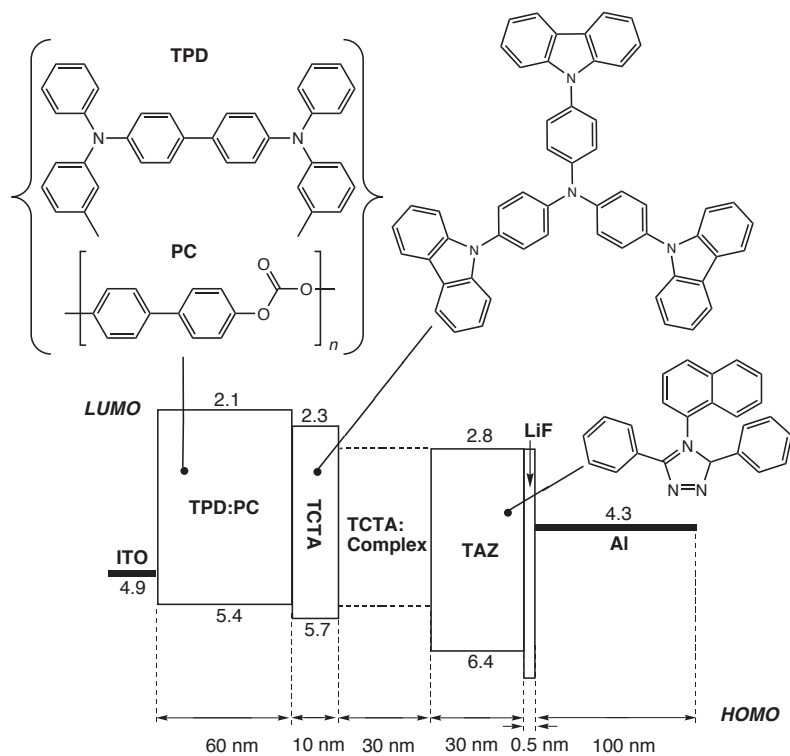


Fig. 5.5 OLED architecture showing the structures of materials used. HOMO and LUMO values refer to the ionisation potentials and molecular electron affinities, respectively, for each material; values are given in electronvolts (eV) relative to the vacuum level at energy zero. The Fermi levels of ITO and Al are included for completeness.

electron injection from the cathode, which lowers operational voltage and improves the optical output.²⁶⁷

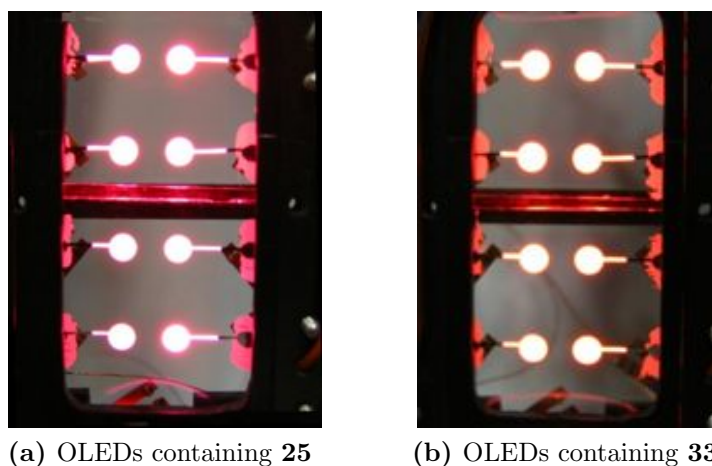


Fig. 5.6 OLEDs fabricated by sublimation under vacuum.

The OLEDs emit with red-orange light, with the device containing Ir(1-diqb)(ppy)Cl,

25 displaying more intense red emission than that of Pt(1-diqb)Cl, **33** (Fig. 5.6). The device characteristics display similar results to the solution photophysics with regard to emission profile and quantum yield. The thin film photoluminescence emission profile shows the same broad band structure seen in CH₂Cl₂ (Fig. 5.7a), with one main peak displaying a shoulder at lower energy for the OLED composed of **25**, and two peaks for the OLED composed of **33** (Fig. 5.7b). Measured quantum yields for the thin films are within experimental error of the values recorded in dilute CH₂Cl₂ solution, at 0.40 for **25** and 0.09 for **33** compared to 0.41 and 0.09, respectively, for the solution measurements.

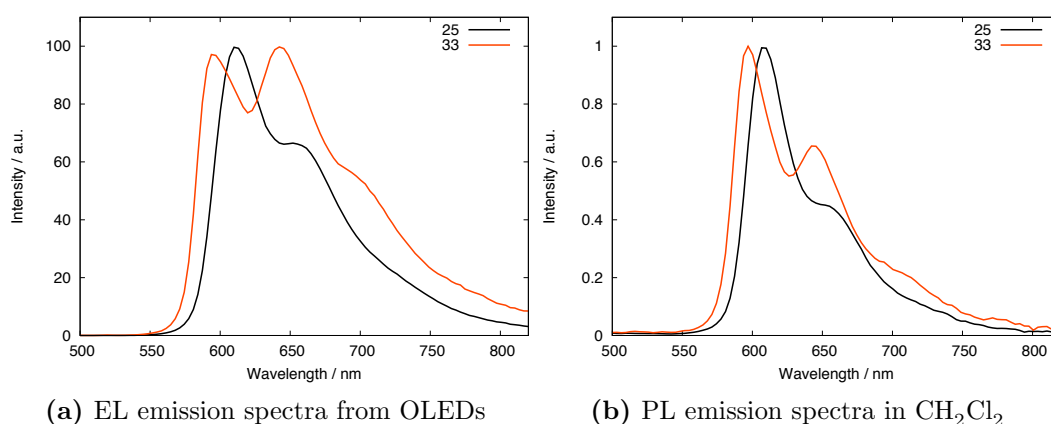


Fig. 5.7 Comparison of the emission spectra of Ir(1-diqb)(ppy)Cl, **25** and Pt(1-diqb)Cl, **33**: (a) Electroluminescence spectra from thin film OLEDs and (b) Photoluminescence spectra recorded in dilute CH₂Cl₂ solution at 298 K.

As expected from the higher quantum yield recorded for the Ir(III) compound in solution, the device efficiency for **25** is much greater than that of **33** (Fig. 5.8). The external electroluminescent quantum efficiency (EL QE), expressed as a percentage of photons/electron, %ph/e, is mostly constant at approximately 7 % for **25** at low current densities, whilst for **33**, values range between 1 and 4 %. Maximum EL QE is ca. 7.4 % for Ir(1-diqb)(ppy)Cl at a current density of 1×10^{-5} A cm⁻¹ and ca. 3.8 % for Pt(1-diqb)Cl at a current density of 5×10^{-4} A cm⁻¹. Luminance increases with applied voltage up to 18 V and the light turn-on voltage was ca. 3 V for both devices.

5.2.2 OLEDs fabricated by spin-coating

Composite OLEDs, in which transport-enhancing materials are combined within layers and spin-coated, are often easier and less expensive to produce than those requiring multiple layers deposited under vacuum, which demand precision of evap-

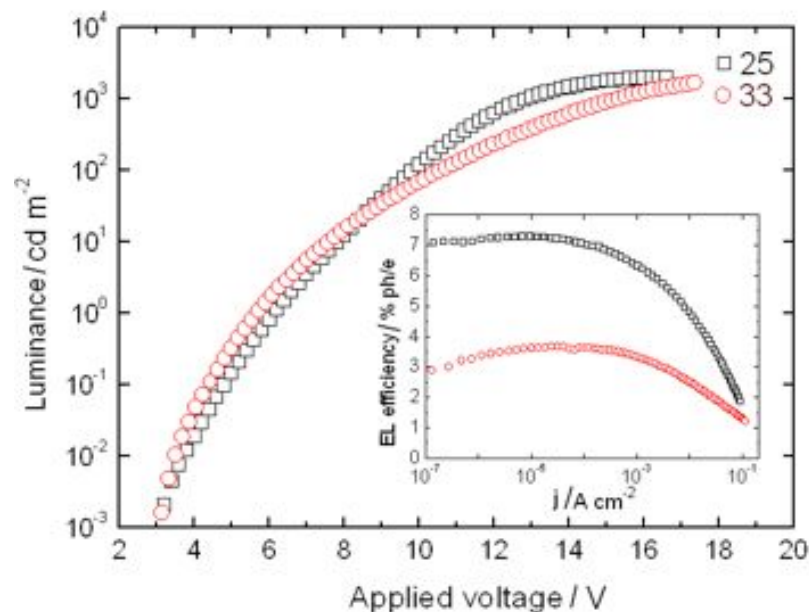


Fig. 5.8 Luminance versus applied voltage of the devices containing **25** and **33**. Inset: EL quantum efficiency as a function of current density, j .

oration rates, ill-suited to the manufacture of large-area devices.⁷⁸ The device structure of the OLEDs prepared in the Engineering Department at Durham University resembles that of the thermally evaporated devices but fewer layers are required due to blending of materials within layers.

The OLED structure (Fig. 5.9) was based upon procedures optimised in previous devices^{170,177} and comprises five layers including the electrodes. The three central layers were spin-coated in turn onto a rigorously cleaned ITO glass substrate, followed by thermal evaporation of the aluminium cathode; all depositions and annealing steps were performed in a glove box. An aqueous solution of poly(3,4-ethylenedioxythiophene)/poly(styrenesulfonate) PEDOT/PSS was filtered through a 2 μL syringe filter to remove residual particles then a 200 μL aliquot was spin-coated onto the ITO plate at a speed of 2500 rpm (revolutions per minute) for 45 s. This 50 nm-thick layer acted as a hole transport layer, and prior measurements for OLEDs with and without PEDOT showed a three-fold improvement in efficiency for devices containing this addition.¹⁷⁰ After each solution was applied to the OLED, they were annealed at 180 $^{\circ}\text{C}$ before the substrates were left to dry overnight in the glovebox.

The remaining spin-coated solutions were prepared by combining the materials in the required ratios in chlorobenzene and mixing them by ultrasonication. The emitting layer (100 nm) was composed of the desired complex doped into a polyvinylcarbazole (PVK) matrix host²⁶⁸ blended with a 1,3-bis[4-*tert*-butylphenyl-

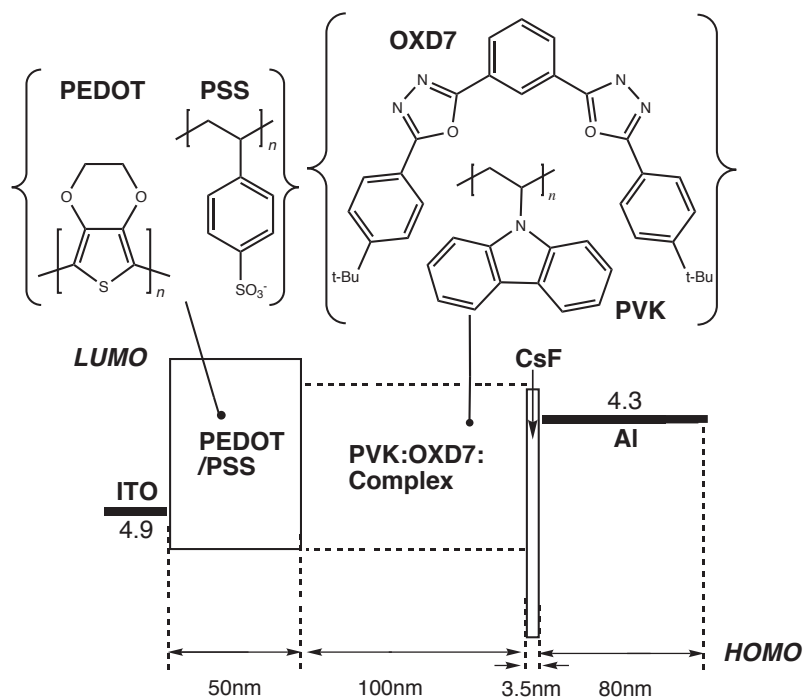


Fig. 5.9 OLED architecture showing the structures of materials used. Triplet energy levels for PVK are under debate so are not reported. The Fermi levels of ITO and Al are displayed in electronvolts (eV) relative to the vacuum level at energy zero.

1,3,4-oxadiazolyl] phenylene (OXD7) electron transport layer. 150 μL of the dopant solution was spun at 1000 rpm for 60 s followed by annealing at 80 $^{\circ}\text{C}$. Solubility of the platinum complex was lower than that of the iridium species, and, consequently, the quality of the film was poor, so further sonication of the Pt(II) complex blend was carried out. However, this appeared to have little effect, thus the performance of the OLEDs containing Pt(1-diqb)Cl is likely to be diminished in comparison with that containing Ir(1-diqb)(ppy)Cl. The final fabrication step was the deposition by thermal evaporation of caesium fluoride (CsF) (3.5 nm) and the aluminium cathode (80 nm) through a shadow mask under a base vacuum of 0.7 mPa.

Batches of six individual OLEDs on an ITO slide were fabricated by spin-coating from chlorobenzene solutions; separate slides were prepared concurrently for each of Ir(1-diqb)(ppy)Cl, **25**, Rh(1-diqb)(ppy)Cl, **32** and Pt(1-diqb)Cl, **33** (Fig. 5.10). Measurements were taken for several individual devices on the same slide, in addition to those in different batches, and average values reported. OLEDs containing the rhodium compound **32** were very dim, to the extent that the initial measurement of PL spectra at varying current densities could not be obtained. Owing to the less effective spin-orbit coupling of rhodium and resultant lower quantum yields of Rh(III) compounds, there are no known examples of rhodium-based OLEDs in

the literature, therefore this result was not wholly unexpected. Due to difficulties with poor solubility in chlorobenzene, rhodium devices were manufactured by spin-coating from a chloroform solution of **32** to discount this factor. The resulting Rh(III) OLEDs produced sufficient light to obtain PL spectra, whereas the devices containing Ir(1-diqb)(ppy)Cl, **25**, prepared from chloroform solution as a control, showed a decrease in efficiency compared to devices manufactured from chlorobenzene solutions of **25**.

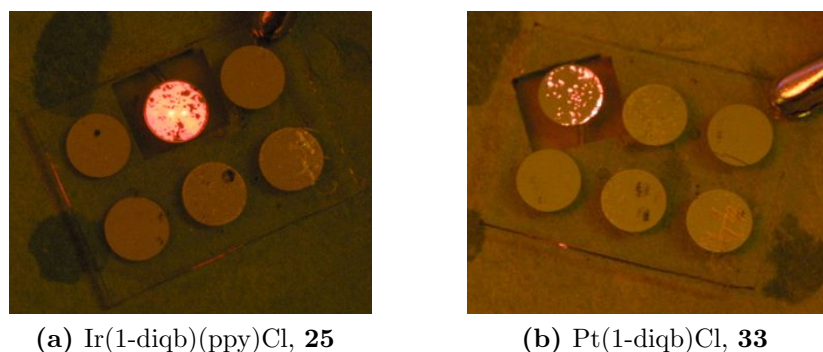


Fig. 5.10 Photographs of the working OLEDs fabricated from chlorobenzene solutions, after storage under vacuum for two weeks. More intense emission for Ir(1-diqb)(ppy)Cl, **25** is still clearly apparent, whereas for the device based on Pt(1-diqb)Cl, **33**, weaker electroluminescence is diminished further by degradation. Devices containing Rh(1-diqb)(ppy)Cl, **32** did not remain bright for long enough to capture suitable photographs.

Degradation of the devices was apparent with repeated measurements, in addition to that seen over time after storage under vacuum (Fig. 5.10); the Ir(III) devices were most robust and withstood higher currents. The electroluminescence spectra obtained from each of the three compound devices matched that of the photoluminescence spectra obtained in solution (Fig. 5.11), in addition to those recorded for the vacuum-sublimed devices discussed in Section 5.2 (see Fig. 5.7). Radiance reaches a maximum value at higher current values, up to a threshold level where the current through the device becomes too great and the OLED fails (undergoing an irreversible change). This is discernible from the Pt(II)-based device (5.11b) where radiance increases with increasing current up to 10 mA but decreases again for the measurement at 20 mA.

Each OLED emits orange-red light, decreasing in brightness following the order Ir(III) > Pt(II) > Rh(III). CIE coordinates, as defined by the Commission Internationale d'Eclairage, are (0.66,0.33), (0.61,0.34) and (0.58,0.40), showing dark orange, light orange and yellow-orange emission for the Ir(III), Pt(II) and Rh(III) complexes, respectively. Variance with current was low, as shown by the CIE coordinates for

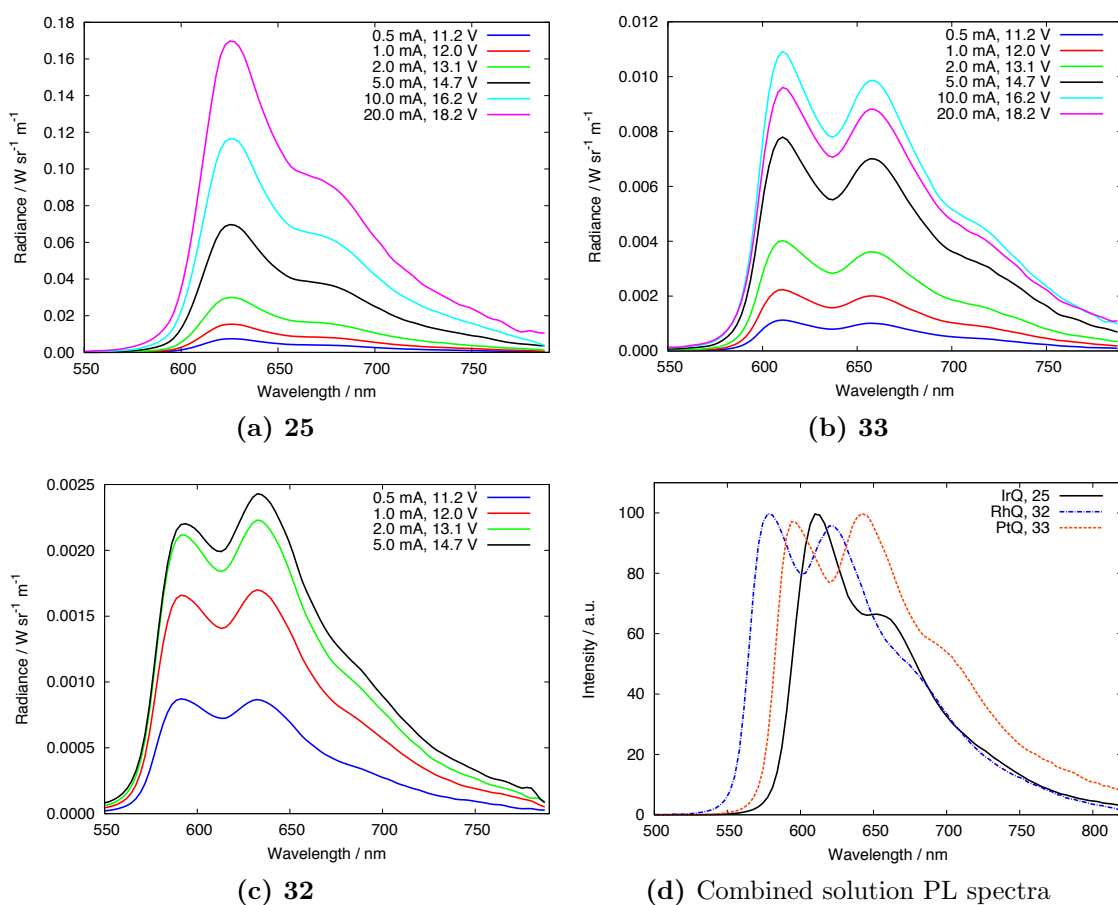


Fig. 5.11 Electroluminescence spectra for OLEDs containing **25** and **32** and **33** compared to the corresponding photoluminescence emission spectra for the three complexes recorded in CH₂Cl₂ at 298 K.

25 and **33** over the measured current range up to 20 mA (Fig. 5.12).

Saturation at higher voltages (high luminance) produces current “roll-off” for all devices fabricated using both procedures, which is a typical observation for OLEDs (Fig. 5.13).³ The device incorporating Ir(1-diqb)(ppy)Cl, **25** as an emitter displayed the highest quantum efficiency, consistent with its higher quantum yield in solution. The luminous efficiency was in the region of 1–4 cd A⁻¹, with the maximum value of ca. 4 cd A⁻¹ recorded at a current of 0.5 mA (applied voltage of ca. 12 V) and a luminous power efficiency of 1.0 lm W⁻¹. This corresponds to a brightness of 206 cd m⁻², which increased to 2 357 cd m⁻² for a current of 20 mA.

As consistent with the solution photophysics and thermally evaporated OLEDs, the devices containing Pt(1-diqb)Cl, **32** were much less efficient, displaying a maximum luminous efficiency of ca. 0.86 cd A⁻¹, peaking at a current of 0.5 mA (applied voltage of ca. 9.0 V). This corresponds to a brightness of 43.5 cd m⁻², which increased to 215.6 cd m⁻² for a current of 15 mA (luminance decreased at higher

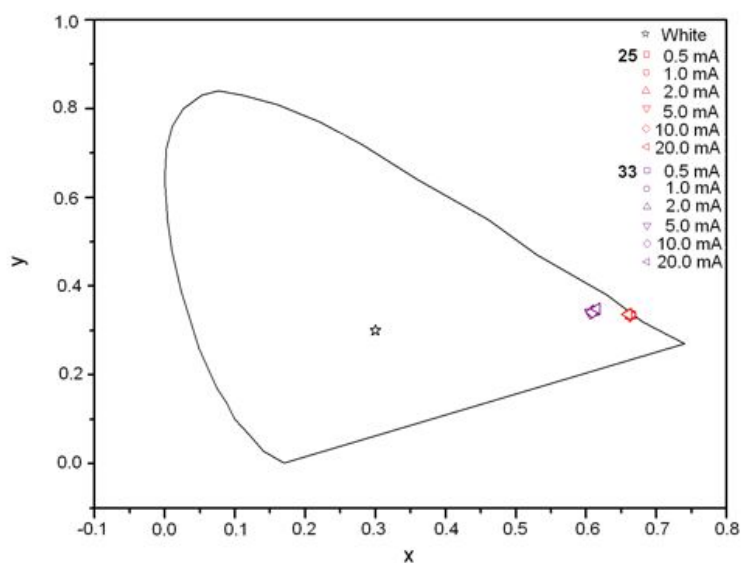


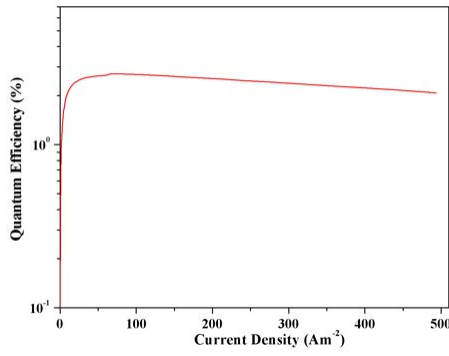
Fig. 5.12 CIE coordinates with varying current for **25** and **33**

applied voltages as the device burned out). Quantum efficiencies for the devices are ca. 4% and 0.8 % for **25** and **33**, respectively, (from chlorobenzene solutions), and ca. 0.5 % for **32** (from a chloroform solution). Current variance with applied bias voltage for each the three OLEDs is shown in Fig. 5.13, demonstrating the rapid increase in device current as the voltage through the OLED increases, leading to irreversible damage to the device.

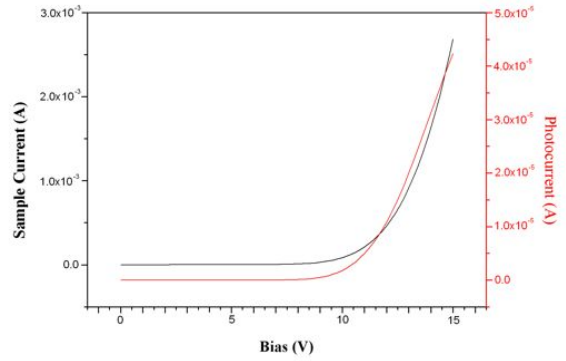
5.2.3 Fabrication of dual phosphor white OLEDs (WOLEDs)

The growing interest in white OLEDs (WOLEDs) for use in solid state lighting has led to the investigation of devices containing more than one phosphor.^{168,169,177} Combining a red emitter and a blue emitter in either the same or adjacent layers of an OLED has proved to be an effective way of achieving white emitters, using Ir(III) compounds containing ppy-derivatives. The blue emitter bis[(4,6-difluorophenyl)pyridinato-*N,C*2'], referred to as FIrpic (Fig. 5.14),¹⁶⁴ was successfully employed in conjunction with a red isoquinoline-containing complex by Pearson *et al.* previously,¹⁷⁰ and so the complex was chosen for use with Ir(1-diqb)(ppy)Cl, **25** to prepare a series of WOLEDs, following the same methods.

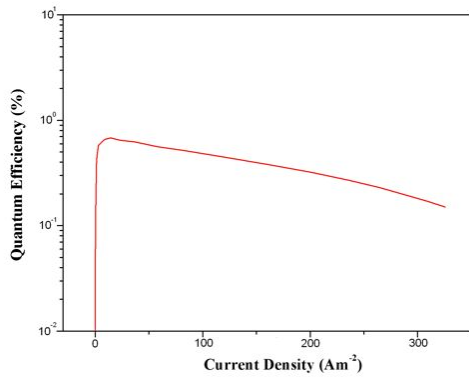
The device fabrication process was identical to that used for the spin-coated single-dopant devices; the layered structure shown in Fig. 5.9 of ITO/PEDOT-PSS/PVK-OXD7-Complex/CsF/Al depicts the architecture for the white device,



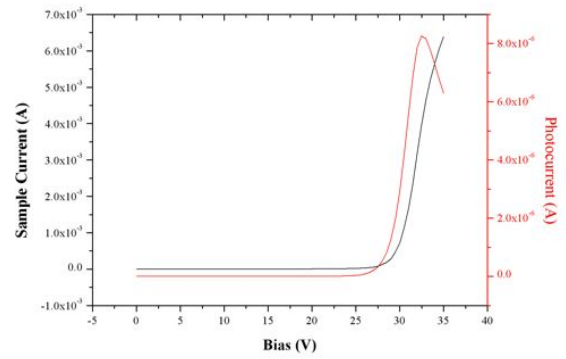
(a) 25



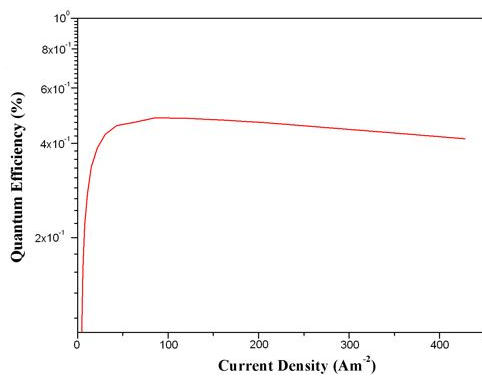
(b) 25



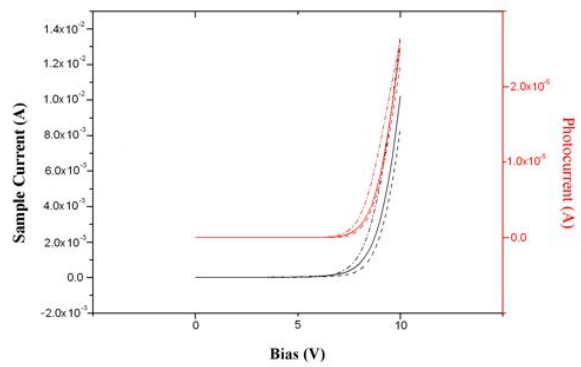
(c) 32



(d) 32



(e) 33



(f) 33

Fig. 5.13 Quantum efficiencies as a function of current density and current versus bias, respectively, of **25**, **32** and **33**.

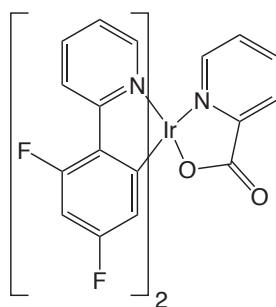


Fig. 5.14 Structure of the blue emitter FIrpic

where the EML comprises a blend of the red and blue-emitting compounds doped into the PVK-OXD7 host. In each case, OLEDs containing solely **25** (3 %) or solely FIrpic (3 %) in the emitting layer were manufactured as standards. Initially, a range of dopant concentrations from 0.1–0.5 % of the red-emitter were tested, before optimisation of the colour was performed with a further series of WOLEDs. These were prepared using 0.3–0.5 % Ir(1-di qb)(ppy)Cl in the emissive layer and the electroluminescence spectra for the WOLEDs show the two distinct emission bands for the two phosphors (Fig. 5.15).

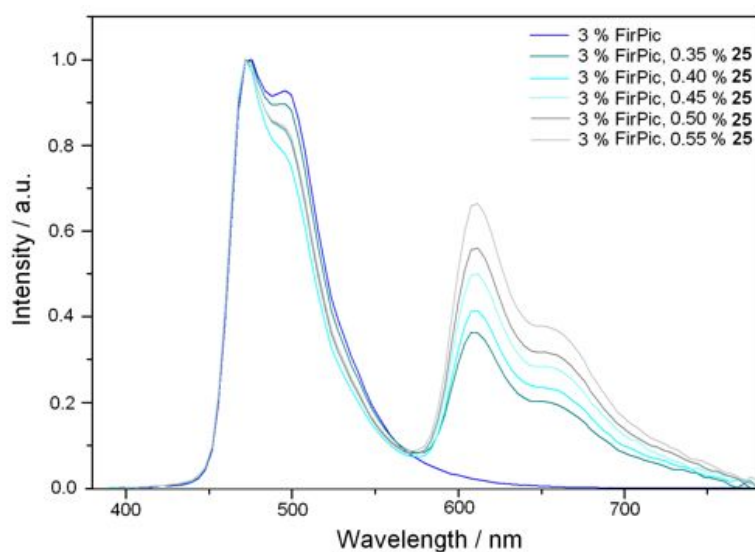


Fig. 5.15 Electroluminescence spectra for WOLEDs containing differing concentrations of Ir(1-di qb)(ppy)Cl, **25** with FIrpic (3 %).

Quantum efficiencies for the devices were comparable with previous WOLEDs (Fig. 5.16), peaking at ca. 5 % for low current densities, although efficiencies approaching 10 % have recently been reported for dual phosphor systems.¹⁶⁹ In common with other FIrpic-based devices,¹⁷⁰ efficiency decreased with increasing concentration of the red emitter (Fig. 5.16), with the maximum luminous power efficiency

just over 4 lm W^{-1} and corresponding luminous efficiency of ca. 12 cd A^{-1} measured for the WOLED containing 3.5 % Ir(1-diqb)(ppy)Cl. These results compare favourably with the dual phosphor devices previously prepared by Pearson *et al.*, which show luminous efficiencies and luminous power efficiencies of 8 cd A^{-1} and 3 lm W^{-1} , respectively.¹⁷⁰

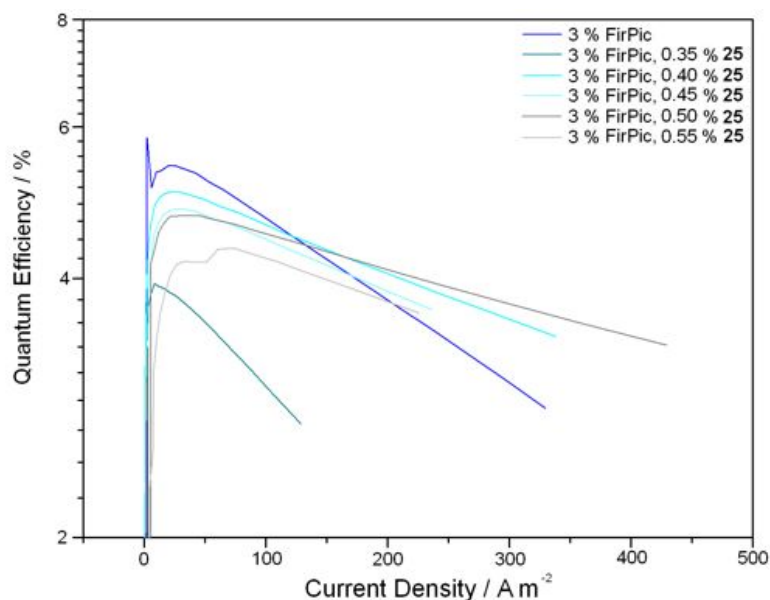


Fig. 5.16 Luminous efficiencies of WOLEDs containing differing concentrations of Ir(1-diqb)(ppy)Cl, **25** and 3 % Firpic.

A significant result from this study is the excellent near-white CIE chromaticity coordinates obtained for these mixed-complex devices, where pure white light is represented by the CIE coordinates $x = 0.33$, $y = 0.33$ (Fig. 5.17). This is demonstrated best by the device containing 0.55 % Ir(1-diqb)(ppy)Cl, which displays CIE coordinates corresponding to 0.33, 0.33, *i.e.* pure white, at varying currents (Fig. 5.18).

Further optimisation would be necessary to achieve the maximum possible efficiency from the devices. A higher concentration of Ir(1-diqb)(ppy)Cl is yet to be investigated, but considering the excellent CIE coordinates obtained from the WOLED containing 0.55 % dopant concentration, it is likely that higher concentrations will shift the light emission towards the red, as well as decreasing the luminous efficiency. Instead, modification of the layer thicknesses and spin-coating conditions would be likely to produce a more favourable result.

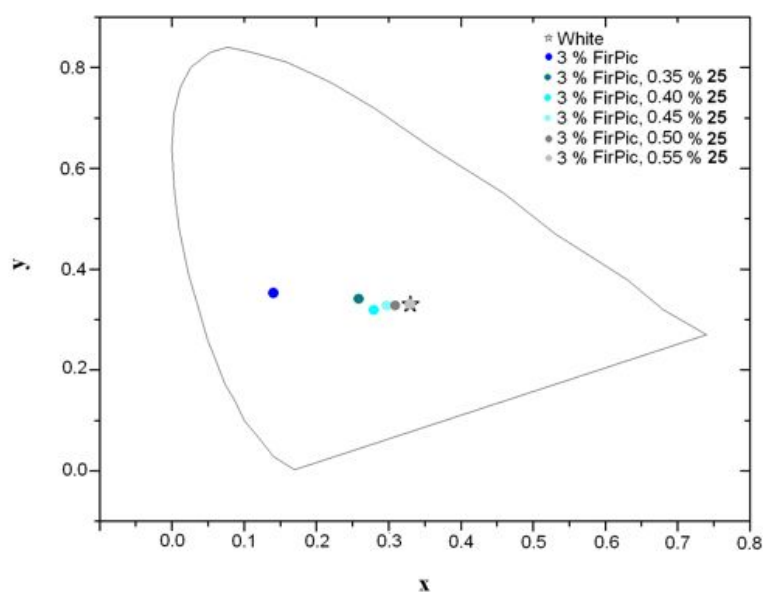


Fig. 5.17 CIE chromaticity coordinates for WOLEDs containing differing concentrations of Ir(1-diqb)(ppy)Cl, **25** and 3 % FIrpic.

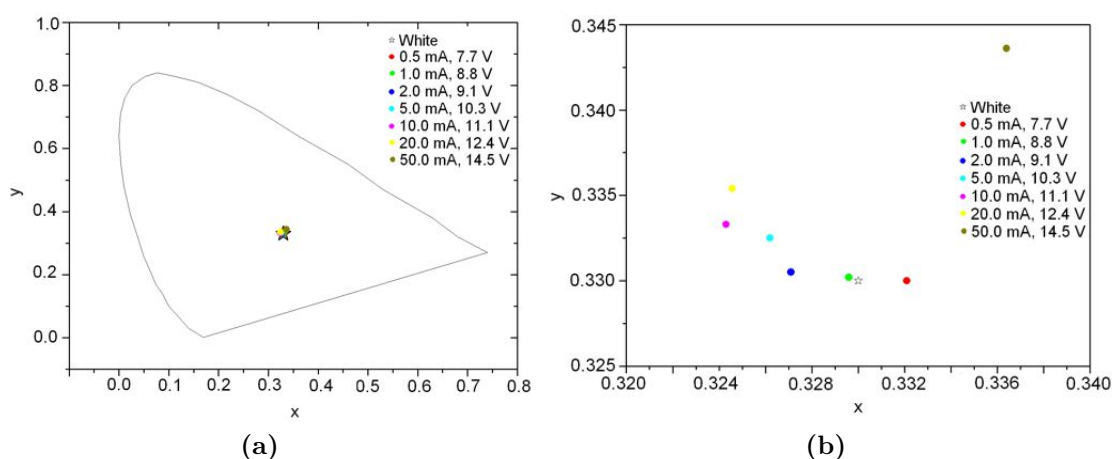


Fig. 5.18 (a) CIE chromaticity coordinates at varying currents for a WOLED containing 0.55 % Ir(1-diqb)(ppy)Cl, **25** and 3 % FIrpic. (b) Expansion of the white light region of (a).

5.3 Concluding remarks

A thorough study of the complexes Ir(1-diqb)(ppy)Cl, **25** and Pt(1-diqb)Cl, **33** by high resolution cryogenic spectroscopy has been performed to investigate the zero field splitting between the MLCT triplet substates I, II and III. Recording spectra at temperatures down to 1.2 K enabled elucidation of the triplet state splitting, resulting in data in agreement with that found for ambient temperature spectroscopy and DFT calculations. Consistent with previously studied systems,^{120,263} a larger

ZFS was seen for the pseudo-octahedral Ir(III) complex, **25** (76 cm^{-1}) than for the pseudo-square planar Pt(II) complex, **33** (15 cm^{-1}). This is likely to influence the nature of the excited state, such that **25** can be described as an MLCT emitter, containing significant admixtures of triplet and singlet states, whilst **33** displays an excited state of largely LC character. Measurement of a higher quantum yield and shorter decay lifetime for **25** reinforce this assignment.

In order to complete this study of quinolyI-based transition metal complexes, Ir(1-diqb)(ppy)Cl, **25**, Rh(1-diqb)(ppy)Cl, **32** and Pt(1-diqb)Cl, **33** were incorporated into a series of organic light-emitting devices. Fabrication either by sublimation under vacuum, or by spin-coating, led to the production of OLEDs that emit red-orange light with moderate efficiency. Devices manufactured by sublimation reached a maximum EL QE of ca. 7.4 % for **25** and ca. 3.8 % for **33**. The same trend was found for the spin-coated devices, albeit, much lower efficiencies were observed. Average EL QE values for the three devices are ca. 4.0% and ca. 0.8 % from chlorobenzene solutions of **25** and **33**, and ca. 0.5 % from a chloroform solution of **32**.

As a conclusion to the investigations, the red emitter Ir(1-diqb)(ppy)Cl, **25** was used in conjunction with the blue emitter FIrpic in a series of white-emitting OLEDs. EL QE for the WOLEDs peaked at ca. 5 % with a maximum luminous efficiency of ca. 12 cd A^{-1} measured for the WOLED containing 3.5 % Ir(1-diqb)(ppy)Cl and 3 % FIrpic. The device containing 0.55 % of the red emitter showed the best CIE coordinates for white light, with x,y-coordinates of (0.33,0.33), corresponding exactly to the desired coordinates at the energy white point for standard white light.

5.4 Research Conclusion

All iridium, rhodium and platinum compounds synthesised during this research were based upon rigid terdentate ligand frameworks and exhibit room temperature luminescence in solution. High quantum yields of up to 0.67 (degassed CH_2Cl_2 or MeCN, 298 K) for iridium(III) complexes containing quinoline-based ligands were recorded, attributed to predominantly MLCT character with admixtures of LC/LLCT character. An important finding was the room temperature luminescence observed for two rhodium(III) complexes containing 1,3-di(1-isoquinolyl)benzene, 1-diqb, in contrast to the majority of monometallic rhodium complexes studied to date, which are largely non-emissive or show very weak luminescence. The quantum yield of 0.1 in particular, measured for $\text{Rh}(1\text{-diqb})(\text{ppy})\text{Cl}$, **32**, is unprecedented amongst compounds presented in the literature.

Building upon research into platinum(II) complexes containing five-membered chelate rings, two complexes containing quinolyl-based terdentate ligands were synthesised. Moderate quantum yields were measured for the species, with $\text{Pt}(3\text{-diqb})\text{Cl}$, **34**, showing excimeric behaviour and a high sensitivity to quenching by oxygen. Utilising $\text{N}^{\wedge}\text{N}^{\wedge}\text{N}$ -coordinating ligands that form six-membered chelate rings with the platinum centre, a novel series of cationic complexes was prepared. By increasing the bite angle at the metal to approaching 180° , ligand field strength is enhanced, leading to room temperature luminescence in solution, whereas simple platinum(II) compounds containing five-membered chelates based upon 2,2':6',2''-terpyridine are non-emissive.

A detailed study into the photophysical and electrochemical properties of the species, reinforced by computational data, enabled a thorough analysis of emission characteristics, suggesting mixed charge transfer and ligand centred character. Incorporation of three complexes into OLEDs yielded promising results for a red-orange device, and in conjunction with a blue phosphor, pure white emission can also be achieved.

Chapter 6

Experimental

6.1 Synthetic reagent specifications and characterisation equipment

The following solvents were of analytical grade and used as supplied: CH_2Cl_2 , *N,N*-dimethylformamide, dimethylsulfoxide, ethanol, ethyl acetate, methanol and tetrahydrofuran. Acetonitrile was HPLC grade and all other solvents were lab reagent grade. Dry THF and dry toluene were obtained from HPLC grade solvent that had been passed through a Pure Solv 400 solvent purification system. Dry DMSO was obtained from Aldrich and used as supplied. Water was purified by the Purite_{STILL} plusTM system and had a conductivity of $< 0.04 \mu\text{S cm}^{-1}$. All commercial reagents were used as supplied, except for triethylamine, which was dried over sodium hydroxide.

Thin-layer chromatography (TLC) was carried out using silica plates (Merck Art 5554), which is fluorescent upon irradiation at 254 nm. Preparative column chromatography was carried out using silica (Merck Silica Gel 60, 230–400 mesh).

Nuclear magnetic resonance (NMR) spectra were recorded on: a Varian Mercury-200 spectrometer (^1H : 200 MHz), Varian Mercury-400 spectrometer (^1H : 400 MHz; ^{13}C : 101 MHz), Bruker Avance-400 spectrometer (^1H : 400 MHz; ^{13}C : 101 MHz; ^{19}F : 376 MHz), Varian Inova-500 spectrometer (^1H : 500 MHz; ^{13}C : 126 MHz; ^{19}F : 470 MHz) or Varian VNMRS-700 spectrometer (^1H : 700 MHz; ^{13}C : 176 MHz; ^{19}F : 658 MHz) and were referenced to residual protiosolvent resonances. ^1H NMR spectra were assigned with assistance from ^1H - ^1H correlation spectroscopy, COSY (through-bond interactions) and ^1H - ^1H nuclear Overhauser effect spectroscopy, NOESY (through-space interactions). ^{13}C NMR spectra were assigned with assistance from ^1H - ^{13}C heteronuclear single quantum correlation/coherence spectroscopy, HSQC (direct bond correlation) and heteronuclear multiple bond correlation spectroscopy, HMBC

(multiple bond correlation).

Solid state NMR spectra were recorded on a Varian VNMRs spectrometer with a 9.4 T (^1H 400 MHz) magnet operating with a static HXY MAS probe. The frequency of the pulses was ca. 85.8 MHz and the duration of the pulses was 3.6 μs for the 90° pulse and 7.2 μs for the 180° pulse. The spectra were run proton decoupled at a nutation rate of 100 kHz with a frequency step of 50 kHz, using potassium hexachloroplatinate as a reference.

Electrospray ionisation mass spectrometry (ES⁺ MS) was performed on a Thermo-Finnigan LTQ FT spectrometer using methanol, chloroform or acetonitrile as the carrier solvent. Solid state mass spectrometry was performed on a Waters Xevo quadrupole time-of-flight (QToF) machine fitted with an atmospheric solids analysis probe (ASAP). Matrix assisted laser desorption ionisation–time-of-flight (MALDI-ToF) spectra were recorded with a Bruker Daltonics Autoflex II ToF/ToF using a matrix of *trans*-2-[3-(4-*tert*-butyl-phenyl)-2-methyl-2-propenyldiene]malononitrile (DCTB). High resolution mass spectrometry was performed on a Thermo-Finnigan LTQ FT spectrometer or a Waters Xevo QToF (ASAP) spectrometer. Elemental analysis was performed using an Exeter Analytical E-440 elemental analyser. Melting points were recorded using a Gallenkamp 889339 capillary melting point apparatus and are quoted to the nearest 1 °C. All characterisation data for known compounds (as cited) match the literature values.

X-ray diffraction data were collected at 120 K on a Bruker SMART 6K CCD diffractometer, using the SMART software, with subsequent data processing carried out in SAINT.²⁶⁹ All of the structures were solved by direct methods in SHELXS-97²⁷⁰ and refined by full matrix least squares on F2 in SHELXL-97.²⁷¹ All of the hydrogen atoms, apart from the solvent water hydrogen atoms, were positioned geometrically (aromatic C–H 0.95 Å and methyl C–H 0.98 Å) and refined using a riding model with the isotropic displacement parameters fixed at $U_{\text{iso}}(\text{H}) = 1.2 \times U_{\text{eq}}$ of the parent carbon atom for the aromatic hydrogens, and $U_{\text{iso}}(\text{H}) = 1.5 \times U_{\text{eq}}$ of the parent carbon atom for the methyl hydrogens. Molecular structures were visualised and images drawn using the software programme OLEX2.²⁷²

6.2 Photophysical measurements

UV-Visible absorption spectra were recorded on a Biotek Instruments UVIKON XS spectrophotometer with LabPower software, using quartz cuvettes of 1 cm path-length. All samples were run against a reference of pure solvent contained in an identical cuvette. Extinction coefficients were obtained by dilution to appropriate

concentrations and extracted graphically using the Beer-Lambert law:

$$A(\lambda) = \epsilon(\lambda) cl \quad (6.1)$$

$A(\lambda)$ is the absorbance at a specified wavelength, $\epsilon(\lambda)$ is the extinction coefficient at that wavelength ($\text{dm}^3 \text{mol}^{-1} \text{cm}^{-1}$), c is the concentration of the species that is absorbing (mol dm^{-3}) and l is the pathlength (cm). Luminescence data were recorded at 90° to the excitation source using a Jobin Yvon Spex Instruments Fluoro Max-2 fluorimeter (photomultiplier), using quartz cuvettes of 1 cm pathlength. Solutions were prepared so that absorbance was less than 0.1 to minimise inner-filter effects, and all spectra were corrected for dark count and the spectral response from the detector. Excepting spectra used for quantum yield calculations, second order peaks were removed using an appropriate filter where necessary. All emission quantum yields refer to the spectrum as corrected using the appropriate correction data for the fluorimeter to account for wavelength dependent spectral response. Excitation correction was carried out automatically for lamp output through the use of a beam splitter, which directs 8 % of the light output to a reference photodiode. Degassing was achieved *via* a minimum of three freeze-pump-thaw cycles whilst connected to the vacuum manifold; final vapour pressure at 77K was $< 5 \times 10^{-2}$ mbar, as monitored using a Pirani gauge. Samples were referenced to a standard of ruthenium(II) tris(2,2'-bipyridine) chloride, $[\text{Ru}(\text{bpy})_3]\text{Cl}_2$ in air-equilibrated aqueous solution $\Phi_{\text{ST}} = 0.028 \pm 0.002$.²⁵⁷ Quantum yields were calculated relative to the standard by applying Equation 6.2:

$$\Phi = \Phi_{\text{ST}} \left(\frac{D}{D_{\text{ST}}} \right) \left(\frac{A_{\text{ST}}(\lambda_x)}{A(\lambda_x)} \right) \left(\frac{n}{n_{\text{ST}}} \right)^2 \quad (6.2)$$

where Φ is the luminescence quantum yield, D is the integrated area under the corrected emission spectrum, $A(\lambda_x)$ is the absorbance intensity at the excitation wavelength and n is the refractive index of the solution. Subscripts, ST, refer to corresponding values for the $\text{Ru}(\text{bpy})_3^{2+}$ standard. Aerated quantum yields were calculated employing the same method, using the integrated areas of the aerated emission spectrum of the same sample concentration. The luminescence lifetimes of complexes with lifetimes below $10 \mu\text{s}$ were measured by time-correlated single-photon counting, following excitation at 374 nm with an EPL-375 pulsed-diode laser. The emitted light was detected at 90° using a Peltier-cooled R928 PMT after passing through a monochromator. The estimated uncertainty in quoted lifetimes is $\pm 10 \%$ or better. Lifetimes at 77 K in excess of $10 \mu\text{s}$ were measured by multi-channel scaling following excitation with a μs -pulsed xenon lamp at the λ_{max} value

taken from the corresponding emission spectrum. Lifetime values were obtained by least-squares fitting to a monoexponential decay:

$$I_t = I_0 \exp\left(\frac{-t}{\tau}\right) \quad (6.3)$$

Rate constants for quenching by molecular oxygen, k_Q , were determined from the lifetimes in degassed and air-equilibrated solution, taking the concentration of oxygen in CH_2Cl_2 at 0.21 atm O_2 to be 2.2 mmol dm^{-3} .²⁷³

Photophysical measurements at 77 K were carried out on residual amounts of the compounds dissolved in a frozen EPA glass (a 2:2:1 (v/v) diethyl ether/isopentane/-ethanol solvent mixture), performed using an in-house apparatus set-up of a 4 mm optical density glass tube inserted into a cold finger containing liquid nitrogen, which encased the tube throughout the measurement. Cryogenic photophysical studies were performed on the complexes dissolved in CH_2Cl_2 at concentrations of ca. $10^{-5} \text{ mol dm}^{-1}$. Measurements were carried out with control over the temperature, helium gas flow and pressure using a helium cryostat (Cryovac Konti Cryostat IT). A pulsed Nd:YAG laser (IB Laser Inc., DiNY pQ 02) with a pulse width of ca. 7 ns was applied as the excitation source.

6.3 Electrochemical measurements

Electrochemistry was performed on a μ -Autolab type III potentiostat controlled by computer and data storage *via* GPES manager. Measurements were taken using recrystallised tetrabutylammonium hexafluorophosphate, stored in the dark under nitrogen, as the supporting electrolyte. A 0.1 M solution was prepared in dry CH_2Cl_2 or acetonitrile, dependent on solubility of the sample. A three-electrode arrangement was used, comprising a glassy carbon working electrode, a platinum wire reference electrode and a platinum wire counter electrode. The experimental set-up consisted of a glass cell containing 1 mL of electrolyte solution with the three electrodes inserted through a lid so that the solution could be thoroughly purged with nitrogen whilst stirring before each measurement. Stirring was ceased for recording of data and the nitrogen source removed to above the solvent level; the working electrode was cleaned with alumina between measurements. All measurements were taken at room temperature. Samples were referenced to the ferrocene couple (Fc^+/Fc^0) under the same conditions (0.40 vs SCE MeCN/ Bu_4NPF_6).²²⁹

6.4 Density functional theory (DFT) calculations

Density functional theory calculations were performed using the Gaussian 09 software package.²⁷⁴ The B3LYP functional²²⁵ with “Double- ζ ” quality basis sets were employed for the ligands (6-31G and 6-311G) and the transition metal centres (LanL2DZ).²²⁸ The inner core electrons were replaced with a relativistic effective core potential (ECP), so calculations were run considering the outer core electrons and the valence electrons: $[(5s)^2(5p)^6]$ and $(5d)^6$ respectively, for iridium; $[(4s)^2(4p)^6]$ and $(4d)^6$ respectively, for rhodium and $[(5s)^2(5p)^6]$ and $(5d)^8$ respectively, for platinum. Geometries were fully optimised without symmetry constraints. Time-dependent DFT (TD-DFT) calculations were performed at the optimised ground-state geometries using the B3-LYP functional. Optimisation data were viewed and molecular orbital plots drawn in Gaussview 4.1.

6.5 Synthesis

6.5.1 General synthetic procedures

Procedure A: Suzuki–Miyaura cross-coupling for ligand synthesisⁱ

The appropriate boronic acid or ester and halogenated precursor in the required ratio (either 1:1.1 or 1:2.1), were combined with a carbonate base in toluene, ethanol and water in a 2:2:1 ratio. The solution was degassed *via* four freeze-pump-thaw cycles and $\text{Pd}(\text{PPh}_3)_4$ was added under positive pressure of nitrogen. The apparatus was evacuated briefly and charged with nitrogen, then the mixture was heated at reflux under nitrogen for 3 d. After cooling to room temperature, water (5 mL) was added and the product was extracted into CH_2Cl_2 (3×35 mL). The combined extracts were dried over K_2CO_3 , filtered and the solvent removed under reduced pressure to yield crude product that was purified as necessary.

Procedure B: Chloro-bridged metal dimer formationⁱⁱ

A suspension of the appropriate ligand and metal trichloride hydrate in a 1:1 ratio in 2-ethoxyethanol (7 mL) and water (3 mL) was heated to 80 °C for 24 h. After cooling to room temperature the precipitate was collected *via* centrifugation, washed with water (3×5 mL), ethanol (3×5 mL) and diethyl ether (3×5 mL) then dried *in vacuo*. Further product was obtained by repeating the centrifugation procedure with the remaining solutions; evaporation of the water washings also

ⁱProcedure based upon work by Suzuki *et al.*²⁷⁵

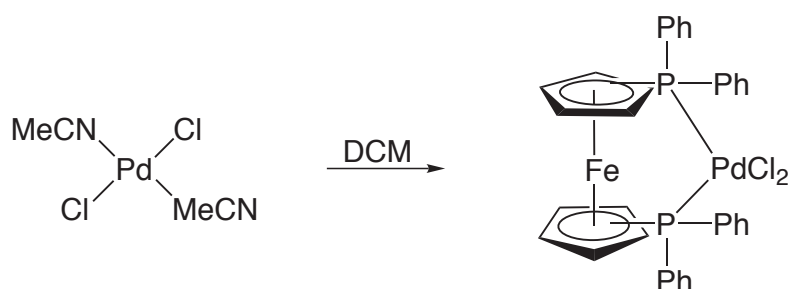
ⁱⁱProcedure based upon work by Williams *et al.*⁵⁴

yielded additional product in some cases. Low solubility in all common solvents made further purification of the dimer products unfeasible and so the dimers were used for the complexation step after washing without further purification.

6.5.2 Catalysts and precursors

[1,1'-Bis(diphenylphosphino)ferrocene]dichloropalladium(II)

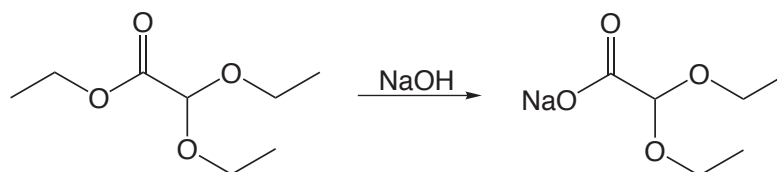
[Pd(dppf)Cl₂]ⁱⁱⁱ



Bis(diphenylphosphino)ferrocene (0.554 g, 1.00 mmol) and *trans*-bis(acetonitrile)-palladium(II)chloride (0.259 g, 1.00 mmol) were dissolved separately in CH₂Cl₂ and stirred at room temperature for 15 min. The solvent was removed under reduced pressure and the orange solid dried *in vacuo* (0.771 g, 94 %).

³¹P NMR (CDCl₃, 400 MHz) δ = 35.09.

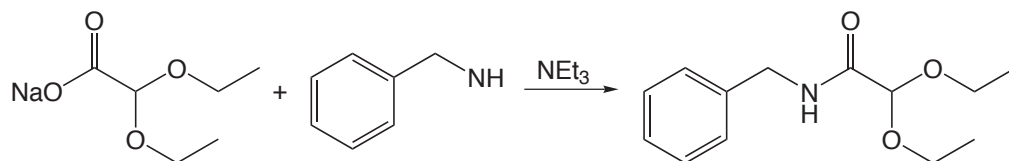
Sodium diethoxyacetate



A solution of sodium hydroxide (1.135 g, 28.4 mmol) in water (5 ml) was added to a solution of ethyl diethoxyacetate (5.000 g, 28.38 mmol) in ethanol (12.5 ml). The resulting mixture was heated at reflux for 5 h then allowed to cool. Evaporation to dryness under reduced pressure yielded an off-white solid, which was dried *in vacuo* and used without further purification or characterisation (4.580 g, 95 %).

ⁱⁱⁱFollowing the procedure of Cullen *et al.*²⁷⁶

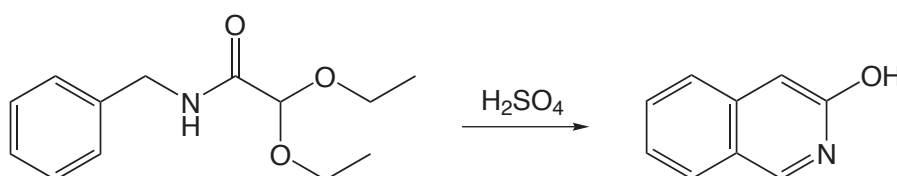
***N*-Benzyl-2,2-diethoxyacetamide**



Sodium diethoxyacetate (2.000 g, 11.76 mmol) was dissolved in dry THF (8 mL) and cooled to 10 °C then thionyl chloride (0.90 mL, 1.468 g, 12.34 mmol) was added under nitrogen. The solution was stirred at 10 °C for 10 min under nitrogen then heated at reflux under nitrogen for 30 min and allowed to cool. A solution of benzylamine (1.258 g, 1.28 mL, 11.73 mmol) and triethylamine (1.189 g, 1.63 mL, 11.74 mmol) was added to the reaction mixture *via* syringe with vigorous stirring. The mixture was heated at reflux for 30 min then cooled to room temperature and poured into ice water (60 mL). The aqueous layer was extracted with toluene (4 × 40 mL) and the organic layers combined, dried over MgSO₄, and the solvent removed under reduced pressure, yielding a yellow-brown residue (0.620 g, 22 %), which was used in its crude state for the next step of the synthesis.

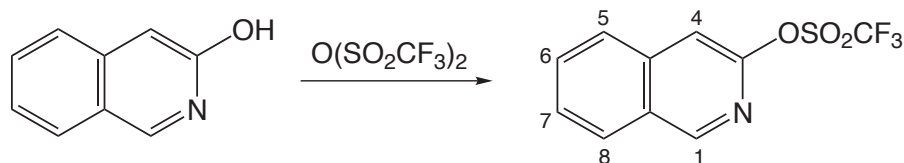
¹H NMR (CDCl₃, 400 MHz) δ = 7.29–7.33 (4H, m), 6.91 (1H, sb, NH), 4.86 (1H, s), 4.49 (2H, d, ³*J* = 6.0), 3.59–2.75 (4H, m), 1.24 (6H, s, CH₃).

Isoquinolin-3-ol



Concentrated sulphuric acid (4 mL) was carefully added to *N*-benzyl-2,2-diethoxyacetate (0.620 g, 2.61 mmol) with stirring at 10 °C. The reaction was stirred at room temperature for 16 h then heated to 60 °C for 1 h. After cooling to room temperature, the mixture was poured into ice water and filtered. The filtrate was neutralised with 35 % aqueous ammonium hydroxide and the organic product extracted into CH₂Cl₂ until the extractions were colourless. The solvent was removed under reduced pressure to give a yellow solid (0.233 g, 61 %), which was used in its crude state for the next step of the synthesis.

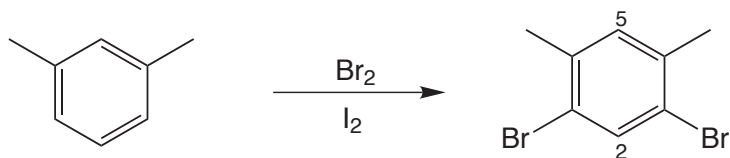
3-Isoquinolyl triflate, 5^{viii}



A flask containing isoquinolin-3-ol (0.215 g, 1.48 mmol) was briefly degassed by evacuating and purging with nitrogen then dry pyridine (10 mL) was added. The solution was cooled to 0 °C and carefully treated with triflic anhydride (0.961 g, 3.407 mmol). The mixture was allowed to warm to room temperature and stirred overnight, then the solvent removed under reduced pressure. Purification was performed by column chromatography (silica, hexane/diethyl ether, 75:25) to yield a white solid (0.246 g, 60 %).

¹H NMR (CDCl₃, 500 MHz) δ = 9.09 (1H, s, H¹) 8.08 (1H, dd, ³J = 8.3, ⁴J = 0.8, H⁵ or H⁸) 7.92 (1H, dd, ³J = 8.3, ³J = 0.8, H⁵ or H⁸), 7.81 (1H, ddd, ³J = 8.2, ³J = 6.9, ⁴J = 1.2, H⁶ or H⁷), 7.70 (1H, ddd, ³J = 8.2, ³J = 6.9, ⁴J = 1.2, H⁶ or H⁷) 7.59 (1H, s, H⁴). MS (ES⁺) m/z 278.1 [M + H]⁺.

1,3-Dibromo-4,6-dimethylbenzene, 6^{iv}



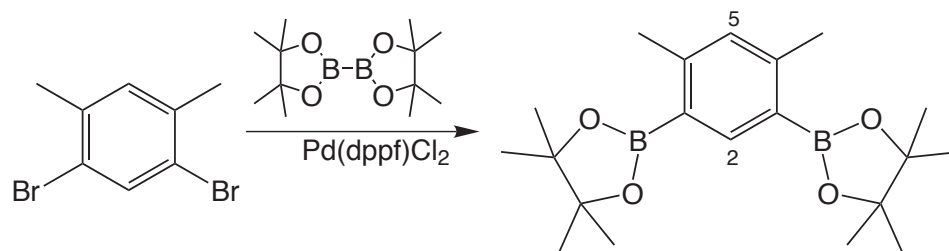
Bromine (13.22 g, 82.71 mmol) was added over 5 min with stirring to *meta*-xylene (3.91 g, 36.83 mmol) followed by addition of iodine (0.15 g, 0.59 mmol) over a further 30 min with stirring. The mixture was stirred at room temperature for an additional 5 h then NaOH solution (4M, 50 mL) was added and the mixture stirred for 15 min. The resulting pale cream precipitate was isolated by filtration, dried *in vacuo* and recrystallised from ethanol to give the product as a crystalline white solid (5.87 g, 60 %).

¹H NMR (CDCl₃, 400 MHz) δ = 7.66 (1H, s, H²), 7.09 (1H, s, H⁵), 2.16 (6H, s, CH₃). ¹³C NMR (CDCl₃, 101 MHz) δ = 137.0, 135.0, 132.5 (C² or C⁵), 122.4 (C² or C⁵), 22.2 (CH₃). MS (ES⁺) m/z 264.0 [M]⁺.

^{viii}Procedure based upon work by Ventura *et al.*¹⁸⁵

^{iv}Procedure as that of Bushby *et al.*,²⁷⁷ following the method of Eckert *et al.*²⁷⁸

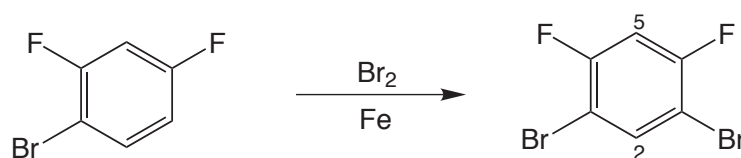
1,3-Di(pinacolatoboron)-4,6-dimethylbenzene 7^{vi}



An oven-dried Schlenk tube was charged with bis(pinacolato)diboron (0.505 g, 1.98 mmol, 2.1 eq.), Pd(dppf)Cl₂ (0.046 g, 0.057 mmol, 6 mol %) and potassium acetate (0.557 g, 5.68 mmol) and degassed 3 times *via* evacuating and backfilling with nitrogen. Dry DMSO (8 mL) was degassed and added under positive pressure of nitrogen together with 1,3-dibromo-4,6-dimethylbenzene (0.250g, 0.950 mmol, 2.1 eq.). The reaction was stirred at 80 °C under nitrogen for 18 h then cooled to room temperature. Toluene (70 mL) was added and the mixture washed with water (3 × 120 mL) to remove DMSO. The organic layer was dried over MgSO₄, filtered and the solvent removed under reduced pressure to produce a brown oil. Purification was carried out by column chromatography (silica, hexane/ethyl acetate, gradient elution from 100:0 to 98:2) to yield a white solid (0.283 g, 69 %).

¹H NMR (CDCl₃, 700 MHz) δ = 8.11 (1H, s, H⁵), 6.97 (1H, s, H²), 2.49 (6H, s, CH₃-Ph), 1.33 (24H, s, CH₃-pin). ¹³C NMR (CDCl₃, 176 MHz) δ = 148.0 (C¹), 143.9 (C⁵), 131.8 (C²), 83.4 (C=O(CH₃)), 25.2 (CH₃), 22.6 (CH₃). MS (ES⁺): *m/z* 376.2 [M + H₂O]⁺. HRMS (ES⁺). Calcd for C₂₀H₃₂B₂NaO₄: *m/z* 379.2468. Found: *m/z* 379.2468 [M + Na]⁺. Elem. anal. Calcd for C₂₀H₃₂B₂O₄: C, 59.07; H, 1.76. Found: C, 58.85; H, 1.79.

1,3-Dibromo-4,6-difluorobenzene, 8^v



1-Bromo-2,4-difluorobenzene (7.53 g, 39.02 mmol) was placed in a 2-neck flask equipped with a dropping funnel and a condenser holding a drying tube filled with KOH. Iron filings (0.100 g, 1.79 mmol) were added and the solution heated to 60 °C. Bromine (9.43 g, 59.0 mmol) was added *via* the dropping funnel dropwise over

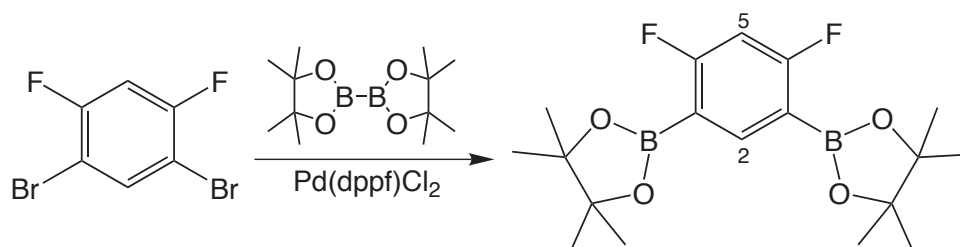
^{vi}Procedure adapted from work by Williams *et al.*¹⁸⁹

^vProcedure as that of Eliseev *et al.*,²⁷⁹ following the method of Kool *et al.*²⁸⁰

1 h. The solution was stirred at 60 °C for an additional 90 min then added to a vigorously stirring solution of NaOH (10 %, 30 mL) and stirred for 15 min. The organic layer was collected and the aqueous layer extracted three times with toluene. The organic layers were combined, dried over MgSO₄ and the solvent removed under reduced pressure, which upon drying *in vacuo* gave a cream solid (5.101 g, 80 %).

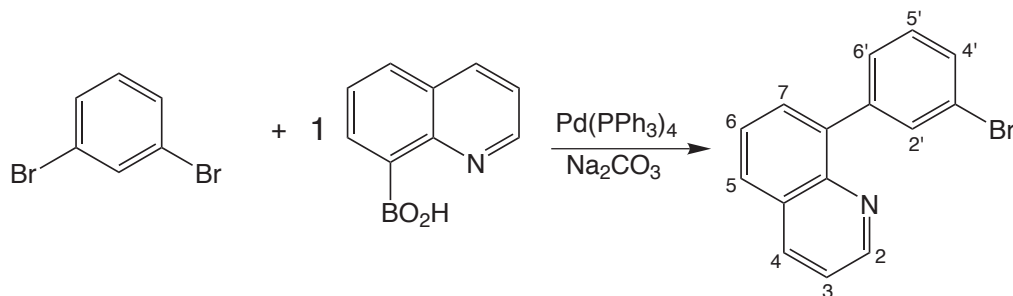
¹H NMR (CDCl₃, 700 MHz) δ = 7.76 (1H, t, 7.2, H⁵), 6.98 (1H, t, 8.1, H²). ¹³C NMR (CDCl₃, 176 MHz) δ = 159.1 (C⁴ or C⁶), 157.7, 136.4 (C⁵), 105.8 (C²), 105.7, 104.7, 104.5. ¹⁹F NMR (CDCl₃, 658 MHz) δ = 103.46 (2F). MS (ES⁺) *m/z* 271.8 [M]⁺.

1,3-Di(pinacolatoboron)-4,6-difluorobenzene, 9



An oven-dried Schlenk tube was charged with bis(pinacolato)diboron (1.520 g, 5.99 mmol), Pd(dppf)Cl₂ (0.093 g, 0.011 mmol) and potassium acetate (1.697 g, 17.10 mmol). Dry DMSO (8 mL) was degassed and added under positive pressure of nitrogen together with 1,3-dibromo-4,6-difluorobenzene (0.775 g, 2.850 mmol). The reaction was stirred at 80 °C under nitrogen for 18 h then cooled to room temperature. Toluene (70 mL) was added and the mixture washed with water (3 × 120 mL) to remove DMSO. The organic layer was dried over MgSO₄, filtered and the solvent removed under reduced pressure to produce a brown oil. Purification was performed by recrystallisation from hexane/diethyl ether to yield the product as a white solid (1.023 g, 98 %). ¹H NMR (CDCl₃, 700 MHz) δ = 8.13 (1H, t, *J*(¹⁹F) = 7.6, H²), 6.73 (1H, t, *J*(¹⁹F) = 9.6, H⁵) 1.36 (24H, s, CH₃). ¹³C NMR (CDCl₃, 176 MHz) δ = 171.6 (C¹), 168.9, 145.8, 103.4 (t, *J*(¹⁹F)), 83.9 (s, OC(CH₃)₂), 24.8 (CH₃). ¹⁹F δ = -94.1 (2F, t, *J*(¹H) = 8.4). MS (ASAP⁺) *m/z* 367.2 [M + H]⁺. HRMS (ES⁺). Calcd for C₂₀H₃₂B₂NaO₄: *m/z* 364.2058. Found: *m/z* 364.2065 [M + Na]⁺. Elem. anal. Calcd for C₂₀H₃₂B₂NaO₄: C, 59.07; H, 1.76. Found: C, 58.85; H, 1.79.

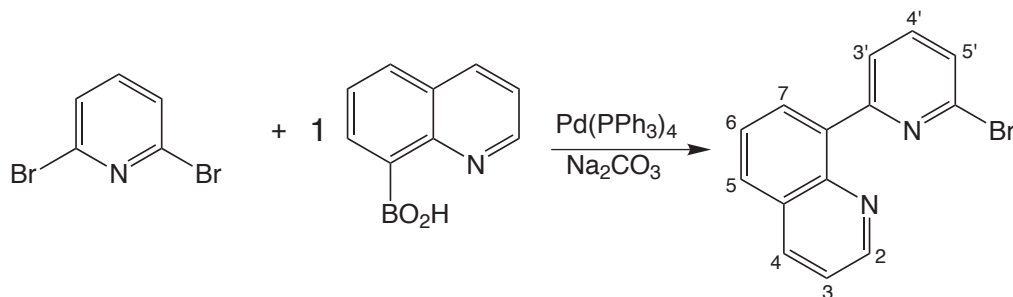
3-Bromo(8-quinolyl)benzene, BrqBz, 15



Procedure A was employed utilising 8-quinolineboronic acid (0.525 g, 3.03 mmol) and 1,3-dibromobenzene (0.480 g, 2.03 mmol), Na_2CO_3 (0.645 g, 2M aq.), $\text{Pd}(\text{PPh}_3)_4$ (0.050 g, 0.043 mmol), toluene (6 mL), ethanol (6 mL) and water (3 mL). After extraction into CH_2Cl_2 and removal of solvent, a light brown oil was obtained. Purification was carried out by column chromatography (silica, hexane/diethyl ether, gradient elution from 100:0 to 85:15) to produce a colourless oil (0.550 g, 95 %).

^1H NMR (CDCl_3 , 700 MHz) δ = 8.96 (1H, dd, 3J = 2.8, 4J = 1.4, H^2), 8.22 (1H, dd, 3J = 8.4, 4J = 2.1, H^4), 7.84–7.86 (2H, m, $\text{H}^{2'}$ and $\text{H}^{6'}$), 7.71 (1H, 3J = 7.7, 4J = 1.4, $\text{H}^{4'}$), 7.64 (1H, d, 3J = 7.7, H^7), 7.61 (1H, t, 3J = 6.3, $\text{H}^{5'}$), 7.55 (1H, d, 3J = 7.7, H^5), 7.44 (1H, dd, 3J = 8.4, 4J = 4.2, H^3), 7.36 (1H, t, 3J = 7.7, H^6). ^{13}C NMR (CDCl_3 , 176 MHz) δ = 150.7 (C^2), 146.0 (C^q), 141.8 (C^q), 136.5 (C^4), 133.7 ($\text{C}^{2'}$), 130.6 (C^7), 130.5 ($\text{C}^{4'}$), 129.7 (C^5 or C^6), 129.6 (C^5 or C^6), 128.9 (C^q), 128.3 ($\text{C}^{6'}$), 126.5 ($\text{C}^{5'}$), 122.3 (C^q), 121.4 (C^3). MS (ES^+) m/z 283.9 [M] $^+$, 281.9 [M] $^+$. HRMS (ES^+). Calcd for $\text{C}_{15}\text{H}_{11}\text{BrN}$: m/z 284.0075. Found: m/z 284.0070 [$\text{M} + \text{H}$] $^+$.

3-Bromo(8-quinolyl)pyridine, qBrpy, 19

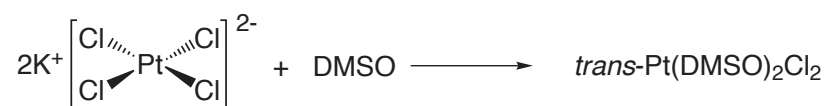


Procedure A was employed utilising 8-quinolineboronic acid (0.166 g, 0.960 mmol) and 2,6-dibromopyridine (0.250 g, 1.055 mmol), Na_2CO_3 (0.645 g, 2M aq.), $\text{Pd}(\text{PPh}_3)_4$ (0.050 g, 0.046 mmol), toluene (6 mL), ethanol (6 mL) and water (3 mL). After extraction into CH_2Cl_2 and removal of solvent, a light brown oil was obtained.

Purification was carried out by column chromatography (silica, hexane/ethyl acetate, gradient elution from 100:0 to 80:20) to produce a colourless oil (0.171 g, 63 %).

^1H NMR (CDCl_3 , 400 MHz) δ = 8.95 (1H, dd, 3J = 4.0, 4J = 1.6, H²) 8.19–8.25 (3H, m), 7.87 (1H, dd, 3J = 8.0, 4J = 1.6), 7.67 (2H, t, 3J = 7.6), 7.49 (1H, dd, 3J = 8.0, 4J = 0.8), 7.45 (1H, dd, 3J = 8.2, 4J = 4.0). ^{13}C NMR (CDCl_3 , 101 MHz) δ = 157.9, 150.4, 145.6, 141.6, 137.8, 136.9, 136.5, 131.7, 129.4, 128.6, 126.5, 126.4, 126.0, 121.1. MS (ES⁺) m/z 285.2 [M + H]⁺. Elem anal. Calcd for $\text{C}_{14}\text{H}_9\text{BrN}_2$: C, 58.97; H, 3.18; N, 9.82. Found: C, 58.04; H, 3.39; N, 9.32.

***Trans*-Bis(dimethylsulfoxide)dichloroplatinum** $[\text{Cl}_2\text{Pt}(\text{DMSO})_2]^{ix}$

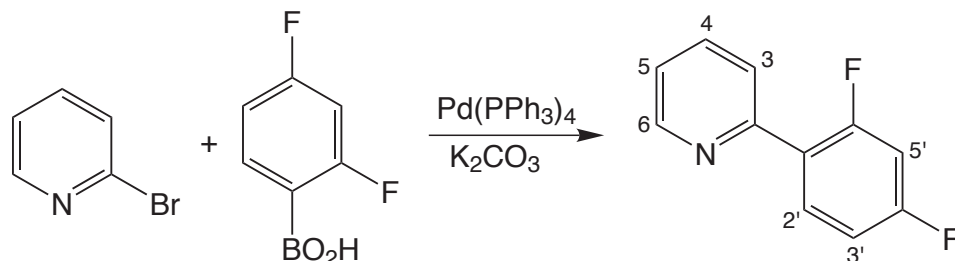


K_2PtCl_4 (0.100 g, 0.240 mmol) was suspended in water (2 mL) and the solution briefly degassed three times *via* evacuating and purging with nitrogen. DMSO (0.20 mL) was added and the mixture was stirred at room temperature overnight (red colouration disappeared after *ca.* 30 min). The white precipitate was collected by centrifugation and washed with water (3×5 mL), ethanol (1×5 mL) and diethyl ether (1×5 mL) then dried *in vacuo* to yield the desired precursor as a white solid (0.073 g, 91 %), which was used as a platinum source with no further purification or characterisation.

^{ix}Following the procedure of Puddephatt.¹⁹⁹

6.5.3 Ligands

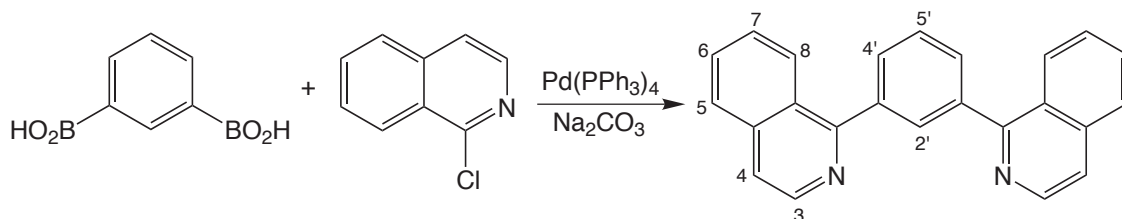
2-(4,6-Difluorophenyl)pyridine[dFppy], **24**^x



A Schlenk tube was charged with 2-bromopyridine (0.179 g, 1.13 mmol), 2,4-difluorophenylboronic acid (0.163 g, 1.03 mmol), K_2CO_3 (1.24 g, 9.00 mmol), water (1.0 mL) and 1,2-dimethoxyethane (10 mL). The Schlenk tube was degassed *via* four freeze-pump-thaw cycles and charged with nitrogen. $\text{Pd(PPh}_3)_4$ (0.065 g, 0.056 mmol) was added under positive pressure of nitrogen, and the apparatus evacuated and charged with nitrogen. The solution was stirred at 85 °C under nitrogen for 24 h then cooled to room temperature. 1,2-Dimethoxyethane was removed under reduced pressure and the resulting residue was dissolved in CH_2Cl_2 (40 mL). The organic layer was washed with aqueous KOH (1M, 3×100 mL), dried over MgSO_4 and the solvent removed under reduced pressure to yield a translucent oil. Purification was achieved by column chromatography (silica, hexane/diethyl ether, gradient elution from 100:0 to 96:4) to yield a colourless oil (0.36 g, 62 %). $^1\text{H NMR}$ (CDCl_3 , 400 MHz) δ = 8.71 (1H, d, 3J = 4.7, H^6), 8.00 (1H, td, 3J = 8.6, 4J = 6.6, $\text{H}^{2'}$), 7.65–7.79 (2H, m, H^3 and H^4), 7.26 (1H, m, H^5), 7.01 (1H, td, 3J = 8.2, 4J = 2.1, $\text{H}^{3'}$) 6.90–7.10 (1H, m, $\text{H}^{5'}$). MS (ES^+) m/z 193.4 [$\text{M} + \text{H}$]⁺.

^xProcedure based on work by Suzuki *et al.*^{281,282}

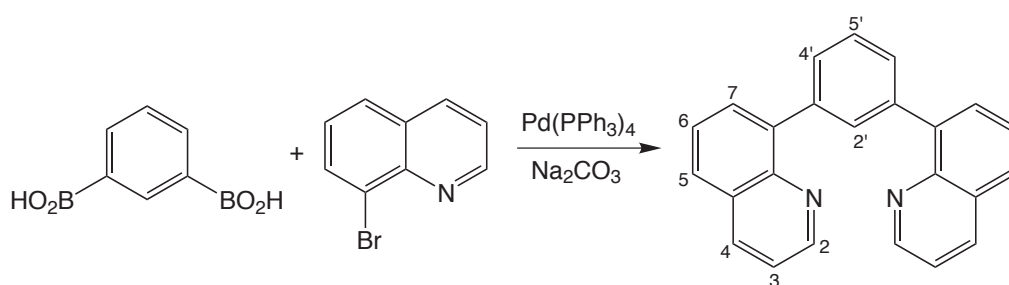
1,3-Di(1-isoquinolyl)benzene [1-diqb] 1^{xi}



Procedure A was followed using benzene-1,3-diboronic acid (0.152 g, 0.917 mmol), 1-chloroisoquinoline (0.297 g, 1.82 mmol), Na₂CO₃ (0.645 g, 2M aq.), and Pd(PPh₃)₄ (0.030 g, 0.026 mmol) in toluene (6 mL), ethanol (6 mL) and water (3 mL). After work-up, the combined CH₂Cl₂ extracts were evaporated to dryness under reduced pressure to yield a yellow solid, which was recrystallised from acetonitrile to give the desired product as a pale yellow solid (0.250 g, 82 %).

¹H NMR (CDCl₃, 500 MHz) δ = 8.63 (2H, d, ³J = 5.6, H³), 8.20 (2H, d, ³J = 8.4, H⁸), 8.04 (1H, s, H^{2'}), 7.89 (2H, d, ³J = 8.0, H⁵), 7.86 (2H, dd, ³J = 7.4, ⁴J = 1.2, H^{4'}), 7.65–7.76 (5H, m, H⁴, H^{5'} and H⁶), 7.55 (2H, t, ³J = 8.0, H⁷). ¹³C NMR (CDCl₃, 126 MHz) δ = 160.6 (C^q), 142.5 (C³), 140.0 (C^q), 137.1 (C^q), 131.7 (C^{2'}), 130.4 (C^{4'}), 130.3 (C^{5'}), 128.8 (C⁴), 127.9 (C⁸), 127.6 (C⁷), 127.2 (C⁵), 127.0 (C^q), 120.3 (C⁶). MS (ES⁺) *m/z* 332.1 [M]⁺. HRMS (ES⁺) Calcd for C₂₄H₁₇N₂: *m/z* 333.1392. Found: *m/z* 333.1409 [M + H]⁺. Elem. anal. Calcd for C₂₄H₁₆N₂: C, 86.72; H, 4.95; N, 8.43. Found: C, 86.61; H, 4.90; N, 8.43. Mp = 132–134 °C.

1,3-Di(8-quinolyl)-benzene [8-dqb] 2

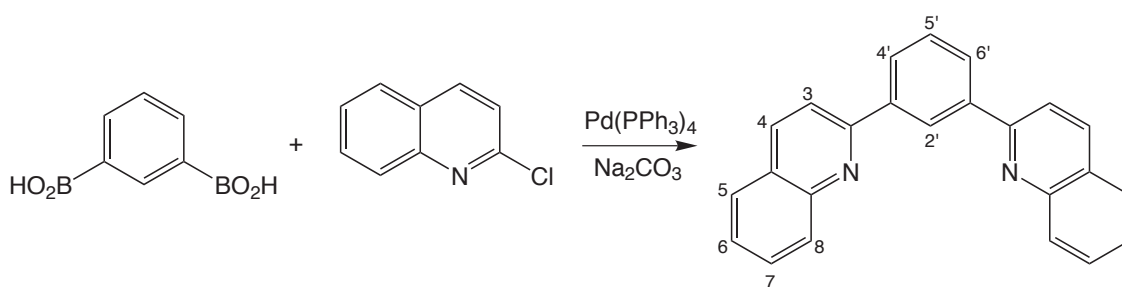


Procedure A was followed using benzene-1,3-diboronic acid (0.100 g, 0.603 mmol), 8-bromoquinoline (0.250 g, 1.201 mmol), Pd(PPh₃)₄ (0.030 g, 0.026 mmol), Na₂CO₃ (0.0645 g, 2M aq.), toluene (6 mL), ethanol (6 mL) and water (3 mL). After work-up and removal of CH₂Cl₂, a translucent oily solid was obtained. Purification was carried out by column chromatography (silica, hexane/ethyl acetate, gradient elution from 100:0 to 70:30) to yield a white solid (0.152 g, 76 %).

^{xi}Synthesis of this ligand was recently reported *via* an alternative route by Li *et al.*¹⁹²

^1H NMR (CDCl_3 , 500 MHz) δ = 8.98 (2H, dd, 3J = 5.0, 4J = 1.6, H^2), 8.21 (2H, dd, 3J = 8.2, 4J = 2.0, H^4), 7.99 (1H, s, $\text{H}^{2'}$), 7.78–7.87 (6H, m, H^6 , H^5 and $\text{H}^{4'}$), 7.60–7.63, (3H, m, H^6 and $\text{H}^{5'}$), 7.42 (2H, dd, 3J = 8.4, 3J = 4.0, H^3). ^{13}C NMR (CDCl_3 , 126 MHz) δ = 157.0, 150.5 (C^2), 150.1, 146.3, 145.7, 141.1, 139.4, 136.5 (C^4), 133.0 ($\text{C}^{2'}$), 130.8, 129.7, 126.6, 121.7, 121.2 (C^3). MS (ES^+) m/z 332.3 $[\text{M}]^+$. HRMS (ES^+). Calcd for $\text{C}_{24}\text{H}_{17}\text{N}_2$: m/z 333.1392. Found: m/z 333.1389 $[\text{M} + \text{H}]^+$. Elem. anal. Calcd for $\text{C}_{24}\text{H}_{16}\text{N}_2$: C, 86.72; H, 4.93; N, 8.43;. Found: C, 86.47; H, 4.93; N, 8.43. Mp = 130–132 °C.

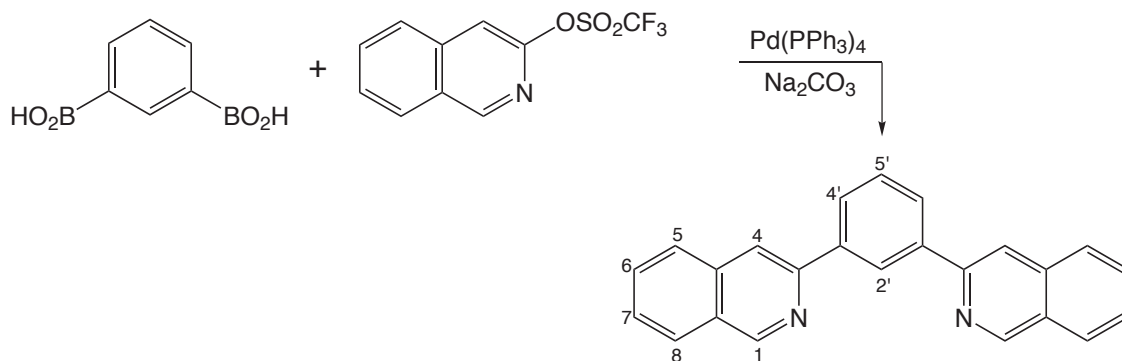
1,3-Di(2-quinoly)benzene [2-dqb] **3**



Procedure A was employed using benzene-1,3-diboronic acid (0.101 g, 0.611 mmol), 2-chloroquinoline (0.200 g, 1.22 mmol), Na_2CO_3 (0.645 g, 2M aq.) and $\text{Pd}(\text{PPh}_3)_4$ (0.030 g, 0.026 mmol) in toluene (6 mL), ethanol (6 mL) and water (3 mL). After work-up, CH_2Cl_2 was removed and the brown solid obtained was recrystallised from acetonitrile to yield a pale yellow solid (0.117 g, 58 %).

^1H NMR (CDCl_3 , 500 MHz) δ = 8.83 (2H, d, 4J = 3.5, $\text{H}^{2'}$), 8.29 (4H, td, 3J = 8.5, 4J = 2.0, $\text{H}^{4'}$, and H^3 or H^4), 8.23 (2H, d, 3J = 8.5, H^8), 8.04 (2H, d, 3J = 8.5, H^3 or H^4), 7.87 (2H, d, 3J = 9.0, H^5), 7.76 (2H, td, 3J = 7.5, 4J = 1.0, H^7), 7.71 (1H, t, 3J = 8.0, $\text{H}^{5'}$), 7.56 (2H, td, 3J = 8.5, 4J = 1.0, H^6). ^{13}C NMR (CDCl_3 , 126 MHz) δ = 157.4, 148.6, 140.5, 137.1, 130.0, 129.7 (C^8), 128.8 (C^7 or $\text{C}^{5'}$), 127.8 ($\text{C}^{4'}$ or C^3 or C^4), 127.5 (C^5), 127.2, 127.0 ($\text{C}^{2'}$), 126.6 (C^6), 119.4 ($\text{C}^{4'}$ or C^3 or C^4). MS (ES^+) m/z 333.2 $[\text{M} + \text{H}]^+$. HRMS (ES^+). Calcd for $\text{C}_{24}\text{H}_{17}\text{N}_2$: m/z 333.1392. Found: m/z 333.1390 $[\text{M} + \text{H}]^+$. Elem. anal. Calcd for $\text{C}_{24}\text{H}_{16}\text{N}_2$: C, 86.72; H, 4.85; N, 8.43. Found: C, 86.43; H, 4.88; N, 8.60. Mp = 140–142 °C.

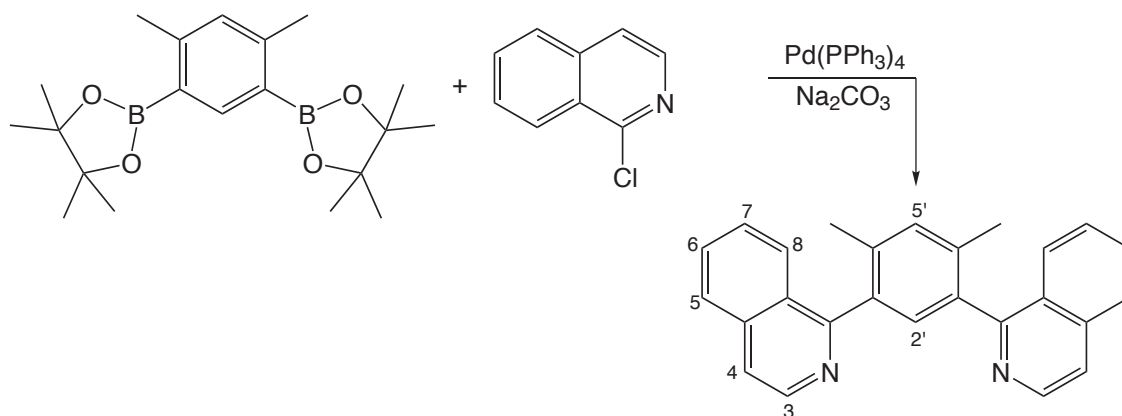
1,3-Di(3-isoquinolyl)benzene [3-diqb] 4 ^{xii}



Procedure A was followed employing 3-isoquinolyl triflate (0.105 g, 0.379 mmol), benzene-1,3-diboronic acid (0.031 g, 0.189 mmol), Na₂CO₃ (0.645 g, 2M aq.) and Pd(PPh₃)₄ (0.013 g 0.011 mmol), toluene (6 mL), ethanol (6 mL) and water (3 mL). CH₂Cl₂ was removed under reduced pressure to yield an oily yellow solid. Purification was performed by column chromatography (silica, hexane/ethyl acetate, gradient elution from 100:0 to 90:10) to give the product as a white solid (0.047g, 75 %).

¹H NMR (CDCl₃, 700 MHz) δ = 9.39 (2H, s, H¹), 8.91 (1H, s, H^{2'}), 8.24 (2H, s, H⁴) 8.22 (2H, dd, ³J = 5.6, ⁴J = 1.7, H^{4'}), 8.02 (2H, d, ³J = 8.4, H⁸), 7.93 (2H, d, ³J = 8.4, H⁵), 7.72 (2H, td, ³J = 7.4, ³J = 0.7, H⁶), 7.67 (1H, t, ³J = 7.7, H^{5'}), 7.61 (2H, td, ³J = 7.3, ⁴J = 1.0, H⁷). ¹³C NMR (CDCl₃, 176 MHz) δ = 152.7 (C¹), 151.4 (C⁹), 144.3 (C⁹), 136.9 (C⁹), 130.8 (C⁶), 129.5 (C^{5'}), 128.1 (C⁹), 127.8 (C⁸), 127.4 (C^{4'} or C⁷), 127.3 (C^{4'} or C⁷), 127.2 (C⁵), 125.8 (C^{1'}), 117.0 (C⁴). MS (ES⁺) *m/z* 333.1 [M + H]⁺. HRMS (ES⁺) Calcd for C₂₄H₁₇N₂ *m/z* 333.1392. Found *m/z* 333.1385 [M + H]⁺. Mp = 137–139 °C.

1,3-Di(1-isoquinolyl)-4,6-dimethylbenzene [1-diqMeb] 10

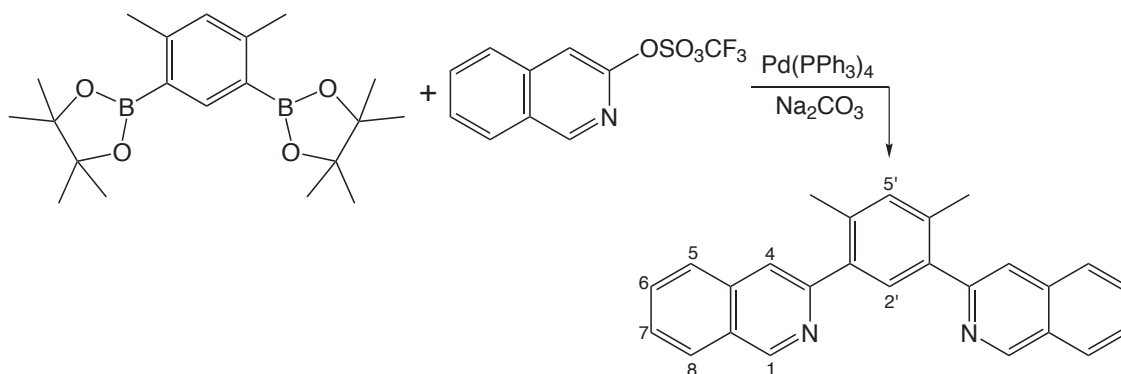


^{xii}Synthesis of this ligand was recently reported *via* an alternative route by Li *et al.*¹⁹²

Procedure A was followed using 1-chloroisoquinoline (0.158 g, 0.968 mmol), 1,3-di(pinacolatoboron)-4,6-dimethylbenzene (0.165 g, 0.461 mmol), K₂CO₃ (0.207 g, 1.50 mmol) and Pd(PPh₃)₄ (0.030 g, 0.026 mmol) in toluene (3 mL), ethanol (3 mL) and water (1.5 mL). After work-up, removal of CH₂Cl₂ yielded a dark yellow oily solid. Purification was performed by column chromatography (silica, hexane/ethyl acetate, gradient elution from 100:0 to 82.5:17.5) to yield the desired product as a white solid (0.126 g, 76 %).

¹H NMR (CDCl₃, 700 MHz) δ = 8.59 (2H, d, ³J = 2.1, H³), 7.81 (4H, d, ³J = 8.4, two of H⁵, H⁶, H⁷ and H⁸), 7.62 (4H, m, H⁴, and H⁵ or H⁶ or H⁷ or H⁸), 7.45 (2H, t, ³J = 7.7, H⁶ or H⁷), 7.35 (1H, s, H^{2'} or H^{5'}), 7.33 (1H, s, H^{2'} or H^{5'}), 2.09 (6H, s, CH₃). ¹³C NMR (CDCl₃, 176 MHz) δ = 161.3 (C^q), 142.2 (C³), 136.9 (C^q), 136.6 (C^q), 132.5 (C^{2'} or C^{5'}), 130.9 (C^{2'} or C^{5'}), 130.4, 128.2, 127.8 (C⁶ or C⁷), 127.5 (C⁶ or C⁷), 126.9, 126.3 (C^q), 120.1, 19.8 (CH₃). MS (ES⁺) *m/z* 361.2 [M + H]⁺, 721.3 [2M + H]⁺. HRMS (ES⁺). Calcd for C₂₆H₂₁N₂: *m/z* 361.1705. Found: *m/z* 361.1715 [M + H]⁺. Mp = 147–148 °C.

1,3-Di(3-isoquinolyl)-4,6-dimethylbenzene [3-diqMeb] 11

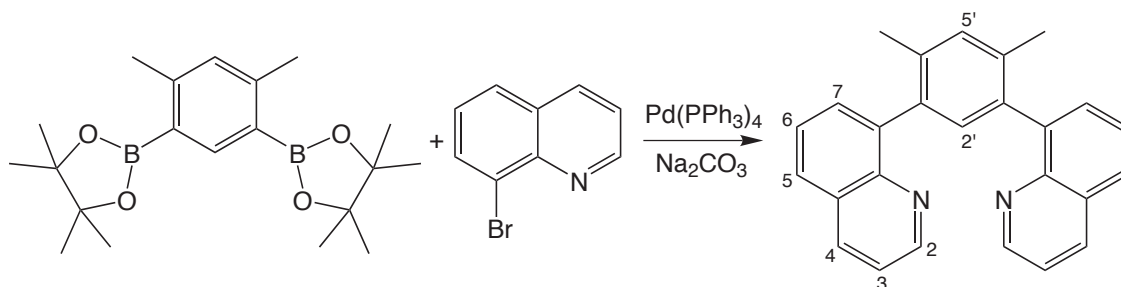


Procedure A was employed using 3-isoquinolyl triflate (0.228 g, 0.821 mmol), 1,3-bis(pinacolatoboron)-4,6-dimethylbenzene (0.140 g, 0.391 mmol), Na₂CO₃ (0.645 g, 2M aq.) and Pd(PPh₃)₄ (0.030 g, 0.026 mmol) in toluene (6 mL), ethanol (6 mL) and water (3 mL). After work-up, CH₂Cl₂ was removed under reduced pressure to give a brown solid, which was taken into hexane and diethyl ether then filtered. The solvent was removed under reduced pressure and purification carried out by column chromatography (hexane/ethyl acetate, gradient elution from 100:0 to 85:15) to yield a colourless oil (0.128 g, 91 %).

¹H NMR (CDCl₃, 700 MHz) δ = 9.32 (2H, s, H¹), 7.98 (2H, d, ³J = 7.7, H⁸), 7.81 (2H, d, ³J = 7.7, H⁵), 7.79 (2H, s, H⁴), 7.69 (3H, td, ³J = 7.7, ⁴J = 2.0, H⁶, and H^{2'} or H^{5'}), 7.57 (2H, t, ³J = 8.4, H⁷), 7.27 (1H, s, H^{2'} or H^{5'}). ¹³C NMR (CDCl₃, 176 MHz) δ = 153.8 (C^q), 152.0 (C¹), 138.4 (C^q), 136.5 (C^q), 136.2 (C^q),

133.6 (C^{2'} or C^{5'}), 132.1 (C⁶ or C^{2'} or C^{5'}), 130.6 (C⁶ or C^{2'} or C^{5'}), 127.7 (C⁸), 127.4 (C⁹), 127.2 (C⁷), 126.9 (C⁵), 120.4 (C⁴), 25.1 (CH₃). MS (ES⁺) 361.3 [M + H]⁺, 721.5 [2M + H]⁺. HRMS (ES⁺). Calcd for C₂₆H₂₁N₂: *m/z* 361.1705. Found: *m/z* 361.1711 [M + H]⁺.

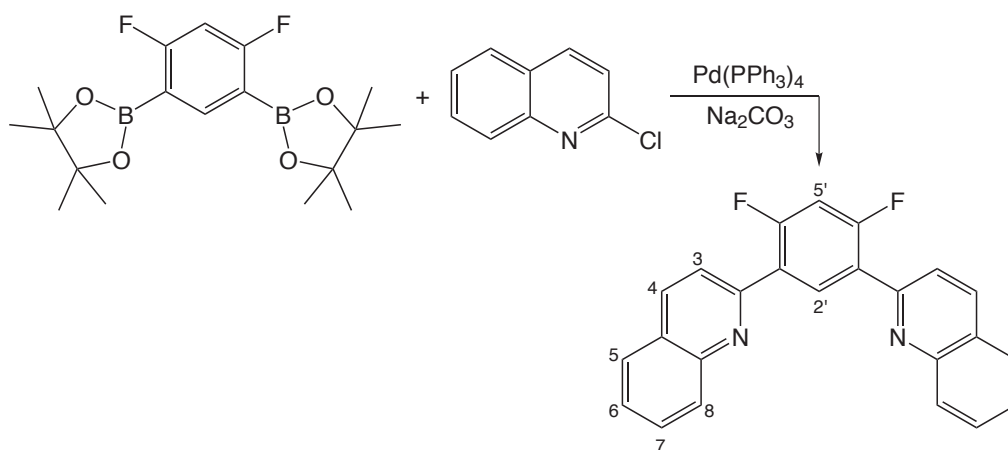
1,3-di(8-Quinoly)-4,6-dimethylbenzene [8-dqMeb] 12



Procedure A was followed using 8-bromoquinoline (0.116 g, 0.560 mmol), 1,3-di(pinacolatoboron)-4,6-dimethylbenzene (0.100 g, 0.280 mmol), Na₂CO₃ (0.645 g, 2M aq.) and Pd(PPh₃)₄ (0.030g, 0.026 mmol) in ethanol (6 mL), toluene (6 mL) and water (3 mL). After work-up and removal of CH₂Cl₂, a light brown oil was obtained. Purification was carried out by column chromatography (silica, hexane/diethyl ether, gradient elution from 100:0 to 65:35) to produce a colourless oil (0.059 g, 58 %).

¹H NMR (CDCl₃, 400 MHz) δ = 8.83 (2H, m, H²), 8.18 (2H, d, ³*J* = 8.0, H⁴), 7.81 (2H, d, ³*J* = 8.0), 7.69 (2H, dd, ³*J* = 7.0, ⁴*J* = 1.6), 7.53–7.57 (2H, m), 7.32–7.39 (2H, m), 7.18–7.27 (2H, m). MS (ES⁺) *m/z* 361.2 [M + H]⁺. HRMS (ES⁺). Calcd for C₂₆H₂₁N₂: *m/z* 361.1705. Found: *m/z* 361.1704 [M + H]⁺.

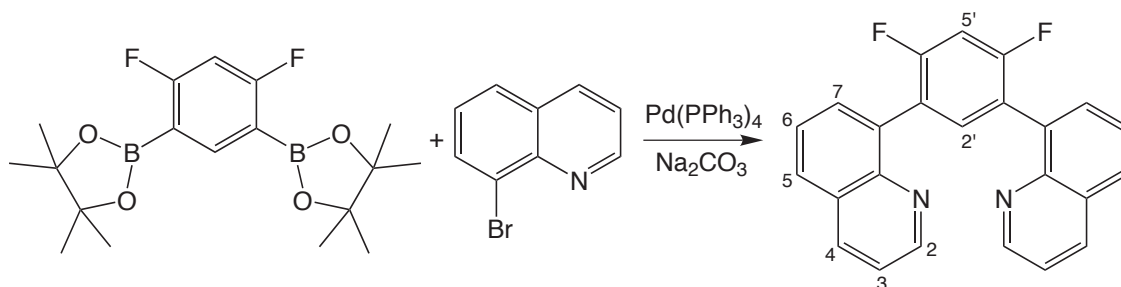
1,3-Di(2-quinoly)-4,6-difluorobenzene [2-dqFb] 13



Procedure A was followed using 2-chloroquinoline (0.107 g, 0.658 mmol), 1,3-di(pinacolatoboron)-4,6-difluorobenzene (0.120 g, 0.328 mmol), Na₂CO₃ (0.645 g, 2M aq.) and Pd(PPh₃)₄ (0.030 g, 0.026 mmol) in toluene (6 mL), ethanol (6 mL) and water (3 mL). After extraction, CH₂Cl₂ was removed under reduced pressure to yield a pale orange solid. Purification by column chromatography (silica, hexane/diethyl ether, gradient elution from 100:0 to 80:20) afforded the product as a white solid (0.096 g, 79 %).

¹H NMR (CDCl₃, 500 MHz) δ = 8.83 (1H, t, ³J = 9.0, H^{5'}), 8.26 (2H, d, ³J = 8.0, H³ or H⁴), 8.18 (2H, d, ³J = 9.0, H⁵ or H⁸), 7.88 (4H, t, ³J = 9.5, H³ or H⁴, and H⁵ or H⁸), 7.74 (2H, td, ³J = 7.7, ³J = 1.5, H⁶ or H⁷), 7.57 (2H, td, ³J = 7.0, ³J = 1.0, H⁶ or H⁷), 7.12 (1H, t, ³J = 10.5, H^{2'}). ¹³C NMR (CDCl₃, 126 MHz) δ = 162.4, 160.3, 153.3, 148.6, 136.6, 134.9, 130.0, 127.7, 127.5, 127.0, 125.5, 122.4, 105.3 (CF₃). ¹⁹F NMR (CDCl₃, 470 MHz) δ = 112.2 (2F, s). MS (ES⁺) 369.4 [M + H]⁺. HRMS (ES⁺). Calcd for C₂₄H₁₅N₂F₂: *m/z* 369.1203. Found: *m/z* 369.1199 [M + H]⁺. Elem. anal. Calcd for C₂₄H₁₅N₂F₂: C, 78.25; H, 3.83; N, 7.60. Found: C, 77.88; H, 3.77; N, 5.72. Mp = 231–232 °C.

1,3-Di(8-quinolyl)-4,6-difluorobenzene [8-dqFb] 14



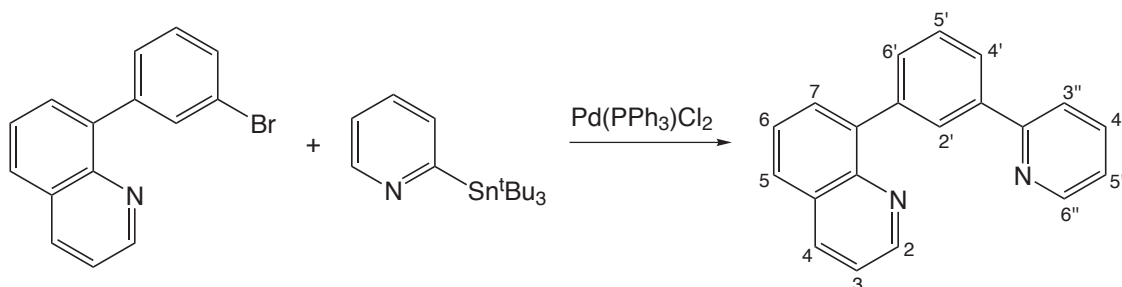
Procedure A was followed using 8-bromoquinoline (0.109 g, 0.694 mmol), 1,3-di(pinacolatoboron)-4,6-difluorobenzene (0.121 g, 0.331 mmol), Na₂CO₃ (0.645 g, 2M aq.), Pd(PPh₃)₄ (0.035 g, 0.026 mmol) in toluene (6 mL), ethanol (6 mL) and water (3 mL). After work-up and removal of CH₂Cl₂, a yellow-brown solid was obtained, which was recrystallised from ethanol and a minimal amount of hexane to yield the product as a pale yellow solid (0.077 g, 63 %).

¹H NMR (CDCl₃, 700 MHz) δ = 8.93 (2H, s, H²), 8.17 (2H, d, ³J = 8.2, H⁴), 8.12 (2H, d, ³J = 8.5, H⁵ or H⁷), 7.83 (2H, d, ³J = 8.1, H⁵ or H⁷), 7.35 (1H, t, ³J = 7.6, H^{2'} or H^{5'}), 7.31 (2H, t, ³J = 7.0, H⁶), 7.55 (2H, t, ³J = 7.5, H³), 7.13 (1H, t, ³J = 9.5, H^{2'} or H^{5'}). ¹³C NMR (CDCl₃, 176 MHz) δ = 161.2 (C^q), 159.2 (C^q), 150.7 (C²), 146.5 (C^q), 136.5 (C⁴), 135.5 (C⁶), 135.0 (C^q), 131.5 (C⁵ or C⁷), 128.8 (C⁵ or C⁷), 126.4 (C^{2'} or C^{5'}), 123.2 (C^q), 121.5 (C³), 104.3 (C^{2'} or C^{5'}). ¹⁹F

NMR (CDCl₃, 658 MHz) δ = 110.3 (2F, s). MS (ES⁺) 368.8 [M]⁺, 370.8 [M + 2H]⁺. HRMS (ES⁺). Calcd for C₂₄H₁₅N₂F₂: m/z 369.1203. Found: m/z 369.1201 [M + H]⁺. Mp = 190–191 °C.

This ligand was also produced using the Buchwald procedure¹⁹⁰ in an attempt to synthesise the mono-substituted product as a precursor for another ligand. The disubstituted ligand was formed preferentially over the mono-substituted product even when reducing the reaction time to 2 h and using a slight excess of the boronic ester. Characterisation data was the same as for using the standard Suzuki method.

1-(8-Quinoly)-3-(2-pyridyl)benzene [qpyb] 16

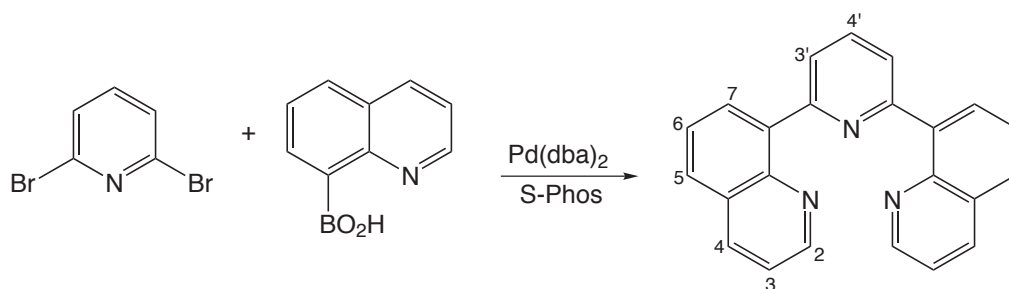


3-bromo(8-quinoly)benzene (0.220 g, 0.774 mmol), 2-tri-*n*-butylstannylpyridine (0.40 mL, 0.610 g, 1.64 mmol), lithium chloride (0.114 g, 2.700 mmol) and bis(triphenylphosphine)palladium(II) dichloride (0.010 g, 0.050 mmol) were combined in toluene (12 mL), degassed by four freeze-pump-thaw cycles and heated at reflux under nitrogen for 45 h. The resultant black solution was stirred with saturated potassium fluoride solution (12 mL) for 30 min then the tin residues were filtered off and washed with toluene. The combined washings and filtrate were evaporated to dryness then taken into CH₂Cl₂ (45 mL) and washed with sodium bicarbonate solution (10%, 3 × 35 mL). The organic layer was dried over MgSO₄ and the solvent removed under reduced pressure to yield a brown oil. Purification was performed by column chromatography (silica, hexane/diethyl ether, gradient elution from 100:0 to 65:35) to give the desired product as a colourless oil (0.142 g, 65 %).

¹H NMR (CDCl₃, 700 MHz) δ = 8.96 (1H, dd, ³*J* = 4.5, ⁴*J* = 1.4, H²), 8.70 (1H, dd, ³*J* = 4.5, ⁴*J* = 0.7, H^{6''}), 8.30 (1H, s, H^{2'}), 8.22 (1H, dd, ³*J* = 8.0, ⁴*J* = 1.4, H⁴), 8.05 (1H, dd, ³*J* = 8.4, ⁴*J* = 1.4, H^{6'}), 7.76–7.86 (4H, m, H⁵, H⁶, H^{5'} and H^{3''}), 7.75 (2H, td, ³*J* = 8.1, ⁴*J* = 2.1, H^{4''}), 7.62 (2H, dd, ³*J* = 7.7, ³*J* = 5.6, H⁷ and H^{4'}), 7.42 (1H, dd, ³*J* = 8.4, ³*J* = 4.9, H³), 7.23 (1H, td, ³*J* = 7.3, ⁴*J* = 1.4, H^{5''}). ¹³C NMR (CDCl₃, 176 MHz) δ = 157.9 (C^q), 150.6 (C²), 149.9 (C^{6''}), 146.3

(C^q), 141.0 (C^q), 140.3 (C^q), 139.4 (C^q), 136.9 (C^{4''}), 136.5 (C⁴), 131.6 (C^{5'}), 130.7 (C⁵ or C⁶), 129.4 (C^q), 129.0 (C^{2'}), 128.6 (C⁷), 127.9 (C⁵ or C⁶), 126.5 (C^{4'}), 126.2 (C^{6'}), 122.2 (C^{5''}), 121.2 (C³), 121.0 (C^{3''}). MS (ES⁺) m/z 283.2 [M + H]⁺. HRMS (ES⁺). Calcd for C₂₀H₁₅N₂: m/z 283.1235. Found: m/z 283.1232 [M + H]⁺.

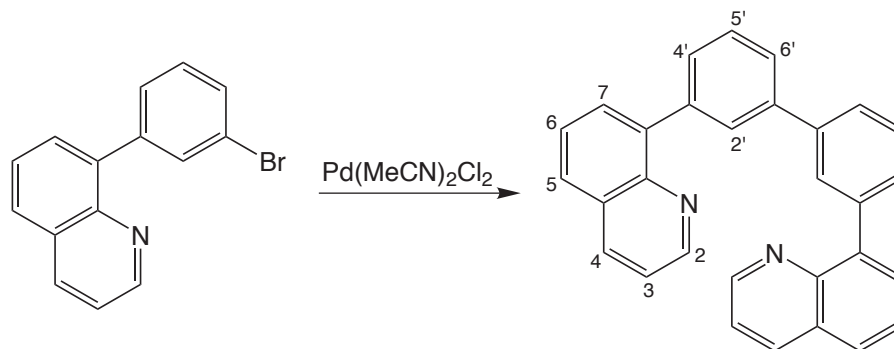
2,6-Di(8-quinoly)pyridine [dqp] 17^{xiii}



An oven-dried Schlenk tube was charged with 8-quinolineboronic acid (0.207 g, 1.20 mmol), 2,6-dibromopyridine (0.133 g, 0.56 mmol), Pd(dba)₂ (0.007g, 0.0012 mmol), 2-dicyclohexylphosphino-2',6'-dimethoxybiphenyl (S-Phos) (0.010 g, 0.0006 mmol) and ground K₃PO₄ (1.14 g, 5.35 mmol). The Schlenk tube was degassed three times *via* evacuating and backfilling with nitrogen then dry toluene (5 mL) was added *via* syringe. The suspension was further degassed *via* four freeze-pump-thaw cycles and stirred at 100 °C under nitrogen for 20 h. The mixture was cooled to room temperature, diluted with CH₂Cl₂ (20 mL) and filtered. The solvent was removed under reduced pressure to yield a yellow solid, which required no further purification (0.179 g, 96 %).

¹H NMR (CDCl₃, 500 MHz) δ = 9.00 (2H, dd, ³*J* = 4.0, ⁴*J* = 1.5, H²), 8.24 (4H, dd, ³*J* = 7.5, ⁴*J* = 1.0, H⁴ and H⁷), 8.08 (2H, d, ³*J* = 8.0, H^{3'}), 7.95 (2H, t, ³*J* = 8.0, H^{4'}), 7.88 (2H, dd, ³*J* = 7.5, ⁴*J* = 1.0, H⁵), 7.66 (2H, td, ³*J* = 8.0, ⁴*J* = 0.8, H⁶), 7.45 (2H, dd, ³*J* = 8.2, ⁴*J* = 4.0, H³). ¹³C NMR (CDCl₃, 126 MHz) δ = 157.1 (C^q), 150.5 (C²), 146.2 (C^q), 139.7 (C^q), 136.7 (C⁴ or C⁷), 135.2 (C^q), 131.8 (C⁴ or C⁷), 128.9 (C⁵ or C^{4'}), 128.8 (C⁵ or C^{4'}), 126.9 (C⁶), 125.7 (C^{3'}), 121.2 (C³). MS (ES⁺) m/z 333.4 [M]⁺. HRMS (ES⁺) Calcd for C₂₄H₁₇N₂: m/z 333.1392. Found: m/z 333.1409 [M + H]⁺. Mp = 159–160 °C.

^{xiii}Procedure as that of Hammarström *et al.* based upon work by Buchwald *et al.*^{34,190}

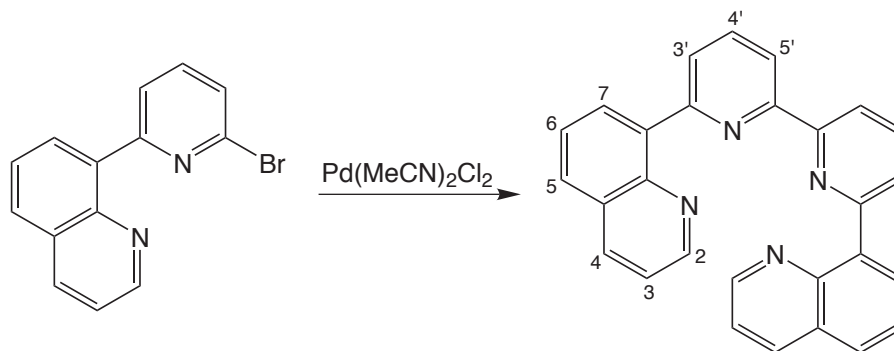
3,3'-Bis(8-quinolyl)-biphenyl [bqbph] 18^{xiv}

A Schlenk tube was evacuated and backfilled with nitrogen (three cycles) and 3-bromo(-8-quinolyl)benzene (0.095 g, 0.334 mmol), dichlorobis(acetonitrile)palladium (0.030 g, 0.116 mmol), dry triethylamine (1.5 mL) and *N,N*-dimethylformamide (10 mL) were all added under flow of nitrogen. The solution was briefly degassed by evacuating and backfilling with nitrogen then heated at reflux overnight. After cooling to room temperature, cold water (20 mL) was added and the solution extracted with diethyl ether. The organic layers were combined, dried over MgSO_4 , filtered and the solvent removed under reduced pressure. Purification was performed by column chromatography (silica, hexane/ethyl acetate, gradient elution from 100:0 to 85:15) to produce a white solid that was dried *in vacuo* (0.035 g, 51 %).

^1H NMR (CDCl_3 , 700 MHz) δ = 8.96 (2H, s, H^2), 8.22 (2H, d, $^3J = 8.4$, H^4), 7.97 (2H, s, $\text{H}^{2'}$), 7.84 (2H, d, $^3J = 7.9$, H^5), 7.80 (2H, d, $^3J = 5.7$, H^7), 7.73 (4H, overlapping d, $^3J = 7.7$ and $^3J = 7.0$, $\text{H}^{4'}$ and $\text{H}^{6'}$), 7.71 (2H, t, $^3J = 7.5$, H^6), 7.65–7.55 (2H, t, $^3J = 7.0$, $\text{H}^{5'}$), 7.42 (2H, dd, $^3J = 8.3$, $^3J = 4.1$, H^3). ^{13}C NMR (CDCl_3 , 176 MHz) δ = 150.1 (C^2), 144.4 (C^q), 141.3, 130.7, 130.6 ($\text{C}^{4'}$ or $\text{C}^{6'}$), 130.6 ($\text{C}^{4'}$ or $\text{C}^{6'}$), 129.6 (C^q), 129.0 (C^q), 128.8 (C^q), 128.4, 128.3, 127.6 (C^5), 126.6 ($\text{C}^{4'}$ or $\text{C}^{6'}$), 126.4 (C^q), 121.0 (C^3). MS (ES^+) m/z 413.3 [M]⁺.

^{xiv}Procedure based on work by Tanaka *et al.*¹⁹¹

6,6'-Bis(8-quinolyl)-2,2'-bipyridine, [bqbpy], 20

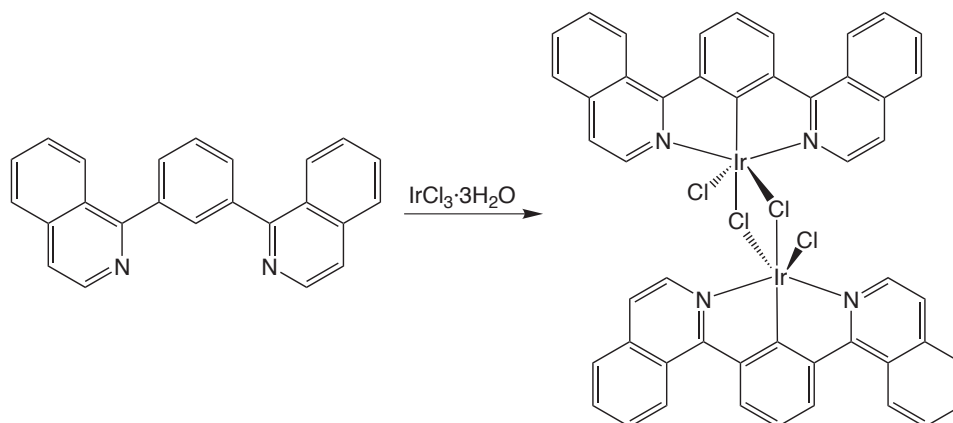


A Schlenk tube was evacuated and backfilled with nitrogen (three cycles) and 3-bromo(8-quinolyl)pyridine (0.050 g, 0.175 mmol), dichlorobis(acetonitrile)palladium (0.030 g, 0.116 mmol), dry triethylamine (1.5 mL) and *N,N*-dimethylformamide (10 mL) were all added under flow of nitrogen. The solution was briefly degassed by evacuating and backfilling with nitrogen then heated at reflux overnight. After cooling to room temperature, cold water (20 mL) was added and the solution extracted with diethyl ether. The organic layers were combined, dried over MgSO_4 , filtered and the solvent removed under reduced pressure to yield a yellow-orange solid. Purification was performed by column chromatography (silica, hexane/ethyl acetate, 50:50) to yield a colourless oil that was dried *in vacuo* (0.064 g, 89 %).

^1H NMR (CDCl_3 , 400 MHz) δ = 9.00 (2H, dd, 3J = 4.0, 4J = 2.0, H^2), 8.63 (2H, dd, 3J = 8.0, 4J = 1.2, H^4), 8.40 (2H, dd, 3J = 7.2, 4J = 1.6), 8.22–8.27 (4H, m), 7.92–7.96 (4H, m), 7.74 (2H, t, 3J = 7.2, H^3 , or H^6 or $\text{H}^{4'}$), 7.46 (2H, dd, 3J = 8.2, 3J = 4.0). ^{13}C NMR (CDCl_3 , 101 MHz) δ = 151.7, 144.8, 139.0, 137.2, 136.2, 130.2, 130.0, 127.5, 126.8, 126.6, 126.6, 120.0. MS (ES^+) m/z 411.2 [$\text{M}+\text{H}$] $^+$. (ASAP $^+$) 410.1 [M] $^+$. HRMS (ASAP $^+$) Calcd for $\text{C}_{28}\text{H}_{19}\text{N}_4$ m/z 411.1610. Found m/z 411.1595 [$\text{M} + \text{H}$] $^+$.

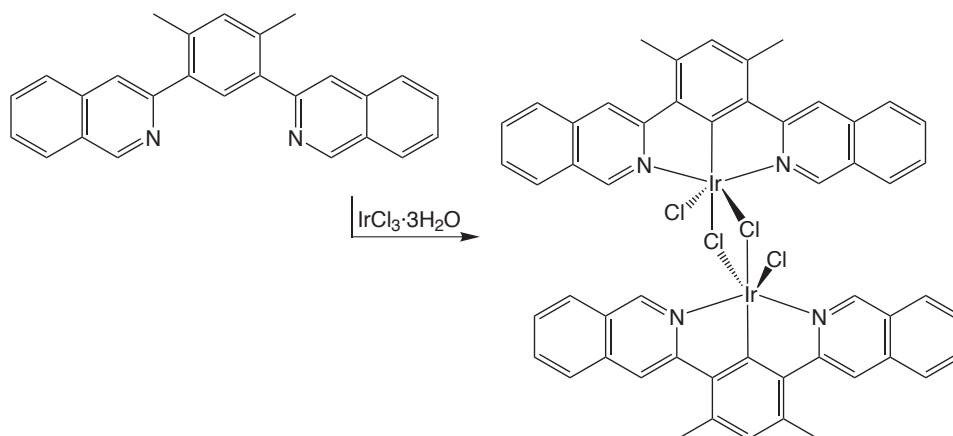
6.5.4 Chloro-bridged metal dimers

Bis(μ -chloro)bis(1,3-di(1-isoquinolyl)-benzene- $N,C^{2'}$, N iridium chloride)
 $[\text{Ir}(1\text{-diqb})(\mu\text{-Cl})\text{Cl}]_2$, **21**



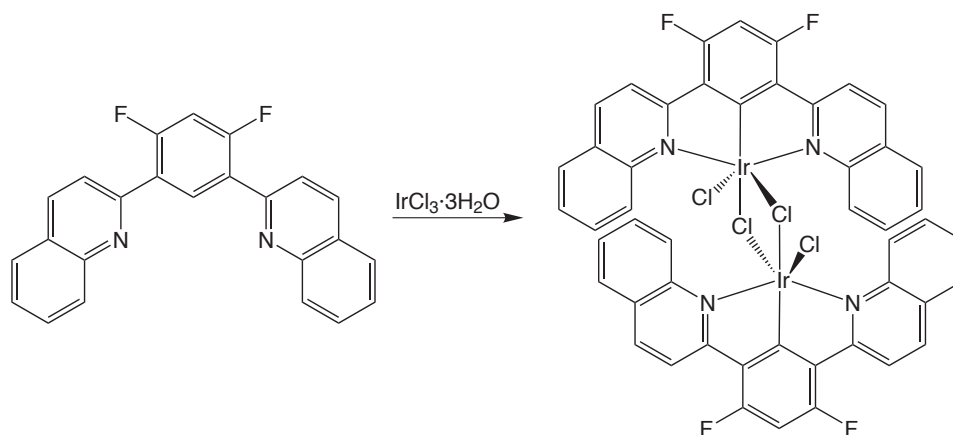
Procedure B was followed using 1,3-di(1-isoquinolyl)-benzene (0.050 g, 0.150 mmol) and iridium trichloride trihydrate (0.053 g, 0.150 mmol). After work-up and drying *in vacuo* the crude product was obtained as a dark orange solid; further product was obtained by repeating procedure B using the reaction solution removed after centrifugation (0.077 g, 86 %).

Bis(μ -chloro)bis(1,3-di(3-isoquinolyl)-4,6-dimethylbenzene- $N,C^{2'}$, N iridium chloride)
 $[\text{Ir}(3\text{-diqMeb})(\mu\text{-Cl})\text{Cl}]_2$, **22**



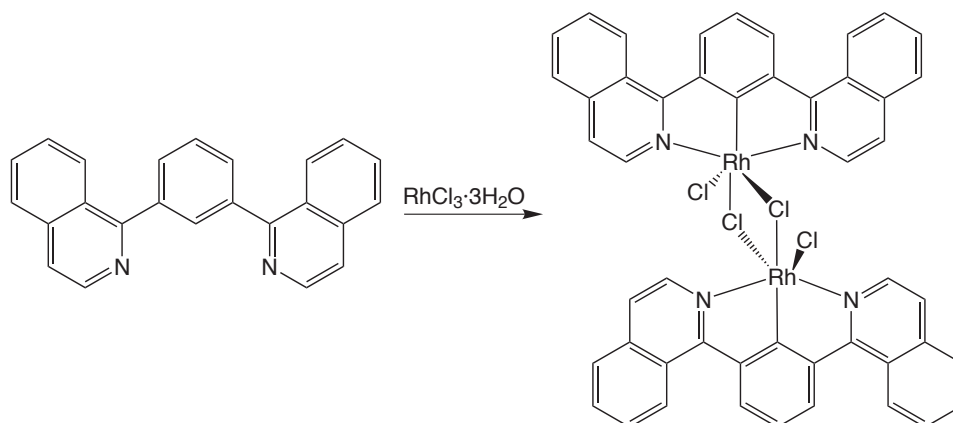
Procedure B was followed using 1,3-di(3-isoquinolyl)-4,6-dimethylbenzene (0.140 g, 0.388 mmol) and iridium trichloride trihydrate (0.137 g, 0.388 mmol). After work-up and drying *in vacuo* the crude product was obtained as an orange solid (0.096 g, 40 %).

Bis(μ -chloro)bis(1,3-di(2-quinolyl)-4,6-difluorobenzene-N,C^{2'},N iridium chloride) [Ir(2-dqFb)(μ -Cl)Cl]₂, **23**



Procedure B was followed using 1,3-di(3-isoquinolyl)-4,6-difluorobenzene (0.070 g, 0.194 mmol) and iridium trichloride trihydrate (0.068 g, 0.194 mmol). After work-up and drying *in vacuo* the crude product was obtained as a dark orange solid (0.073g, 61 %).

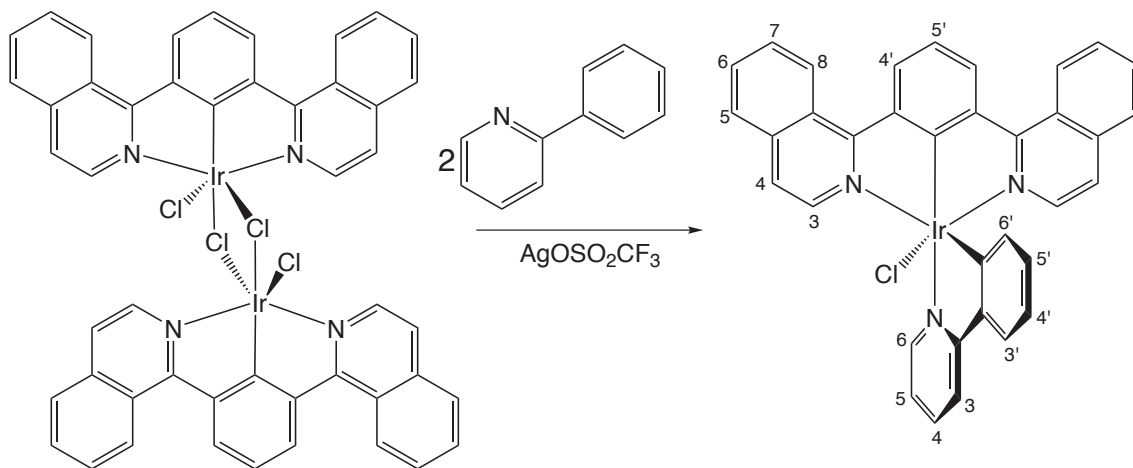
Bis(μ -chloro)bis(1,3-di(1-isoquinolyl)-benzene-N,C^{2'},N rhodium chloride) [Rh(1-diqb)(μ -Cl)Cl]₂, **31**



Procedure B was followed using 1,3-di(1-isoquinolyl)-benzene (0.050 g, 0.150 mmol) and rhodium trichloride trihydrate (0.053 g, 0.150 mmol). After work-up and drying *in vacuo* the crude product was obtained as a yellow solid; further product was obtained by repeating the procedure with the remaining solutions (0.059 g, 66 %).

6.5.5 Iridium complexes

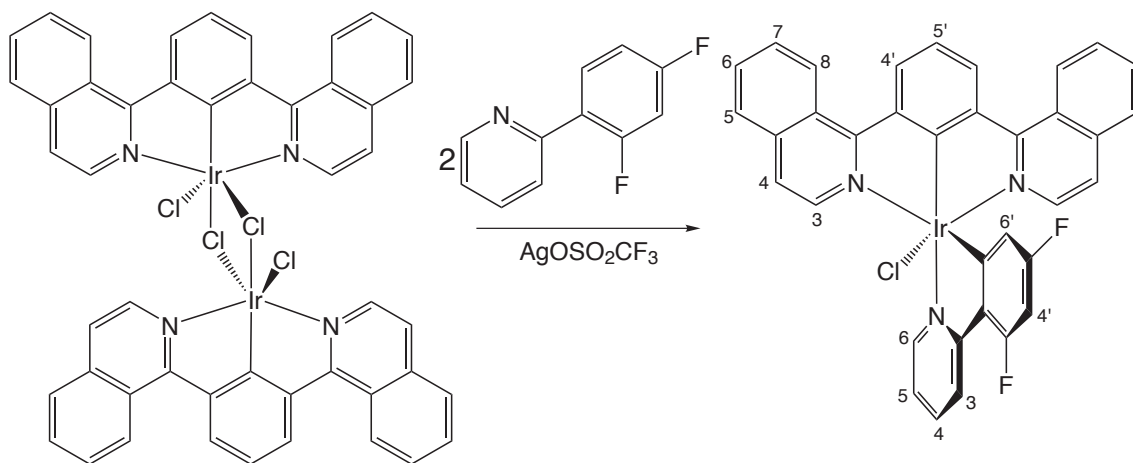
Iridium (1,3-di(1-isoquinolyl)benzene-N,C^{2'},N)(2-phenylpyridine-N,C^{2'}) chloride [Ir(1-diqb)(ppy)Cl], **25**



Bis(μ -chloro)bis(1,3-di(1-isoquinolyl)benzene-N,C^{2'},N)-iridium chloride (0.065 g, 0.055 mmol), silver triflate (0.078 g, 0.300 mmol) and 2-phenylpyridine (200 μ L, 1.780 mmol) were placed in a Schlenk tube, which was degassed three times *via* evacuating and backfilling with nitrogen. The mixture was heated at 110 °C under nitrogen for 20 h then cooled to room temperature and CH₂Cl₂ (35 mL) added. Solid residue was removed by filtration and the filtrate washed with HCl (1M, 3 \times 35 mL), dried over MgSO₄ and the solvent removed under reduced pressure to give a dark red solid. Purification was carried out by column chromatography (silica, CH₂Cl₂/methanol, gradient elution from 100:0 to 99.75:0.25) to give the product as a red solid (0.018 g, 46 %).

¹H NMR (CDCl₃, 700 MHz) δ = 10.24 (1H, d, ³*J* = 4.8, H⁶-ppy), 9.16 (2H, d, ³*J* = 9.1, H³-NCN), 8.65 (2H, d, ³*J* = 8.4, H^{4'}-NCN), 8.13 (1H, d, ³*J* = 4.2, H³-ppy), 8.03 (1H, t, ³*J* = 3.8, H⁴-ppy), 7.99 (2H, d, ³*J* = 7.7, H⁴-NCN), 7.72–7.80 (4H, m, H⁵-NCN or H⁸-NCN, and H⁶-NCN or H⁷-NCN), 7.60–7.68 (3H, m, H⁵-ppy, and H⁶-NCN or H⁷-NCN), 7.59 (1H, d, ³*J* = 8.4, H^{3'}-ppy), 7.54 (1H, t, ³*J* = 7.7, H^{5'}-NCN), 7.40–7.50 (1H, m, H⁵-NCN or H⁸-NCN), 7.18 (1H, d, ³*J* = 6.3, H⁵-NCN or H⁸-NCN), 6.65 (1H, t, ³*J* = 6.3, H^{4'}-ppy), 6.44 (1H, t, ³*J* = 6.3, H^{5'}-ppy), 5.71 (1H, d, ³*J* = 7.7, H^{6'}-ppy). MS (ES⁺) *m/z* 713.2 [M]⁺. HRMS (ASAP⁺) Calcd for C₃₅H₂₃Cl¹⁹¹IrN₃: *m/z* 711.1187. Found: *m/z* 711.1153. Mp > 250 °C.

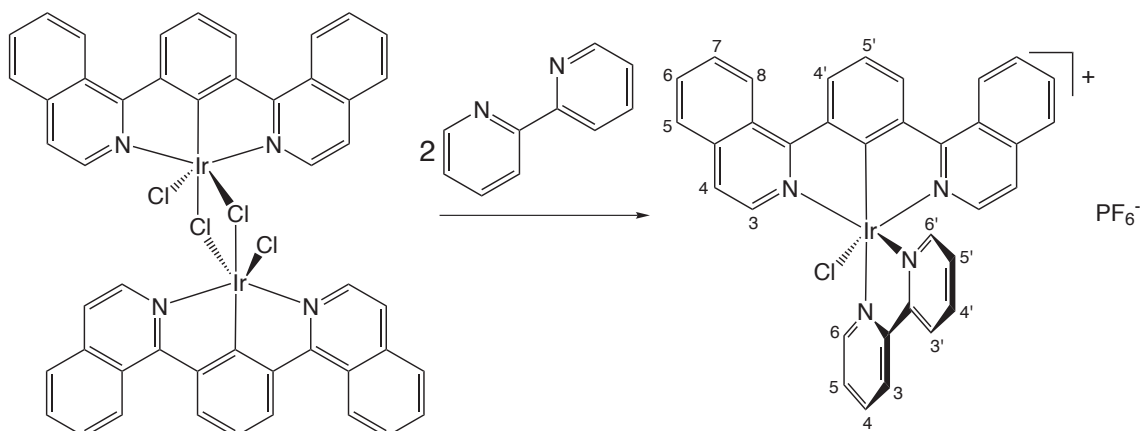
Iridium (1,3-di(1-isoquinoly)benzene- $N,C^{2'}$, N)(2-(4,6-difluorophenyl)pyridine- $N,C^{2'}$) chloride [Ir(1-diqb)(dFppy)Cl], **26**



Bis(μ -chloro)bis(1,3-di(1-isoquinoly)benzene- $N,C^{2'}$, N)-iridium chloride (0.075 g, 0.063 mmol), silver triflate (0.048 g, 0.18 mmol) and 2-(2,4-difluorophenyl)pyridine (0.048 g, 0.25 mmol) were suspended in ethylene glycol and degassed three times *via* evacuating and backfilling with nitrogen. The mixture was heated at 196 °C under nitrogen for 2 h then cooled to room temperature and CH_2Cl_2 (35 mL) added. Solid residue was removed by filtration and the filtrate washed with HCl (1M, 3 \times 35 mL), dried over MgSO_4 and the solvent removed under reduced pressure to give a red solid. Purification was carried out by column chromatography (silica, CH_2Cl_2 /methanol, gradient elution from 100:0 to 99.85:0.15) to give the product as a red solid (0.016 g, 34 %).

^1H NMR (CDCl_3 , 700 MHz) δ = 10.28 (1H, d, 3J = 4.9, H^6 -ppy), 9.17 (2H, d, 3J = 8.4, H^3 -NCN), 9.10 (1H, t, 3J = 7.7, $\text{H}^{5'}$ -NCN), 8.65 (2H, d, 3J = 7.0, H^5 -NCN or H^8 -NCN), 8.50 (1H, d, 3J = 7.7, H^3 -ppy), 8.06 (1H, t, 3J = 5.6, H^4 -ppy), 7.75–7.81 (4H, m, H^4 -NCN and $\text{H}^{4'}$ -NCN), 7.69 (2H, d, 3J = 6.3, H^6 -NCN or H^7 -NCN), 7.64 (1H, t, 3J = 6.3, H^5 -ppy), 7.54–7.57 (3H, m, $\text{H}^{5'}$ -ppy and H^6 -NCN or H^7 -NCN), 7.23 (2H, d, 3J = 6.3, H^5 -NCN or H^8 -NCN), 6.14 (1H, t, 3J = 9.4, $\text{H}^{6'}$ -ppy). MS (ES^+) m/z 748.6 $[\text{M}]^+$. HRMS (ASAP $^+$) Calcd for $\text{C}_{35}\text{H}_{21}\text{ClF}_2^{191}\text{IrN}_3$ m/z 747.0998. Found m/z 747.0987. Mp > 250 °C.

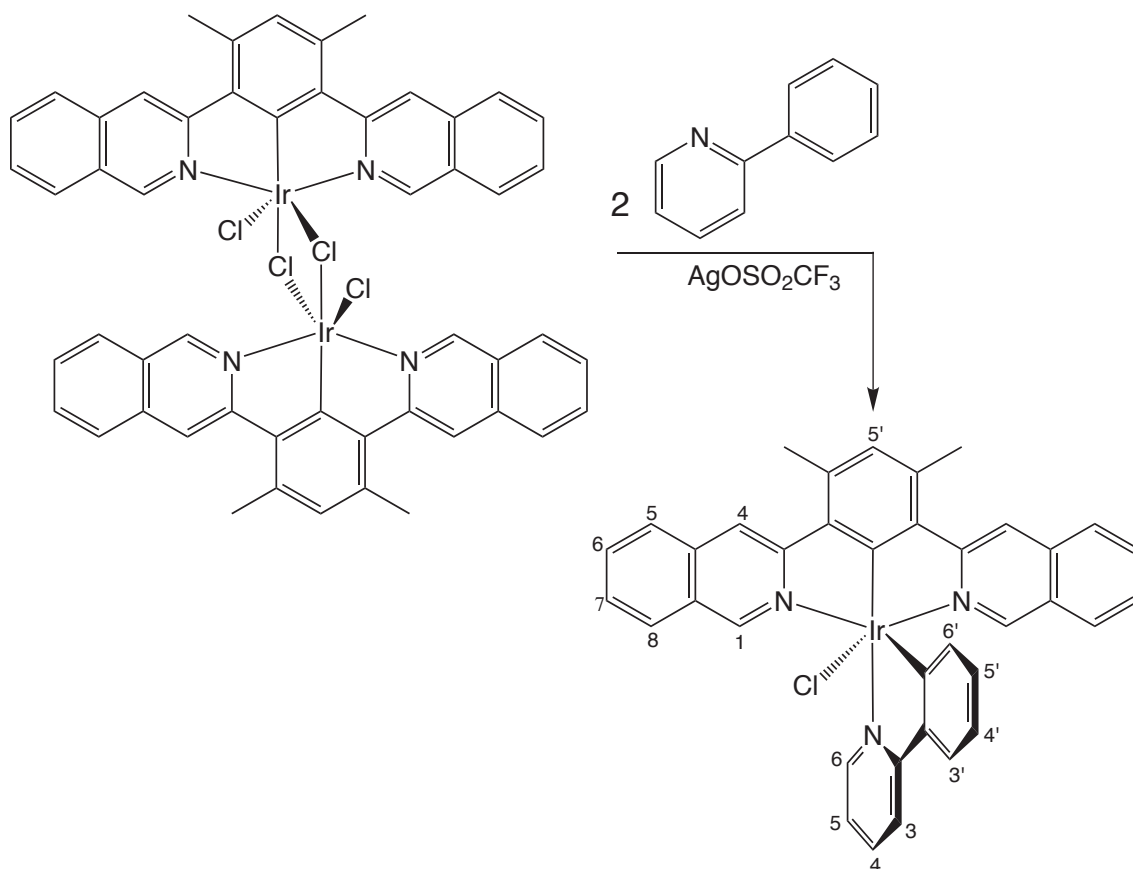
Iridium(1,3-di(1-isoquinolyl)benzene-N,C^{2'},N)(2,2'-bipyridine-N,N) chloride hexafluorophosphate [Ir(1-diqb)(bpy)Cl][PF₆], 27



A suspension of bis(μ -chloro)bis(1,3-di(quinolin-1-yl)benzene-N,C^{2'},N)-iridium chloride) (0.089 g, 0.075 mmol) and 2,2'-bipyridine (0.012 g, 0.075 mmol) in ethylene glycol (7 mL) was heated at 196 °C for 2 h under nitrogen. After cooling to room temperature, the reaction mixture was added to water (5 mL), and a saturated solution of aqueous KPF₆ (3 mL) was added. The solution was filtered through a sinter and the yellow-orange precipitate collected by centrifugation and washed with water (5 \times 10 mL) and THF (3 \times 10 mL) then dried *in vacuo*. Purification by column chromatography (silica, CH₂Cl₂/methanol, gradient elution from 100:0 to 97:3) yielded an orange solid, which was purified further by column chromatography (silica, CH₂Cl₂/methanol, gradient elution from 100:0 to 99.5:0.5) and an ion exchange performed, as before, to give the product as an orange solid (41 mg, 38 %).

¹H NMR (CDCl₃, 500 MHz) δ = 9.98 (1H, d, ³J = 5.0, H^{6'}-bpy) 9.10 (2H, d, ³J = 9.0, H⁸-NCN), 8.82 (2H, d, ³J = 8.0, H³-NCN), 8.69 (1H, d, ³J = 6.4, H³-bpy), 8.53 (1H, td, ³J = 7.0, ⁴J = 2.0, H^{4'}-bpy), 8.35 (1H, dd, ³J = 7.5, ⁴J = 2.4, H³-bpy or H⁶-bpy), 8.24 (1H, td, ³J = 7.0, ⁴J = 2.0, H^{5'}-bpy), 8.02 (2H, dd, ³J = 6.8, ⁴J = 1.2, H⁵-NCN), 7.95 (2H, td, ³J = 7.2, ⁴J = 1.6, H⁶-NCN), 7.87 (1H, td, ³J = 8.0, ⁴J = 1.5, H⁷-NCN), 7.70–7.76 (2H, m, H^{4'}-NCN, and H⁴-bpy or H⁵-bpy), 7.55–7.82 (4H, m, H²-NCN and H³-NCN), 7.27 (1H, dd, ³J = 6.0, ⁴J = 2.4, H³-bpy or H⁶-bpy), 7.01 (1H, td, ³J = 6.0, ⁴J = 1.5, H⁴-bpy or H⁵-bpy). MS (ES⁺) m/z 715.2 [M]⁺. HRMS (ES⁺) Calcd for C₃₄H₂₃³⁵Cl¹⁹³IrN₄: m/z 715.1235. Found: m/z 715.1246 [M]⁺. Mp > 250 °C.

Iridium (1,3-di(3-isoquinolyl)-4,6-dimethylbenzene-N,C^{2'},N)(2-phenylpyridine-N,C^{2'}) chloride [Ir(3-diqMeb)(ppy)Cl], **28**

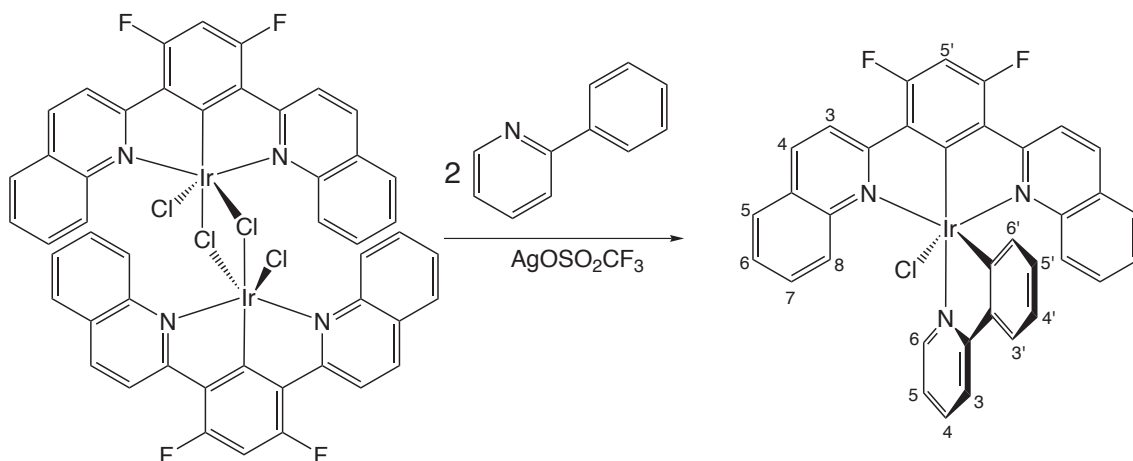


An oven-dried Schlenk tube was charged with bis(μ -chloro)bis(1,3-di(1-isoquinolyl)-4,6-dimethylbenzene-N,C^{2'},N)-iridium (0.080 g, 0.064 mmol), 2-phenylpyridine (200 μ L) and silver triflate (0.069 g, 0.270 mmol) and degassed *via* three cycles of evacuation and backfilling with nitrogen. The mixture was heated to 110 °C for 20 h under nitrogen then cooled to room temperature and CH₂Cl₂ (35 mL) added. Solid residue was removed by filtration and the filtrate washed with HCL (1M, 3 \times 35 mL), dried over MgSO₄ and the solvent removed under reduced pressure to give an orange solid. Purification was carried out by column chromatography (silica, CH₂Cl₂/methanol, gradient elution from 100:0 to 99.8:0.2) and the solid dried *in vacuo* to give a yellow solid (0.036 g, 38 %).

¹H NMR (CDCl₃, 700 MHz) δ = 10.27 (1H, d, ³J = 4.9, H⁶-ppy), 8.31 (4H, s, H¹ and H⁴), 8.14 (1H, d, ³J = 8.4, H³-ppy), 8.06 (1H, td, ³J = 8.4, ⁴J = 1.4, H⁴-ppy), 7.80 (2H, d, ³J = 8.4, H⁵-NCN or H⁸-NCN), 7.65 (1H, d, ³J = 7.7, ⁴J = 1.4, H⁵-ppy), 7.61 (1H, d, ³J = 8.4, H^{3'}-ppy), 7.55 (2H, t, ³J = 7.0, H⁶-NCN or H⁷-NCN), 7.48 (2H, d, ³J = 8.4, H⁵-NCN or H⁸-NCN), 7.38 (2H, t, ³J = 7.7, H⁶-NCN or H⁷-NCN), 6.94 (1H, s, H^{5'}-NCN), 6.68 (1H, t, ³J = 7.7, ⁴J = 0.7, H^{4'}-ppy), 6.53

(1H, t, $^3J = 7.0$, $^4J = 1.4$, H^{5'}-ppy), 6.26 (1H, d, $^3J = 7.7$, H^{6'}-ppy) 2.95 (6H, s, CH₃). ¹³C NMR (CDCl₃, 176 MHz) $\delta = 177.4, 163.4, 154.3, 150.1, 139.9, 137.1, 136.3, 136.1, 136.1, 136.0, 131.6, 129.8, 129.3, 127.3, 127.1, 127.0, 126.8, 124.2, 123.9, 123.1, 121.5, 119.1, 118.9$. MS (ASAP⁺) m/z 742.2 [M + H]⁺. HRMS (ASAP⁺) Calcd for C₃₇H₂₇N₃³⁵Cl¹⁹¹Ir: m/z 739.1500. Found: m/z 739.1487. Mp > 250 °C.

Iridium (1,3-di(2-quinolyl)-4,6-difluorobenzene-N,C^{2'},N)(2-phenyl-pyridine-N,C^{2'}) chloride [Ir(2-dqFb)(ppy)Cl], **29**

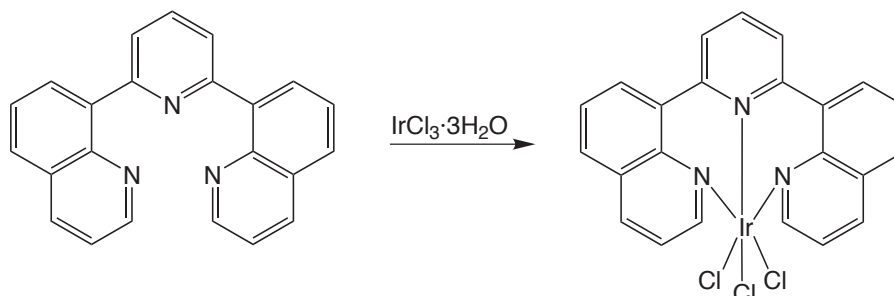


An oven-dried Schlenk tube was charged with bis(μ -chloro)bis(1,3-di(2-quinolyl)-4,6-difluorobenzene-N,C^{2'},N)-iridium (0.065 g, 0.052 mmol), 2-phenylpyridine (200 μ L) and silver triflate (0.033 g, 0.129 mmol) and degassed *via* three cycles of evacuation and backfilling with nitrogen. The mixture was heated to 110 °C for 20 h under nitrogen then cooled to room temperature and CH₂Cl₂ (35 mL) added. Solid residue was removed by filtration and the filtrate washed with HCL (1M, 3 \times 35 mL), dried over MgSO₄ and the solvent removed under reduced pressure. Purification was carried out by column chromatography to give a bright orange solid (silica, CH₂Cl₂/methanol, gradient elution from 100:0 to 99:1) (0.054 g, 70 %).

¹H NMR (CDCl₃, 500 MHz) $\delta = 10.57$ (1H, d, $^3J = 5.5$, H⁶-ppy), 8.26 (2H, d, $^3J = 9.0$, H³-NCN or H⁴-NCN), 8.03 (3H, d, $^3J = 9.0$, H⁴-ppy and H³-NCN or H⁴-NCN), 7.95 (1H, d, $^3J = 8.0$, H³-ppy), 7.76 (1H, t, $^3J = 7.0$, H⁵-ppy), 7.66 (2H, d, $^3J = 9.5$, H⁵-NCN or H⁸-NCN), 7.59 (2H, dd, $^3J = 8.0$, $^4J = 1.5$, H⁵-NCN or H⁸-NCN), 7.39 (1H, d, $^3J = 8.0$, H^{3'}-ppy), 7.30 (2H, td, $^3J = 7.5$, $^4J = 1.0$, H⁶-NCN or H⁷-NCN), 7.04 (2H, td, $^3J = 7.7$, $^4J = 1.5$, H⁶-NCN or H⁷-NCN), 6.95 (1H, t, $^3J = 12.0$, H^{5'}-NCN) 6.56 (2H, m, H^{5'}-ppy and H^{4'}-ppy), 5.91 (1H, d, $^3J = 7.5$, H^{6'}-ppy). ¹³C NMR (CDCl₃, 126 MHz) $\delta = 168.6, 165.9, 150.5, 144.4, 143.5, 139.1, 138.5, 136.4, 134.1, 129.8, 129.7, 128.4, 127.8, 126.9, 126.1, 124.1, 122.9, 121.9, 120.4, 119.6$. ¹⁹F NMR (CDCl₃, 470 MHz) $\delta = 107.0$ (2F, s). MS (ASAP⁺) m/z 747.1

[M]⁺. HRMS (ASAP⁺) Calcd for C₃₅H₂₁ClN₃F₂¹⁹¹Ir: *m/z* 747.0998. Found: *m/z* 747.0963 [M]⁺. Mp > 250 °C.

Iridium(2,6-di(8-quinolyl)pyridine) trichloride [Ir(dqp)Cl₃]

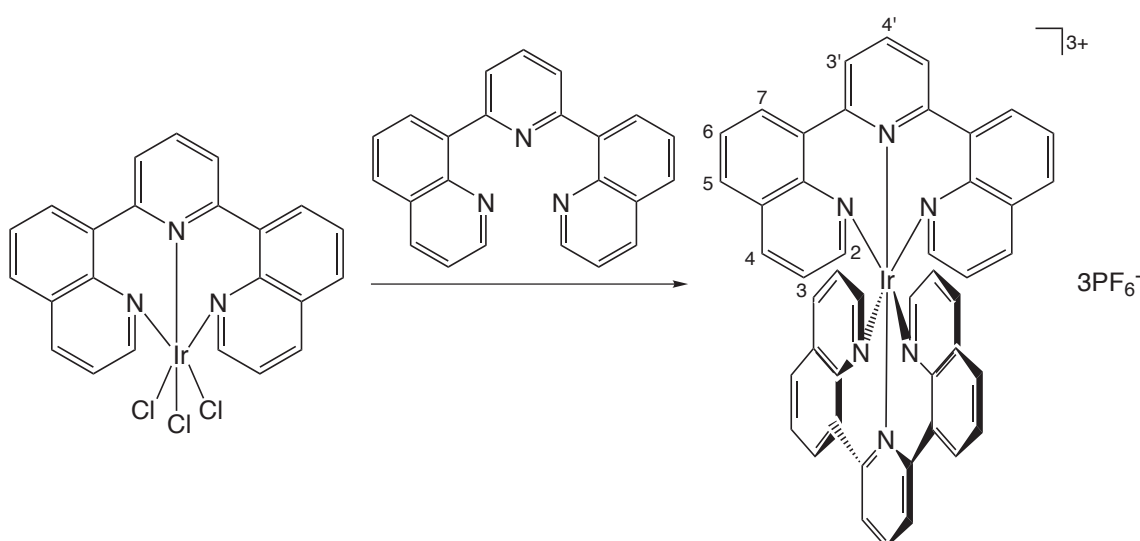


A suspension of 1,3-di(8-quinolyl)pyridine (0.080 g, 0.240 mmol) and 2,6-di(8-quinolyl)pyridine (0.085 g, 0.24 mmol) in ethylene glycol (5 mL) was degassed three times *via* evacuating and backfilling with nitrogen, then heated at 160 °C for 30 min. After cooling to room temperature, the precipitate was collected by centrifugation and washed with water (3 × 3 mL), ethanol (3 × 3 mL) and diethyl ether (3 × 3 mL) to yield a red solid (0.109 g, 72 %), which was dried *in vacuo*, identified by mass spectrometry and used for the next step without further characterisation.

MS (MALDI⁺, DCTB matrix) *m/z* 532.9 [M + H]⁺.

Bis(2,6-di(8-quinolyl)pyridine)iridium hexafluorophosphate

[Ir(dqp)₂][PF₆]₃, **30**

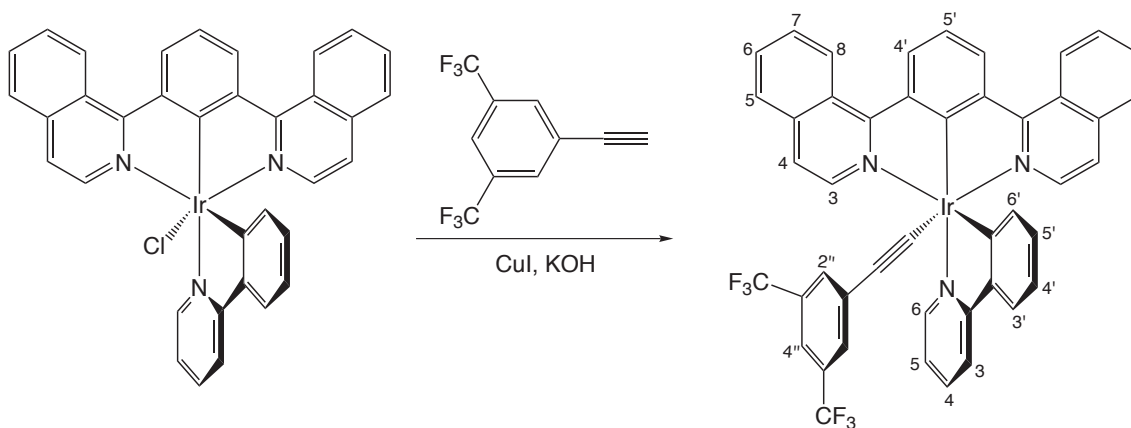


A suspension of 2,6-di(8-quinolyl)pyridine iridium trichloride (0.065 g, 0.102 mmol) and 1,3-di(8-quinolyl)pyridine (0.034 g, 0.102 mmol) and iridium trichloride trihydrate in ethylene gly-

col (5 mL) was degassed 3 times *via* evacuating and backfilling with nitrogen then heated to 198 °C under nitrogen for 2 h. After cooling to room temperature the precipitate was collected by centrifugation and washed with water (3 × 3 mL). Purification was achieved by column chromatography (silica, acetonitrile/water/KNO₃ (aq.), gradient elution from 100:0:0 to 87.75:12.00:0.25) with fractions containing product (as determined by TLC) dissolved in the minimum amount of acetonitrile and one drop of water, heated gently and added slowly to a saturated solution of aqueous KPF₆. The precipitate was collected by centrifugation, washed with water (3 × 3 mL), ethanol (3 × 3 mL) and diethyl ether (3 × 3 mL) to yield a yellow solid (0.022 g, 25 %).

¹H NMR (CD₃CN, 700 MHz) δ = 8.47 (6H, m, H² and H^{4'}), 8.38 (4H, d, ³J = 5.6, H⁴), 8.10 (4H, d, ³J = 7.7, H^{3'}), 8.00 (4H, d, ³J = 7.7, H⁵ or H⁷), 7.93 (4H, d, ³J = 7.7, H⁵ or H⁷), 7.67 (4H, t, ³J = 7.7, H⁶), 7.40 (4H, td, ³J = 6.3 ⁴J = 2.3, H³). MS (ES⁺) m/z 502.3 [M + PF₆]²⁺, 286.6 [M]³⁺. MS (MALDI⁺, DCTB matrix) m/z 1149.1 [M + 2PF₆]⁺. HRMS (ASAP⁺) Calcd for C₄₆H₂₈N₆¹⁹¹Ir: m/z 855.1981. Found: m/z 855.2334 [M]⁺. Mp > 250 °C.

Iridium (1,3-di(1-isoquinolyl)benzene-N,C^{2'},N)(2-phenylpyridine-N,C^{2'}) trifluoromethylphenylacetylide [Ir(1-diqb)(ppy)(CC-tfp)], 44



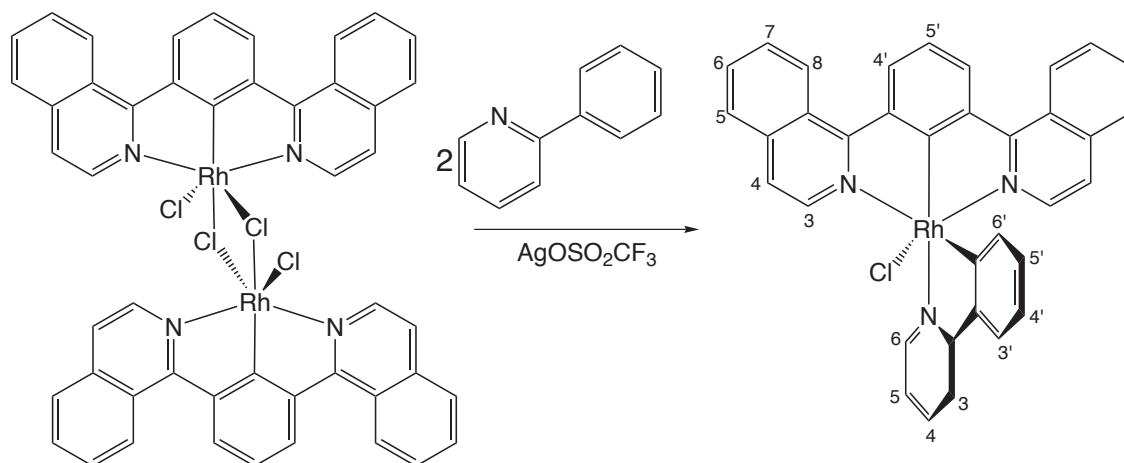
A Schlenk tube containing 1-ethynyl-3,5-bis(trifluoromethyl)benzene (100 μ L) and KOH (0.030 g, 0.535 mmol) in methanol (2 mL) was briefly evacuated then a rapid stream of nitrogen bubbled through the solution. The solution was stirred under nitrogen for 1 h whilst a separate solution of Ir(1-diqb)(ppy)Cl (0.025 g, 0.035 mmol) and CuI (0.004 g) in methanol (2 mL) was degassed using the same method. The complex was transferred *via* syringe under nitrogen to the initial Schlenk tube and a further degassing step performed, as before. The mixture was stirred under nitrogen at room temperature for 18 h and the red precipitate collected

by centrifugation then washed with methanol (3×3 mL). Upon drying *in vacuo* the product was isolated as a dark red solid (0.008 g, 25 %).

^1H NMR (CDCl_3 , 400 MHz) $\delta = 10.30$ (1H, t, $^3J = 4.4$, $\text{H}^6\text{-ppy}$), 9.21 (2H, d, $^3J = 8.7$, $\text{H}^3\text{-NCN}$), 8.72 (2H, d, $^3J = 8.0$, $\text{H}^{4'}\text{-NCN}$), 8.14 (1H, d, $^3J = 8.2$, $\text{H}^3\text{-ppy}$), 8.05 (1H, td, $^3J = 7.4$, $^4J = 1.4$, $\text{H}^4\text{-ppy}$), 7.73–7.78 (6H, m, $\text{H}^4\text{-NCN}$ and $\text{H}^6\text{-NCN}$ and $\text{H}^7\text{-NCN}$), 7.60–7.70 (4H, m, $\text{H}^{3'}\text{-ppy}$ and $\text{H}^{5'}\text{-ppy}$, and $\text{H}^5\text{-NCN}$ or $\text{H}^8\text{-NCN}$), 7.54–7.60 (2H, m, $\text{H}^{5'}\text{-NCN}$ and $\text{H}^{4''}\text{-CCtfp}$), 7.33 (2H, d, $^3J = 11.2$, $\text{H}^{2''}\text{-CCtfp}$), 7.17 (2H, d, $^3J = 7.0$, $\text{H}^5\text{-NCN}$ or $\text{H}^8\text{-NCN}$), 6.70 (1H, td, $^3J = 7.2$, $^4J = 1.6$, $\text{H}^{4'}\text{-ppy}$), 6.48 (1H, td, $^3J = 7.6$, $^4J = 1.2$, $\text{H}^{5'}\text{-ppy}$), 5.58 (1H, d, $^3J = 6.2$, $\text{H}^{6'}\text{-ppy}$). ^{19}F NMR (CDCl_3 , 376 MHz) $\delta = -63.3$ (6F, s, CF_3). MS (ASAP⁺) m/z 916.2 $[\text{M} + \text{H}]^+$. HRMS (ASAP⁺) Calcd for $\text{C}_{45}\text{H}_{26}\text{N}_3\text{F}_6^{191}\text{Ir}$: m/z 913.1637. Found: m/z 913.1648. Mp > 250 °C.

6.5.6 Rhodium complexes

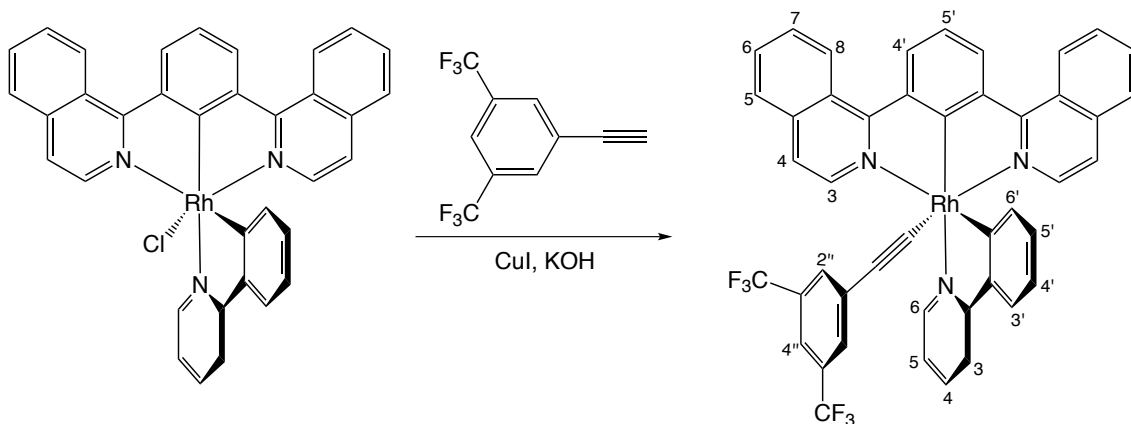
Rhodium (1,3-di(1-isoquinoly)benzene- $N,C^{2'}$, N)(2-phenylpyridine)- $N,C^{2'}$) chloride [Rh(1-diqb)(ppy)Cl], **32**



Bis(μ -chloro)bis(1,3-di(quinolin-1-yl)benzene- $N,C^{2'}$, N) rhodium chloride (0.050 g, 0.049 mmol), silver triflate (0.056 g, 0.22 mmol) and 2-phenylpyridine (200 μ L, 1.78 mmol) were placed in a Schlenk tube, which was degassed three times *via* evacuating and backfilling with nitrogen. The mixture was heated at 110 $^{\circ}$ C under nitrogen for 20 h then cooled to room temperature and CH_2Cl_2 (35 mL) was added. Solid residue was removed by filtration and the filtrate washed with HCl (1M, 3 \times 35 mL), dried over MgSO_4 and the solvent removed under reduced pressure. Purification was carried out by column chromatography (silica, CH_2Cl_2 /methanol, gradient elution from 100:0 to 99:1) to give the product as a yellow solid (0.065 g, 35 %).

^1H NMR (CDCl_3 , 700 MHz) δ = 10.27 (1H, d, 3J = 5.0, H^6 -ppy), 9.12 (2H, d, 3J = 7.7, H^3 -NCN), 8.62 (2H, d, 3J = 7.7, $\text{H}^{4'}$ -NCN), 8.14 (1H, d, 3J = 11.2, H^3 -ppy), 8.10 (1H, td, 3J = 8.4, 3J = 1.4, $\text{H}^{4'}$ -ppy), 7.63–7.70 (8H, m, H^4 -NCN and H^5 -ppy and $\text{H}^{3'}$ -ppy and H^5 -NCN or H^8 -NCN and H^6 -NCN or H^7 -NCN), 7.53–7.56 (3H, m, $\text{H}^{5'}$ -NCN and H^6 -NCN or H^7 -NCN), 7.22 (2H, d, 3J = 4.5, H^5 -NCN or H^8 -NCN), 6.74 (1H, td, 3J = 6.0, 4J = 1.0, $\text{H}^{4'}$ -ppy), 6.51 (1H, td, 3J = 5.5, 4J = 1.0, $\text{H}^{5'}$ -ppy), 5.91 (1H, d, 3J = 8.4, $\text{H}^{6'}$ -ppy). ^{13}C NMR (CDCl_3 , 176 MHz) δ = 188.5, 167.9, 165.7, 157.9, 150.7, 143.8, 143.8, 142.7, 138.0, 136.8, 130.7, 129.8, 128.2, 127.7, 127.6, 125.9, 123.0, 122.6, 122.3, 121.9, 120.9, 119.0, 113.6, 110.2, 92.3, 92.1. MS (ASAP $^+$) m/z 623.0 $[\text{M}]^+$. HRMS (ASAP $^+$) Calcd for $\text{C}_{35}\text{H}_{23}\text{ClN}_3^{108}\text{Rh}$: m/z 623.0636. Found: m/z 623.0643. Mp > 250 $^{\circ}$ C.

Rhodium(di-(1,3-1-isoquinoly)benzene-N,C^{2'}-N-(2-phenylpyridine-N,C^{2'}) trifluoromethylphenylacetylide [Rh(1-diqb)(ppy)CC-tfp], 45

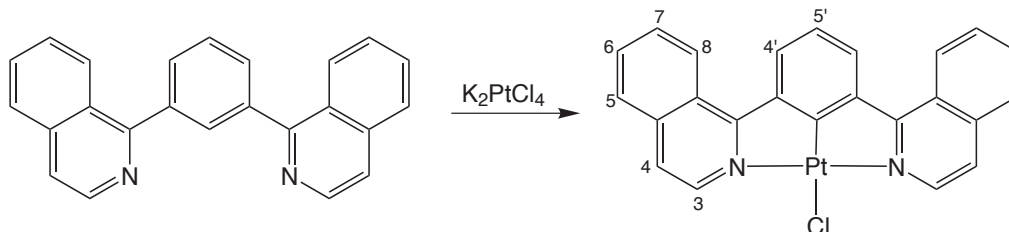


A Schlenk tube containing 1-ethynyl-3,5-bis(trifluoromethyl)benzene (150 μ L) and KOH (0.030 g) in methanol (2 mL) was briefly evacuated then a rapid stream of nitrogen was bubbled through the solution. The solution was stirred under nitrogen for 1 h whilst a separate solution of Rh(1-diqb)(ppy)Cl (0.015 g, 0.024 mmol) and CuI (0.004 g) in methanol (2 mL) was degassed using the same method. The complex was transferred *via* syringe under nitrogen to the initial Schlenk tube and a further degassing step performed. The reaction was stirred under nitrogen at room temperature for 18 h and the yellow precipitate collected by centrifugation then washed with methanol (3 \times 3 mL). Upon drying *in vacuo* the product was obtained as a yellow solid (0.010 g, 50 %).

¹H NMR (CDCl₃ 500 MHz) δ = 10.23 (1H, d, ³*J* = 4.0, H⁶-ppy), 9.15 (2H, d, ³*J* = 8.5, H³-NCN), 8.68 (2H, d, ³*J* = 8.0, H^{4'}-NCN), 8.15 (1H, d, ³*J* = 8.5, H³-ppy), 8.08 (1H, td, ³*J* = 8.5, ⁴*J* = 1.0, H⁴-ppy), 7.61–7.76 (8H, m, H⁴-NCN and H⁵-ppy and H^{3'}-ppy, and H⁵-NCN or H⁸-NCN, and H⁶-NCN or H⁷-NCN), 7.56 (2H, t, ³*J* = 8.0, H⁶-NCN or H⁷-NCN), 7.33 (2H, m, H^{4''}-CCtfp, or H^{5'}-NCN and H^{2''}-CCtfp), 7.30 (2H, d, ³*J* = 6.3, H^{4''}-CCtfp, or H^{5'}-NCN and H^{2''}-CCtfp), 7.20 (2H, d, ³*J* = 6.5, H⁵-NCN or H⁸-NCN), 6.74 (1H, t, ³*J* = 7.5, H^{4'}-ppy), 6.51 (1H, t, ³*J* = 6.0, H^{5'}-ppy), 5.77 (1H, d, ³*J* = 7.0, H^{6'}-ppy). ¹⁹F NMR (CDCl₃, 376 MHz) δ = –63.6 (6F, s, CF₃). MS (ASAP⁺) *m/z* 825.1 [M]⁺. HRMS (ASAP⁺) Calcd for C₄₅H₂₆N₃F₆¹⁰⁸Rh: *m/z* 825.1086 [M]⁺. Found: *m/z* 825.1069 [M]⁺. Mp > 250 ° C.

6.5.7 Platinum complexes

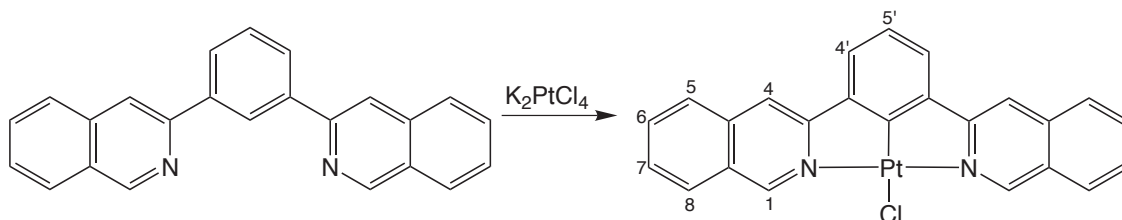
Platinum (1,3-di(1-isoquinoly)benzene-N,C^{2'},N) chloride [Pt(1-diqb)Cl], **33**



1,3-Di(1-isoquinoly)benzene (0.075 g, 0.226 mmol) and K_2PtCl_4 (0.103 g, 0.248 mmol) were combined in glacial acetic acid (4 mL) and degassed *via* four freeze-pump-thaw cycles then charged with nitrogen. The solution was heated at reflux under nitrogen for 3 d then cooled to room temperature and the precipitate collected by centrifugation. The solid was washed with methanol (3×5 mL), water (3×5 mL), ethanol (3×5 mL) and diethyl ether (3×5 mL). The solid was extracted into CH_2Cl_2 , agitating between each extraction until the CH_2Cl_2 became colourless. The solvent was removed under reduced pressure to yield an orange solid, which was washed with acetone (2×5 mL) and dried *in vacuo* to give an orange solid (0.084 g, 66 %).

^1H NMR (CDCl_3 , 400 MHz) δ = 9.52 (2H, d, 3J = 6.4, H³), 8.98 (2H, d, 3J = 8.4, H⁵ or H⁸), 8.29 (2H, d, 3J = 8.0, H^{4'}), 7.94 (2H, d, 3J = 8.0, H⁵ or H⁸), 7.82 (2H, t, 3J = 7.0, H⁶ or H⁷), 7.77 (2H, t, 3J = 8.0, H⁶ or H⁷), 7.68 (2H, d, 3J = 8.0, H⁴), 7.44 (1H, t, 3J = 8.0, H^{5'}). MS (ASAP⁺) m/z 561.1 [M]⁺. HRMS (ASAP⁺) Calcd for $\text{C}_{24}\text{H}_{15}\text{ClN}_2^{194}\text{Pt}$: m/z 560.0551. Found: m/z 560.0560. Elem. anal. Calcd for $\text{C}_{24}\text{H}_{15}\text{ClN}_2\text{Pt}$: C, 51.30 ; H, 2.69 ; N, 4.99. Found: C, 52.13; H, 3.88; N, 4.52. Mp > 250 °C.

Platinum (1,3-di(3-isoquinoly)benzene-N,C^{2'},N) chloride [Pt(3-diqb)Cl], **34**

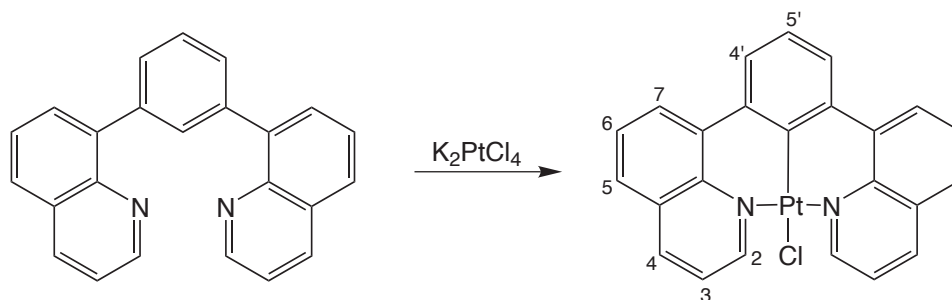


1,3-Di(3-isoquinoly)benzene (0.065 g, 0.196 mmol) and K_2PtCl_4 (0.089 g, 0.215 mmol) were combined in glacial acetic acid (3 mL) and degassed *via* four freeze-pump-thaw cycles then charged with nitrogen. The solution was heated at reflux

under nitrogen for 3 d then cooled to room temperature and the precipitate collected by centrifugation. The precipitate was washed with methanol (3×5 mL), water (3×5 mL), ethanol (3×5 mL) and diethyl ether (3×5 mL). The solid was extracted into CH_2Cl_2 , agitating between each extraction until the CH_2Cl_2 became colourless and the solvent removed under reduced pressure to yield a yellow solid, which was dried *in vacuo* (0.072 g, 66 %).

^1H NMR (CDCl_3 , 700 MHz) δ = 10.08 (2H, s, $^3J(^{195}\text{Pt}) = 21$, H^1) 8.08 (2H, d, $^3J = 8.4$, H^8), 7.98 (2H, s, H^4), 7.88 (2H, d, $^3J = 8.4$, H^5), 7.90 (2H, t, $^3J = 1.4$, H^6), 7.64 (2H, d, $^3J = 1.4$, H^7), 7.50 (2H, d, $^3J = 7.7$, $\text{H}^{4'}$), 7.28 (2H, m, $\text{H}^{5'}$). ^{13}C NMR δ = 156.3 (C^q), 141.1 (C^1), 136.6 (C^q), 133.3 (C^q), 129.3 (C^6), 129.2 (C^8), 128.4 (C^q or C^7), 128.4 (C^q or C^7), 128.0 (C^q), 127.0 (C^5), 123.9 ($\text{C}^{5'}$), 123.1 ($\text{C}^{4'}$), 115.8 (C^4). MS (ASAP⁺) m/z 562.0 [M]⁺. HRMS (ASAP⁺) Calcd for $\text{C}_{24}\text{H}_{15}\text{ClN}_2^{194}\text{Pt}$: m/z 560.0551. Found: m/z 560.0524. Elem. anal. Calc for $\text{C}_{24}\text{H}_{15}\text{ClN}_2\text{Pt}$: C, 51.30; H 2.69; N, 4.99. Found: C, 48.81; H, 2.70; N, 4.50. Mp > 250 °C.

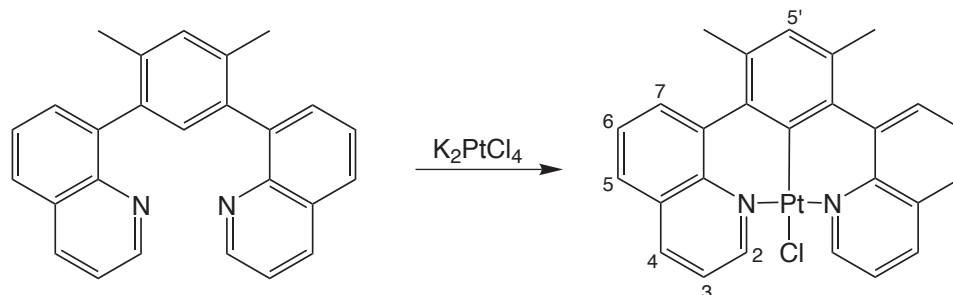
Platinum (1,3-di(8-quinolyl)benzene- $\text{N},\text{C}^{2'}$, N) chloride [$\text{Pt}(\text{8-dqb})\text{Cl}$], **38**



Separate solutions of 1,3-di(8-isoquinolyl)benzene (0.065 g, 0.196 mmol) in acetonitrile (3 mL) and K_2PtCl_4 (0.106 g, 0.255 mmol) in water (1 mL) were degassed *via* three freeze-pump-thaw cycles and charged with nitrogen. The aqueous solution was transferred under positive pressure of nitrogen *via* syringe to the acetonitrile solution and the mixture heated at reflux under nitrogen for 3 d. After cooling, the precipitate was isolated by centrifugation and washed successively with water (3×5 mL), ethanol (3×5 mL) and diethyl ether (3×5 mL). Drying *in vacuo* yielded the complex as a grey-green solid (0.029 g, 26 %)

^1H NMR (CDCl_3 , 500 MHz) δ = 9.76 (2H, d, $^3J = 5.0$, $^3J(^{195}\text{Pt}) = 48$, H^2), 8.41 (2H, d, $^3J = 7.5$, H^4), 8.37 (2H, d, $^3J = 7.5$, H^7), 7.86 (2H, d, $^3J = 7.5$, H^5), 7.72 (2H, dd, $^3J = 7.5$, $^3J = 7.5$, H^6), 7.58 (2H, d, $^3J = 8.0$, $^4J(^{195}\text{Pt}) = 20$, $\text{H}^{3'}$), 7.36 (3H, m, H^3 and $\text{H}^{4'}$). MS (ES^+) 560.1 [$\text{M} + \text{H}$]⁺ (ES^+) HRMS (ES^+). Calcd for $\text{C}_{24}\text{H}_{15}\text{ClN}_2^{195}\text{Pt}$: m/z 560.0552. Found: m/z 560.0542. Elem. anal. Calcd for $\text{C}_{24}\text{H}_{15}\text{ClN}_2\text{Pt}$: C, 51.3; H, 2.7; N, 5.0. Found: C, 51.1; H, 2.8; N, 4.9. Mp > 250 °C.

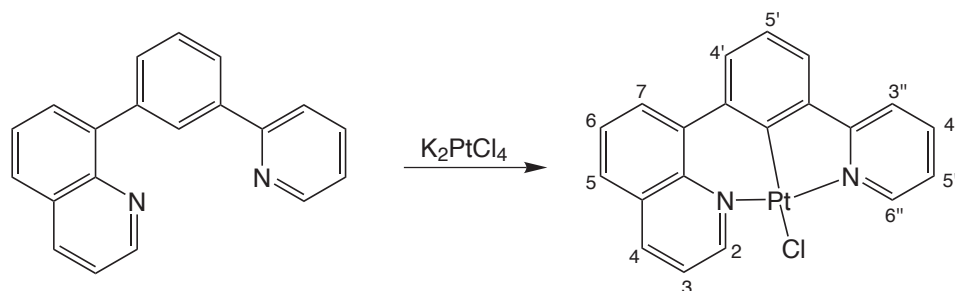
Platinum (1,3-di(8-quinolyl)-4,6-dimethylbenzene-N,C^{2'},N) chloride
[Pt(8-dqMeb)Cl], **39**



Separate solutions of 1,3-di(8-quinolyl)-4,6-dimethylbenzene (0.050 g, 0.139 mmol) in acetonitrile (3 mL) and K_2PtCl_4 (0.075 g, 0.0180 mmol) in water (1 mL) were degassed *via* four freeze-pump-thaw cycles then charged with nitrogen. The solution was heated at reflux under nitrogen for 3 d then cooled to room temperature and the precipitate collected by centrifugation. The precipitate was washed with methanol (3×5 mL), water (3×5 mL), ethanol (3×5 mL) and diethyl ether (3×5 mL). The solid was extracted into CH_2Cl_2 , agitating between each extraction until the CH_2Cl_2 became colourless, and the solvent removed under reduced pressure to obtain the product as a yellow solid (0.035 g, 43 %)

^1H NMR (CDCl_3 , 700 MHz) 9.47 (2H, d, $^3J = 4.9$, H^2), 8.37 (2H, d, $^3J = 7.7$, H^4), 8.04 (2H, d, $^3J = 7.0$, H^5 or H^7), 7.79 (2H, d, $^3J = 8.4$, H^5 or H^7), 7.64 (2H, t, $^3J = 7.7$, H^6), 7.31 (2H, dd, $^3J = 8.0$, $^4J = 4.9$, H^3), 7.13 (1H, s, $\text{H}^{5'}$). ^{13}C NMR (CDCl_3 , 176 MHz) $\delta = 155.6$ (C^2), 148.3 (C^q), 145.1 (C^q), 140 (C^q), 139.5 (C^q), 138.0 (C^4), 134.1 ($\text{C}^{5'}$ or C^q), 134.1 ($\text{C}^{5'}$ or C^q), 132.2 (C^5 or C^7), 128.8 (C^q), 126.5 (C^6), 125.7 (C^5 or C^7), 120.9 (C^3), 24.1 (CH_3). MS (ASAP⁺) 590.09 [$\text{M} + \text{H}$]⁺. HRMS (ASAP⁺) Calcd for $\text{C}_{26}\text{H}_{19}\text{ClN}_2^{194}\text{Pt}$: m/z 588.0864. Found: 588.0864 [M]⁺. Mp > 250 °C.

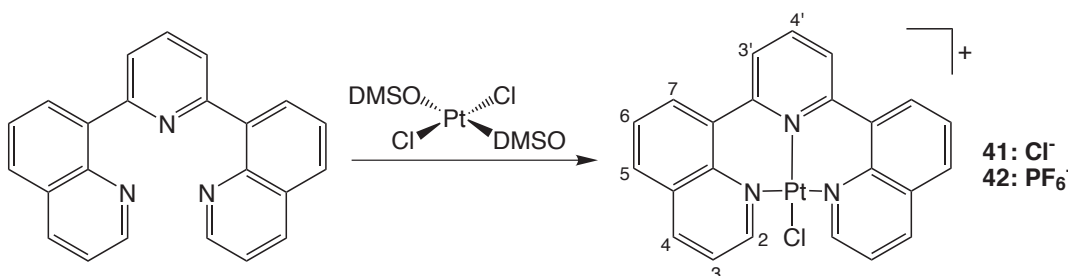
Platinum(1-(8-quinolyl)-3-(2-pyridyl)benzene-N,C^{2'},N) chloride
[Pt(qpyb)Cl], **40**



Separate solutions of 1,3-(8-quinolyl)(2-pyridyl)benzene (0.028 g, 0.10 mmol) in acetonitrile (3 mL) and K_2PtCl_4 (0.045 g, 0.11 mmol) in water (1 mL) were degassed *via* four freeze-pump-thaw cycles and charged with nitrogen. The aqueous solution was added to the acetonitrile solution *via* syringe under a positive pressure of nitrogen. The mixture was heated at reflux under nitrogen for 4 d and cooled to room temperature. The volume of solution was reduced by evaporation and the precipitate collected by centrifugation then washed with water (3×5 mL), methanol (3×5 mL) and diethyl ether (3×5 mL). After drying *in vacuo*, the product was obtained as a yellow solid (0.022, 40 %).

1H NMR ($CDCl_3$, 400 MHz,) $\delta = 10.85$ (1H, dd, $^3J = 5.6$, $^4J = 1.6$, H^2 or $H^{6''}$), 9.95 (1H, d, $^3J = 6.0$, H^2 or $H^{6''}$), 8.31 (1H, t, $^3J = 0.8$), 8.26 (1H, dd, $^3J = 8.4$, $^4J = 1.6$), 8.10 (1H, d, $^3J = 7.6$), 7.70–7.98 (5H, m), 7.67 (2H, td, $^3J = 9.2$, $^4J = 2.8$, H^3 and 1H), 7.46 (1H, dd, $^3J = 4.0$, $^3J = 4.0$, $H^{5''}$). MS (ES^+) 512.0 [$M + H$] $^+$. MS (MALDI $^+$, DCTB matrix) 512.0 [$M + H$] $^+$. Mp > 250 °C.

[Platinum (2,6-di(8-quinolyl)pyridine-N,N,N) chloride] chloride
[Pt(dqp)Cl]Cl, **41** and **[Platinum (2,6-di(8-quinolyl)pyridine-N,N,N) chloride] hexafluorophosphate** [Pt(dqp)Cl]PF₆, **42**



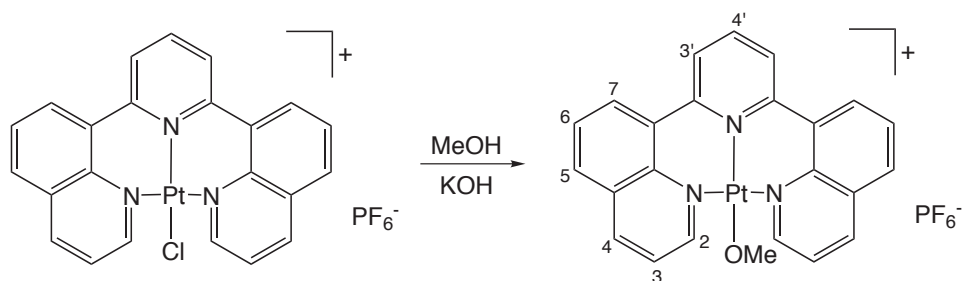
2,6-Di(8-quinolyl)pyridine (0.051 g, 0.15 mmol) and $Cl_2Pt(DMSO)_2$ (0.078 g, 0.19 mmol) were combined in methanol (1.5 mL) and degassed *via* three freeze-pump-thaw cycles then charged with nitrogen. The solution was heated at reflux

under nitrogen for 3 d then cooled to room temperature and the precipitate collected by centrifugation and washed with water (3×5 mL), methanol (3×5 mL) and diethyl ether (3×5 mL) and dried *in vacuo* to yield a grey-white solid (0.041 g, 48 %). Conversion to the hexafluorophosphate salt was achieved by dissolution of the chloride salt in the minimum volume of DMSO and addition to an excess of saturated aqueous solution of KPF_6 . The resulting precipitate was washed successively with water (3×5 mL), methanol (3×5 mL) and diethyl ether (3×5 mL) and dried *in vacuo* to give $[\text{Pt}(\text{dqp})\text{Cl}]\text{PF}_6$ (0.040 g, 44 %).

Data for the chloride salt: ^1H NMR (d_6 -DMSO, 500 MHz) $\delta = 9.25$ (2H, d, $^3J = 4.5$, H^2), 9.01 (2H, d, $^3J = 7.5$, H^4), 8.92 (2H, d, $^3J = 7.0$, H^7), 8.53 (2H, d, $^3J = 7.5$, H^5), 8.47 (1H, t, $^3J = 8.5$, $\text{H}^{4'}$), 8.32 (2H, d, $^3J = 7.5$, $\text{H}^{3'}$), 8.09 (2H, dd, $^3J = 7.5$, $^3J = 7.0$, H^6), 7.81 (2H, dd, $^3J = 7.5$, $^4J = 4.5$, H^3). MS (ES) $^+$ m/z 564.3 $[\text{M}]^+$. HRMS (ES $^+$). Calcd for $\text{C}_{23}\text{H}_{15}\text{ClN}_3^{195}\text{Pt}$: m/z 563.0577. Found: m/z 563.0581. Elem. anal. Calcd for $\text{C}_{23}\text{H}_{15}\text{ClN}_3\text{Pt}$: C, 46.1; H, 2.5; N, 7.0. Found: C, 45.7; H, 2.7; N, 6.6. Mp > 250 $^\circ\text{C}$.

Data for the hexafluorophosphate salt: (d_6 -acetone, 700 MHz) $\delta = 9.37$ (2H, dd, $^3J = 5.0$, $^4J = 1.5$, H^2), 9.02 (2H, dd, $^3J = 7.5$, $^4J = 1.5$, H^4), 8.97 (2H, d, $^3J = 7.5$, H^7), 8.57 (2H, d, $^3J = 7.5$, H^5), 8.54 (1H, t, $^3J = 8.5$, $\text{H}^{4'}$), 8.40 (2H, d, $^3J = 8.5$, $\text{H}^{3'}$), 8.13 (2H, dd, $^3J = 7.5$, $^3J = 7.5$, H^6), 7.84 (2H, td, $^3J = 7.5$, $^4J = 5.0$, H^3). ^{13}C NMR (d_6 -acetone, 176 MHz) $\delta = 158.1$ (C^2), 151.5 (C^q), 142.0 (C^q), 141.9 (C^4), 141.5 ($\text{C}^{3'}$), 133.9 (C^q), 133.4 (C^7), 132.6 (C^5), 129.2 (C^q), 129.2 (C^6), 127.8 ($\text{C}^{4'}$), 123.3 (C^3). MS (ES $^+$) m/z 564 $[\text{M}]^+$. HRMS (ES $^+$). Calcd. for $\text{C}_{23}\text{H}_{15}\text{ClN}_3^{195}\text{Pt}$: m/z 563.0597. Found: m/z 563.0611. Mp > 250 $^\circ\text{C}$.

Platinum (2,6-di(8-quinolyl)pyridine-N,N,N) methoxide hexafluorophosphate $[\text{Pt}(\text{dqp})\text{OMe}]\text{PF}_6$, **46**

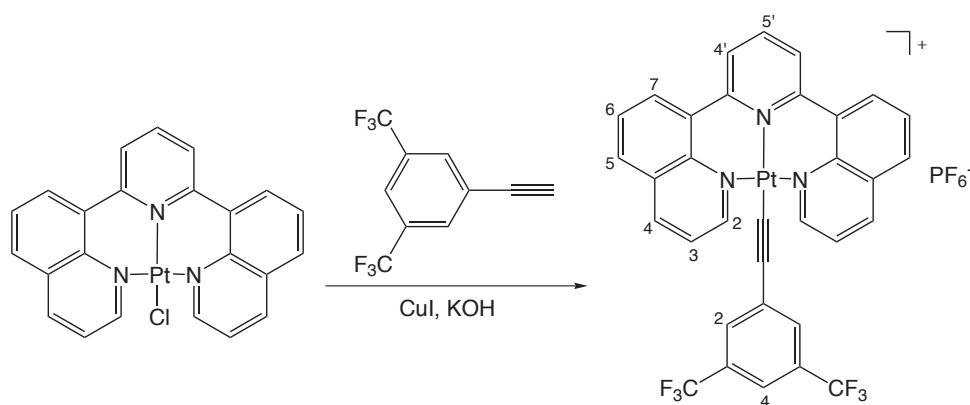


A mixture of $[\text{Pt}(\text{dqp})\text{Cl}]\text{PF}_6$ (0.030 g, 0.042 mmol) and KOH (0.030 g, 0.53 mmol) in methanol (3 mL) was stirred at room temperature for 18 h. The solution was concentrated and then added to saturated aqueous solution of KPF_6 , leading to a bright yellow precipitate, which was collected by centrifugation, washed with

water (3 × 5 mL), methanol (1 × 5 mL) and diethyl ether (1 × 5 mL). The solid was ion exchanged by dissolution in a minimum volume of acetonitrile and addition to a saturated solution of aqueous KPF₆ then the precipitate was collected by centrifugation and washed as before then dried *in vacuo* to give the product as a pale yellow solid (0.016 g, 67 %).

¹H NMR (CDCl₃, 400 MHz) δ = 9.09 (2H, dd, ³J = 5.0, ⁴J = 1.5, H²), 8.74 (2H, dd, ³J = 7.5, H⁷), 8.67 (2H, dd, ³J = 8.0, ³J = 1.5, H⁴), 8.42 (1H, t, ³J = 8.0, H^{4''}), 8.25 (2H, d, ³J = 8.0, H^{3'}), 8.16 (2H, d, ³J = 8.0, H⁵), 8.01 (2H, dd, ³J = 8.0, ³J = 7.5, H⁶), 7.71 (2H, dd, ³J = 8.0, ⁴J = 5.0, H³), 2.82 (3H, s, CH₃). MS (ES⁺). *m/z* 559 [M]⁺. HRMS (ES⁺). Calcd for C₂₄H₁₈N₃O¹⁹⁵Pt: 559.1094. Found: *m/z* 559.1102. Mp > 250 ° C.

Platinum (2,6-di(8-quinolyl)pyridine-N,N,N)(3,5-bis(trifluoromethyl)phenyl)acetylide [Pt(dqp)(CC-tfp)]PF₆, 47



Ethynyl-3,5-bis(trifluoromethyl)benzene (250 μL, 1.41 mmol) and potassium hydroxide (0.030 g, 0.53 mmol) in methanol (5 mL) were stirred at room temperature for 1 h. A solution of [Pt(dqp)Cl]PF₆ (0.040 g, 0.071 mmol) and CuI (4.0 mg, 0.021 mmol) in methanol (5 mL) was added and the solution stirred overnight. The yellow precipitate formed was collected by centrifugation and washed with methanol to yield a yellow solid (0.017 g, 31 %).

¹H NMR (*d*₆-acetone, 700 MHz) δ = 9.86 (2H, dd, ³J = 5.0, ⁴J = 1.0, H²), 9.07 (2H, dd, ³J = 8.0, ⁴J = 1.0, H⁴), 9.00 (2H, dd, ³J = 7.5, ⁴J = 1.0, H⁵), 8.55–8.57 (3H, m, H^{4'} and H⁷), 8.47 (2H, ³J = 7.5, H^{3''}), 8.13 (2H, dd, ³J = 7.5, ³J = 7.5, H⁶), 7.88 (2H, dd, ³J = 8.0, ⁴J = 5.0, H³), 7.80 (1H, s, H⁴-tfp), 7.78 (2H, s, H²-tfp). ¹³C NMR (*d*₆-acetone, 176 MHz) δ = 160.3 (C²), 151.2 (C^q), 142.6 (C^q), 142.3 (C⁴), 141.7 (C⁴), 134.7 (C⁵ or C⁷ or C^{5'}), 133.4 (C³), 132.8 (C⁵ or C⁷ or C^{5'}), 131.8 (C^q), 131.4 (C^{2''} or C^{4''}), 131.1 (C^q), 129.8 (C^q), 129.2 (C^q), 127.6 (C⁶), 123.5 (C^{4'}), 119.2 (C^{2''} or 4''), 110.2 (C≡C or CF₃), 99.5 (C≡C or CF₃), 97.2 (C≡C or CF₃).

^{19}F NMR (d_6 -acetone, 658 MHz) $\delta = -63.9$ (6F, s, CF_3), -73.4 (6F, d, $^2J = 700$, PF_6^-). MS (MALDI $^+$, DCTB matrix, m/z 765.2 $[\text{M}]^+$). HRMS (ASAP $^+$) Calcd for $\text{C}_{33}\text{H}_{18}\text{N}_3\text{F}_6^{192}\text{Pt}$: m/z 762.1015. Found: 762.1017. Mp >250 ° C.

References

1. H. Yersin and W. Finkenzeller, *Highly Efficient OLEDs with Phosphorescent Materials*, Wiley-VCH, Weinheim, 2008.
2. C. Adachi, M. A. Baldo, M. E. Thompson and S. R. Forrest, *J. Appl. Phys.*, 2001, **90**, 5048–5051.
3. J. Kalinowski, *Organic light-emitting diodes: principles, characteristics, and processes*, CRC Press, New York, 2005, vol. 91.
4. J. A. G. Williams, S. Develay, D. Rochester and L. Murphy, *Coord. Chem. Rev.*, 2008, **252**, 2596–2611.
5. P. K. M. Siu, S.-W. Lai, W. Lu, N. Zhu and C.-M. Che, *Eur. J. Inorg. Chem.*, 2003, 2749–2752.
6. W. Tang, X. Lu, K. Wong and V. Yam, *J. Mater. Chem.*, 2005, **15**, 2714–2720.
7. V. Guerschais, L. Ordroneau and H. Le Bozec, *Coord. Chem. Rev.*, 2010, **254**, 2533–2545.
8. V. Aubert, L. Ordroneau, M. Escadeillas, J. A. G. Williams, A. Boucekkine, E. Coulaud, C. Dragonetti, S. Righetto, D. Roberto, R. Ugo, A. Valore, A. Singh, J. Zyss, I. Ledoux-Rak, H. Le Bozec and V. Guerschais, *Inorg. Chem.*, 2011, **50**, 5027–5038.
9. S. W. Botchway, M. Charnley, J. W. Haycock, A. W. Parker, D. L. Rochester, J. A. Weinstein and J. A. G. Williams, *Proc. Natl. Acac. Sci. U. S. A.*, 2008, **105**, 16071–16076.
10. C.-K. Koo, K.-L. Wong, C. W.-Y. Man, Y.-W. Lam, K.-Y. So, H.-L. Tam, S.-W. Tsao, K.-W. Cheah, K.-C. Lau, Y.-Y. Yang, J.-C. Chen and M. H.-W. Lam, *Inorg. Chem.*, 2009, **48**, 872–878.
11. D.-L. Ma, T. Y.-T. Shum, F. Zhang, C.-M. Che and M. Yang, *Chem. Commun.*, 2005, 4675–7.

REFERENCES

12. I. Eryazici, C. N. Moorefield and G. R. Newkome, *Chem. Rev.*, 2008, **108**, 1834–1895.
13. A. Naught and A. Wilkinson, *IUPAC Compendium of Chemical Terminology*, Blackwell Science, 1997.
14. N. Turro, *Modern Molecular Photochemistry*, Univ. Science Books, Sausalito, CA., 1991.
15. J. Lakowicz, *Principles of Fluorescence Spectroscopy*, Springer, New York, NY., 2006.
16. M. Kasha, *Discuss. Faraday Soc.*, 1950, **9**, 14–19.
17. W. Richards and P. Scott, *Energy Levels in Atoms and Molecules*, Oxford University Press, Oxford, 1994.
18. R. Wayne, *Principles and Applications of Photochemistry*, Oxford University Press, Oxford, 1988.
19. J. Paris and W. Brandt, *J. Am. Chem. Soc.*, 1959, **81**, 5001–5002.
20. A. Juris and V. Balzani, *Coord. Chem. Rev.*, 1988, **84**, 85–277.
21. A. Juris, V. Balzani, S. Campagna, G. Denti, S. Serroni, G. Frei and H. U. Güdel, *Inorg. Chem.*, 1994, **33**, 1491–1496.
22. J. G. Vos and J. M. Kelly, *Dalton Trans.*, 2006, 4869–4883.
23. G. A. Crosby and W. H. Elfring, *J. Phys. Chem.*, 1976, **80**, 2206–2211.
24. S. Welter, N. Salluce, P. Belser, M. Groeneveld and L. D. Cola, *Coord. Chem. Rev.*, 2005, **249**, 1360–1371.
25. J. Sauvage, J. Collin, J. Chambron, S. Guillerez, C. Coudret, V. Balzani, F. Barigelletti, L. De Cola and L. Flamigni, *Chem. Rev.*, 1994, **94**, 993–1019.
26. L. Flamigni, E. Baranoff, J.-P. Collin and J.-P. Sauvage, *Chem.-Eur. J.*, 2006, **12**, 6592–6606.
27. G. Morgan and F. Burstall, *J. Chem. Soc.*, 1934, 965–971.
28. J. Winkler, T. Netzel, C. Creutz and N. Sutin, *J. Am. Chem. Soc.*, 1987, **109**, 2381–2392.

REFERENCES

29. D. Fink and W. Ohnesorge, *J. Am. Chem. Soc.*, 1969, **91**, 4995–4998.
30. J. Calvert, J. Caspar, R. Binstead, T. Westmoreland and T. Meyer, *J. Am. Chem. Soc.*, 1982, **104**, 6620–6627.
31. F. Schramm, V. Meded, H. Fliegl, K. Fink, O. Fuhr, Z. Qu, W. Klopper, S. Finn, T. E. Keyes and M. Ruben, *Inorg. Chem.*, 2009, **48**, 5677–5684.
32. A. Breivogel, C. Förster and K. Heinze, *Inorg. Chem.*, 2010, **49**, 7052–7056.
33. K. Lashgari, M. Kritikos, R. Norrestam and T. Norrby, *Acta Cryst. C*, 1999, **55**, 64–67.
34. M. Abrahamsson, M. Jäger, T. Österman, L. Eriksson, P. Persson, H. Becker, O. Johansson and L. Hammarström, *J. Am. Chem. Soc.*, 2006, **128**, 12616–12617.
35. H. Wolpher, O. Johansson, M. Abrahamsson, M. Kritikos, L. Sun and B. Åkermark, *Inorg. Chem. Commun.*, 2004, **7**, 337–340.
36. M. Abrahamsson, H. Wolpher, O. Johansson, J. Larsson, M. Kritikos, L. Eriksson, P. Norrby, J. Bergquist, L. Sun and B. Åkermark, *Inorg. Chem.*, 2005, **44**, 3215–3225.
37. B. Martin and G. Waind, *J. Chem. Soc.*, 1958, 4284–4288.
38. R. DeSimone and R. Drago, *Inorg. Chem.*, 1969, **8**, 2517–2519.
39. C. M. Flynn Jr. and J. N. Demas, *J. Am. Chem. Soc.*, 1974, **96**, 1959–1960.
40. N. P. Ayala, C. M. Flynn Jr., L. Sacksteder, J. N. Demas and B. A. DeGraff, *J. Am. Chem. Soc.*, 1990, **112**, 3837–3844.
41. J.-P. Collin, I. M. Dixon, J.-P. Sauvage, J. A. G. Williams, F. Barigelletti and L. Flamigni, *J. Am. Chem. Soc.*, 1999, **121**, 5009–5016.
42. J. A. G. Williams, A. J. Wilkinson and V. L. Whittle, *Dalton Trans.*, 2008, 2081–2099.
43. M. Licini and J. A. G. Williams, *Chem. Commun.*, 1999, **19**, 1943–1944.
44. W. Leslie, A. S. Batsanov, J. A. K. Howard and J. A. G. Williams, *Dalton Trans.*, 2004, 623–631.

REFERENCES

45. L. Flamigni, B. Ventura, F. Barigelletti, E. Baranoff, J.-P. Collin and J.-P. Sauvage, *Eur. J. Inorg. Chem.*, 2005, **2005**, 1312–1318.
46. D. R. McMillin and J. J. Moore, *Coord. Chem. Rev.*, 2002, **229**, 113–121.
47. K. A. King, P. J. Spellane and R. J. Watts, *J. Am. Chem. Soc.*, 1985, **107**, 1431–1432.
48. R. J. Watts, J. S. Harrington and J. V. Houten, *J. Am. Chem. Soc.*, 1976, 2179–2187.
49. W. Wickramasinghe, P. Bird and N. Serpone, *J. Chem. Soc., Chem. Commun.*, 1981, 1284–1286.
50. S. Sprouse, K. A. King, P. J. Spellane and R. J. Watts, *J. Am. Chem. Soc.*, 1984, **106**, 6647–6653.
51. A. B. Tamayo, B. D. Alleyne, P. I. Djurovich, S. Lamansky, I. M. Tsyba, N. N. Ho, R. Bau and M. E. Thompson, *J. Am. Chem. Soc.*, 2003, **125**, 7377–7387.
52. S. Lamansky, P. I. Djurovich, D. Murphy, A.-R. Feras, H.-E. Lee, C. Adachi, P. E. Burrows, S. R. Forrest and M. E. Thompson, *J. Am. Chem. Soc.*, 2001, **123**, 4304–4312.
53. T. Yutaka, S. Obara, S. Ogawa, K. Nozaki, N. Ikeda, T. Ohno, Y. Ishii, K. Sakai and M. Haga, *Inorg. Chem.*, 2005, **44**, 4737–4746.
54. A. J. Wilkinson, A. E. Goeta, C. E. Foster and J. A. G. Williams, *Inorg. Chem.*, 2004, **43**, 6513–6515.
55. A. Mamo, I. Stefio, M. F. Parisi, A. Credi, M. Venturi, C. Di Pietro and S. Campagna, *Inorg. Chem.*, 1997, **36**, 5947–5950.
56. M. Polson, S. Fracasso, V. Bertolasi, M. Ravaglia and F. Scandola, *Inorg. Chem.*, 2004, **43**, 1950–1956.
57. M. Polson, M. Ravaglia, S. Fracasso, M. Garavelli and F. Scandola, *Inorg. Chem.*, 2005, **44**, 1282–1289.
58. S. Obara, M. Itabashi, F. Okuda, S. Tamaki, Y. Tanabe, Y. Ishii, K. Nozaki and M.-A. Haga, *Inorg. Chem.*, 2006, **45**, 8907–8921.
59. A. J. S. Bexon and J. A. G. Williams, *C.R. Chim.*, 2005, **8**, 1326–1335.

REFERENCES

60. A. J. Wilkinson, H. Puschmann, J. A. K. Howard, C. E. Foster and J. A. G. Williams, *Inorg. Chem.*, 2006, **45**, 8685–8699.
61. V. L. Whittle and J. A. G. Williams, *Inorg. Chem.*, 2008, **47**, 6596–6607.
62. M. E. Frink, S. D. Sprouse, H. A. Goodwin, R. J. Watts and P. C. Ford, *Inorg. Chem.*, 1988, **27**, 1283–1286.
63. R. J. Watts and J. Van Houten, *J. Am. Chem. Soc.*, 1978, **100**, 1718–1721.
64. C. Harris and E. McKenzie, *J. Inorg. Nucl. Chem.*, 1963, **25**, 171–174.
65. M. T. Indelli, R. Ballardini and F. Scandola, *J. Phys. Chem.*, 1984, **88**, 2547–2551.
66. M. T. Indelli, C. A. Bignozzi, A. Harriman, J. R. Schoonover and F. Scandola, *J. Am. Chem. Soc.*, 1994, **116**, 3768–3779.
67. P. Bradley, B. Bursten and C. Turro, *Inorg. Chem.*, 2001, **40**, 1376–1379.
68. M. T. Indelli, C. Chiorboli, L. Flamigni, L. De Cola and F. Scandola, *Inorg. Chem.*, 2007, **46**, 5630–5641.
69. K. Erkkila, D. Odom and J. Barton, *Chem. Rev.*, 1999, **99**, 2777–2795.
70. S. Chan, M. Chou, C. Creutz, T. Matsubara and N. Sutin, *J. Am. Chem. Soc.*, 1981, **103**, 369–379.
71. M. G. Colombo, T. C. Brunold, T. Riedener, H. U. Güdel, M. Fortsch and H.-B. Bürgi, *Inorg. Chem.*, 1994, **33**, 545–550.
72. M. G. Colombo, A. Hauser and H. U. Güdel, *Inorg. Chem.*, 1993, **32**, 3088–3092.
73. P. Didier, I. Ortmans, A. Kirsch-De Mesmaeker and R. J. Watts, *Inorg. Chem.*, 1993, **32**, 5239–5245.
74. L. Ghizdavu, O. Lentzen, S. Schumm, A. Brodkorb, C. Moucheron and A. Kirsch-De Mesmaeker, *Inorg. Chem.*, 2003, **42**, 1935–1944.
75. K. K.-W. Lo, C.-K. Li, K.-W. Lau and N. Zhu, *Dalton Trans.*, 2003, **2**, 2–9.
76. E. C. Constable, R. P. G. Henney, T. A. Leese and D. A. Tocher, *Dalton Trans.*, 1990, 443–449.

REFERENCES

77. M. Feng and K. Chan, *Organometallics*, 2002, **21**, 2743–2750.
78. W. Mroóz, C. Botta, U. Giovanella, E. Rossi, A. Colombo, C. Dragonetti, D. Roberto, R. Ugo, A. Valore and J. A. G. Williams, *J. Mater. Chem.*, 2011, **21**, 8653–8661.
79. M. Maestri, D. Sandrini, V. Balzani, A. von Zelewsky, C. Deuschel-Cornioley and P. Jolliet, *Helv. Chim. Acta*, 1988, **71**, 1053–1059.
80. L. Chassot, E. Müller and A. von Zelewsky, *Inorg. Chem.*, 1984, **23**, 4249–4253.
81. C. A. Craig, F. O. Garces, R. J. Watts, R. Palmans and A. J. Frank, *Coord. Chem. Rev.*, 1990, **97**, 193–208.
82. M. M. Mdleleni, J. S. Bridgewater, R. J. Watts and P. C. Ford, *Inorg. Chem.*, 1995, **34**, 2334–2342.
83. H. Yersin, P. Huber and H. Wiedenhofer, *Coord. Chem. Rev.*, 1994, **132**, 35–42.
84. É. Shpol'skii, *Sov. Phys. Usp. (Engl. Transl.)*, 1960, **3**, 372–389.
85. J. Brooks, Y. Babayan, S. Lamansky, P. I. Djurovich, I. Tsyba, R. Bau and M. E. Thompson, *Inorg. Chem.*, 2002, **41**, 3055–3066.
86. J. Dewan, S. Lippard and W. Bauer, *J. Am. Chem. Soc.*, 1980, **102**, 858–860.
87. J. A. Bailey, M. G. Hill, R. E. Marsh, V. M. Miskowski, W. P. Schaefer and H. B. Gray, *Inorg. Chem.*, 1995, **34**, 4591–4599.
88. E. C. Constable, *Chem. Soc. Rev.*, 2007, **36**, 246–253.
89. D. K. Crites, C. T. Cunningham and D. R. McMillin, *Inorg. Chim. Acta*, 1998, **273**, 346–353.
90. R. McGuire, M. Clark and D. R. McMillin, *Coord. Chem. Rev.*, 2010, **254**, 2574–2583.
91. J. F. Michalec, S. A. Bejune, D. G. Cuttell, G. Summerton, J. A. Gertenbach, J. S. Field, R. J. Haines and D. R. McMillin, *Inorg. Chem.*, 2001, **40**, 2193–2200.
92. M. Wilson, L. Ledwaba, J. Field and D. McMillin, *Dalton Trans.*, 2005, 2754–2759.
93. V. W. W. Yam, R. P. L. Tang, K. M. C. Wong and K. K. Cheung, *Organometallics*, 2001, **20**, 4476–4482.

REFERENCES

94. E. Shikhova, E. O. Danilov, S. Kinayyigit, I. E. Pomestchenko, A. D. Tregubov, F. Camerel, P. Retailleau, R. Ziessel and F. N. Castellano, *Inorg. Chem.*, 2007, **46**, 4180–4190.
95. M. L. Muro, S. Diring, X. Wang, R. Ziessel and F. N. Castellano, *Inorg. Chem.*, 2008, **47**, 6796–6803.
96. E. C. Constable, R. P. G. Henney, T. A. Leese and D. A. Tocher, *J. Chem. Soc., Dalton Trans.*, 1990, 443–449.
97. E. C. Constable, R. P. G. Henney, T. A. Leese and D. A. Tocher, *J. Chem. Soc., Chem. Commun.*, 1990, 513–515.
98. S.-W. Lai, M. C.-W. Chan, T.-C. Cheung, S.-M. Peng and C.-M. Che, *Inorg. Chem.*, 1999, **1**, 4046–4055.
99. W. Lu, B.-X. Mi, M. C. W. Chan, Z. Hui, N. Zhu, S.-T. Lee and C.-M. Che, *Chem. Commun.*, 2002, 206–207.
100. W. Lu, M. Chan, N. Zhu, C. Che, C. Li and Z. Hui, *J. Am. Chem. Soc.*, 2004, **126**, 7639–7651.
101. S. C. F. Kui, I. H. T. Sham, C. C. C. Cheung, C.-W. Ma, B. Yan, N. Zhu, C.-M. Che and W.-F. Fu, *Chem.-Eur. J.*, 2007, **13**, 417–435.
102. P. Shao, Y. Li, A. Azenkeng, M. R. Hoffmann and W. Sun, *Inorg. Chem.*, 2009, **48**, 2407–2419.
103. W. Lu, B.-X. Mi, M. C. W. Chan, Z. Hui, C.-M. Che, N. Zhu and S.-T. Lee, *J. Am. Chem. Soc.*, 2004, **126**, 4958–4971.
104. J. Schneider, P. Du, P. Jarosz, T. Lazarides, X. Wang, W. W. Brennessel and R. Eisenberg, *Inorg. Chem.*, 2009, **48**, 4306–4316.
105. D. J. Cárdenas, A. M. Echavarren and M. C. Ramírez de Arellano, *Organometallics*, 1999, **18**, 3337–3341.
106. J. A. G. Williams, A. Beeby, E. S. Davies, J. A. Weinstein and C. Wilson, *Inorg. Chem.*, 2003, **42**, 8609–8611.
107. W. Sotoyama, T. Satoh, H. Sato, A. Matsuura and N. Sawatari, *J. Phys. Chem. A*, 2005, **109**, 9760–9766.

REFERENCES

108. D. L. Rochester, S. Develay, S. Zálíš and J. A. G. Williams, *Dalton Trans.*, 2009, 1728–1741.
109. S. J. Farley, D. L. Rochester, A. L. Thompson, J. A. K. Howard and J. A. G. Williams, *Inorg. Chem.*, 2005, **44**, 9690–703.
110. Z. Wang, E. Turner, V. Mahoney, S. Madakuni, T. Groy and J. Li, *Inorg. Chem.*, 11276–11286.
111. L. Murphy, *Ph.D. thesis*, Durham University, 2010.
112. S. Develay, O. Blackburn, A. L. Thompson and J. A. G. Williams, *Inorg. Chem.*, 2008, **47**, 11129–11142.
113. C. Cornioley-Deuschel, T. Ward and A. von Zelewsky, *Helv. Chim. Acta*, 1988, **71**, 130–133.
114. G. W. V. Cave, N. W. Alcock and J. P. Rourke, *Organometallics*, 1999, **18**, 1801–1803.
115. G. W. V. Cave, F. P. Fanizzi, R. J. Deeth, W. Errington and J. P. Rourke, *Organometallics*, 2000, **19**, 1355–1364.
116. M. Maestri, C. Deuschel-Cornioley and A. von Zelewsky, *Coord. Chem. Rev.*, 1991, **111**, 117–123.
117. J. R. Berenguer, E. Lalinde and J. Torroba, *Inorg. Chem.*, 2007, **46**, 9919–9930.
118. G. S. M. Tong and C. M. Che, *Chem.-Eur. J.*, 2009, **15**, 7225–7237.
119. W. Lu, M. C. W. Chan, K. K. Cheung and C. M. Che, *Organometallics*, 2001, **20**, 2477–2486.
120. Rausch, Andreas F. and Homeier, Herman H. H. and Djurovich, Peter I. and Thompson, Mark E. and Yersin, Hartmut, *Proc. SPIE*, 2007, **6655**, 66550F.
121. H.-K. Yip, L.-K. Cheng, K.-K. Cheung and C.-M. Che, *J. Chem. Soc. Dalton Trans.*, 1993, 2933–2938.
122. Y. Hu, M. Wilson, R. Zong, C. Bonnefous, D. McMillin and R. Thummel, *Dalton Trans.*, 2004, 354–358.
123. D. Ravindranathan, D. A. K. Vezzu, L. Bartolotti, P. D. Boyle and S. Huo, *Inorg. Chem.*, 2010, **49**, 8922–8928.

REFERENCES

124. D. A. K. Vezzu, J. C. Deaton, J. S. Jones, L. Bartolotti, C. F. Harris, A. P. Marchetti, M. Kondakova, R. D. Pike and S. Huo, *Inorg. Chem.*, 2010, **49**, 5107–5119.
125. H.-M. Wen, Y.-H. Wu, Y. Fan, L.-Y. Zhang, C.-N. Chen and Z.-N. Chen, *Inorg. Chem.*, 2010, **49**, 2210–2221.
126. H.-M. Wen, Y.-H. Wu, L.-J. Xu, L.-Y. Zhang, C.-N. Chen and Z.-N. Chen, *Dalton Trans.*, 2011, **40**, 6929–6938.
127. K. Hanson, L. Roskop, P. Djurovich, F. Zahariev, M. Gordon and M. Thompson, *J. Am. Chem. Soc.*, 2010, **132**, 16247–16255.
128. G. Destriau, *J Chim Physique*, 1936, **33**, 587–590.
129. A. Bernanose, *Br. J. Appl. Phys.*, 1955, **6**, S54–S55.
130. N. Holonyak and S. Bevacqua, *Appl. Phys. Lett.*, 1962, **1**, 82–83.
131. M. Pope, P. Magnante and H. P. Kallmann, *J. Chem. Phys.*, 1963, **38**, 2042–2043.
132. W. Helfrich and W. G. Schneider, *Phys. Rev. Lett.*, 1965, **14**, 229–231.
133. J. Dresner, *RCA Rev.*, 1969, **30**, 332–333.
134. D. Williams and M. Schadt, *Proc. IEEE*, 1970, **58**, 476–476.
135. G. Wang, X. Tao and H. Huang, *Color. Technol.*, 2005, **121**, 132–138.
136. S. Kim, H.-J. Kwon, S. Lee, H. Shim, Y. Chun, W. Choi, J. Kwack, D. Han, M. Song, S. Kim, S. Mohammadi, I. Kee and S. Y. Lee, *Adv. Mater.*, 2011, **23**, 3511–3516.
137. M. A. Baldo, M. Deutsch, P. E. Burrows, H. Gossenberger, M. Gerstenberg, V. Ban and S. R. Forrest, *Adv. Mater.*, 1998, **10**, 1505–1514.
138. D. Pardo, G. Jabbour and N. Peyghambarian, *Adv. Mater.*, 2000, **12**, 1249–1252.
139. F. Pschenitzka and J. C. Sturm, *Appl. Phys. Lett.*, 1999, **74**, 1913–1915.
140. J. A. Rogers, Z. Bao and L. Dhar, *Appl. Phys. Lett.*, 1998, **73**, 294–296.
141. S.-C. Chang, J. Bharathan, Y. Yang, R. Helgeson, F. Wudl, M. B. Ramey and J. R. Reynolds, *Appl. Phys. Lett.*, 1998, **73**, 2561–2563.

REFERENCES

142. M. A. Baldo, M. E. Thompson and S. R. Forrest, *Pure Appl. Chem.*, 1999, **71**, 2095–2106.
143. D. Dexter, *J. Chem. Phys.*, 1953, **21**, 836–850.
144. T. Förster, *Discuss. Faraday Soc.*, 1959, **27**, 7–17.
145. R. Evans, P. Douglas and C. Winscom, *Coord. Chem. Rev.*, 2006, **250**, 2093–2126.
146. D. F. O'Brien, M. A. Baldo, M. E. Thompson and S. R. Forrest, *Appl. Phys. Lett.*, 1999, **74**, 442–444.
147. M. A. Baldo, D. F. O'Brien, Y. You, A. Shoustikov, S. Sibley, M. E. Thompson and S. R. Forrest, *Nature*, 1998, **395**, 151–154.
148. M. A. Baldo, D. F. O'Brien, S. R. Forrest and M. E. Thompson, *Phys. Rev. B*, 1999, **60**, 14422–14428.
149. C. Adachi, S. Tokito, T. Tsutsui and S. Saito, *Japn J. Appl. Phys.*, 1988, **27**, L269–L271.
150. C. Adachi, S. Tokito, T. Tsutsui and S. Saito, *Japn J. Appl. Phys.*, 1988, **27**, L713–L715.
151. V. Cleave, G. Yahioglu, P. L. Barny, R. H. Friend and N. Tessler, *Adv. Mater.*, 1999, **11**, 285–288.
152. J. Burroughes, D. Bradley, A. Brown, R. Marks, K. Mackay, R. Friend, P. Burns and A. Holmes, *Nature*, 1990, **347**, 539–541.
153. C. Chen and J. Shi, *Coord. Chem. Rev.*, 1998, **171**, 161–174.
154. U. Mitschke and P. Bäuerle, *J. Mater. Chem.*, 2000, **10**, 1471–1507.
155. L. Hung, *Mater. Sci. Eng. R*, 2002, **39**, 143–222.
156. B. W. D'Andrade, J. Brooks, V. Adamovich, M. E. Thompson and S. R. Forrest, *Adv. Mater.*, 2002, **14**, 1032–1036.
157. J. Borchardt, *Mater. Today*, 2004, **7**, 42–46.
158. T. Hofbeck and H. Yersin, *Inorg. Chem.*, 2010, 9290–9299.
159. P.-T. Chou and Y. Chi, *Eur. J. Inorg. Chem.*, 2006, 3319–3332.

REFERENCES

160. M. Maestri, D. Sandrini, V. Balzani, U. Maeder and A. von Zelewsky, *Inorg. Chem.*, 1987, **26**, 1323–1327.
161. C. Adachi, M. A. Baldo, S. R. Forrest, S. Lamansky, M. E. Thompson and R. C. Kwong, *Appl. Phys. Lett.*, 2001, **78**, 1622–1624.
162. M. K. Nazeeruddin, R. T. Wegh, Z. Zhou, C. Klein, Q. Wang, F. De Angelis, S. Fantacci and M. Grätzel, *Inorg. Chem.*, 2006, **45**, 9245–9250.
163. A. Tsuboyama, H. Iwawaki, M. Furugori, T. Mukaide, J. Kamatani, S. Igawa, T. Moriyama, S. Miura, T. Takiguchi, S. Okada, M. Hoshino and K. Ueno, *J. Am. Chem. Soc.*, 2003, **125**, 12971–12979.
164. J. Lee, N. Chopra, S.-H. Eom, Y. Zheng, J. Xue, F. So and J. Shi, *Appl. Phys. Lett.*, 2008, **93**, 123306–01–03.
165. P.-T. Chou and Y. Chi, *Chem.-Eur. J.*, 2007, **13**, 380–395.
166. J. Kalinowski, V. Fattori, M. Cocchi and J. A. G. Williams, *Coord. Chem. Rev.*, 2011, **255**, 2401–2425.
167. J. Kavitha, S. Chang, Y. Chi, J. Yu, Y. Hu, P. Chou, S. Peng, G. Lee, Y. Tao, C. Chien and A. Carty, *Adv. Funct. Mater.*, 2005, **15**, 223–229.
168. B. W. D’Andrade and S. R. Forrest, *Adv. Mater.*, 2004, **16**, 1585–1595.
169. E. Williams, K. Haavisto, J. Li and G. Jabbour, *Adv. Mater.*, 2007, **19**, 197–202.
170. C. Pearson, D. H. Cadd, M. C. Petty and Y. L. Hua, *J. Appl. Phys.*, 2009, **106**, 064516–01–10.
171. S. Tokito, T. Iijima, T. Tsuzuki and F. Sato, *Appl. Phys. Lett.*, 2003, **83**, 2459–2461.
172. B. W. D’Andrade, M. E. Thompson and S. R. Forrest, *Adv. Mater.*, 2002, **14**, 147–151.
173. B. W. D’Andrade, R. J. Holmes and S. R. Forrest, *Adv. Mater.*, 2004, **16**, 624–628.
174. P. Schlotter, R. Schmidt and J. Schneider, *Appl. Phys. A: Mater. Sci. Process.*, 1997, **64**, 417–418.

REFERENCES

175. A. Duggal, J. Shiang, C. Heller and D. Foust, *Appl. Phys. Lett.*, 2002, **80**, 3470–3472.
176. Y. Wang, Y. Hua, X. Wu, G. Zhang, J. Hui, L. Zhang, Q. Liu, L. Ma, S. Yin and M. C. Petty, *J. Phys. D, Appl. Phys.*, 2008, **41**, 025104–01–04.
177. B. Krummacher, V. Choong, M. Mathai, S. Choulis, F. So, F. Jermann, T. Fiedler and M. Zachau, *Appl. Phys. Lett.*, 2006, **88**, 113506–01–03.
178. M. Cocchi, D. Virgili, V. Fattori, D. L. Rochester and J. A. G. Williams, *Adv. Func. Mater.*, 2007, **17**, 285–289.
179. M. Cocchi, J. Kalinowski, D. Virgili, V. Fattori, S. Develay and J. Williams, *Appl. Phys. Lett.*, 2007, **90**, 163508–01–03.
180. M. Cocchi, J. Kalinowski, V. Fattori, J. A. G. Williams and L. Murphy, *Appl. Phys. Lett.*, 2009, **94**, 073309–01–03.
181. M. Cocchi, J. Kalinowski, L. Murphy, J. A. G. Williams and V. Fattori, *Org. Electron.*, 2010, **11**, 388–396.
182. G. D. Batema, M. Lutz, A. L. Spek, C. A. van Walree, C. d. M. Donega, A. Meijerink, R. W. A. Havenith, J. Perez-Moreno, K. Clays, M. Buechel, A. van Dijken, D. L. Bryce, G. P. M. van Klink and G. van Koten, *Organometallics*, 2008, **27**, 1690–1701.
183. B. W. D’Andrade, J. Brooks, V. Adamovich, M. E. Thompson and S. R. Forrest, *Adv. Mater.*, 2002, **14**, 1032–1036.
184. M. Abrahamsson, M. Jäger, R. J. Kumar, T. Österman, P. Persson, H. Becker, O. Johansson and L. Hammarström, *J. Am. Chem. Soc.*, 2008, **130**, 15533–15542.
185. B. Ventura, F. Barigelletti, F. Durola, L. Flamigni, J.-P. Sauvage and O. S. Wenger, *Dalton Trans.*, 2008, 491–498.
186. K. Roesch and R. Larock, *J. Org. Chem.*, 1998, **63**, 5306–5307.
187. K. Roesch and R. Larock, *Org. Lett.*, 1999, **1**, 553–556.
188. T. Ishiyama, M. Murata and N. Miyaoura, *J. Org. Chem.*, 1995, **60**, 7508–7510.
189. C. J. Aspley and J. A. G. Williams, *New J. Chem.*, 2001, **25**, 1136–1147.

REFERENCES

190. T. Barder, S. Walker, J. Martinelli and S. Buchwald, *J. Am. Chem. Soc.*, 2005, **127**, 4685–4696.
191. M. Kuroboshi, Y. Waki and H. Tanaka, *J. Org. Chem.*, 2003, **68**, 3938–3942.
192. C. Li, M. Liu, N. G. Pschirer, M. Baumgarten and K. Müller, *Chem. Rev.*, 2010, **110**, 6817–6855.
193. A. Suzuki, *J. Organomet. Chem.*, 2002, **653**, 83–90.
194. A. Hijazi, M. E. Walther, C. Besnard and O. S. Wenger, *Polyhedron*, 2010, **29**, 857–863.
195. C. E. Buss and K. R. Mann, *J. Am. Chem. Soc.*, 2002, **124**, 1031–1039.
196. T. Wadas, Q. Wang, Y. Kim, C. Flaschenreim, T. Blanton and R. Eisenberg, *J. Am. Chem. Soc.*, 2004, **126**, 16841–16849.
197. W. Leslie, R. A. Poole, P. R. Murray, L. J. Yellowlees, A. Beeby and J. A. G. Williams, *Polyhedron*, 2004, **23**, 2769–2777.
198. B. Soro, S. Stoccoro, G. Minghetti, A. Zucca, M. A. Cinellu, S. Gladiali, M. Manassero and M. Sansoni, *Organometallics*, 2005, **24**, 53–61.
199. R. J. Puddephatt, *Inorg. Synth.*, 2002, **33**, 192–195.
200. K. Sonogashira, *Tetrahedron*, 1975, 4467 – 4470.
201. A. J. Wilkinson, *Ph.D. thesis*, Durham University, 2004.
202. P. Brulatti, *Ph.D. thesis*, Durham University, 2010.
203. K.-W. Wang, J.-L. Chen, Y.-M. Cheng, M.-W. Chung, C.-C. Hsieh, G.-H. Lee, P.-T. Chou, K. Chen and Y. Chi, *Inorg. Chem.*, 2010, **49**, 1372–83.
204. B. Soro, S. Stoccoro, G. Minghetti, A. Zucca, M. A. Cinellu, M. Manassero and S. Gladiali, *Inorg. Chim. Acta*, 2006, **359**, 1879–1888.
205. D. A. K. Vezzu, J. C. Deaton, J. S. Jones, L. Bartolotti, C. F. Harris, A. P. Marchetti, M. Kondakova, R. D. Pike and S. Huo, *Inorg. Chem.*, 2010, **49**, 5107–19.
206. I. Kuprov, *Ph.D. thesis*, Novosibirsk State University, 2002.
207. V. Bakhmutov and J. Wiley, *Practical NMR relaxation for chemists*, Wiley Online Library, 2004.

REFERENCES

208. T. Duncan, *A compilation of chemical shift anisotropies*, The Farragut Press, Chicago, 1990.
209. E. Fukushima and S. Roeder, *Experimental pulse NMR: a nuts and bolts approach*, Addison-Wesley, Reading, MA, 1981.
210. R. Boéré and R. Kidd, *Annu. Rep. NMR Spectrosc.*, 1983, **13**, 319–385.
211. P. Ghosh, P. Desrosiers and G. Parkin, *J. Am. Chem. Soc.*, 1998, **120**, 10416–10422.
212. H. Dias and X. Wang, *Polyhedron*, 2004, **23**, 2533–2539.
213. R. Claramunt, D. Sanz, M. Santa Maria, J. Elguero and S. Trofimenko, *J. Organomet. Chem.*, 2004, **689**, 463–470.
214. M. Stepień, L. Latos-Grazynski, L. Szterenberga, J. Panek and Z. Latajka, *J. Am. Chem. Soc.*, 2004, **126**, 4566–4580.
215. J. Lallemand, J. Soulié and J. Chottard, *J. Chem. Soc., Chem. Commun.*, 1980, 436–438.
216. S. Reinartz, M. Baik, P. White, M. Brookhart and J. Templeton, *Inorg. Chem.*, 2001, **40**, 4726–4732.
217. M.-H. Thibault, B. E. G. Lucier, R. W. Schurko and F.-G. Fontaine, *Dalton Trans.*, 2009, 7701–7716.
218. A. Abragam and H. Carr, *Phys. Today*, 1961, **14**, 56.
219. E. Andrew, A. Bradbury and R. Eades, *Nature*, 1958, **182**, 1659.
220. S. Meiboom and D. Gill, *Rev. Sci. Instrum.*, 1958, **29**, 688–691.
221. H. Carr and E. Purcell, *Phys. Rev.*, 1954, **94**, 630–638.
222. B. A. Demko and R. E. Wasylshen, *Inorg. Chem.*, 2008, **47**, 2786–2797.
223. T. Sajoto, P. I. Djurovich, A. B. Tamayo, J. Oxgaard, W. A. Goddard, III and M. E. Thompson, *J. Am. Chem. Soc.*, 2009, **131**, 9813–9822.
224. P. J. Hay, *J. Phys. Chem. A*, 2002, **106**, 1634–1641.
225. A. Becke, *Chem. Phys.*, 1993, **98**, 5648–5652.
226. C. Lee, W. Yang and R. G. Parr, *Phys. Rev. B*, 1988, **37**, 785–789.

227. A. Vlček and S. Zálíš, *Coord. Chem. Rev.*, 2007, **251**, 258–287.
228. P. Hay and W. Wadt, *J. Chem. Phys.*, 1985, **82**, 270.
229. N. Connelly and W. Geiger, *Chem. Rev.*, 1996, **96**, 877–910.
230. A. Kapturkiewicz, T. Chen, I. Laskar and J. Nowacki, *Electrochem. Commun.*, 2004, **6**, 827–831.
231. I. M. Dixon, J.-P. Collin, J.-P. Sauvage, L. Flamigni, S. Encinas and F. Barigelletti, *Chem. Soc. Rev.*, 2000, **29**, 385–391.
232. Y. Ohsawa, S. Sprouse, K. A. King, M. K. DeArmond, K. W. Hanck and R. J. Watts, *J. Phys. Chem.*, 1987, **91**, 1047–1054.
233. V. L. Whittle, *Ph.D. thesis*, Durham University, 2008.
234. S. Lamansky, P. I. Djurovich, D. Murphy, F. Abdel-Razzaq, R. C. Kwong, I. M. Tsyba, M. Bortz, B. Mui, R. Bau and M. E. Thompson, *Inorg. Chem.*, 2001, **40**, 1704–11.
235. D. Sandrini, M. Maestri, V. Balzani, U. Maeder and A. von Zelewsky, *Inorganic Chemistry*, 1988, **27**, 2640–2643.
236. J. Demas and G. Crosby, *J. Am. Chem. Soc.*, 1971, **93**, 2841–2847.
237. Y.-T. Huang, T.-H. Chuang, Y.-L. Shu, Y.-C. Kuo, P.-L. Wu, C.-H. Yang and I.-W. Sun, *Organometallics*, 2005, **24**, 6230–6238.
238. A. Cannizzo, A. M. Blanco-Rodríguez, A. El Nahhas, J. Šebera, S. Zálíš, A. Vlček, Jr. and M. Chergui, *J. Am. Chem. Soc.*, 2008, **130**, 8967–8974.
239. G. J. Hedley, A. Ruseckas and I. D. W. Samuel, *J. Phys. Chem. A*, 2009, **113**, 2–4.
240. A. Mamo, S. Nicoletti and N. C. Tat, *Molecules*, 2002, **7**, 618–627.
241. J. Kahl, K. Hanck and K. DeArmond, *J. Phys. Chem.*, 1978, **82**, 540–545.
242. C.-M. Che, K.-T. Wan, L.-Y. He, C.-K. Poon and V. W.-W. Yam, *J. Chem. Soc., Chem. Commun.*, 1989, 943–944.
243. E. C. Constable, R. P. G. Henney and D. A. Tocher, *Dalton Trans.*, 1991, 2335.
244. M. Maestri, D. Sandrini, A. von Zelewsky and C. Deuschel-Cornioley, *Inorg. Chem.*, 1991, **30**, 2476–2478.

REFERENCES

245. C. Pettijohn, E. Jochowitz, B. Chuong, J. Nagle and A. Vogler, *Coord. Chem. Rev.*, 1998, **171**, 85–92.
246. S. Hobert, *Inorg. Chim. Acta*, 2001, **318**, 89–96.
247. J. A. G. Williams, *Chem. Soc. Rev.*, 2009, **38**, 1783–1801.
248. L. Shi, T. Li, S. Zhao, H. Li and Z. Su, *Theor. Chem. Acc.*, 2009, **124**, 29–36.
249. P. Kvam, M. Puzyk, K. Balashev and J. Songstad, *Acta Chem. Scand.*, 1995, **49**, 335–343.
250. P. L. Brothwood, *MChem Report, Durham University*, 2008.
251. B. W. Ma, P. I. Djurovich and M. E. Thompson, *Coord. Chem. Rev.*, 2005, **249**, 1501–1510.
252. R. C. Evans, P. Douglas, J. A. G. Williams and D. L. Rochester, *J. Fluor.*, 2006, **16**, 201–206.
253. R. C. Evans and P. Douglas, *Anal. Chem.*, 2006, **78**, 5645–5652.
254. R. Rakhimov, Y. A. Weinstein, E. V. Lileeva and N. N. Zheligovskaya, *Russ. Chem. Bull., Int. Ed.*, 2003, **52**, 1150–1156.
255. J. Moore, J. Nash, P. Fanwick and D. McMillin, *Inorg. Chem.*, 2002, **41**, 6387–6396.
256. J. A. G. Williams, *Top. Curr. Chem.*, 2007, **281**, 205–268.
257. K. Nakamaru, *Bull. Chem. Soc. Jpn.*, 1982, **55**, 2697–2705.
258. C. Baik, W. Han, Y. Kang, S. Kang and J. Ko, *J. Organomet. Chem.*, 2006, **691**, 5900–5910.
259. A. F. Rausch, L. Murphy, J. A. G. Williams and H. Yersin, *Inorg. Chem.*, 2009, **48**, 11407–11414.
260. M. A. Baldo, S. Lamansky, P. E. Burrows, M. E. Thompson and S. R. Forrest, *Appl. Phys. Lett.*, 1999, **75**, 4–6.
261. C. Adachi, M. A. Baldo, S. R. Forrest and M. E. Thompson, *Appl. Phys. Lett.*, 2000, **77**, 904–906.
262. H. Yersin, and D. Donges, *Top. Curr. Chem.*, 2001, **214**, 81–186.

263. A. F. Rausch, H. H. H. Homeier and H. Yersin, *Top. Organomet. Chem.*, 2010, **29**, 193–235.
264. A. F. Rausch and H. Yersin, *Chem. Phys. Lett.*, 2010, **484**, 261–265.
265. T. Fischer, R. Czerwieniec, T. Hofbeck, M. M. Osminina and H. Yersin, *Chem. Phys. Lett.*, 2010, **486**, 53–59.
266. A. F. Rausch, M. E. Thompson and H. Yersin, *Chem. Phys. Lett.*, 2009, **468**, 46–51.
267. M. Cocchi, J. Kalinowski, D. Virgili and J. A. G. Williams, *Appl. Phys. Lett.*, 2008, **92**, 113302.
268. J. Pina, J. de Melo, H. Burrows, A. Monkman and S. Navaratnam, *Chem. Phys. Lett.*, 2004, **400**, 441–445.
269. Bruker 2003 SAINT-Plus. Version 6.45. Bruker AXS Inc., Madison, Wisconsin, USA,.
270. G. M. Sheldrick, *Acta Cryst. A*, 2008, **64**, 112–122.
271. G. M. Sheldrick, *SHELXL-97, Crystal Structure Refinement Program, University of Göttingen.*
272. O. V. Dolomanov, L. J. Bourhis, R. J. Gildea, J. A. K. Howard and H. Puschmann, *J. Appl. Crystallogr.*, 2009, **42**, 339–341.
273. S. Murov, G. Hug and I. Carmichael, *Handbook of Photochemistry*, CRC Press, New York, 1993.
274. M. J. Frisch, G. W. Trucks, H. B. Schlegel, G. E. Scuseria, M. A. Robb, J. R. Cheeseman, G. Scalmani, V. Barone, B. Mennucci, G. A. Petersson, H. Nakatsuji, M. Caricato, X. Li, H. P. Hratchian, A. F. Izmaylov, J. Bloino, G. Zheng, J. L. Sonnenberg, M. Hada, M. Ehara, K. Toyota, R. Fukuda, J. Hasegawa, M. Ishida, T. Nakajima, Y. Honda, O. Kitao, H. Nakai, T. Vreven, J. A. Montgomery, Jr., J. E. Peralta, F. Ogliaro, M. Bearpark, J. J. Heyd, E. Brothers, K. N. Kudin, V. N. Staroverov, R. Kobayashi, J. Normand, K. Raghavachari, A. Rendell, J. C. Burant, S. S. Iyengar, J. Tomasi, M. Cossi, N. Rega, J. M. Millam, M. Klene, J. E. Knox, J. B. Cross, V. Bakken, C. Adamo, J. Jaramillo, R. Gomperts, R. E. Stratmann, O. Yazyev, A. J. Austin, R. Cammi, C. Pomelli, J. W. Ochterski, R. L. Martin, K. Morokuma, V. G. Zakrzewski, G. A. Voth, P. Salvador, J. J. Dannenberg, S. Dapprich, A. D. Daniels, . Farkas, J. B.

REFERENCES

- Foresman, J. V. Ortiz, J. Cioslowski and D. J. Fox, *Gaussian 09 Revision A.1*, Gaussian Inc. Wallingford CT 2009.
275. N. Miyaura and A. Suzuki, *Chem. Rev.*, 1995, **95**, 2457–2483.
276. I. Butler, W. Cullen, T. Kim, S. Rettig and J. Trotter, *Organometallics*, 1985, **4**, 972–980.
277. G. Allinson, R. J. Bushby, M. V. Jesudason, J.-L. Paillaud and N. Taylor, *J. Chem. Soc., Perkin Trans. 2*, 1997, 147–156.
278. A. Eckert and F. Seidel, *J. Prakt. Chem.*, 1921, **102**, 338–360.
279. N. Nazarpack-Kandlousy, M. Nelen, V. Goral and A. Eliseev, *J. Org. Chem.*, 2002, **67**, 59–65.
280. B. A. Schweitzer and E. T. Kool, *J. Org. Chem.*, 1994, **59**, 7238–7242.
281. N. Miyaura, T. Yanagi and A. Suzuki, *Synth. Commun.*, 1981, **11**, 513–519.
282. T. Watanabe, N. Miyaura and A. Suzuki, *Synlett*, 1992, 207–210.

Appendix A

A1: Crystal data and structure refinement for 1-diqb, 1

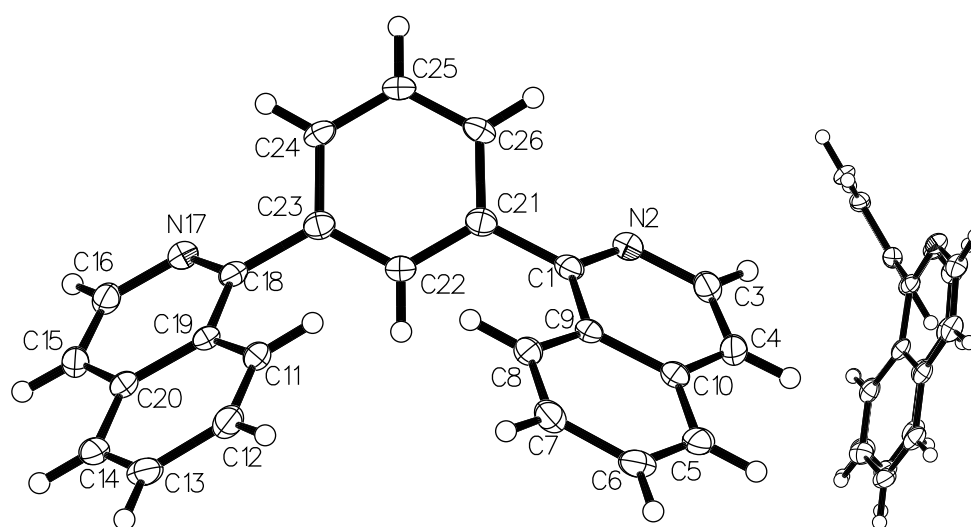


Fig. 1 Molecular structure of 1-diqb, 1 with ellipsoids at the 50 % probability level.

Table 1 Refinement data for 1-diqb, **1**.

Empirical formula	C ₂₄ H ₁₆ N ₂
Formula weight	332.39
Temperature/K	393(2)
Crystal system	Monoclinic
Space group	Cm
a/Å, b/Å, c/Å	8.6722(15), 24.417(4), 3.9321(6)
$\alpha/^\circ, \beta/^\circ, \gamma/^\circ$	90.00, 103.73(4), 90.00
Volume/Å ³	808.8(2)
Z	2
$\rho_{calc}/\text{mg mm}^{-3}$	1.365
μ/mm^{-1}	0.080
F(000)	348
Crystal size/mm ³	0.2 × 0.015 × 0.015
2 Θ range for data collection	3.34 to 50.02°
Index ranges	-10 ≤ h ≤ 10, -29 ≤ k ≤ 28, -4 ≤ l ≤ 4
Reflections collected	3258
Independent reflections	741[R(int) = 0.0675]
Data/restraints/parameters	741/2/121
Goodness-of-fit on F ²	1.076
Final R indexes [I > 2 σ (I)]	R ₁ = 0.0384, wR ₂ = 0.0908
Final R indexes [all data]	R ₁ = 0.0495, wR ₂ = 0.0979
Largest diff. peak/hole/e Å ⁻³	0.164/-0.302

A2: Crystal data and structure refinement for 8-dqb, 2

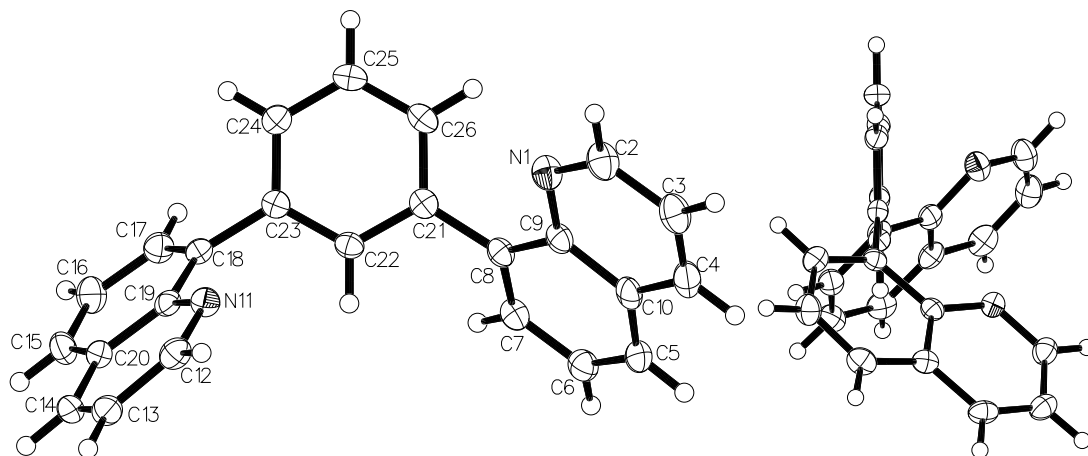


Fig. 2 Molecular structure of 8-dqb, 2 with ellipsoids at the 50 % probability level.

Table 2 Refinement data for 8-dqb, 2.

Empirical formula	$C_{24}H_{16}N_2$
Formula weight	332.39
Temperature/K	666(2)
Crystal system	Orthorhombic
Space group	Pcba
a/Å, b/Å, c/Å	12.2613(10), 10.4430(8), 26.645(2)
$\alpha/^\circ, \beta/^\circ, \gamma/^\circ$	90.00, 90.00, 90.00
Volume/Å ³	3411.7(5)
Z	8
$\rho_{calc}/\text{mg mm}^{-3}$	1.294
μ/mm^{-1}	0.076
F(000)	1392
Crystal size/mm ³	0.50 × 0.10 × 0.03
2 θ range for data collection	3.06 to 50°
Index ranges	$-14 \leq h \leq 14, -12 \leq k \leq 12, -31 \leq l \leq 31$
Reflections collected	27666
Independent reflections	3004[R(int) = 0.0641]
Data/restraints/parameters	3004/0/235
Goodness-of-fit on F ²	1.100
Final R indexes [I > 2 σ (I)]	R ₁ = 0.0435, wR ₂ = 0.0884
Final R indexes [all data]	R ₁ = 0.0656, wR ₂ = 0.0966
Largest diff. peak/hole/e Å ⁻³	0.155/−0.206

A3: Crystal data and structure refinement for dMeBpin, 7

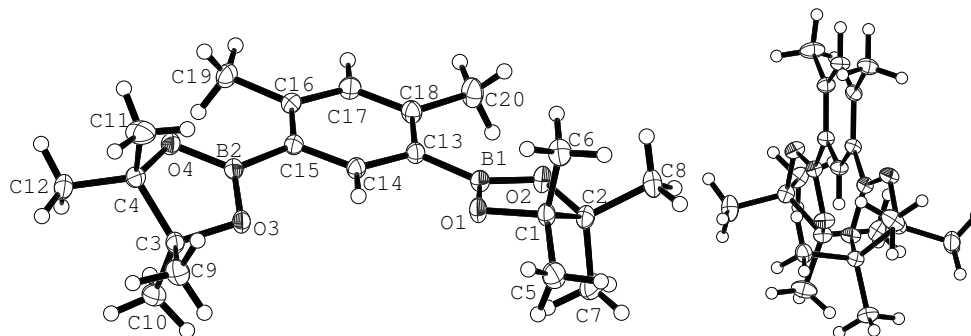


Fig. 3 Molecular structure of dMeBpin, **7**, with ellipsoids at the 50 % probability level.

Table 3 Refinement data for dMeBpin, **7**.

Empirical formula	$C_{20}H_{32}B_2O_4$
Formula weight	358.08
Temperature/K	120
Crystal system	Triclinic
Space group	P-1
a/Å, b/Å, c/Å	10.4454(13), 20.7164(13), 11.1709(14)
$\alpha/^\circ, \beta/^\circ, \gamma/^\circ$	69.084(6), 63.120(6), 88.136(7)
Volume/Å ³	1029.3(2)
Z	2
$\rho_{calc}/\text{mg mm}^{-3}$	1.155
μ/mm^{-1}	0.076
F(000)	388.0
Crystal size/mm ³	0.42 × 0.32 × 0.11
2 Θ range for data collection	4.12 to 59.94°
Index ranges	-13 ≤ h ≤ 14, -14 ≤ k ≤ 12, -15 ≤ l ≤ 15
Reflections collected	12177
Independent reflections	5678[R(int) = 0.0190]
Data/restraints/parameters	5678/0/255
Goodness-of-fit on F ²	1.015
Final R indexes [I > 2 σ (I)]	R ₁ = 0.0416, wR ₂ = 0.1112
Final R indexes [all data]	R ₁ = 0.0487, wR ₂ = 0.1172
Largest diff. peak/hole/e Å ⁻³	0.42/-0.22

A4: Crystal data and structure refinement for 2-dqFb, 13

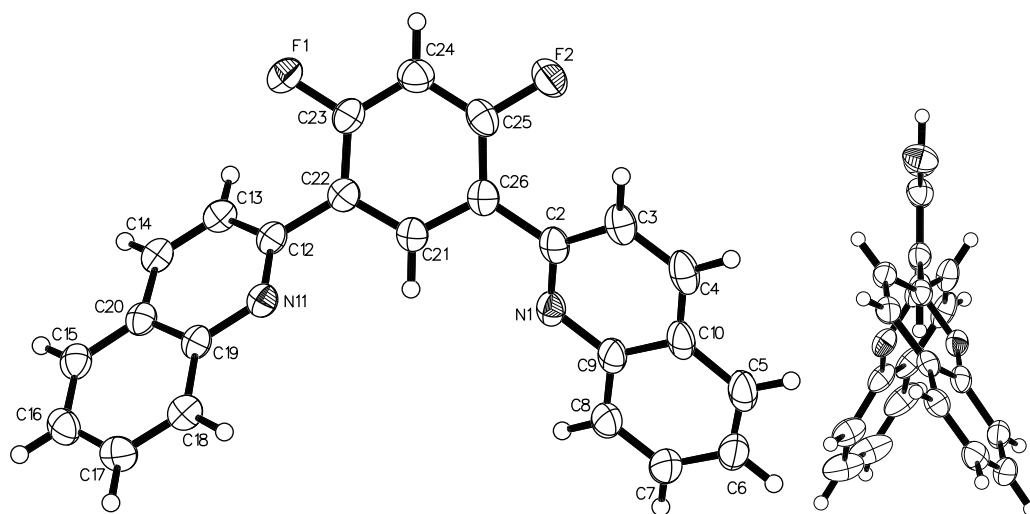


Fig. 4 Molecular structure of 2dqFb, 13 with ellipsoids at the 50 % probability level.

Table 4 Refinement data for 2-dqFb, **13**.

Empirical formula	C ₂₄ H ₁₄ F ₂ N ₂
Formula weight	368.37
Temperature/K	393(2)
Crystal system	Monoclinic
Space group	C2/c
a/Å, b/Å, c/Å	19.2493(4), 5.91410(10), 30.6178(7)
$\alpha/^\circ, \beta/^\circ, \gamma/^\circ$	90.00, 94.1730(10), 90.00
Volume/Å ³	3476.36(12)
Z	8
$\rho_{calc}/\text{mg mm}^{-3}$	1.408
μ/mm^{-1}	0.098
F(000)	1520
Crystal size/mm ³	0.40 × 0.20 × 0.12
2 Θ range for data collection	4.24 to 52.72°
Index ranges	-23 ≤ h ≤ 24, -7 ≤ k ≤ 7, -38 ≤ l ≤ 38
Reflections collected	17480
Independent reflections	3562[R(int) = 0.0444]
Data/restraints/parameters	3562/0/253
Goodness-of-fit on F ²	1.015
Final R indexes [I > 2 σ (I)]	R ₁ = 0.0432, wR ₂ = 0.1073
Final R indexes [all data]	R ₁ = 0.0711, wR ₂ = 0.1254
Largest diff. peak/hole/e Å ⁻³	0.182/-0.211

A5: Crystal data and structure refinement for dqp, 17

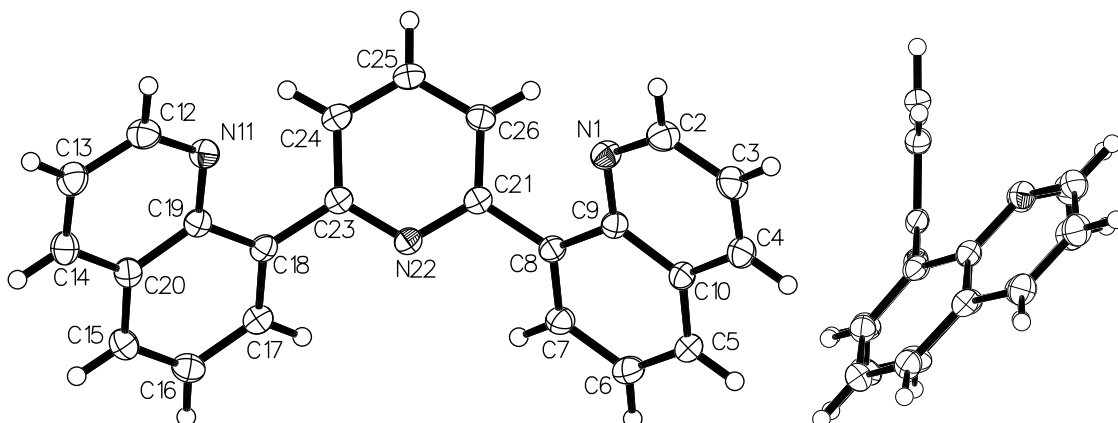


Fig. 5 Molecular structure of dqp, 17 with ellipsoids at the 50 % probability level.

Table 5 Refinement data for dqp, 17.

Empirical formula	$C_{23}H_{15}N_3$
Formula weight	333.38
Temperature/K	393(2)
Crystal system	Trigonal
Space group	$P3_2$
$a/\text{\AA}$, $b/\text{\AA}$, $c/\text{\AA}$	13.3380(2), 13.3380(2), 8.0192(2)
$\alpha/^\circ$, $\beta/^\circ$, $\gamma/^\circ$	90.00, 90.00, 120.00
Volume/ \AA^3	1235.50(4)
Z	3
$\rho_{calc}/\text{mg mm}^{-3}$	1.344
μ/mm^{-1}	0.081
F(000)	522
Crystal size/ mm^3	$0.27 \times 0.12 \times 0.08$
2θ range for data collection	3.52 to 60.98°
Index ranges	$-19 \leq h \leq 19$, $-19 \leq k \leq 18$, $-11 \leq l \leq 11$
Reflections collected	19784
Independent reflections	2516[R(int) = 0.0338]
Data/restraints/parameters	2516/1/236
Goodness-of-fit on F^2	1.059
Final R indexes [$I > 2\sigma(I)$]	$R_1 = 0.0363$, $wR_2 = 0.0957$
Final R indexes [all data]	$R_1 = 0.0394$, $wR_2 = 0.0984$
Largest diff. peak/hole/ $e \text{\AA}^{-3}$	0.293/ -0.176

A6: Crystal data and structure refinement for qBrpy, 19

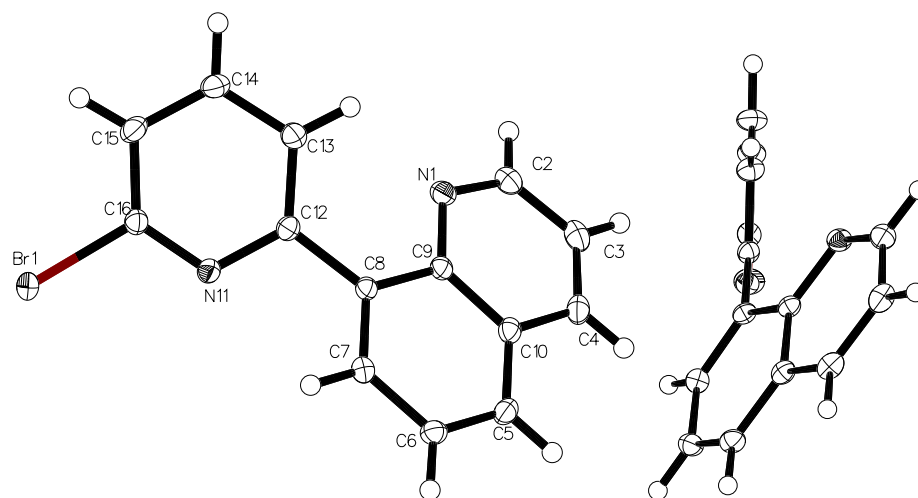


Fig. 6 Molecular structure of qBrpy, **19** with ellipsoids at the 50 % probability level.

Table 6 Refinement data for qBrpy, **19**.

Empirical formula	C ₁₄ H ₉ BrN ₂
Formula weight	285.14
Temperature/K	393(2)
Crystal system	Monoclinic
Space group	P2 ₁ /c
a/Å, b/Å, c/Å	3.92230(10), 15.1592(3), 18.7481(4)
α/°, β/°, γ/°	90.00, 95.3570(10) 90.00
Volume/Å ³	1109.87(4)
Z	4
ρ _{calc} /mg mm ⁻³	1.706
μ/mm ⁻¹	3.678
F(000)	568
Crystal size/mm ³	0.40 × 0.24 × 0.14
2Θ range for data collection	3.46 to 56.64°
Index ranges	-5 ≤ h ≤ 5, -20 ≤ k ≤ 20, -24 ≤ l ≤ 24
Reflections collected	14991
Independent reflections	2760[R(int) = 0.0261]
Data/restraints/parameters	2760/0/154
Goodness-of-fit on F ²	1.020
Final R indexes [I > 2σ(I)]	R ₁ = 0.0194, wR ₂ = 0.0499
Final R indexes [all data]	R ₁ = 0.0228, wR ₂ = 0.0514
Largest diff. peak/hole/e Å ⁻³	0.428/-0.363

**A7: Crystal data and structure refinement for Ir(1-diqb)(ppy)Cl,
25**

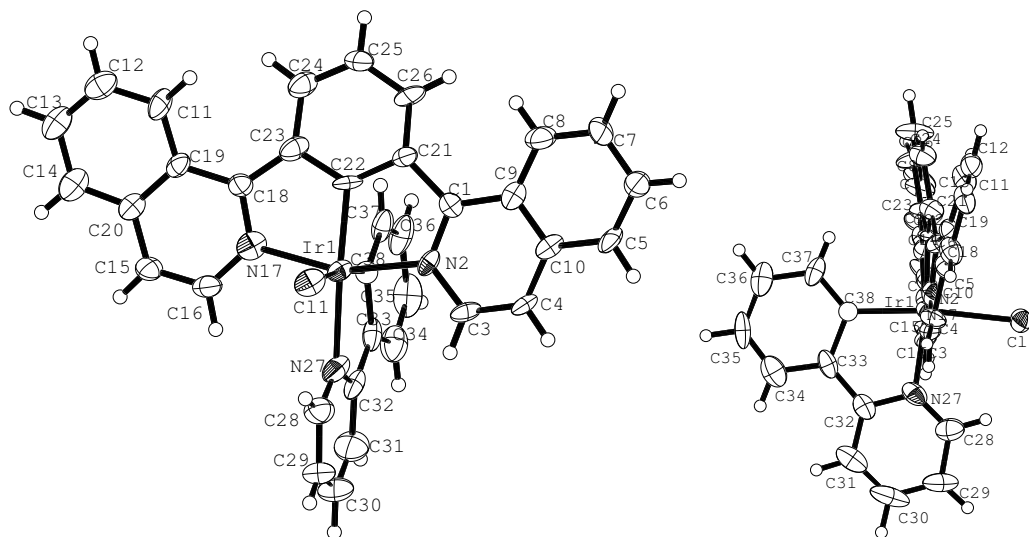


Fig. 7 Molecular structure of Ir(1-diqb)(ppy)Cl, 25

Table 7 Refinement data for Ir(1-diqb)(ppy)Cl, **25**.

Empirical formula	$C_{36} \cdot 666667 H_{30} \cdot 666667 N_3 O_2 \cdot 333333 ClIr$
Formula weight	778.29
Temperature/K	120
Crystal system	Monoclinic
Space group	Im
a/Å, b/Å, c/Å	10.6873(11), 32.019(4), 14.1789(19)
$\alpha/^\circ, \beta/^\circ, \gamma/^\circ$	90.00, 104.476(13), 90.00
Volume/Å ³	4697.9(10)
Z	6
$\rho_{calc}/mg\ mm^{-3}$	1.651
μ/mm^{-1}	4.387
F(000)	2306.0
Crystal size/mm ³	0.2 × 0.1 × 0.01
2 Θ range for data collection	3.22 to 49.98°
Index ranges	-12 ≤ h ≤ 11, -38 ≤ k ≤ 25, -16 ≤ l ≤ 16
Reflections collected	13063
Independent reflections	7756[R(int) = 0.0561]
Data/restraints/parameters	7756/386/615
Goodness-of-fit on F ²	1.018
Final R indexes [I > 2 σ (I)]	R ₁ = 0.0501, wR ₂ = 0.0967
Final R indexes [all data]	R ₁ = 0.0752, wR ₂ = 0.1074
Largest diff. peak/hole/e Å ⁻³	1.27/-1.22
Flack parameter	0.013(13)

A8: Crystal data and structure refinement for Rh(1-diqb)(ppy)Cl, **32**

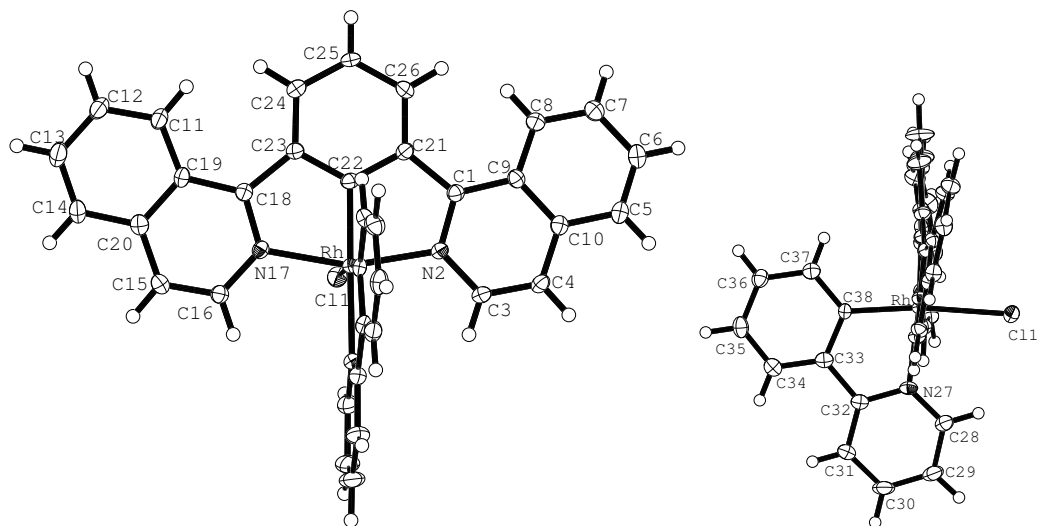


Fig. 8 Molecular structure of Rh(1-diqb)(ppy)Cl, **32** with solvent molecules omitted for clarity.

Table 8 Refinement data for Rh(1-diqb)(ppy)Cl, **32**.

Empirical formula	C ₃₈ H ₂₃ N ₃ Cl ₁₀ RhD ₃
Formula weight	985.05
Temperature/K	120
Crystal system	Monoclinic
Space group	P2 ₁ /n
a/Å, b/Å, c/Å	12.7369(5), 20.9651(9), 15.5635(5)
α/°, β/°, γ/°	90.00, 110.547(14), 90.00
Volume/Å ³	3891.5(3)
Z	4
ρ _{calc} /mg mm ⁻³	1.681
μ/mm ⁻¹	1.160
F(000)	1960.0
Crystal size/mm ³	0.37 × 0.08 × 0.04
2θ range for data collection	3.4 to 59.98°
Index ranges	-17 ≤ h ≤ 17, -29 ≤ k ≤ 29, -21 ≤ l ≤ 21
Reflections collected	52935
Independent reflections	11325[R(int) = 0.0377]
Data/restraints/parameters	11352/0/489
Goodness-of-fit on F ²	2.047
Final R indexes [I > 2σ(I)]	R ₁ = 0.0582, wR ₂ = 0.1595
Final R indexes [all data]	R ₁ = 0.0694, wR ₂ = 0.1626
Largest diff. peak/hole/e Å ⁻³	3.15/-1.10

A9: Crystal data and structure refinement for Pt(8-dqMeb)Cl, 39

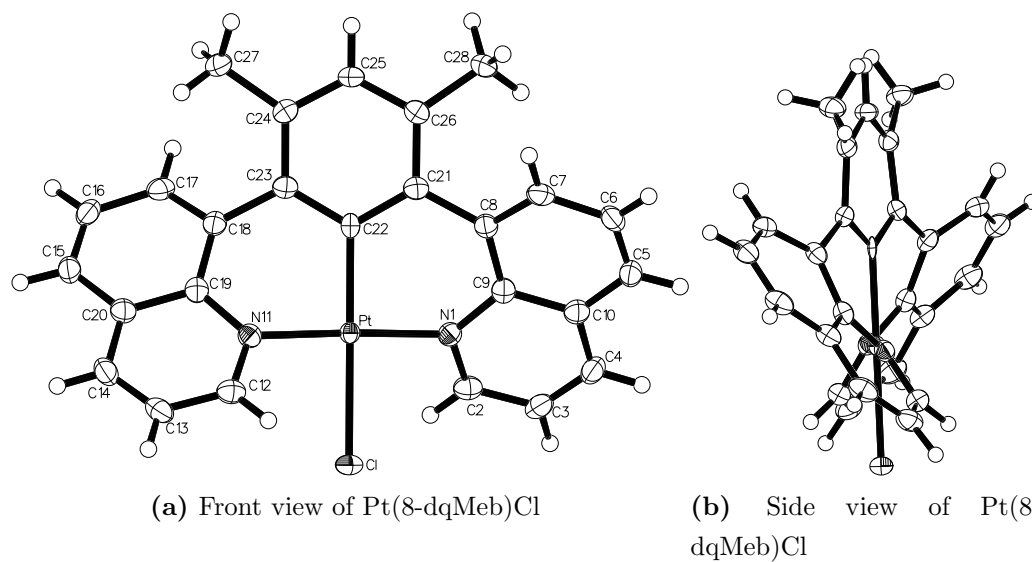


Fig. 9 Molecular structure of Pt(8-dqMeb)Cl, **39**, with ellipsoids at the 50 % probability level.

Table 9 Refinement data for Pt(8-dqMeb)Cl, **39**.

Empirical formula	C ₂₆ H ₁₉ N ₂ ClPt
Formula weight	589.97
Temperature/K	393(2)
Crystal system	Orthorhombic
Space group	Pbcn
a/Å, b/Å, c/Å	14.8633(4), 13.6416(4), 9.5078(3)
α /°, β /°, γ /°	90.00, 90.00, 90.00
Volume/Å ³	1927.79(10)
Z	4
ρ_{calc} /mg mm ⁻³	2.033
μ /mm ⁻¹	7.434
F(000)	1136
Crystal size/mm ³	0.28 × 0.26 × 0.04
2 Θ range for data collection	4.06 to 52.74°
Index ranges	-18 ≤ h ≤ 16, -15 ≤ k ≤ 17, -11 ≤ l ≤ 11
Reflections collected	12194
Independent reflections	1972[R(int) = 0.0400]
Data/restraints/parameters	1972/0/139
Goodness-of-fit on F ²	1.028
Final R indexes [I > 2 σ (I)]	R ₁ = 0.0201, wR ₂ = 0.0485
Final R indexes [all data]	R ₁ = 0.0304, wR ₂ = 0.0565
Largest diff. peak/hole/e Å ⁻³	2.163/-0.830

Appendix B

B1: Additional orbital plots for 1-diqb-based complexes

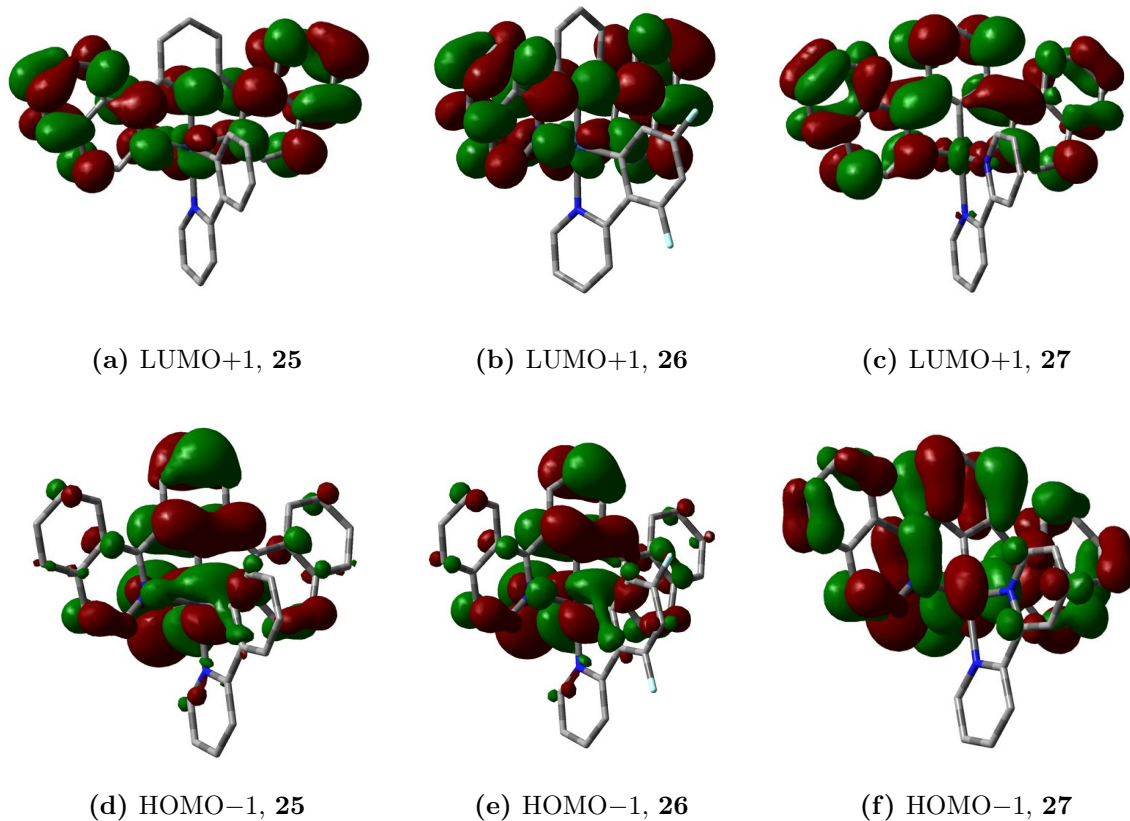


Fig. 10 Orbital plots for Ir(1-diqb)(ppy)Cl, **25**, Ir(1-diqb)(dFppy)Cl, **26** and [Ir(1-diqb)(bpy)Cl]⁺, **27**, calculated by DFT.

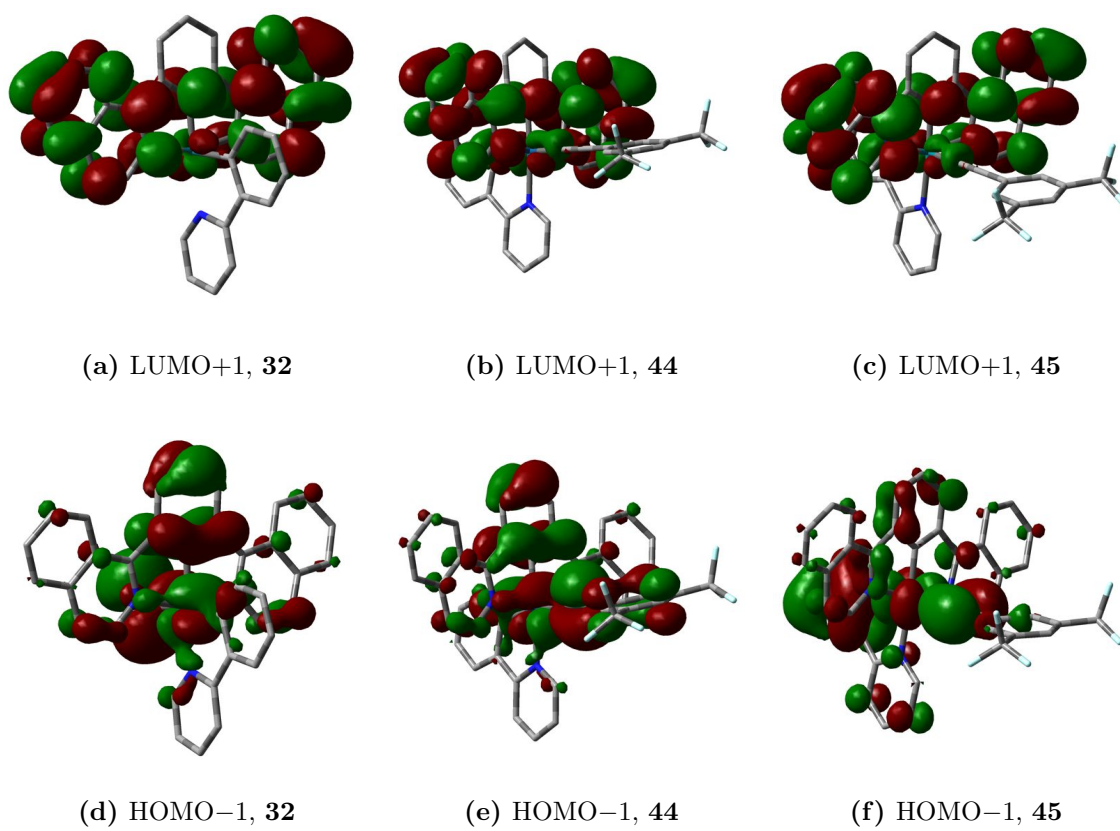


Fig. 11 Orbital plots for Rh(1-diqb)(ppy)Cl, **32**, Ir(1-diqb)(ppy)CC-tfp, **44** and Rh(1-diqb)(ppy)CC-tfp, **45**, calculated by DFT.

B2: Additional orbital plots for Ir(III) complexes based upon further isomers of terdentate quinolyl ligands

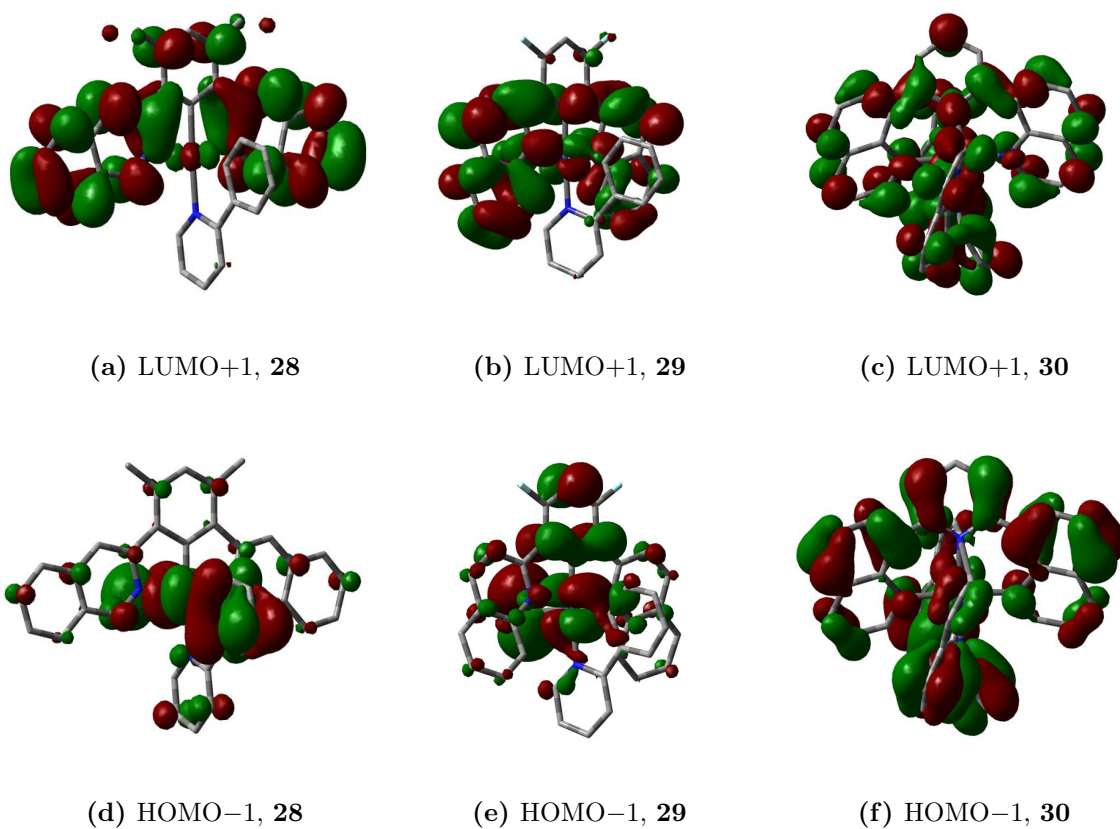
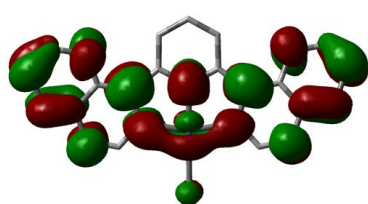
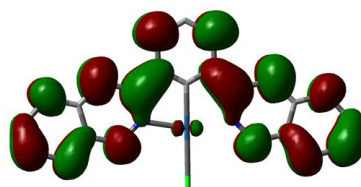


Fig. 12 Orbital plots for Ir(3-diqMeb)(ppy)Cl, **28**, Ir(2-dqFb)(ppy)Cl, **29** and [Ir(dqp)₂]³⁺, **30**, calculated by DFT.

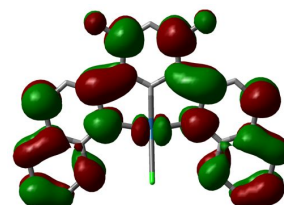
B3: Additional orbital plots for platinum complexes containing five-membered chelate rings



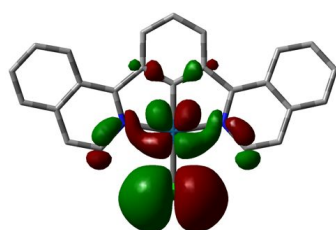
(a) LUMO+1, **33**



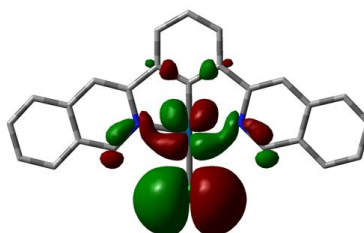
(b) LUMO+1, **34**



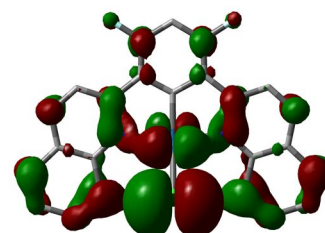
(c) LUMO+1, **37**



(d) HOMO-1, **33**



(e) HOMO-1, **34**



(f) HOMO-1, **37**

Fig. 13 Orbital plots for Pt(1-diqb)Cl, **33**, Pt(3-diqMeb)Cl, **34** and Pt(2-dqFb)Cl, **37**, calculated by DFT.

B4: Additional orbital plots for platinum complexes containing six-membered chelate rings with N⁺C⁺N-coordinating ligands

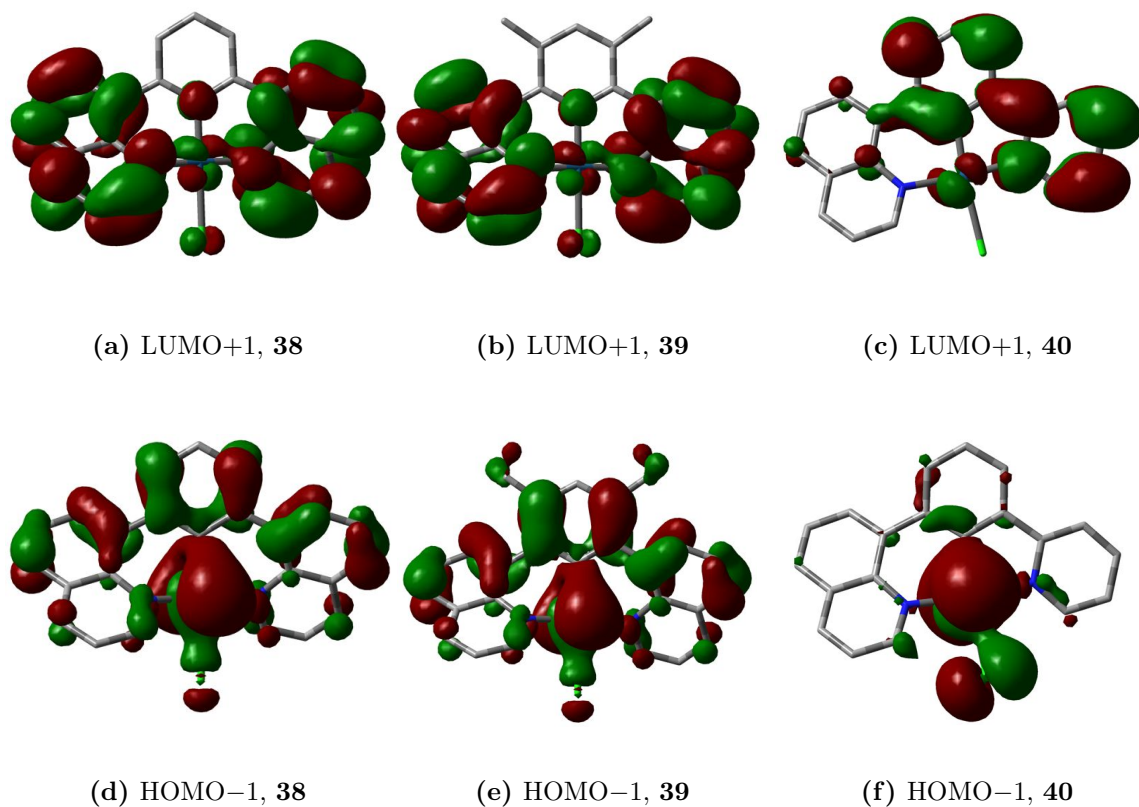


Fig. 14 Orbital plots for Pt(8-dqb)Cl, **38**, Pt(8-dqMeb)Cl, **39** and Pt(qpyb)Cl, **40**, calculated by DFT.

B5: Additional orbital plots for platinum complexes containing six-membered chelate rings with N[^]N[^]N-coordinating ligands

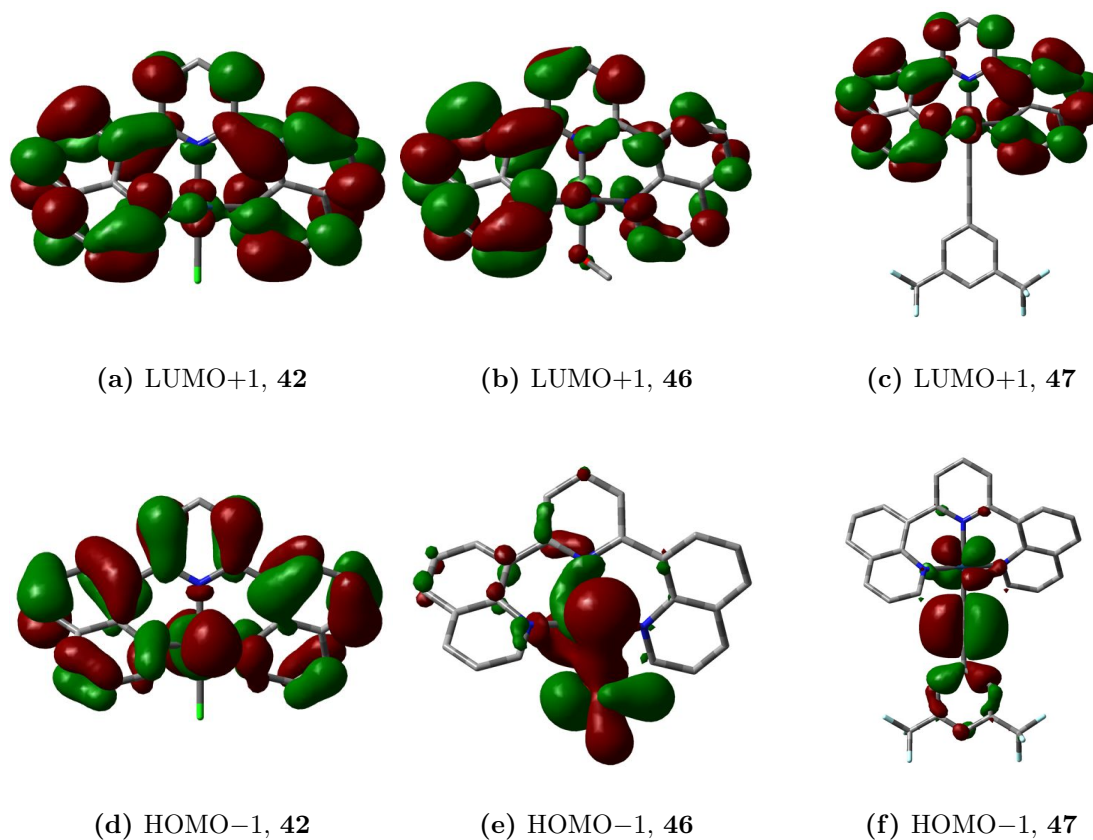


Fig. 15 Orbital plots for $[\text{Pt}(\text{dqp})\text{Cl}]^+$, **42**, $[\text{Pt}(\text{dqp})\text{OMe}]^+$ **46** and $[\text{Pt}(\text{dqp})\text{CC-tfp}]^+$, **47**, calculated by DFT.

B6: DFT plots for the six-membered N[^]N[^]N-coordinated complex Pt(7-aza-indolyl)Cl, Pt(azi)Cl

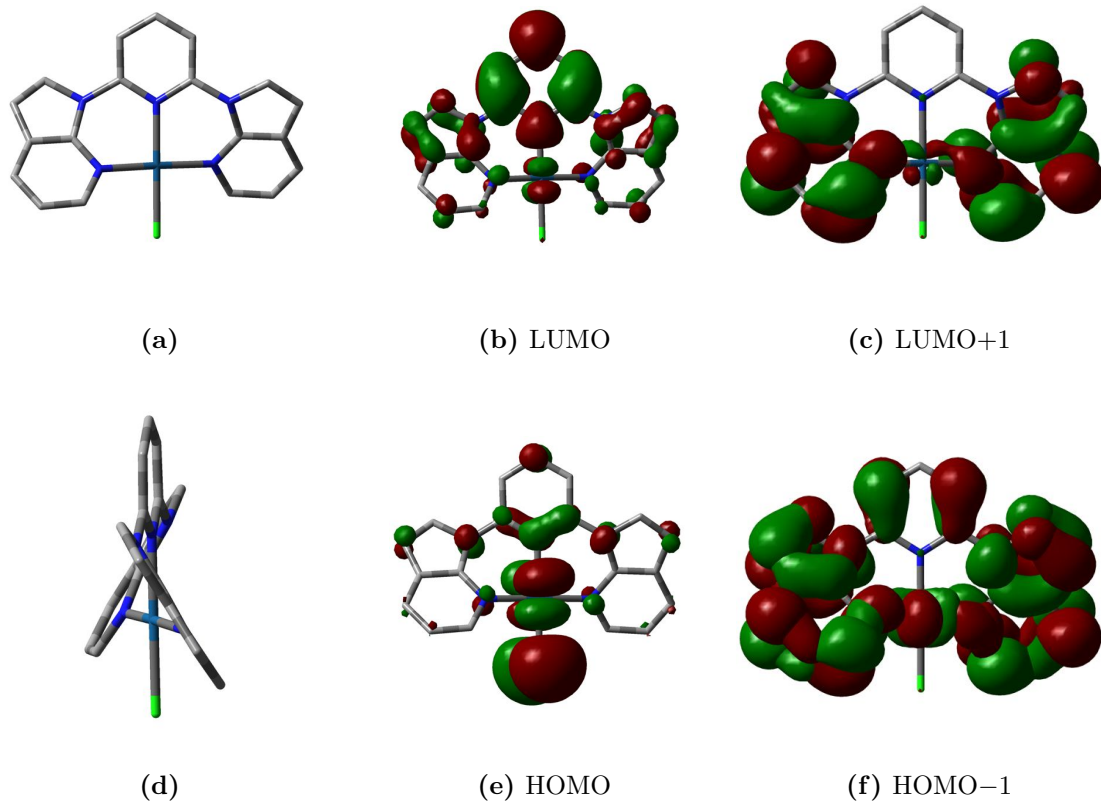


Fig. 16 Structural optimisation and frontier orbital plots for Pt(azi)Cl, calculated by DFT.

Appendix C

C1: Conferences attended

- Universities of Scotland Inorganic Chemistry (USIC) Conference 2008, Glasgow, UK (Sep 2008). *Poster Presentation*: Luminescent Terdentate Iridium Complexes for use in Light-Emitting Devices.
- COST Meeting, Bologna, Italy (Aug 2009). *Oral Presentation*: Exploring New Luminescent Complexes Containing Quinolines and Six-Membered Chelating Units.
- Universities of Scotland Inorganic Chemistry (USIC) Conference 2009, Edinburgh, UK (Sep 2009). *Oral Presentation*: Exploring New Luminescent Complexes Containing Quinolines and Six-Membered Chelating Units. Received first prize in the oral presentations category.
- Young and Early Careers Researchers' Meeting: Photochemistry Group, Durham, UK (Jan 2010). *Poster Presentation*: Luminescent Terdentate Iridium Complexes for use in Light-Emitting Devices.
- Universities of Scotland Inorganic Chemistry (USIC) Conference 2010, Durham, UK (Jul 2010). *Poster Presentation*: Luminescent Terdentate Transition Metal Complexes for OLEDs. Received an honourable mention.

C2: Publications

Aspects of this work have been published in the following publication:

K. L. Garner, L. F. Parkes, J. D. Piper and J. A. G. Williams —
“Luminescent Platinum Complexes with Terdentate Ligands forming 6-Membered Chelate Rings: Advantageous and Deleterious Effects in N^3 and N^2C -coordinated Complexes”, *Inorg. Chem.*, 2010, **49**, 476–487.